Inference and modeling of biological networks : from active matter to the immune system

Victor Chardès

PSL UNIVERSITÉ PARIS

THÈSE DE DOCTORAT
DE L'UNIVERSITÉ PSL

Préparée à l'Ecole Normale Supérieure

Inference and modeling of biological networks

From active matter to the immune system

Soutenue par
Victor Chardès
Le 21 septembre 2022

École doctorale n°564
Physique en Île-de-France

Spécialité
Physique

Composition du jury :

Sarah Cobey University of Chicago	*Rapporteure*
Ville Mustonen University of Helsinki	*Rapporteur*
Olivier Tenaillon Université Paris Diderot	*Président du jury*
Olivier Rivoire Collège de France	*Examinateur*
Thierry Mora École Normale Supérieure	*Directeur de thèse*
Aleksandra Walczak École Normale Supérieure	*Directrice de thèse*

ENS | PSL

LPENS
LABORATOIRE DE PHYSIQUE
DE L'ÉCOLE NORMALE SUPÉRIEURE

À Louis, Louis-même

Remerciements

J'aimerais d'abord remercier Aleksandra Walczak et Thierry Mora pour avoir encadré mon travail de thèse avec une immense bienveillance. À un long moment de flottement entre deux domaines, la matière active et l'immunologie, a succédé une période de pandémie difficile pour nous tous à bien des égards. Votre patience et votre confiance ont été indispensables pour affronter ces obstacles et pour construire un projet de recherche, certes bigarré, mais dont je suis plutôt fier. Je vous suis infiniment reconnaissant pour toutes les opportunités que m'avez offertes, tant sur le plan scientifique que sur le plan humain.

I would like to thank Sarah Cobey and Ville Mustonen for having agreed to review this manuscript, as well as Olivier Tenaillon and Olivier Rivoire for having agreed to be members of the jury. Our discussions have been particularly interesting and have brought me to consider in a new light some of the conclusions of this work.

Je crois qu'il est important de reconnaître ici que ce doctorat s'est fait dans la douleur, en témoigne l'aspect hétéroclite des travaux présentés dans ce manuscrit. Dans ce contexte, j'ai eu l'immense chance d'être entouré d'amis formidables qui constituent la véritable réussite de mes quatre dernières années. J'aimerais les remercier pour tout le soutien qu'ils m'ont apporté.

À mes amis du laboratoire avec qui j'ai partagé la barque durant toutes ces années. Natanael, for our never-ending discussions on all possible topics, with this delightful sarcastic take on our everyday struggles. María, for our constant fights over every possible topic, always ending on the realization of how miserable we were. Federica, pour ces moments partagés au tout début de cette aventure, et pour ce soutien mutuel que l'on s'accorde depuis. Meriem, pour ton enthousiasme à toute épreuve. Francesco, pour ta sincérité et ton sens de la convivialité. Andrea, for your chill take on life, and your recurrent advices not to work too much. Xiaowen, for your sarcasm always right on point. Maria Francesca, for your infinite energy. Paul, pour ton sens de l'humour discret mais tout aussi incisif. Enfin, à ceux qui étaient là pour une bonne partie du voyage, Jacopo, Giulio, Cosimo, Daniele, Marco, et tout les autres.

À mes copains du LPENS, Clément, Arnaud, Hugo, Stéphane, Tristan, Simon, Romaine, Alexandre, Antoine, pour tout ces cafés, ces repas, et ces discussions. Simon, Antoine, j'ai une pensée émue pour ces mémorables séances de sport.

À mes amis doctorants d'autres horizons, Romain, Guillaume, Flavien, Maxime, Renaud, Léa, pour tout ces repas improvisés et ces cafés à la dérobée.

À mes fidèles amis de PC. Gwen, pour ces dernières années passées à boire beaucoup de très bonnes bières et à regarder avec trop d'enthousiasme des émissions douteuses. À Lulu, pour ces milliards d'années passées ensemble, pour ce confinement, pour ce Noël à deux, pour toutes ces très bonnes et très mauvaises blagues, et à toutes celles qu'il nous reste à faire.

À mes copains d'Assas, pour la chance immense que j'ai de vous retrouver à chaque

fois que je reviens dans le Sud, avec ce sentiment de n'être jamais vraiment parti.

À Julien et Timothée, mes deux acolytes. Pour tout nos moments passés à boire du très bon vin aux frais de Juju, pour votre mémorable poisson d'avril, pour nos vacances, pour nos soirées au Sully Jazz Circle (sans Julien le rabat joie), pour les jeux de société auxquels j'ai refusé et je refuserai de jouer, mais surtout, pour toutes les parties de pétanque qu'il nous reste à faire.

À Giulia, for our secret romance, in Boulder, Rome, Siena, Lyon, Paris. These moments have been by far among the bests of these last four years.

Comme souvent, quand vient le tour de la famille je suis à court de mots. Merci pour votre soutien inconditionnel et votre patience à l'épreuve de mes absences et de mes états d'âmes. Lilou, Brieux, merci de supporter sans broncher mes pitreries et d'être à la fois mon meilleur et mon pire public. Je pense à Aimé qui était très fier de nous trois. Mapi, merci pour tout l'amour et l'attention que tu me donnes, j'ai une chance immense de t'avoir. Maman, papa, merci pour votre simplicité et votre éducation, vous êtes mon unique modèle.

Contents

1 Introduction **3**

2 Résumé **7**

3 Modeling and inferring collective behavior **11**
3.1 Modeling collective behavior . . . 11
3.1.1 The Vicsek model . . . 11
3.1.2 Inertial dynamics . . . 13
3.2 Learning equations of motion from data . . . 15
3.2.1 Learning dynamical models . . . 15
3.2.2 Inference in the Vicsek model . . . 17

4 Building general Langevin models from discrete datasets **19**
4.1 Abstract . . . 19
4.2 Introduction . . . 19
4.3 Results . . . 21
4.3.1 Maximum-likelihood inference approach for Langevin dynamics . . . 21
4.3.2 Alternative non-Bayesian approach . . . 34
4.3.3 Role of the unobserved initial condition . . . 36
4.3.4 Interacting case . . . 37
4.3.5 Effect of experimental errors . . . 40
4.4 Conclusions . . . 42
4.5 Methods . . . 44
4.5.1 ISM simulations . . . 44

5 Modeling the immune response **47**
5.1 Overview of the immune system . . . 47
5.2 The adaptive immune system . . . 48
5.2.1 Receptor diversity . . . 48
5.2.2 Clonal selection theory . . . 49
5.3 B-cell repertoire . . . 50
5.3.1 Affinity maturation . . . 50
5.3.2 Typical immune response . . . 52
5.4 Modeling adaptive immunity . . . 53
5.4.1 Repertoire dynamics . . . 54
5.4.2 Optimal immune response . . . 55
5.5 Theory of decision making . . . 56

6 Affinity maturation for an optimal balance between long-term immune coverage and short-term resource constraints 59
6.1 Introduction . . . 59
6.2 Results . . . 61
6.2.1 Affinity maturation strategies for recurring infections . . . 61
6.2.2 Phase diagram of optimal affinity maturation strategies . . . 65
6.2.3 Analytical results in a solvable model . . . 67
6.2.4 Population dynamics of optimized immune systems . . . 68
6.2.5 Comparison to experimental clone-size distributions . . . 70
6.2.6 Inhibition of affinity maturation and antigenic imprinting . . . 71
6.3 Discussion . . . 73
6.4 Methods . . . 76
6.4.1 Mathematical model . . . 76
6.4.2 Monte-Carlo estimation of the optimal strategies . . . 76

7 Eco-evolutionary stability of viral strategies 77
7.1 Introduction . . . 77
7.2 Results . . . 78
7.2.1 Coarse-grained SI(R) model for antigenically evolving pathogens . . . 78
7.2.2 Finite size induced cross-over in antigenic evolution . . . 80
7.2.3 Invasion criteria and the evolution of viral strategies . . . 82
7.2.4 Evolutionary stable virulence . . . 84
7.2.5 Evolutionary stable mutation rate . . . 86
7.3 Conclusions . . . 88
7.4 Methods . . . 89
7.4.1 Simulations of viral immune co-evolution . . . 89
7.4.2 Simulations of the evolutionary dynamics of viral strategies . . . 90

8 Conclusions 91
8.1 Main contributions of this thesis . . . 91
8.2 Directions for future research . . . 93

A Appendix 95
A.1 Building general Langevin models from discrete datasets . . . 95
A.1.1 Discretization procedure . . . 95
A.1.2 Inference formulas . . . 96
A.1.3 Equations of motion of the ISM in the spin wave approximation . . . 108
A.2 Affinity maturation for an optimal balance between long-term immune coverage and short-term resource constraints . . . 111
A.2.1 Mean-field de novo coverage . . . 111
A.2.2 Transition from monoclonal to de novo phase at $\sigma_v = 0$ . . . 112
A.2.3 Analytical results in a solvable model . . . 113
A.2.4 Population dynamics in sequential immunization . . . 116
A.3 Eco-evolutionary stability of viral strategies . . . 121
A.3.1 Calculation of the speed of the wave . . . 121
A.3.2 Solution of the diffusion equation with linear growth rate . . . 123

Bibliography **125**

1

Introduction

Biological networks can be loosely defined as an ensemble of interacting biologically active entities. Actin filaments and molecular motors self-organizing in the cells cytoskeleton, birds collectively moving in a flock or immune cells interacting in the immune system are examples of biological networks. In these systems, constituents at the smallest scales consume energy to self-organize and induce an emergent functional behavior at a larger scale. For instance, microtubules and molecular motors self-organize in a non-linear elastic cytoskeleton to ensure tissue integrity (1; 2), birds collectively align in flocks to increase their ability to escape predators (3; 4), and immune cells cluster in diverse cell subsets to efficiently recognize and eradicate pathogens. Inspired by statistical physics, models treating statistically the interactions between each constituent of the network have been successfully applied to describe self-organization in the cell cytoskeleton or collective motion in bird flocks. In the first part of this thesis we develop inference methods to learn statistical physics models directly from experimental biological data. Despite their success in the field of active matter, these models are unusuable to describe networks spanning multiple scales of space and time, and in particular the immune system. To fill this gap, models describing the organization of biological networks as resulting from an optimality principle have been developed. In the recent years, this approach, which shares similarities with machine learning methods (5; 6), has been repeatedly applied to model the immune system (7; 8; 9). Following this line of thinking, in the second part of this thesis we model the B-cell immune response to pathogens using tools of decision theory and we describe how the resulting immune pressure shapes the evolution of viral populations.

Historically, statistical physics approaches to self-organization originated with the work of Vicsek et al. (10), which introduced an agent-based first order stochastic model to describe the collective motion observed in flocks of birds. Along with the hydrodynamic theory of flocking developed a few years later by Toner et al. (11), these ideas gave birth to the field of active matter and triggered an intensive experimental research on active biological systems like biopolymers (12; 13; 14), bacteria colonies (15) and cell assemblies (16). However, while the original Vicsek model aimed at describing collective motion in groups of animals, experimental evidence on these systems remained scarse. Recent recordings of flocks of European starlings have filled this gap and have led to challenging observations unaccounted for by active matter models (17; 18; 19). In particular, while the static properties of real flocks are well captured by the Vicsek model (20), it does not predict the linear dispersion relation for the transfer of information observed during collective turns (17; 18). This observation motivated the development of a second order stochastic model (19), called the inertial spin model, which introduces a rotational inertia in the velocity degree of freedom of the birds. While this model predicts a linear dispersion relation in agreeement with experiments, in the absence of an appropriate inference scheme it has not been fully confronted to data.

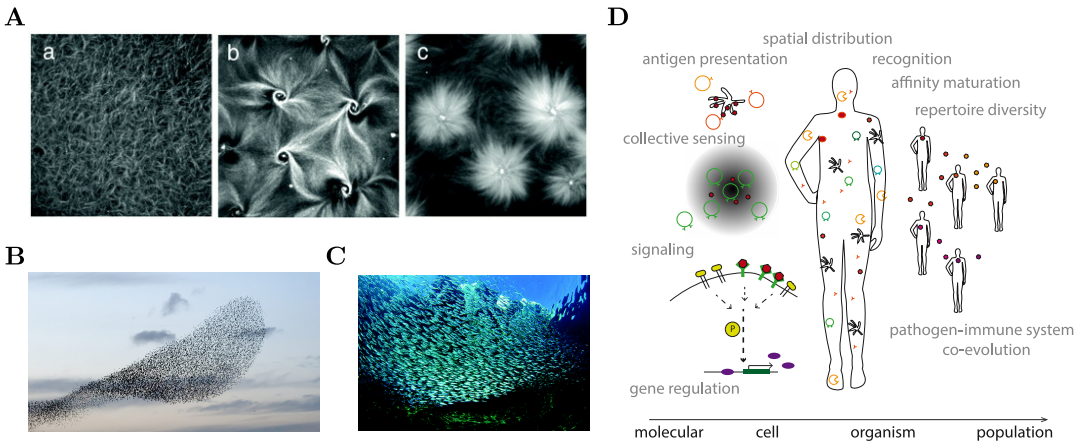

Figure 1.1: **Biological networks at various scales.** **A.** Self-organized patterns by the action of molecular motors on microtubules. The concentration of kinesin (molecular motor) increases from left to right: (a) disordered array of microtubules, (b) spiral patterns and (c) astern patterns. **B.** Collective motion in a flock of starlings and **C.** in a school of fish. **D.** The many scales of the immune system. The immune network spans multiple scales, from molecular receptor-antigen interactions to the co-evolution of viruses and hosts. Figures **A** and **C** were adapted from (21). Figure **D** was adapted from (22).

To fill this gap, after a brief overview in chapter 3 of the models used to describe collective behaviour, we develop in chapter 4 a novel inference scheme for second order stochastic dynamics. We first investigate the failure of naive inference approaches usually applied to first order models, and we connect it to the problem of inferring partially observed stochastic dynamics. Finally, we apply our novel inference scheme to bird flocks simulated with the inertial spin model and we quantify its robustness to measurement noise.

Optimization approaches in the immune system were introduced by Perelson et al. (23; 24) to study the optimal B-cell population dynamics minimizing the duration of an infection, and have recently been revived to study the optimal organization of T- (9) and B-cell repertoires (7). As a common feature, these models assume that adaptive immunity has evolved as a mechanism maximizing the recognition and the neutralization of foreign pathogens. Under this constraint, they predict how the size, the diversity, and the turnover of the different cell subsets depend on the pathogenic environment in which the immune system evolves. Unfortunately, in the absence of high-throughput experimental data quantifying receptor-protein interactions, these approaches are bound to describe immune repertoires in abstract mathematical terms of limited predictive power. However, a number of processes in the immune response remain far from being empirically explained, and we believe that this downside should not hold back attempts to theoretically rationalize their existence. For instance, the general consensus is that memory B cells generated upon affinity maturation are a built-in anticipation mechanism for future infections by antigenic variants (25; 26), yet no model has (i) showed that this is a potentially useful strategy (ii) described what could constrain the resulting size and diversity of this memory pool. On a similar note, the origins and consequences of the phenomenon of antigenic imprinting or "original antigenic sin", in which the immune system seemingly underperforms by reusing

old memory cells in spite of forming a de novo response, are still largely debated (27; 28; 29; 30).

After an introduction in chapter 5 about the adaptive immune system and the models used to describe it, we investigate in chapter 6 how the B cell repertoire is organized to respond optimally to evolving pathogens. Using the theory of decision making we show how both anticipation of future infections by a diverse memory pool and inhibition of affinity maturation by existing memory cells emerge as long-term optimal strategies balancing protection and resource costs.

Having investigated the optimal immune response to evolving pathogens, it is natural to ask how in return the immune pressure exerted by recovered hosts influences the evolution of a viral population. To model the spread of infectious diseases, classical models study the time evolution of populations of infected and recovered hosts (31; 32). Within these models, viral evolution is summarized by a viral strategy which encompasses the viral mutation rate, the transmission rate and the infection-induced death rate. In agreement with experimental observations on influenza, these models of co-evolution have shown that immune pressure promotes antigenic evolution, and as a result immune escape, repeated epidemics and reinfections (33; 34; 35; 36). Building on this knowledge, recent theoretical work has shown that this antigenic escape can in return drive the evolution of more transmissible and deadly variants (37). However, to this date no theoretical work addresses in a general framework how the immune pressure drives the evolution of viral strategies. In particular, the interplay between the cross-reactivity of antibodies elicited by the infection and the finite size of the viral population have so far been ignored, while they have been shown to be essential in antigenic evolution (38; 39).

In chapter 7 we investigate eco-evolutionary feedbacks at play between finite-size host and viral populations. We derive a new general result stating that evolutionary stable viral strategies obey a trade-off between maximizing the speed of antigenic evolution when the cross-reactiviy of antibodies is low and maximizing the basic reproduction ratio as it becomes larger. We apply this result to study the evolution of virulence and the mutation rate, and we derive new analytical predictions for their evolutionary stable states under the effect of immune pressure.

Finally, in chapter 8 we conclude this thesis by summarizing its main contributions and we anticipate future research directions building on our results.

Publications

This thesis collects published articles, and yet to be submitted ones. Chapter 4 was the fruit of a collaboration with Federica Ferretti and was published in *Physical Review X* (40). The results presented in chapter 6 were published in the *Proceedings of the National Academy of Sciences* (41), and the results of chapter 7 constitute an article still in preparation in collaboration with Andrea Mazzolini. The published chapters have been reprinted in this manuscript with minor modifications, and the yet unpublished one has been written as a draft for a future publication. Chapters 3 and 5 are original to this manuscript and aim at providing context and motivations for the research carried out in the rest of the manuscript.

2

Résumé

Cette thèse rassemble des travaux publiés aux chapitres 4 et 6, ainsi que des travaux en voie de soumission au chapitre 7. Le chapitre 3 introduit et motive les travaux présentés au chapitre 4, tandis que le chapitre 5 introduit et motive les travaux présentés aux chapitres 6 et 7. Les chapitres 4, 6 et 7 sont présentés sous la forme d'articles et peuvent donc être lus indépendamment du reste du manuscrit.

Le chapitre 4 de cette thèse s'intéresse à l'étude des processus stochastiques du second ordre et à l'inférence de leurs paramètres à partir de données expérimentales. Ce travail trouve son origine dans plusieurs résultats expérimentaux (42; 43; 17; 44) indiquant que certains phénomènes observés dans des systèmes vivants ne peuvent pas être expliqués à l'aide de dynamiques du premier ordre dans le degré de liberté d'intérêt. Par exemple, dans les nuées d'oiseaux l'information de changement de direction d'un oiseau se propage selon une loi de dispersion linéaire en désaccord avec les prédictions du premier ordre (17). Pour concilier théorie et expérience, il apparaît donc nécessaire d'étudier des dynamiques du second ordre.

Afin de pouvoir confronter ces nouveaux modèles aux observations, nous développons au chapitre 4 une nouvelle méthode d'inférence Bayésienne. Dans ce contexte, les problèmes qui se posent découlent de la combinaison de trois ingrédients : l'ordre de la dynamique des degrés de liberté mesurables indépendamment, le caractère stochastique des processus biologiques, et l'échantillonnage des données en temps discret. Nous démontrons que l'ordre du développement de Taylor-Itô nécessaire à la discrétisation est essentiel pour assurer une inférence fiable à partir des données. En particulier, nous montrons que la précision minimale est $O(\Delta t^{3/2})$, et que les approximations d'ordre inférieur conduisent à un estimateur biaisé pour le coefficient d'amortissement, comme cela a déjà été observé dans des contextes non Bayésiens (45; 46; 47). Fort de ce résultat théorique, en employant des schéma numériques disponibles dans la littérature (48; 49), nous développons une méthode d'inférence de maximum de vraisemblance applicable à une large variété de processus hors et à l'équilibre. Au moyen de simulations numériques et de résultats analytiques, nous démontrons que cette méthode se généralise aux modèles utilisés pour décrire l'évolution des nuées d'oiseaux.

Ces résultats constituent, à notre connaissance, la première approche d'inférence de maximum de vraisemblance pour des dynamiques non-Markoviennes (ou, de manière équivalente, des dynamiques Markoviennes partiellement observées). Finalement, nous quantifions les limites de cette méthode en présence d'erreurs de mesure, ce qui nous amène à proposer au chapitre 8, en ouverture de ce travail de thèse, un certain nombre de pistes d'amélioration.

Le chapitre 6 étudie l'organisation de l'immunité adaptative au moyen d'outils mathématiques inspirés de la théorie de la prise de décision. L'immunité adaptative repose sur des populations de lymphocytes exprimant à leur surface des récepteurs capables de

reconnaître les antigènes d'agents infectieux. Lors d'une infection le processus de maturation d'affinité permet aux lymphocytes B d'adapter par mutations répétées leur récepteur (BCR) aux antigènes de l'agent infectieux (50). Le système immunitaire génère ainsi des plasmocytes, lymphocytes B ayant une forte affinité pour ces antigènes et qui assurent une immunité de long terme grâce à la sécrétion d'anticorps - la version soluble du BCR. Il produit également un répertoire de cellules mémoires ayant une affinité variable pour les antigènes de l'agent infectieux (51). Malgré une connaissance biologique détaillée de ces phénomènes, la diversité et la taille de ce répertoire mémoire, ainsi que les contraintes biologiques à l'œuvre, n'ont pas encore été totalement élucidés.

Afin de pouvoir éclairer ces questions, nous proposons au chapitre 6 un modèle de prise de décision en temps discret décrivant la réorganisation du répertoire de lymphocytes B à la suite d'une infection. Avec cette approche, le répertoire immunitaire est constamment réactivé à la suite de réinfections, à l'instar des infections saisonnières dues la grippe ou désormais au SARS-Cov-2. Ces réinfections sont le fruit d'une évolution antigénique virale induite par la pression de sélection exercée à l'échelle de la population (52; 53; 36). L'objet de notre approche est alors de déterminer, du point de vue d'un système immunitaire prototypique, la stratégie optimale garantissant une protection sur le long terme tout en limitant la création de nouveaux lymphocytes. Les processus intervenant dans cette prise de décision sont au nombre de deux : la production de lymphocytes mémoires au moyen de la maturation d'affinité, et la réactivation de cellules immunitaires produites lors d'infections antérieures. En exploitant ce cadre théorique, nous déterminons la taille et la diversité du répertoire mémoire généré à la suite d'une infection. Lorsque le virus évolue peu entre deux réinfections la réponse optimale est monoclonale, ce qui correspond en pratique aux plasmocytes. Lorsque le virus évolue suffisamment pour rendre inopérante la réactivité croisée des lymphocytes, la réponse optimale est polyclonale, avec une diversité d'autant plus grande que le virus évolue. En pratique cette stratégie est implémentée par les lymphocytes B mémoires. Fort de ce résultat, nous démontrons que la réactivation de lymphocytes B mémoires déjà existants peut conduire à l'apparition d'une empreinte antigénique réduisant la production de nouveaux lymphocytes par maturation d'affinité. Cette observation rationalise dans un cadre théorique la notion de "péché antigénique originel" (54; 29; 55). Enfin, notre modèle prédit que la distribution du nombre de lymphocytes portant un récepteur identique décroît comme une loi de puissance, en accord avec les distributions mesurées par séquençage des immunoglobulines de type G chez des donneurs sains.

Ces résultats offrent une perspective nouvelle sur la modélisation de la réponse immunitaire des lymphocytes B en permettant de décrire non seulement la taille et la diversité du répertoire immunitaire généré et réactivé à la suite d'une infection, mais également le phénomène d'empreinte antigénique. En ouverture de ce travail de thèse, au chapitre 8, nous proposons des pistes de recherche qui permettraient de confronter plus en profondeur ces résultats aux données expérimentales.

Forts de ces résultats, il est naturel de se demander comment en retour la pression immunitaire influence l'évolution virale, et en particulier le taux de mutation. C'est la question que nous abordons dans le chapitre 7 en nous intéressant aux stratégies virales sélectionnées par la pression immunitaire.

La survie des souches virales est dictée par leur capacité à se propager d'hôte en hôte dans la population. Dans les modèles SIR (Susceptible, Infected, Recovered) classiques

(31; 32) cette capacité est mesurée par le nombre de reproduction de base qui désigne le nombre moyen d'infections secondaires qu'un individu infecté engendre dans une population sans immunité préexistante. En l'absence d'évolution antigénique des souches viral, tout variant augmentant ce nombre moyen d'infections secondaires se propage avec succès dans la population (56; 32), et par conséquent la population virale tend à maximiser son nombre de reproduction de base (57). Cependant, certains virus responsables d'infections saisonnières peuvent s'adapter et échapper à l'immunité grâce à des mutations modifiant les antigènes ciblés par les anticorps. En particulier, chez certains virus comme le virus de la grippe, cette évolution est caractérisée par une onde solitaire d'adaptation où de nouveaux variants antigéniques apparaissent continuellement dans la population (58; 53; 59; 60). Par conséquent, la survie de ces souches virales dépend non seulement de leur nombre de reproduction de base, mais aussi de leur capacité à générer des variations antigéniques pour échapper à l'immunité acquise (61). Dans le chapitre 6 nous proposons un cadre théorique inspiré des modèles SIR pour étudier la coévolution de populations de tailles finies d'hôtes et de souches virales. Nous montrons à l'aide de simulations numériques et d'approximations analytiques que la capacité des anticorps à neutraliser différents variants viraux, appelée réactivité (ou immunité) croisée, détermine la vitesse de l'évolution antigénique des souches virales. Ces résultat nous amènent à observer que la stratégie virale optimale sur le plan évolutif est dictée par un compromis entre la maximisation de la vitesse d'évolution antigénique lorsque la réactivité croisée est faible, et la maximisation du nombre de reproduction de base lorsqu'elle devient plus importante. En conséquence, nous montrons qu'une réactivité croisée limitée favorise l'évolution de pathogènes hautement transmissibles et mortels avec des taux de mutation très élevés, amenant la population virale très proche de l'extinction en raison de l'accumulation de mutations délétères. Ces observations sont en accord avec les taux de mutation très élevés mesurés chez les virus à ARN (62), les rendant notoirement très sensibles à de petites élévations de leur taux de mutation provoquées par des médicaments mutagènes (63; 64).

Dans l'ensemble, ce travail offre un cadre analytique robuste pour étudier l'évolution des stratégies virales pour des pathogènes susceptibles d'évoluer antigéniquement, à l'instar du virus de la grippe ou du SARS-Cov-2. Il apporte un nouvel éclairage sur les rétroactions éco-évolutives qui dictent l'évolution des stratégies virales, et concilie dans cadre théorique unique des résultats récents sur l'évolution de la virulence en présence de variations antigéniques (37) et les études classiques sur les pathogènes à l'équilibre endémique (65; 57).

3

Modeling and inferring collective behavior

From the mechanics of the cellular cytoskeleton (66; 67) to the collective motion of cells and animal groups (21), classical physics has been remarkably successful in modeling living matter systems. In particular, the similarities between the emergence of large scale properties in living and inanimate matter have fueled physicists hope to describe both within a statistical-physics inspired approach (68). However, despite a strong qualitative success of these models, their connections with experimental data has been tenuous. In the last decade, inference frameworks have been developed to fill this gap and interrogate statistical physics models directly from data (68). While inverse approaches have been successfully applied to describe overdamped stochastic dynamical systems, they cannot be readily applied to systems exhibiting inertial dynamics like bird flocks (17; 19). To solve this issue, in chapter 4 we develop a new Bayesian inference approach for underdamped Langevin dynamics. As an introduction, in this chapter we present the modeling approaches used to study collective behavior and to learn equations of motion from time-resolved data.

3.1. Modeling collective behavior

Collective behaviors are ubiquitous in biological systems and appear at multiple scales, from the cellular cytoskeletal network (69) to cell tissues (70), bacterial suspensions (71) and large animal groups (72). Owing to a constant injection of energy at the individual level, these many-body systems are intrinsically not at equilibrium. However, generalizations of equilibrium statistical physics models have proven accurate to describe their behavior, and a large corpus of models have been developped to study active matter systems (21). Historically, agent-based models were the first one introduced (10), readily followed by hydrodynamic theories (11). In the following manuscript we will focus on the former, and in particular on the variants of the Vicsek model (10).

3.1.1 The Vicsek model

Vicsek et al. introduced in 1995 (10) a dynamical agent-based model to describe self-organized collective motion in biological systems. In this model, N particles move at a constant speed in a two-dimensional space and are subject to noisy local alignment interactions. In this assembly of particles, also called a flock, each particle has position $\mathbf{r}_i$ and a velocity $\mathbf{v}_i = v_0\mathbf{u}_i$ with $\mathbf{u}_i$ its normalized particle orientation. Particle i interacts with particle i with a strength J_{ij}, and the evolution of the flock is governed by a set of discrete-time update rules for the position and the orientation of each particle:

$$\begin{cases} \mathbf{r}_i(t+\Delta t) = \mathbf{r}_i(t) + v_0\mathbf{u}_i(t)\Delta t \\ \mathbf{u}_i(t+\Delta t) = \mathcal{R}_\epsilon\Theta\left(\sum_j J_{ij}\mathbf{u}_i(t)\right), \end{cases} \tag{3.1}$$

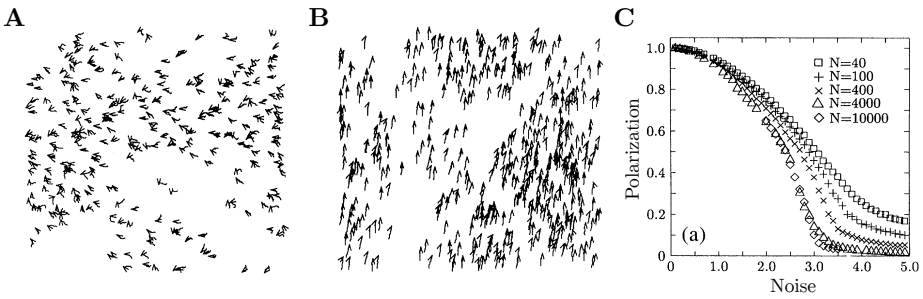

Figure 3.1: **Collective motion in the Vicsek model. A.** Disordered phase. The flock does not have a collective direction of motion and $\Phi \simeq 0$. **B.** Ordered phase. The flock has a collective direction of motion and $\Phi \simeq 1$. **C.** Phase transition from a polarized phase to a disordered phase as the noise is increased at a fixed density of particles. This figure was adapted from (10).

where Θ is the normalization operator $\theta(\mathbf{x}) = \mathbf{x}/\|\mathbf{x}\|$, Δt is the time step and $\mathcal{R}_\epsilon$ is the noise operator which applies a random rotation in the angle $[-2\pi\epsilon, 2\pi\epsilon]$ to its argument. According to Eq. 3.1 the orientation of particle i is updated as a noisy weighted estimate of other particles' orientations. To ensure a local alignment, the interaction strength is required to decay fast enough with the interparticle distance. This distance can be *metric*, in which case J_{ij} is a function of $\mathbf{r}_{ij} = \|\mathbf{r}_i - \mathbf{r}_j\|$, or *topological* and J_{ij} is non-zero if and only if particle j is among the n_c nearest neighbours of particle i. In the absence of self-propulsion, $v_0 = 0$ and the orientations $\{\mathbf{u}_i\}_{i=1,\dots,N}$ can be formally identified as spins of an XY Heisenberg model of a ferromagnet. However, in presence of self-propulsion the network constantly rearranges and this formal equivalence does not hold. In particular, this reshuffling of the particles' positions breaks detailed balance and the system is not at equilibrium (73).

Emergence of collective motion

Following the analogy with the Heisenberg model, the natural order parameter to investigate collective motion is the average direction of the flock, also called polarization:

$$\Phi = \frac{1}{N}\left\|\sum_{i=1}^{N}\mathbf{u}_i\right\|. \tag{3.2}$$

While in the absence of self-propulsion the Mermin-Wagner theorem forbids any phase transition between a disordered phase $\Phi = 0$ and an ordered phase $\Phi > 0$ (74), in the presence of self-propulsion spontaneous collective motion emerges (10; 75). As a matter of fact, as the noise is lowered (with respect to the average interaction strength) or the average density is increased (at fixed interaction range), the flocks goes from a disordered phase Fig. 3.1A to a collectively moving phase Fig. 3.1B. For metric interactions this transition (Fig. 3.1B) is of first order, with a coexistence phase consisting of dense traveling bands of particles (76). While it has long been thought to be a second order transition for topological interactions, recent developments have shown that it is of first order (77).

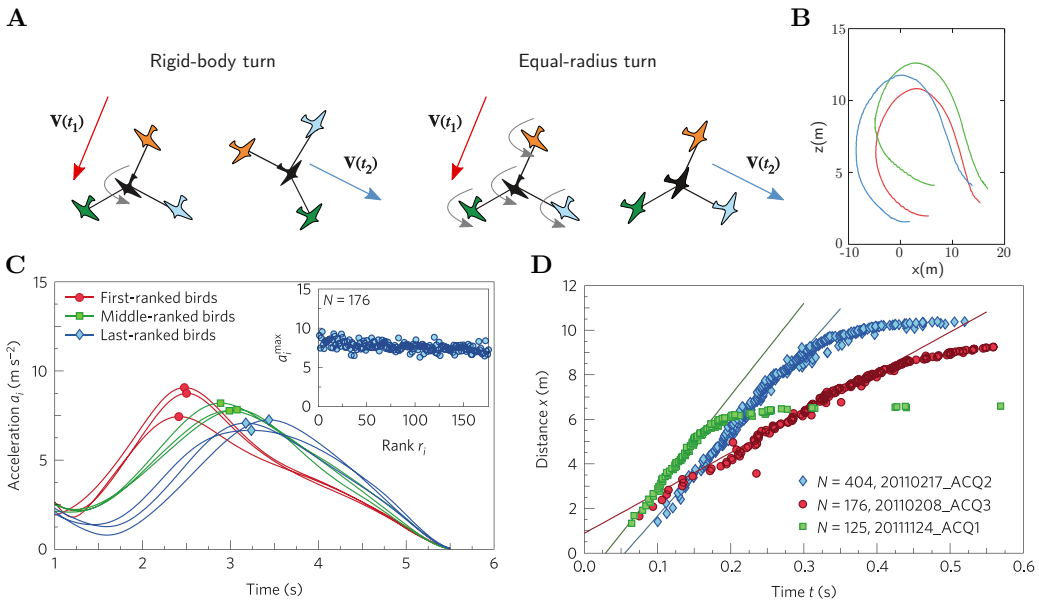

Figure 3.2: **Collective turns in real bird flocks. A.** Schematic representation of a rigid-body turn and an equal-radius turn. In the rigid-body turn, the bird in black is the center of rotation. **B.** Equal-radius trajectories of three birds taken coming from a camera acquisition of a turning flock of starlings. Figures **A-B** have been adapted from (78). **C.** Radial accelerations in three turning flocks of starlings. The information propagates from the first-ranked birds (closest to the perturbation) to the last-ranked birds. This information propagates almost undamped: as shown in the inset $a_{\max}$ doesn't decay as the rank of the bird increases. **D.** Linear dispersion relation for the transfer of information as measured from the radial acceleration profiles. Figures **C-D.** have been adapted from (18).

Continuous-time formulation

In the continuous-time limit and in d dimensions the Vicsek model Eq. 3.1 is conveniently replaced by the following set of equations for the velocities $\mathbf{v}_i$ (78):

$$\begin{cases} \dot{\mathbf{r}}_i = \mathbf{v}_i \\ \eta \dot{\mathbf{v}}_i = \left(\sum_j J_{ij} \mathbf{v}_j + v_0 \boldsymbol{\xi}_i \right)_\perp , \end{cases} \tag{3.3}$$

with η the dissipation, $\boldsymbol{\xi}_i$ a d-dimensional white noise $\langle \xi_{i,\alpha}(t) \xi_{j,\beta}(t') \rangle = 2T\eta\delta_{\alpha\beta}\delta_{ij}\delta(t-t')$, and T the statistical temperature. This is a first order stochastic differential equation in the velocity degree of freedom, which physicists equivalently refer to as an overdamped Langevin equation. The $\perp$ symbol denotes the projection onto the plan perpendicular to the velocity $\mathbf{v}_i$, which enforces the self-propulsion constraint. Notably, this overdamped Langevin equation is the constant speed limit of a broader class of models called active Brownian particles, in which the speed is allowed to fluctuate (79).

3.1.2 Inertial dynamics

Despite its remarkable success in reproducing the self-organized collective motion observed in a variety of biological systems, the Vicsek model is unable to provide a realistic

description of bird flocks, and in particular of their collective turns (17; 18; 78). Turns occur as a collective response to an external stimulus, they are sustained by a bird to bird transmission of information and they are initiated locally as a sudden change of orientation. By measuring the radial acceleration profile (Fig. 3.2C) of each bird in real flocks of starlings (17), authors showed that the turn perturbation propagates according to a linear dispersion law Fig. 3.2D, with negligible reshuffling of the birds' positions. This observation is in striking disagreement with Vicsek-like models, as they only allow for a diffusive transfer of information (17).

Modeling collective turns

In order to modify the Vicsek model to account for collective turns, it is necessary to understand the mechanisms at play in the birds sudden change of orientation (18; 19). Particles in a many-body system can rotate in two ways: as a rigid body with all the points rotating at the same angular velocity with respect to a common fixed point, or on paths with equal radius of curvature Fig. 3.2A. Mathematically, these two types of rotations are very similar: the rigid-body rotation is acting in the position space $\mathbf{r}_i$, while an equal-radius turn is a rotation acting in the space of the birds' orientations $\mathbf{u}_i$. In position space, rotations are generated by the angular momentum $\boldsymbol{\ell}_i = \mathbf{r}_i \times m\dot{\mathbf{r}}_i$ with m the mass of the particle. Correspondingly, rotations in the space of the birds' orientations can be described through the definition of another angular momentum called *spin* $\mathbf{s}_i = \mathbf{u}_i \times \chi\dot{\mathbf{u}}_i$ and with the introduction of a generalized inertia χ (80). This inertia is unrelated to the mass and accounts for the particles' resistance to sudden orientational changes.

Inertial spin model

Experimental evidence supports the model of equal-radius turns and hints at the existence of a generalized inertia (17; 18) Fig. 3.2B. This observation lead to a new dynamical model, called inertial spin model (ISM), which amounts to a minimal modification of the Vicsek model Eq. 3.3 by making use of the spin $\mathbf{s}_i$ degree of freedom (19):

$$\begin{cases} \dot{\mathbf{r}}_i = \mathbf{v}_i \\ \dot{\mathbf{v}}_i = -\frac{1}{\chi}\mathbf{v}_i \times \mathbf{s}_i \\ \dot{\mathbf{s}}_i = -\frac{\eta}{\chi}\mathbf{s}_i + \frac{1}{v_0^2}\mathbf{v}_i \times \sum_j J_{ij}\mathbf{v}_j + \boldsymbol{\xi}_{i\perp}, \end{cases} \tag{3.4}$$

where $\perp$ again denotes the projection on the space perpendicular to $\mathbf{v}_i$ and $\boldsymbol{\xi}_i$ is a 3-dimensional white noise $\langle \xi_{i,\alpha}(t)\xi_{j,\beta}(t')\rangle = 2T\eta\delta_{\alpha\beta}\delta_{ij}\delta(t-t')$. By taking advantage of the constant speed assumption, the dynamics for the velocity Eq. 3.4 can be rewritten as a generalization of Eq. 3.3:

$$\chi\ddot{\mathbf{v}}_i = \left(-\eta\dot{\mathbf{v}}_i + \sum_j J_{ij}\mathbf{v}_j + v_0\boldsymbol{\xi}_i\right)_\perp - \chi\left\|\frac{\dot{\mathbf{v}}_i}{v_0}\right\|^2\mathbf{v}_i. \tag{3.5}$$

This is a second order differential stochastic equation in velocity, also referred to as an underdamped Langevin equation. Importantly, the introduction of the additional spin degree of freedom promotes the first order Vicsek model Eq. 3.3 to a second order model, allowing for a transfer of information obeying a linear dispersion relation (17). This model is a generalization of the Vicsek model Eq. 3.3, and in the overdamped limit $\chi/\eta^2 \to 0$ the Vicsek model Eq. 3.3 is recovered (78). In chapter 4 we will develop a new inference

method to learn the parameters of Eq. 3.5 from discrete-time trajectories. However, before doing so we will present existing inference methods and discuss their limitations.

3.2. Learning equations of motion from data

Despite the theoretical understanding provided by agent-based models, they need to be adjusted to measurements in order to produce accurate real-life predictions. This task of learning models from real data is referred to as *inference*. When dealing with dynamical models, measurements generally consist of discrete time series. While a large corpus of literature has been dedicated to the reconstruction of deterministic models from time series (81), in collective behavior models the stochastic component cannot be ignored. Importantly, this source of stochasticity is distinct from the measurement noise accumulated during the acquisition of trajectories. While the former is essential to the emergence of collective behaviors, the latter is a source of confusion in the reconstruction of the trajectories. The problem of disentagling one from the other is ubiquitous to the inference of stochastic trajectories (82; 83) and is discussed in chapter 4.

3.2.1 Learning dynamical models

Generically, to perform the inference of a stochastic process we assume it is a diffusion process, with $\mathbf{F}$ the deterministic force, $\mathbf{D}$ the diffusion matrix, and $\boldsymbol{\xi}$ a white noise with unit variance:

$$\dot{\mathbf{x}} = \mathbf{F}(\mathbf{x}, t) + \sqrt{2\mathbf{D}(\mathbf{x}, t)}\boldsymbol{\xi}. \tag{3.6}$$

This description Eq. 3.6 is not restrictive to first order processes, as for any process of arbitrary order we can always reformulate it as a first order equation Eq. 3.6 by changing variable $\mathbf{x} \leftarrow (\mathbf{x}, \dot{\mathbf{x}}, ...)$. In particular, in this formulation the variable $\mathbf{x}$ follows a Markovian evolution. Within this framework, the goal of inference is to learn the force field $\mathbf{F}$ and the diffusion matrix $\mathbf{D}$ given a dataset of m observed trajectories $\mathcal{D}_m = \{\mathbf{x}^\alpha_{0:L}, \alpha = 1, ..., m\}$.

Importantly, if the process $\mathbf{x}(t)$ partially observed, in the sense that the measurement apparatus does not provide an independent observation of all its degrees of freedom, the dynamics of the observed degrees of freedom is not Markovian anymore. This problem is closely related to the task of building novel inference scheme for second order stochastic differential equation, and is discussed at length in chapter 4. For sake of simplicity, in this introduction we consider that the process is fully observed.

Non-parametric & Semi-parametric inference

The task of learning a general force field and diffusion matrix from measurements is referred to as non-parametric inference. Most common strategies require to bin the phase space in order to reconstruct locally $\mathbf{F}$ and $\mathbf{D}$ (84). This daunting task requires an enormous amount of data, which makes these strategies unusable for non-stationary processes and large phase spaces. To circumvent some of these difficulties, a method called stochastic force inference has been recently introduced (82; 85). Under the same stationarity assumption, authors approximate the force field and the diffusion matrix using a finite basis of functions $\{c_\alpha(\mathbf{x})\}_{\alpha=1,...,n_b}$:

$$F_i(\mathbf{x}) \simeq \sum_{\alpha=1}^{n_b} F_{i,\alpha} c_\alpha(\mathbf{x}), \text{ with } \int d\mathbf{x} c_\alpha c_\beta P(\mathbf{x}) = \delta_{\alpha\beta}, \tag{3.7}$$

where $P(\mathbf{x})$ is the stationary measure and the parameters $F_{i,\alpha}$ are the coefficients of projections of the force field components on the basis:

$$F_{i,\alpha} = \int d\mathbf{x} P(\mathbf{x}) F_i(\mathbf{x}) c_\alpha(\mathbf{x}). \tag{3.8}$$

Under the additional assumption that the process is ergodic, the ensemble averages can be replaced by time averages and estimated from measured trajectories. A similar estimator using the same basis of functions can be derived for the diffusion matrix. The improvement of this approach over the previous ones is drastic: not only the phase space does not require binning anymore, but the number of parameters to learn drops to a manageable number $n_b \times d$, where n_b is the number of basis functions used and d is the phase space dimension. In particular, the choice of the basis of functions can be informed by physical knowledge of the dynamics, increasing even more the efficiency of the method. Additionaly, making use of the Itô-Stratonovich correspondance, authors were able to derive estimators unbiased by measurement noise.

However, this method solely applies to stationary processes and only allows for metric parametrizations of the force field. As we have mentionned, the use of topological interaction networks is common to model collective motion, and this inference approach does not offer a satisfying framework to learn the Vicsek model and its inertial generalization the ISM. Additionally, this method does not provide a probabilistic framework to evaluate the likelihood of the data given the learnt parametrization. In particular, in the field of collective behavior a probabilistic inference approach is needed to perform model selection and assess the validity of the inertial spin model over the Vicsek model. Before developing probabilistic inference methods solving these issues in chapter 4, we introduce Bayesian inference methods.

Bayesian inference

A statistical model is determined by its functional form $\mathcal{M}$, for instance inertial or non-inertial in the case of collective motion, its parameters θ, and the predictions $P(\mathcal{D}_m|\theta, \mathcal{M})$ it makes about the data $\mathcal{D}_m$. Additionaly, the prior distribution $P(\theta|\mathcal{M})$ denotes the a priori knowledge we have about the parameters, which for instance may come from past experiments. The term *Bayesian inference* refers to a set of inference methods where the validity of the parameters θ, given the measured data $\mathcal{D}_m$, is estimated using Bayes theorem (86). Assuming the model $\mathcal{M}$ is the one generating the data, the probability of the model parameters being θ given the measured data $\mathcal{D}_m$ reads:

$$P(\theta|\mathcal{D}_m, \mathcal{M}) = \frac{P(\mathcal{D}_m|\theta, \mathcal{M}) P(\theta|\mathcal{M})}{P(\mathcal{D}_m|\mathcal{M})} \tag{3.9}$$

The probability $P(\mathcal{D}_m|\mathcal{M})$ is the evidence of the model and is independent of the parameters. Therefore, it is commonly ignored when looking for the parameters θ best fitting the data $\mathcal{D}_m$. Performing Bayesian inference finally amounts to maximizing $P(\theta|\mathcal{D}_m, \mathcal{M})$ the posterior distribution. The corresponding estimator, called *maximum a posteriori* reads:

$$\hat{\theta}_{MAP} = \arg\max_\theta P(\theta|\mathcal{D}_m, \mathcal{M}). \tag{3.10}$$

The choice of the prior distribution can be driven by prior experiments, or simply by considerations about the validity range of the model parameters. In the absence of both, the general rule is to use the least informed prior $P(\theta|\mathcal{M}) = \text{constant}$. The inference task becomes driven by the data likelihood $P(\mathcal{D}_m|\theta, \mathcal{M})$ only, and the maximum a posteriori estimator Eq. 3.10 coincides with the *maximum likelihood* estimator:

$$\hat{\theta}_{ML} = \arg\max_{\theta} P(\mathcal{D}_m|\theta, \mathcal{M}). \tag{3.11}$$

In the limit of an infinite number of samples $m \to \infty$ the maximum likelihood estimator is in general consistent, in the sense that it converges in probability to the true value generating the data (87).

As the process is Markovian, the likelihood of any trajectory $\mathbf{x}_{0:L}$ sampled with a timestep Δt can be written as:

$$P(\mathbf{x}_{0:L}, \theta) = \prod_{i=1}^{L} P_{\Delta t}(\mathbf{x}_i|\mathbf{x}_{i-1}, \theta) P(\mathbf{x}_0|\theta), \tag{3.12}$$

where $P_{\Delta t}(\mathbf{x}'|\mathbf{x}) = P(\mathbf{x}', t + \Delta t|\mathbf{x}, t)$ is the propagator of the diffusion process over a duration Δt, and $P(\mathbf{x}_0|\theta)$ is the probability distribution of the initial condition x_0. With this equation, we see that performing Bayesian inference for dynamical stochastic models amounts to finding the propagator $P_{\Delta t}$. In most applications, it cannot be explicitely calculated and it is approximated for small time steps using a Taylor-Itô expansion. In the last section of this introduction we illustrate this with previous inference results obtained with the Vicsek model (80; 88). Importantly, Eq. 3.12 can be written as the product of propagators over successive couples of data points because the process is fully observed. As we mentionned, in the partially observed case the Markov property does not hold, and in particular the trajectory likelihood does not split over successive couples of points like in Eq. 3.12. In chapter 4 we develop a novel inference scheme that circumvents this problem.

3.2.2 Inference in the Vicsek model

Bayesian inference has been successfully applied to dynamical recordings of bird flocks (88; 80) using the Vicsek model Eq. 3.3. To achieve this task, authors focused on the velocity fluctuations around the collective direction of motion of the flock $\mathbf{n}$. Following previous evidence indicating that birds are interacting through topological interactions (89), authors chose a nearest neighbour parametrization of the interaction network. Assuming the flock is highly polarized $\Phi \simeq 1$, at first order in the fluctuations $\boldsymbol{\pi}_i$ orthogonal to $\mathbf{n}$, Eq. 3.3 reads as:

$$\eta \dot{\boldsymbol{\pi}}_i = -J \sum_j \Lambda_{ij} \boldsymbol{\pi}_j + \boldsymbol{\xi}_{i\perp}, \tag{3.13}$$

with $\langle \boldsymbol{\xi}_{i\perp}(t) \boldsymbol{\xi}_{j\perp}(t') \rangle = 2(d-1)T\eta\delta_{ij}\delta(t-t')$ and $\Lambda_{ij} = n_c\delta_{ij} - n_{ij}$ is the discrete Laplacian. Using Euler discretization and denoting $\boldsymbol{\pi} = (\boldsymbol{\pi}_1, ..., \boldsymbol{\pi}_N)$, the short time propagator $P_{\Delta t}$ reads:

$$P_{\Delta t}(\boldsymbol{\pi}'|\boldsymbol{\pi}) = (4\pi T\eta\Delta t)^{-N(d-1)/2} \exp\left[-\frac{(\boldsymbol{\pi}' - \boldsymbol{\pi} + J\Delta t \boldsymbol{\Lambda}\boldsymbol{\pi})^2}{4T\eta\Delta t} \right]. \tag{3.14}$$

Expanding the argument of the exponential, the propagator depends on a set of correlations between the fluctuations at time t and $t + \Delta t$ (80; 88). With an hybrid analytical and numerical maximization of the likelihood, authors obtained estimates for $n_c \sim 5$, J and T. In particular, they learnt from this inference that the local relaxation of the velocity degrees of freedom is much faster than the network reshuffling, leading to the conclusion that flocks are locally at equilibrium (88). In chapter 4 we follow the line of thinking outlined in this section to develop inference schemes for second order stochastic processes. We also discuss in length the role of discretization and of partial observability on the consistency of the maximum likelihood estimators.

4

Building general Langevin models from discrete datasets

4.1. Abstract

This chapter was previously published in:

- Ferretti F, Chardès V, Mora T, Walczak AM, Giardina I (2020) Building general langevin models from discrete datasets. *Physical Review X*, 10:031018.

The section "ISM simulations" was moved from Appendix to section Methods. Figures fonts have been changed.

Many living and complex systems exhibit second order emergent dynamics. Limited experimental access to the configurational degrees of freedom results in data that appears to be generated by a non-Markovian process. This poses a challenge in the quantitative reconstruction of the model from experimental data, even in the simple case of equilibrium Langevin dynamics of Hamiltonian systems. We develop a novel Bayesian inference approach to learn the parameters of such stochastic effective models from discrete finite length trajectories. We first discuss the failure of naive inference approaches based on the estimation of derivatives through finite differences, regardless of the time resolution and the length of the sampled trajectories. We then derive, adopting higher order discretization schemes, maximum likelihood estimators for the model parameters that provide excellent results even with moderately long trajectories. We apply our method to second order models of collective motion and show that our results also hold in the presence of interactions.

4.2. Introduction

Recent experimental findings on a variety of living systems, from cell migration (83), bacterial propulsion (90), worm dynamics (91), to the larger scale of animal groups on the move (42; 43; 17; 44), indicate that the observed behavior cannot be explained with a first order dynamical process, but requires a higher order description. For bird flocks and insect swarms, the case which interests us most, data show that propagating directional information during collective turns in flocks requires rotational inertia, i.e. a reversible dynamical term, to account for the measured dispersion law (17). The shape of the velocity-velocity correlation function in swarms, which flattens at short times, also points to a second order dynamics for these systems, as suggested by the value of the dynamical critical exponent (44). Overall, data indicate that considering second order dynamics is required to explain how animal groups behave on their natural size and time scales — even though overdamping might theoretically occur for very large systems and on very large time scales.

The emergent dynamics of all the above systems share three fundamental ingredients: an effective inertia, dissipation, and a stochastic contribution. Disentangling such con-

tributions is often crucial to understand the processes at stake and reliable methods are required to extract that information from available data. The example of animal groups, which motivates the present work, is also helpful to discuss the theoretical objectives and experimental constraints of the inference procedure. Ideally, we would like to build the simplest continuous second order model consistent with experimental findings. We seek a continuous time model for several reasons: i) it allows computations to be performed; ii) it is a reasonable assumption for systems where microscopic update times are much smaller than observational scales (cognitive processes occur on tenths of milliseconds, whereas behavioral changes on scales of seconds); iii) it circumvents the inherent arbitrariness of discrete time modelling. Experimental data, on the other hand, come in the form of discrete time series, where the discretization interval is set by the time resolution of the experimental apparatus.

In the presence of stochasticity, the nature of the data poses two major problems. First of all, if the dynamics is of second order, all signals (including initial condition and noise) are propagated in time with a memory kernel, making the relation between the coarse grained data that we observe and the underlying process far more complex than in the first order case. The memory kernel arises from the contraction of the dynamical description of the second order stochastic process from the full phase space to a lower dimensional subspace — usually that of measurable degrees of freedom (92; 93; 94). For example, were we able to experimentally measure with the same accuracy a pair of conjugate variables, e.g. positions and velocities of moving individuals, we could seek a model for their joint evolution. But in common experiments that is not the case, as one typically measures one degree of freedom (e.g., positions) and must derive the other. To confront the data, we therefore need to work in a reduced space. Secondly, the goal of the inference procedure is to retrieve a continuous stochastic model from a collection of discrete sample paths occurring on finite observational time scales Δt. In absence of an explicit solution for the stochastic process, the most reasonable thing to do is to transform the stochastic differential equation (SDE) into an approximated difference equation. Such discretization must be performed very carefully, since the resulting equation should correctly represent the underlying stochastic process both at the scales of the sampled data (at which inference works), and in the microscopic limit of vanishing increments.

These two problems are quite general and do not depend on the presence of interactions in the system, but rather on the nature of the dynamics. Although the issue has been considered before, the literature is sparse and a satisfying Bayesian inference approach is still lacking. Previous attempts to provide systematic inference strategies for second order dynamics consist of building converging estimators for the different terms of the model from proper combinations of measurable quantities (95; 46; 96), or in exploiting known relations between model parameters and accessible observables (47).

In a more general and refined way, the problem can be reformulated in terms of a dynamical inverse problem, and much work has been done in this field in the last years (97; 98; 86). However most analyses have focused on first order processes in time (99; 100; 101; 80; 88; 82; 102; 103). Second order processes have been considered within this framework in Refs. (45; 104), yet the proposed method differs from a proper maximum likelihood approach, due to the difficulty of deducing a pseudo-likelihood function in the case of non-Markovian processes.

To the best of our knowledge, we present here the first maximum likelihood inference

approach for non-Markovian inertial processes. It differs from previous studies in its first principle derivation and absence of a Markovian embedding. We derive explicit formulas for the parameter estimators, and test our approach on synthetic data in a variety of models, including non-linear forces, multiplicative noise and many-body interactions. Results show that the method is accurate and robust, providing an important tool in the analysis and understanding of real systems. The paper is organized in the following way: in Sec. 4.3.1 we formalize the problem and discuss in detail how to build an appropriate dynamical inference strategy for inertial systems with linear dissipation. We explain the interplay between the order of convergence of discretized SDEs obtained from Taylor-Itô expansions and the consistency of the corresponding max-likelihood parameter estimators. We show that to get accurate results the simplest Euler-like schemes, which work well with first order dynamics, are insufficient, so that one needs to go to the next order of approximation. Theoretical predictions are compared with numerical data to consolidate our results. Sec. 4.3.2 introduces non-Bayesian inference schemes, while in Sec. 4.3.3 we discuss the problem of eliminating the initial velocity. In Sec. 4.3.4 we address the case of a strongly interacting system: the inference procedure is applied to synthetic data obeying the Inertial Spin Model, a model of self-propelled particles that describes the phenomenology of natural flocks of birds (17). The effect of experimental measurement noise is discussed in Sec. 4.3.5. Finally, in Sec. 4.4 we summarize all our results, discuss their conceptual relevance, and outline their potential for applications to real data.

4.3. Results

4.3.1 Maximum-likelihood inference approach for Langevin dynamics

Problem definition

Let us assume that the available experimental data are sequences of points $(x_0, x_1, \dots x_L)$ uniformly separated in time by Δt, and that the underlying dynamics is described by the complete Langevin equation of the form:

$$\ddot{x} = -\eta\dot{x} + f(x) + \sigma\xi, \tag{4.1}$$

where $f(x) = -V'(x)$ is a conservative force, $\sigma^2 = 2T\eta$, and ξ is a standard white noise: $\langle\xi\rangle = 0$, $\langle\xi(t)\xi(t')\rangle = \delta(t - t')$. Without lack of generality, the inertial mass is set to 1. Since the noise is additive, it is unnecessary to distinguish between Itô and Stratonovich integration.

Let us call $\boldsymbol{\lambda}$ the irreducible set of parameters that enter in Eq. 4.1, namely the effective damping coefficient η, the effective temperature T, and the parameters entering in the definition of the potential $V(x)$. The aim of dynamical statistical inference is to provide an estimate of their values. Following a Bayesian approach, the posterior distribution of parameters given the data reads:

$$P(\boldsymbol{\lambda}|\{(x_0, \dots, x_L)^\alpha\}) \propto P(\{(x_0, \dots, x_L)^\alpha\}|\boldsymbol{\lambda})\rho(\boldsymbol{\lambda}), \tag{4.2}$$

where each Greek index labels a different experimental sample. By choosing a uniform prior $\rho(\boldsymbol{\lambda})$, the maximum of Eq. 4.2 corresponds to the maximum likelihood estimator. The conceptual and technical difficulty of the whole inference problem is then only about finding a tractable expression for the dynamical likelihood.

The theory of stochastic processes provides us with an explicit but formal expression for the transition probability $P\left(x(t)|x(0),\dot{x}(0)\right)$, involving, in general, integro-differential operators. A closed form solution for the stochastic process may be generally unknown or complicated [1], especially for many body or off-equilibrium systems, but finely time-resolved data may be available. What we look for is then an (eventually approximated) expression for the probability of the discrete trajectory, for which a practical connection with the data can be established.

A first general strategy is the following:

1. As a preliminary step, Eq. 4.1 can be conveniently rewritten as a set of two first order equations:
$$\begin{cases} \dot{x} = v \\ \dot{v} = -\eta v + f(x) + \sigma\xi. \end{cases} \tag{4.3}$$

2. Since the dynamics is Markovian when parametrized by the vector variable $\mathbf{q} = (x, v)$, the probability of a discrete trajectory in this space, given the initial condition $\mathbf{q}_0 = (x_0, v_0)$, can be split into a product of propagators:
$$P(\mathbf{q}_L, \ldots, \mathbf{q}_1|\mathbf{q}_0) = \prod_{n=1}^{L} P(\mathbf{q}_n|\mathbf{q}_{n-1}). \tag{4.4}$$

3. Following (105), one can exploit any update rule based on a Taylor-Itô expansion to approximate, within a certain order of accuracy, the propagator over a small time interval Δt:
$$P(\mathbf{q}_n|\mathbf{q}_{n-1}) = P_{(k)}(\mathbf{q}_n|\mathbf{q}_{n-1}) + o(\Delta t^k). \tag{4.5}$$
Eq. 4.5 can be replaced into Eq. 4.4 to get an approximated expression for the probability density of the sequence of points in phase space:
$$P_{(k)}(\mathbf{q}_L, \ldots \mathbf{q}_1|\mathbf{q}_0) = \prod_{n=1}^{L} P_{(k)}(\mathbf{q}_n|\mathbf{q}_{n-1}) + o(\Delta t^k). \tag{4.6}$$

4. Marginalizing over the velocity-like degrees of freedom one gets a probability distribution depending on the x's only. This projection operation on the subspace of x variables is where the original Markovian property of Eq. 4.4 is generally lost. A crucial remark, beyond the non-Markovian nature of the resulting dynamics, is that this procedure does not simply consist of removing the intermediate variables $v_1, \ldots, v_L$, but also of eliminating the initial condition v_0. This is at the same time a further technical difficulty and a fundamental conceptual issue in the context of stochastic dynamics. We refer to Sec. 4.3.3 for a broader discussion.

When this strategy is adopted, the first thing we need is then a discrete integration scheme for Eq. 4.1 or Eq. 4.3. Although the naive intuition is that any convergent — even if slowly — discretization scheme should work for small Δt, in fact the order of approximation of the temporal discretization is able to affect the mathematical properties of the discrete path integral measure and, consequently, the correctness of estimators obtained through

[1] We seek a solution of the stochastic process either as an explicit sample-path solution in position space that does not involve integro-differential operators, or as the time-dependent solution of the associated Fokker-Planck equation (73).

a maximum likelihood inference procedure (105; 45).

Alternatively, one can follow a second strategy, summarized as *'first marginalize, then discretize'*, in contrast to the *'first discretize, then marginalize'* strategy discussed above. The starting point is here the generalized Langevin equation (GLE) corresponding to the desired process, Eq. 4.1, which can be obtained adopting the Mori-Zwanzig formalism (92) (see App. A.1.1):

$$\dot{x} = v_0 e^{-\eta t} + \int_0^t ds K(t-s) f(x(s)) + \zeta(t). \tag{4.7}$$

In this equation, $K(t) = e^{-\eta t}$ and the effective noise is given by $\zeta(t) = \int_0^t ds e^{-\eta(t-s)} \xi(s)$. This formalism shows that, when projected from the full phase space into the x space, the dynamics acquires a memory, described by a friction kernel $K(t)$ and color in the noise. We note that the relation $\langle \zeta(t)\zeta(t') \rangle \propto K(|t-t'|)$ holds asymptotically in the limit of infinitely long trajectory, and it reduces to the second fluctuation dissipation theorem when $f(x)$ is linear. Discrete update equations can now be obtained by integrating Eq. 4.7 on Δt intervals, and self-consistently removing v_0. We notice that, for arbitrary forces $f(x)$, the corresponding term cannot be exactly integrated and it needs to be approximated at small Δt. The fact that the derivative of the measured coordinate – position, x, – enters parametrically through v_0 in the GLE stems from the second order nature of the process. Its elimination, which is necessary to retrieve a stochastic difference equation where only the x variable appears, is connected to the problem anticipated in point 4 of the procedure outlined above.

The two strategies must be equivalent: the order of the discretization and marginalization operations should be exchangeable. In the following section we show how the simplest inference schemes derived from Euler-like discretizations of Eq. 4.3 do not satisfy this requirement, whereas higher order discretization schemes, strongly convergent as at least $O(\Delta t^{3/2})$, retrieve correct maximum likelihood estimators.

Failure of naïve inference schemes

Discrete integration approaches for SDEs are well known in the literature in connection to numerical computation methods (see, e.g. (106)). Here, we summarize how the order of approximation of these discretization schemes interferes with the non-Markovian character of the observed dynamics. This makes standard claims about the convergence of these integrators not generally valid in cases when only a projection of the original Markovian process is observed. Rigorous results can be found in (45). We are mainly interested in, from an application point of view, the bias that this fact introduces in naïve inference approaches, and possible correction strategies.

Let us start then with the simplest possible construction, i.e. the Euler-Maruyama scheme applied to Eq. 4.1 (in this case corresponding to the Milstein scheme) (106). The discrete update equations for the Markov process read:

$$\begin{cases} x_{n+1} - x_n = \Delta t \, v_n \\ v_{n+1} - v_n = -\eta \Delta t \, v_n - \Delta t \, f(x_n) + \sigma \Delta t^{1/2} \, r_n, \end{cases} \tag{4.8}$$

with r_n i.i.d. random variables of normal distribution $\mathcal{N}(0,1)$, for $n = 0, \ldots, L-1$. We remind that the first neglected terms in Eq. 4.8 are $O(\Delta t^{3/2})$. The scheme provides then a deterministic update for the x variables, which manifests itself through δ-functions; a

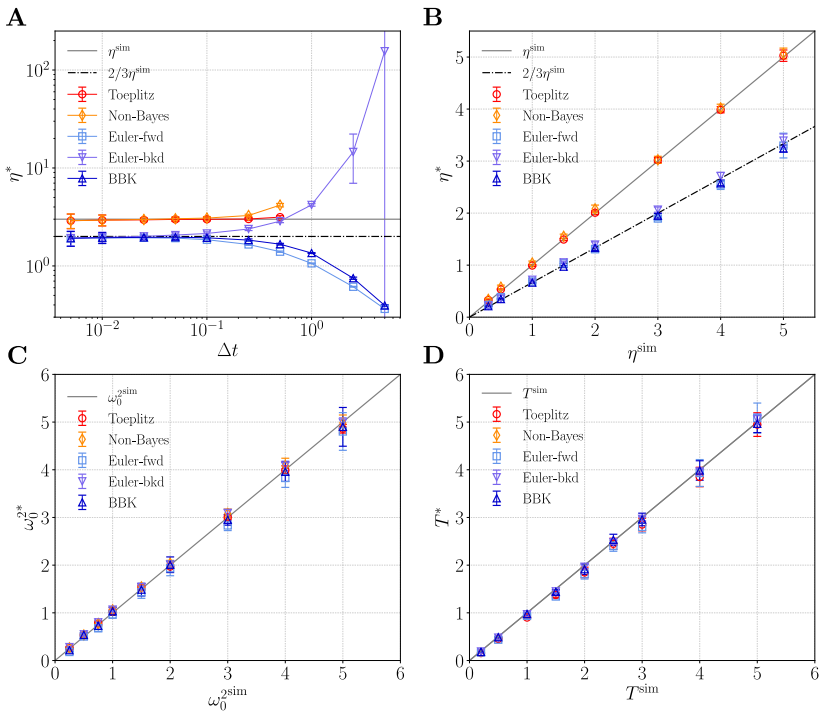

Figure 4.1: **Inference results for the stochastic harmonic oscillator.** Sample trajectories are obtained from exact numerical integration of the set of first order equations with parameters $\eta^{\rm sim}$, $\omega_0^{\rm sim}$ and $T^{\rm sim}$. The simulation time step $\tau^{\rm sim}$ is always equal to 0.005, and it corresponds to the minimum displayed value of Δt in **A**. Points at higher values of Δt are obtained applying the inference procedure to sub-trajectories extracted from the original one. Each of the points displayed in **B-D** is obtained as a weighted average of the inference results for different Δt values in the range where the small Δt approximation is valid. Weights correspond to the squared inverse of the errorbars, displayed in **A** for the η parameter. We compare the accuracy of all the schemes derived in App. A.1.2 from a first order Taylor-Itô expansion (Euler-fwd, Euler-bkd, BBK) and from a second order expansion (Toeplitz, Non-Bayes). **A.** Inferred values for the damping coefficient of the harmonic oscillator, η^*. Averages over 10 sample trajectories of 5000 points (for any Δt) are reported with their 0.95 CI. Simulation parameters: $T = 1$, $\omega_0 = 1$, $\eta = 3$. **B.** Inferred damping coefficient η^* vs true simulation parameter $\eta^{\rm sim}$: results from higher order methods follow the line of slope 1, whereas numerical results from naïve methods fall on the line of slope 2/3. The remaining parameters are fixed: $T = 1$, $\omega_0 = 1$. **C.** Inferred squared frequency of the harmonic oscillator ω_0^{2*} vs true simulation parameter $\omega_0^{2\rm sim}$. All the schemes give correct results in this case in the whole explored range of values. Simulation parameters: $\eta = 3$, $T = 1$. **D.** Inferred temperature T^* vs the true value of the simulation parameter T^{sim}: again, results from all schemes fall on the line of slope 1 in the whole explored range of values. Remaining simulation parameters: $\eta = 1.5$, $J = 1$.

simple change of variables from r_n to v_{n+1} immediately completes the derivation of the discrete propagator in (x, v) space. Finally, in this case one can explicitly marginalize over the velocity degrees of freedom, and eliminate the initial condition v_0. Indeed, to this order of approximation, information on v_0 is fully equivalent to information on x_1. From this marginalization, a fully factorized probability distribution for the discrete sequence is obtained:

$$P_{(1)}(x_L, \ldots, x_2|x_0, x_1) = \prod_{n=1}^{L-1} P_{(1)}(x_{n+1}|x_n, x_{n-1}), \tag{4.9}$$

where transition probabilities are defined as follows:

$$P_{(1)}(x_{n+1}|x_n, x_{n-1}) = \frac{1}{Z_n} e^{-S_n(x_{n+1}, x_n, x_{n-1})}, \tag{4.10}$$

with

$$Z_n = \sqrt{2\pi\sigma^2\Delta t^3}; \tag{4.11}$$

$$S_n = \frac{1}{2\sigma^2\Delta t^3}\left[x_{n+1} - 2x_n + x_{n-1} + \eta\Delta t(x_n - x_{n-1}) - \Delta t^2 f(x_n)\right]^2. \tag{4.12}$$

A factorization of $P(x_L, \ldots x_2|x_1, x_0)$ into a product of transition probabilities of this kind is possible because the random variables appearing in the x difference equation, obtained from Eq. 4.8 through variable elimination, are independent. This is a crucial but artificial feature occurring only at this level of approximation: more accurate discretization procedures produce an effective noise for the x variables which is correlated in time. As a matter of fact, when the description of a Brownian motion is contracted from the full phase space to position space, a colored noise emerges, which is incompatible with the independence of subsequent random variables at any Δt.

Nonetheless, we find it useful to compute the associated dynamical likelihood, as defined in Eq. 4.2, and develop the corresponding inference scheme. For the sake of clarity, we will focus on the example of the harmonic oscillator, where $f(x) = -\omega_0^2 x$. Using Eqs. 4.10–4.12 , an expression for the likelihood as product of transition probabilities for a second order master equation is recovered. This corresponds to the discrete path probability one would obtain adopting a maximum caliber approach (97) when certain time-dependent observables are taken as fixed. For the one-dimensional harmonic oscillator, they are the equal-time correlations, one-time-step correlations and two-time-step correlations of the process. Indeed, rearranging the sum of S_n's in Eq. 4.9, the reduced minus-log-likelihood can be written as:

$$\begin{aligned}\frac{\mathcal{L}(\eta, T, \omega_0^2)}{L-1} = \frac{1}{2}\ln(2\pi\sigma^2\Delta t^3) + \frac{1}{2\sigma^2\Delta t^3}\Big[&C_s' + (2 - \eta\Delta t + \omega_0^2\Delta t^2)^2 C_s + (1 - \eta\Delta t)^2 C_s'' \\ &+ 2(1-\eta\Delta t)F_s - 2(2 - \eta\Delta t + \omega_0^2\Delta t^2)G_s - 2(1-\eta\Delta t)(2 - \eta\Delta t + \omega_0^2\Delta t^2)G_s'\Big],\end{aligned} \tag{4.13}$$

where we introduced the following notation for the experimental temporal correlation

functions, evaluated at a time distance of 0, Δt and $2\Delta t$:

$$C_s = \tfrac{1}{L-1}\textstyle\sum_{n=1}^{L-1} x_n x_n; \qquad C'_s = \dfrac{1}{L-1}\displaystyle\sum_{n=1}^{L-1} x_{n+1}x_{n+1};$$

$$C''_s = \tfrac{1}{L-1}\textstyle\sum_{n=1}^{L-1} x_{n-1}x_{n-1}; \quad G_s = \dfrac{1}{L-1}\displaystyle\sum_{n=1}^{L-1} x_n x_{n+1};$$

$$G'_s = \tfrac{1}{L-1}\textstyle\sum_{n=1}^{L-1} x_n x_{n-1}; \qquad F_s = \dfrac{1}{L-1}\displaystyle\sum_{n=1}^{L-1} x_{n-1}x_{n+1}.$$

Minimization of the quantity in Eq. 4.13 with respect to η, T and ω_0^2 yields the inference formulas for the parameters of the harmonic oscillator. We express here only the estimator of the damping coefficient η, while the remaining ones can be found in App. A.1.2:

$$\eta^* = \frac{1}{\Delta t}\frac{2C_s - G_s - G'_s - \dfrac{G'_s}{C''_s}(2G'_s - C''_s - F_s)}{C_s + C''_s - 2G'_s - \dfrac{(C''_s - G'_s)^2}{C''_s}}. \tag{4.14}$$

At this point, having an explicit inference method, it can be both numerically and analytically tested. We simulated discrete trajectories of the stochastic harmonic oscillator in several damping conditions using an exact integrator (107), with a numerical time step $\tau^{\mathrm{sim}} = 0.005$. We applied inference formulas to discrete data sets sampled from synthetic trajectories at time intervals $\Delta t \geq \tau^{\mathrm{sim}}$. This choice mimics real experiments, where the time resolution is fixed by the acquisition apparatus, while the true microscopic time-scale of the dynamics is unknown. Filtering the synthetic trajectories in time is a good blind inspection tool to check the robustness of the continuous description given by the inferred parameters, without prior knowledge about the time scales of the process. Moreover, this test on numerical simulations can help us identifying the time window in which any dynamical inference scheme is expected to work: in discretizing the equations of motion, the implicit assumption is that Δt must be much smaller than the typical time scales of the process (η^{-1} and ω_0^{-1} in this example).

Results, reported in Fig. 4.1, show that a systematic error in the estimation of the damping coefficient emerges, which can be cast into a constant rescaling factor close to 2/3 for the inferred value η^* as compared to the true value η^{sim}. It is worth remarking that this rescaling is *independent of* Δt, as clearly visible in Fig. 4.1A, so increasing the resolution of the acquisition instruments is of no help in improving the estimation of the damping coefficient. The same problem also occurs when using other variants of the EM scheme obtained from a Taylor-Itô expansion of the same order, as we illustrate in App. A.1.2. On the contrary, the estimation of the remaining parameters is in agreement with the parameter values used in the simulations, as shown in Figs. 4.1C–D.

Numerical evidence for the stochastic harmonic oscillator agrees with the results of Refs. (47; 46), who pointed out, in a non-Bayesian framework, the failure of the same naïve embedding strategy for second order SDEs. We stress that the EM discretization is the simplest and most commonly used extrapolation of the derivative of an observed variable from its finite increment. This approximated estimation of the velocity works if one observes the system in the overdamped regime, i.e. when $\eta\Delta t \gg 1$ and $\omega_0/\eta < \infty$,

and the effective dynamics can be described by a first order equation. In this case, EM-based inference schemes provide in effect excellent results (80; 88). However, when a non-Markovian signal is observed, such as the partial observation of a higher dimensional Markovian process, these schemes are bound to fail.

A simple argument can help us to understand what is missing, and why the parameter η is the one affected by the approximation. Assuming that experimental averages perfectly reproduce ensemble averages, we can replace into Eq. 4.14 the known analytical expression for the self-correlation of the harmonic oscillator in the stationary regime $C(0)$, $C(\Delta t)$ and $C(2\Delta t)$. Since the underlying assumption of the whole procedure is that the time lag Δt between subsequent points is small, compared to the typical time scales of the dynamics, we can perform a Taylor expansion around $t = 0$, obtaining from Eq. 4.14 an expression for η^* depending only on the derivatives of $C(t)$ at $t = 0$:

$$\eta^* \simeq \frac{1}{\Delta t} \frac{2\dot{C}(0) - \frac{2}{3}\dddot{C}(0)\Delta t^2 - \frac{\ddot{C}(0)\dot{C}(0)}{C(0)}\Delta t^3}{2\dot{C}(0) + \ddot{C}(0)\Delta t + \frac{1}{C(0)}\left[\dot{C}(0) + \frac{1}{2}\ddot{C}(0)\Delta t\right]^2 \Delta t}. \tag{4.15}$$

Knowing explicitly $C(t)$ for the harmonic oscillator (also in App. A.1.2, Eq. A.27), one can compute the desired derivatives:

$$C(0) = \frac{T}{\omega_0^2}\,; \quad \dot{C}(0) = 0\,; \quad \ddot{C}(0) = -T\,; \quad \dddot{C}(0) = \eta T\,. \tag{4.16}$$

Proper combinations of these quantities allow us to extrapolate all the parameters of the model. The importance of the first derivative as a quantity to discriminate between first and second order dynamics in oscillator-like models has already been stressed in (108; 78), with explicit reference to complex interacting systems. Our point is that we can go beyond the binary answer provided by $\dot{C}(0)/C(0)$, proportional – through a time scale factor – to 1 or to 0 for first or second order dynamics respectively, and give a quantitative estimation of the damping regime in which a system operates, employing all the derivatives at $t = 0$ up to the third one.

By replacing Eqs. 4.16 into Eq. 4.15, we obtain:

$$\eta^* = -\frac{2}{3}\frac{\dddot{C}(0)}{\ddot{C}(0)}\left[1 + O(\Delta t)\right] = \frac{2}{3}\eta + O(\Delta t). \tag{4.17}$$

We find then, at the leading order, a rescaling factor of 2/3, as observed in numerical tests. No rescaling factors appear for the other inferred parameters: performing the same replacement and expansion of the analytical correlation functions in the inference formulas of T and ω_0, we see that temperature and pulsation are correctly retrieved from proper combinations of $C(0)$ and $\ddot{C}(0)$.

This result gives us a clue to understand the origin of the Δt-independent rescaling factor for η. Looking back at Eq. 4.8, one realizes from simple dimensional analysis that the elimination of the velocity variables makes terms of order $O(\Delta t^{3/2})$ appear, even if the starting accuracy of the expansion is $O(\Delta t)$. This means that Eq. 4.13 has been inconsistently derived retaining only some of the $O(\Delta t^{3/2})$ contributions; in turn this produces missing $O(\Delta t^3)$ contributions to the fluctuations of x. This explains why Eq. 4.14 is incorrect and shows the need of higher order discretization schemes for stochastic second

order dynamics.

We finally remark that this 2/3 rescaling factor is not a specific feature of the stochastic harmonic oscillator, but a recurrent trait in stochastic models of the form of Eq. 4.1. As rigorously proven by Gloter, the so-called quadratic variation of the discretized velocities (corresponding to an empirical estimate of the squared acceleration) uniformly converges to the expected value for the quadratic variation of the real unobserved velocities rescaled by 2/3 (45). These quadratic variations are $O(\Delta t^3)$, and the former one is the only directly measurable quantity containing the necessary dynamical information to disentangle the contribution of dissipation from diffusion and infer η in our setting [2].

Higher order inference schemes

The lowest order of convergence required to develop any reasonable dynamical maximum likelihood scheme is $O(\Delta t^{3/2})$. Since the mean square convergence of the infinitesimal increment of the process is what determines its statistical properties at any time, the minimum requirement for an inference method exploiting only local dynamical information is to reproduce fluctuations correctly at the leading order in Δt.

Independently of the details of the discretization, following the procedure outlined in Sec. 4.3.1, with $O(\Delta t^{3/2})$ accuracy one reduces to a sequence of intertwined Gaussian integrals for the marginalization of $v_1 \dots v_L$, which may be cumbersome to compute for arbitrary length of the trajectory. Therefore, it is convenient to work again with update equations in x space. They can be obtained either from a temporal discretization of the GLE 4.7 or from the elimination of the velocity variables in the discrete-time equations resulting from a second order Taylor-Itô expansion of the Markov process in Eq. 4.3. In the first case, since the same exponentially decaying kernel propagates both the noise and the initial condition in Eq. 4.7, it is possible to manipulate the integrated GLE to find a stochastic difference equation that does not contain v_0 and is driven by a short correlated effective noise:

$$x_{n+1} - x_n - e^{-\eta\Delta t}(x_n - x_{n-1}) = \frac{1 - e^{-\eta\Delta t}}{\eta} \int_{t_{n-1}}^{t_{n+1}} \Psi(t - t_n) f(x(t)) dt + \zeta_n \quad (4.18)$$

where

$$\zeta_n = \int_{t_{n-1}}^{t_{n+1}} \Psi(t - t_n)\xi(t)dt; \quad (4.19)$$

$$\Psi(t) = \begin{cases} \frac{e^{\eta t} - e^{-\eta\Delta t}}{1 - e^{-\eta\Delta t}} & \text{if } -\Delta t < t < 0\ ; \\ \frac{1 - e^{\eta(t-\Delta t)}}{1 - e^{-\eta\Delta t}} & \text{if } \quad 0 < t < \Delta t\ . \end{cases} \quad (4.20)$$

Correspondingly, the *'first discretize, then marginalize'* strategy provides a stochastic difference equation with the same properties. We detail both procedures in App. A.1.1.

Concentrating on the case of the stochastic harmonic oscillator, any consistent discrete-time description in x space takes the form of a linear stochastic difference equation like:

$$x_{n+1} + \alpha x_n + \beta x_{n-1} = \zeta_n, \quad (4.21)$$

[2] The class of models considered by Gloter in (45) isn't exactly the same as the one we consider in Eq. 4.1 ($f(x) = 0$ is assumed and the presence of nonlinear nonconservative forces and of a multiplicative noise of the form of $\sigma(v)\xi$ is allowed) but we think that the result in (45) may be extended also to the $f(x) \neq 0$ case.

where the inhomogeneous terms ζ_n are still Gaussian random variables of null mean, but they are no longer independent. This is the crucial difference with the Euler-Maruyama scheme, which takes into account only the diagonal entries of the covariance matrix $C_{nm} = \langle \zeta_n \zeta_m \rangle$.

Eq. 4.21 defines an affine map:

$$\boldsymbol{\zeta} = (\zeta_1, \dots, \zeta_{L-1})^\top \mapsto \mathbf{x} = (x_2, \dots, x_L)^\top = \mathbf{M}^{-1}\boldsymbol{\zeta} + \mathbf{x}_0, \tag{4.22}$$

where $M_{ij} = \delta_{i,j} + \alpha\delta_{i,j-1} + \beta\delta_{i,j-2}$ and $\mathbf{x}_0 = (x_0, x_1, 0, \dots, 0)^\top$, which can be generalized to a nonlinear transformation when anharmonic forces are present. This map can be exploited, when the covariance matrix $\mathbf{C}$ and its inverse are known, to write the new, higher order, dynamical likelihood. For the harmonic oscillator, it reads:

$$\begin{aligned} P_{(2)}(x_L, \dots, x_2 | x_1, x_0) &= \frac{1}{Z} \exp \\ -\frac{1}{2} \sum_{n,m=1}^{L-1} &(x_{n+1} + \alpha x_n + \beta x_{n-1}) {C^{-1}}_{nm} (x_{m+1} + \alpha x_m + \beta x_{m-1}), \end{aligned} \tag{4.23}$$

where Z is the normalization constant:

$$Z = \left[(2\pi)^{L-1} \det \mathbf{C} \right]^{1/2} = \left[\prod_{k=1}^{L-1} 2\pi\lambda_k \right]^{1/2}, \tag{4.24}$$

with λ_k the k-th eigenvalue of the covariance matrix $\mathbf{C}$. The effective parameters α and β, as well as the entries of the covariance matrix, are known combinations of the parameters of the model, whose details depend on the adopted discretization scheme. In the following results we adopt $\alpha = -1 - e^{-\eta\Delta t} + \omega_0^2 \Delta t \left(1 - e^{-\eta\Delta t}\right)/\eta$ and $\beta = e^{-\eta\Delta t}$.

For well-chosen α, β and C_{nm}, Eq. 4.21 and Eq. 4.23 are exact, in the limit $L \to \infty$. Thanks to linearity, it is possible to design an exact integration algorithm for the Markov process 4.3 at any time step increment Δt (107). For nonlinear generalizations of $f(x)$, the exact Gaussian character of the random increment is lost. However, at leading order in Δt, a multivariate Gaussian distribution still represents a good approximation for the distribution of the random increments ζ_n appearing in the x update equation, which takes the form:

$$x_{n+1} + F(x_n, x_{n-1}; \boldsymbol{\mu}) = \zeta_n, \tag{4.25}$$

with $\boldsymbol{\mu}$ a set of effective parameters. The corresponding generalization of Eq. 4.23 can be obtained (see App. A.1.2).

To order $O(\Delta t^3)$, for both linear and nonlinear second order processes, one can deduce from Eq. 4.19 that $\mathbf{C}$ has a 'nearest-neighbour' structure of the kind:

$$C_{nm} = \langle \zeta_n \zeta_m \rangle = a\, \delta_{n,m} + b\, \delta_{n,m\pm1} \tag{4.26}$$

where

$$a \simeq \frac{2}{3} 2T\eta\Delta t^3\,; \quad b \simeq \frac{1}{6} 2T\eta\Delta t^3. \tag{4.27}$$

Hence the covariance matrix has the form of a symmetric tridiagonal Toeplitz matrix of order $L-1$. These mathematical features carry a deep physical meaning: first of all,

the presence of non-vanishing off-diagonal elements is the signature of a colored noise. Secondly, the fact that the matrix is banded means that the correlation of the noise variables is short-ranged, i.e. that the associated memory kernel, in a continuous-time description, decays fast (93). Finally, the Toeplitz structure is synonymous with shift invariance.

A more careful derivation of the update equations in x space would require shift invariance not to hold and the first entry of the covariance matrix C_{11} to be different from the other elements of the main diagonal. Eq. 4.21 is in fact not valid for the first integration step, where the initial conditions intervene. In this respect the structure of the data also poses the problem of the elimination of the initial condition v_0 in favour of x_0 and x_1. Even if not able to perform it explicitly without stationarity assumptions, we can argue (see App. A.1.1) that it has the effect of modifying the covariance matrix in the following way:

$$C = \begin{pmatrix} \tilde{a} & b & \dots & 0 \\ b & a & . & \vdots \\ \vdots & . & \ddots & b \\ 0 & \dots & b & a \end{pmatrix}, \tag{4.28}$$

where the shift invariance expressed by the Toeplitz structure of Eq. 4.26 is then broken at the beginning of the time series. Despite that, the error we make by replacing $\tilde{a}$ with a in the quasi-Toeplitz matrix 4.28 is negligible in the limit of long trajectories, as discussed in Sec. 4.3.3 and checked in Fig. 4.4. Intuitively, since the breaking of the shift invariance occurs only at the first step, the longer the trajectory, the more similar this is to a truly shift invariant situation. Notice that what matters is not the total length $(L+1)\Delta t$ of the trajectory in units of the physical time scales of the process, but just the number of points $L+1$ of which the trajectory is made up [3].

Apart from the difficulty in determining correctly $\tilde{a}$, the advantage of replacing the true covariance matrix Eq. 4.28 with a Toeplitz matrix is that the inverse of the Toeplitz matrix is explicitly known, as well as the eigenvalues (109; 110):

$$C^{-1}{}_{nm} = \frac{2}{L} \sum_{k=1}^{L-1} \frac{\sin\left(\frac{nk\pi}{L}\right) \sin\left(\frac{mk\pi}{L}\right)}{a + 2b\cos\left(\frac{k\pi}{L}\right)}; \tag{4.29}$$

$$\lambda_k = a + 2b\cos\left(\frac{k\pi}{L}\right). \tag{4.30}$$

Let us highlight that the inverse of the covariance matrix does not preserve a banded structure. This means that, even if noise correlations are local in time, two-time functions of every pair of points of the trajectory enter into the minus-log-likelihood. Hence Eq. 4.23 cannot be factorized. Factorization corresponds to a block structure for $\mathbf{C}^{-1}$, which implies a block structure for $\mathbf{C}$. This is incompatible with the tridiagonal Toeplitz or quasi-Toeplitz nature of the covariance matrix, where off-diagonal elements are of the same order as the diagonal ones.

[3] This is not surprising if one carefully looks at the expression of the inverse of the tridiagonal Toeplitz matrix Eq. 4.29, which closely resembles Fourier series expansions. Increasing the number of points corresponds to including an increasing number of harmonics; finite size corrections to parameters estimators can be seen as a counterpart of the Gibbs phenomenon.

Nonetheless, having built an explicit discrete path integral measure, a maximum likelihood approach reduces to minimizing the quantity $\mathcal{L} = -\ln P(x_L, \ldots, x_2|x_1, x_0)$ with respect to the parameters of the model. Thanks to the regularities of Eq. 4.23, the minimization of $\mathcal{L}$ can be performed analytically in the case of the harmonic oscillator and, in general, of simple single-particle systems. The optimization procedure can be performed semi-analytically also for many-particle systems, like active agent-based microscopic models or spatially discrete counterparts of field theoretical models. In these cases an additional parameter is typically the interaction range of effective pair-wise potentials, which may depend on a different (measurable) variable than the field-like observable x. In general, once an expression for $\mathcal{L}$ is given, a large number of optimization algorithms are available to minimize it with respect to all the extra parameters that do not allow for a full analytical approach.

Complete inference formulas for one-dimensional harmonic and anharmonic oscillators and for a system of many coupled harmonic oscillators with parameter-dependent connectivity matrix are reported in Apps. A.1.2–A.1.2. In all cases, optimal parameter values are given by combinations of all the two-time functions up to the length of the trajectory, and not only those computed at a temporal distance of 0, 1 and 2 time steps.

For the non-interacting case, we tested the developed schemes numerically by applying the inference formulas to synthetic stochastic trajectories of two reference processes: the Brownian motion in a harmonic potential, and the Brownian motion in a symmetric anharmonic potential $V(x) = \frac{1}{2}kx^2 + \frac{1}{4}\lambda x^4$. The equations of motion corresponding to the latter read:

$$\begin{cases} \dot{x} = v \\ \dot{v} = -\eta v - kx - \lambda x^3 + \sigma\xi\,, \end{cases} \tag{4.31}$$

where we chose a unitary mass particle, $\sigma^2 = 2T\eta$ and $\xi(t)$ as a white noise. We generated synthetic trajectories as in (48) and subsampled them by progressively increasing the time separation Δt between subsequent observed points.

The comparison with naïve inference schemes for the example of the harmonic oscillator confirms the analytical predictions (Fig. 4.1). In any damping regime, the higher order inference method outperforms the naïve scheme in two ways: perturbatively, since the convergence of the parameter estimators is extended to a larger Δt window due to the higher order Taylor-Itô expansion (an example in Fig. 4.1A), and non perturbatively in Δt, since no rescaling factor for the η parameter is required (Fig. 4.1B). The different behaviour of the various schemes at large Δt, where the series expansion is non-asymptotic, is probably related to the details of the discretization rules and their stability properties.

Fig. 4.2 shows numerical results based on the Toeplitz inference scheme for the anharmonic stochastic oscillator for varying values of the parameters λ^{sim} (Figs. 4.2A–D) and k^{sim} (Figs. 4.2E–G). In all the explored regimes the inference scheme provides excellent results, showing, in particular, that no bias is introduced by the possible imbalance between linear and nonlinear force terms (values close to the origin are correctly estimated in Fig. 4.2D and Fig. 4.2F), even if, for a fixed Δt, an increase in the relative error or more noisy estimations cannot be prevented in these conditions (Fig. 4.2G). Moreover, no bias is introduced by the fact that, when k assumes a negative value, the particle may be confined in a single minimum of the double-well potential for all the length of the sampled trajectory (see Fig. 4.2E).

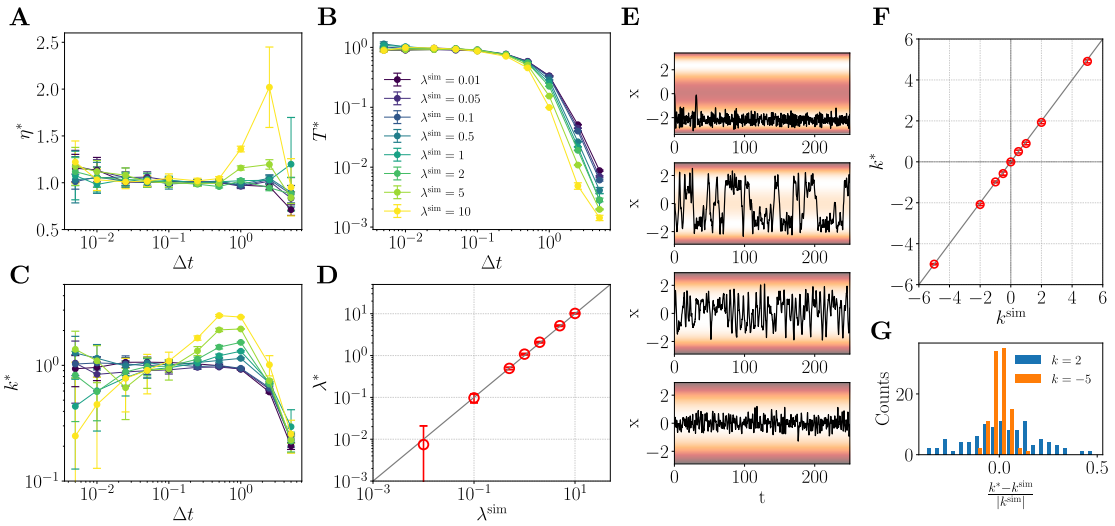

Figure 4.2: **Inference of a Brownian motion in a force field**. We perform Bayesian inference of a Brownian motion in a force field $f(x) = V'(x)$, with $V(x) = \frac{1}{2}kx^2 + \frac{1}{4}\lambda x^4$. Only the Toeplitz method is applied; as for the harmonic oscillator, in **A-D** and **F** 10 sample trajectories of length 5000 points are considered for each Δt. Errorbars are 0.95 CI. **A-C.** Inferred model parameters against subsampling parameter Δt. The true value is equal to 1 in all cases and is marked by the straight grey line. **D.** Inferred vs true value of the nonlinear coefficient λ. **E.** Excerpts of sample trajectories in various landscapes. The strength of the confining potential is qualitatively indicated by the colormap, with light areas corresponding to the minimum of the potential. The following parameters of the simulation are kept fixed: $T = 1$, $\eta = 1$, $\lambda = 1$. By varying the parameter k we realize, from top to bottom: a strong confinement in a double well potential, with long exit times, at $k = -5$; a switching dynamics with relatively short switching times, at $k = -2$; a marginal situation at $k = 0$; confined Brownian motion in the vicinity of the origin at positive values of k ($k = 5$). **F.** Inferred vs true value of the parameter of the linear force k, assuming both positive and negative values. **G.** Histogram of counts for the relative distance of the inferred parameter k^* to the simulation parameter $k^{\rm sim}$. With fixed $\lambda^{\rm sim} = 1$ and $k^{\rm sim} = \{2, -5\}$, the weight of anharmonicity varies, but the variance of all the estimated parameters seems to be unaffected. As a result, relative errors decrease for larger $|k|$. 100 trajectories are sampled for each k value shown in the histogram, and $\Delta t = 0.025$ in all cases.

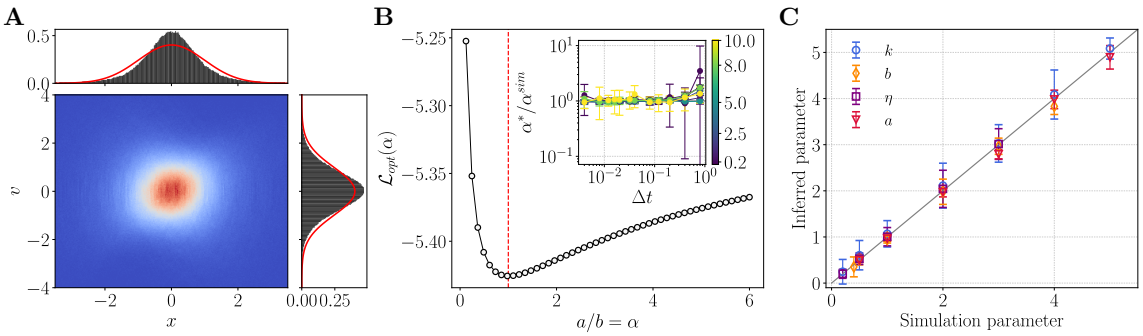

Figure 4.3: **Inference method applied to a multiplicative process.** The process is described by Eq. 4.32 with $f(x) = -kx$ and $\sigma(x) = \sqrt{a + bx^2}$. **A.** The fraction of time spent by the system in each region of the phase space for a sample trajectory of length $4 \cdot 10^4$, with $k = 1$, $\eta = 1$, $a = 1$, $b = 1$ and initial condition $(x_0 = 0, v_0 = 0)$. There is a clear difference with the Gaussian distribution having the same second moment (red line), showing the effect of the multiplicative noise. **B.** Analytically optimized negative log-likelihood as a function of the effective parameter $\alpha = a/b$, computed on a sample sub-trajectory of 5000 points, $\Delta t = 0.016$, with the same parameters as in **A.** In the inset optimal values of α as a function of Δt are reported. Errorbars correspond to 0.95 CI on 10 sample trajectories of 5000 points for each Δt. The color code refers to the value of α^{sim}, measuring the relative contribution of additive and multiplicative part of the noise term. **C.** Performance of the method in inferring the whole set of parameters of the model.

Generalization to multiplicative noise

In order to understand the limits and full potential of the method, we focus in this section on possible generalizations to the case of non-additive noise. An adaptation of our non-Markovian Bayesian inference scheme can be developed for the following class of multiplicative processes:

$$\ddot{x} = -\eta\dot{x} + f(x) + \sigma(x)\xi, \tag{4.32}$$

with $\xi(t)$ a standard white noise and initial conditions $x(0) = x_0$, $\dot{x}(0) = v_0$. This model has two features: linear dissipation, and a velocity-independent diffusion coefficient only proportional to $\sigma^2(x)$. Under these conditions, the memory kernel of the GLE associated to Eq. 4.32 is explicitly known and, following the same procedure that led to the discretization of the additive process in Sec. 4.3.1, we obtain an approximated discrete time update rule of the form:

$$x_{n+1} - x_n - e^{-\eta\Delta t}(x_n - x_{n-1}) - \frac{1 - e^{-\eta\Delta t}}{\eta}\Delta t f(x_n) = \zeta_n, \tag{4.33}$$

where the stochastic term is defined as

$$\zeta_n = \frac{1 - e^{-\eta\Delta t}}{\eta}\int_{t_{n-1}}^{t_{n+1}} dt' \Psi(t' - t_n)\sigma(x(t'))\xi(t'). \tag{4.34}$$

The function $\Psi(t)$ is defined in the same way as in Eq. 4.20.

The approximation of the force term in Eq. 4.33 corresponds to that of the Langevin impulse integrator (49). Alternative numerical integration schemes for GLEs, such as the stochastic Verlet algorithm (111), can also be used.

From now on we will implicitly refer to the Itô integration prescription. However, due to the fact that $\sigma(x)$ only depends on the configurational degree of freedom, x, the mean square convergence of ζ_n is not affected by a switch to the Stratonovich convention. As a result, one can say that, up to $O(\Delta t^3)$, stochastic terms satisfy

$$\langle \zeta_n \zeta_m \rangle \simeq \frac{2}{3}\Delta t^3 \sigma^2(x_n)\delta_{n,m} + \frac{1}{6}\Delta t^3 \sigma(x_n)\sigma(x_m)\delta_{n,m\pm 1}\,. \tag{4.35}$$

This choice of off-diagonal terms ensures the positiveness of the matrix, if $\sigma(x) > 0$ [4]. The covariance matrix also preserves a tridiagonal symmetric structure. However, the Toeplitz property is lost since, in the presence of multiplicative noise, shift invariance cannot hold. Nevertheless, we can build an efficient maximum likelihood inference routine. Let us rewrite the minus-log-likelihood associated to Eq. 4.33 as

$$\mathcal{L} = \frac{1}{2}\sum_{k=1}^{L-1} \ln \lambda_k(\mathbf{x};\boldsymbol{\nu}) + \sum_{n,m=1}^{L-1} \left[x_{n+1} + F(x_n, x_{n-1};\boldsymbol{\mu})\right] {C^{-1}}_{nm}(\mathbf{x};\boldsymbol{\nu}) \left[x_{m+1} + F(x_m, x_{m-1};\boldsymbol{\mu})\right], \tag{4.36}$$

so that we can distinguish between the subset of parameters $\boldsymbol{\mu}$, including η and the parameters of the conservative potential, and the subset $\boldsymbol{\nu}$ appearing in the x-dependent diffusion coefficient $\sigma(x;\boldsymbol{\nu})$. For the parameters in the former set, analytical formulas for their max-likelihood estimators can be found as functions of $\boldsymbol{\nu}$, while the latter generally requires numerical optimization (unless $\sigma(\mathbf{x};\boldsymbol{\nu})$ is univariate and has a purely multiplicative dependence on its single parameter). The effective cost function can be evaluated, also in the case of long trajectories, once the inverse and the spectrum of the symmetric tridiagonal matrix are computed.

To illustrate the method, we applied it to the multiplicative process in Eq. 4.32, with $f(x) = -kx$ and $\sigma(x) = \sqrt{a + bx^2}$, where a and b are non-negative parameters. In this case the max-likelihood procedure can be reduced to a one-dimensional numerical optimization. Complete inference formulas are reported in App. A.1.2 and the results are shown in Fig. 4.3. These confirm that the method provides a reliable inference tool also in the case of a nonequilibrium multiplicative process, independently of the relative strength of the additive and multiplicative contributions to the noise term, and that the procedure does not require equilibrium assumptions to work, nor does it exploit the fluctuation dissipation theorem.

4.3.2 Alternative non-Bayesian approach

Alternative inference approaches to the maximum likelihood method are also possible. Several examples are known in the literature: the most general ones, applicable to a vast class of second order stochastic processes, derive the parameters of the assumed model (in the form of a SDE or of a chosen set of projection functions) through a fitting procedure on measurable quantities, typically involving conditional moments of the increments of the process (95; 46; 96; 47). Also in this case the relations used for fitting can be found through a Taylor-Itô expansion even when a nonlocal solution in time is unknown. Other

[4] There exists a similarity transformation that transforms the matrix in Eq. 4.35 into a strictly diagonally dominant matrix with positive entries. Since the spectrum is unchanged and it is real, this ensures the non-negativity of all the eigenvalues.

strategies have been proposed with a reformulation of the task – having relevant application in chemical physics and molecular dynamics – i.e. not to learn the best model for the measured variables, but to find from higher dimensional data the coarse-grained dynamics of a given system (112; 113).

In this section we put ourselves in a simpler framework than that of Ref. (95; 46; 96) and derive non-Bayesian parameter estimators just for the stochastic harmonic oscillator, in order to compare on this example the non Bayesian methodology and the maximum likelihood dynamical inference scheme we developed. From update equations in position space like Eq. 4.21, obtained from an $O(\Delta t^{3/2})$ Taylor-Itô expansion, some relations between experimental correlation functions and model parameters can be found. Let's take the update equation of the Langevin impulse integrator (49):

$$x_{n+1} = x_n + e^{-\eta\Delta t}(x_n - x_{n-1}) + \frac{1 - e^{-\eta\Delta t}}{\eta}\omega_0^2 \Delta t x_n + \zeta_n. \tag{4.37}$$

with ζ_n the Gaussian random variables characterized by Eq. 4.26. Multiplying both sides of Eq. 4.37 by x_m, for $m \in \{n-1, n, n+1\}$, and self-consistently averaging over the noise distribution, yields a set of three independent equations, from which all the parameters of the dynamical model can be extracted (explicit formulas are derived in Appendix A.1.2).

Notice that, in contrast to the max-likelihood inference method, the obtained relations can involve only three types of temporal correlation functions: equal-time, one-time-step and two-time-step correlations. Even if we are not using all the exploitable information carried by an N-point trajectory (the operation outlined above could in principle be performed for all x_m), this is the optimal minimal choice. Indeed, the shape of the temporal correlation function at small times contains substantial dynamical information. Moreover, due to the finite length of the trajectories, two-time quantities, like correlation functions, are typically better estimated at small time differences than at large ones.

As expected, parameter estimators provide good values without rescaling. Unfortunately, however, we cannot extend this approach to interacting systems, where an interaction range is needed to parametrize the potential. As these formulas do not come from the optimization of any cost function, there is no efficient numerical strategy to find the best parameters of the interaction potential. The problem is bypassed if no assumption is made about the structure of the interaction, and a different parameter is associated to each element pair in the system. In this framework, however, severe overfitting issues may emerge as well as numerical scaling problems, since the number of parameters grows roughly quadratically with the system size. We remark that this scaling curse does not afflict all non-Bayesian inference methods (95), but only the simple one used here to compare its results with our Bayesian scheme.

Finally, it is important to specify the probability density function with respect to which we are taking the averages in Eq. 4.37. Since, in order to compute $\langle x_n \xi_n \rangle$ and $\langle x_{n+1} \xi_n \rangle$, we self-consistently used the same update rule and the same shift-invariant noise statistics, we argue that we implicitly introduced a stationarity assumption, overcoming the problem anticipated in Sec. 4.3.1 and better discussed in Sec. 4.3.3. As a result, the inference formulas obtained in this way do not require any rescaling factor, for any length of the trajectory.

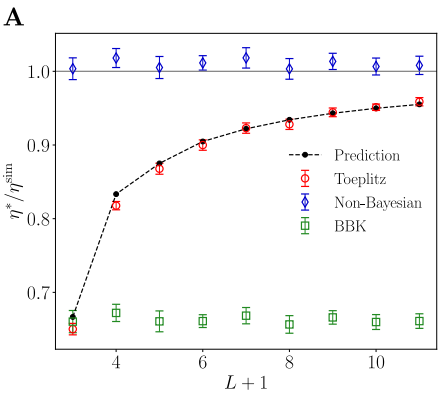

Figure 4.4: **Asymptotic consistency of the ML estimator.** Numerical validation of the finite-size distortion introduced by the shift-invariant approximation. Black points connected by dashed lines represent the analytical prediction about the rescaling factor $\varrho(L+1) = \eta^*(L+1)/\eta^{\rm sim}$, with $\varrho(L=3) = 2/3$ (shortest possible trajectory) and $\varrho(L+1) \to 1$ monotonically as $L \to \infty$. Numerical results are in agreement with this prediction. As expected, no dependence on trajectory length is found for the non-Bayesian method, nor for Euler-like methods (BBK used here – see App. A.1.2 for details).

4.3.3 Role of the unobserved initial condition

Once colored noise is included to take into account the non-Markovian character of the partially observed process, the remaining problem in the application of the Bayesian methodology to second order stochastic models lies in the elimination of the unobserved initial condition. To explain this, let us take a step back.

In a maximum likelihood setting, the first task is to calculate the probability of observing a given sequence of datapoints, knowing the parameters of the model $\boldsymbol{\lambda}$. In first order stochastic processes, when all the degrees of freedom allowing for a Markovian description of the dynamics are experimentally accessible, there is no ambiguity on how this likelihood should be computed (see, for example, (80)). On the other hand, for second order stochastic processes the inference problem may turn out to be ill-defined. For a first order model

$$\dot{y} = g(y) + \xi, \tag{4.38}$$

with initial condition $y(0) = y_0$ the propagator is defined as $P(y_L, \dots, y_1|\boldsymbol{\lambda}; y_0)$. Here y_0 represents quantities that do not change in the inference procedure and the same in the posterior, the likelihood and the prior: the initial condition and the structure of the model. We will introduce a semicolon to separate the quantities that do are not updated in the inference. For a second order stochastic process the initial condition is given by the pair $x(0) = x_0$, $\dot{x}(0) = v_0$ and the propagator is $P(x_L, \dots, x_1|\boldsymbol{\lambda}, x_0, v_0)$. However, unlike x_0, the initial condition on the velocity is not empirically known, so we the propagator does not result in a likelihood of the form of $P(x_L, \dots, x_1|\boldsymbol{\lambda}; x_0, v_0)$.

Let us briefly note that this is strictly connected to the embedding problem in stochastic processes, and that the only consistent way to bypass it is to use the steady state distribution of v_0. Nonetheless, in Sec. 4.3.1 we decided to deal with the initial condition problem in a different way. First, the choice of the discretization scheme confined the initial condition problem only to the first timestep, independently of the total number of

datapoints and the relation of the decay time of the memory kernel to Δt. Neglecting the breaking of shift invariance, we introduced a Toeplitz approximation for the noise covariance matrix: this approximation works well for long trajectories (with many datapoints), whereas it fails for very short ones. The convergence is however quite fast, as shown in Fig. 4.4. The advantage of this strategy is twofold: it is simpler than exact marginalization, and applies even when a steady state distribution is not available (e.g. in the multiplicative case).

Remarkably, the problem of the elimination of the initial condition on the first derivative of the observed variable doesn't affect the non-Bayesian approach. This tells us that non-Bayesian methods apply even to (multiple) disconnected triplets of points or, in general, to disconnected small sequences, if a fragmented observation of the system is the only one achievable. On the contrary, the Toeplitz method is exact only in the infinite trajectory limit, so the smaller the number of subsequent points, the less accurate the inference scheme becomes. In other words, what matters in this case is not only the total number of points for statistical reasons — which is the only thing to worry about in all the other developed schemes — but also their succession in time.

We checked this in numerical simulations of the stochastic harmonic oscillator, keeping constant the total number of points used in the inference procedure, $(L+1)n_S$, and adapting the number of samples n_S as the length $L+1$ of the sample trajectories is varied. A significant deviation of the inferred value from the simulated one is visible in Fig. 4.4 for small values of L. For small L it is also possible to approximately estimate the distortion introduced by the finite size of the trajectory under the Toeplitz assumption. Following the same idea that led to the prediction of the $2/3$ function for the η parameter of the harmonic oscillator, one can expand the two time correlation functions appearing in the Toeplitz inference formulas for small L, obtaining

$$\eta^* \simeq -\frac{1}{\Delta t} \ln \left(1 + \varrho(L+1) \frac{\dddot{C}(0)}{\ddot{C}(0)} \Delta t \right) [1 + O(\Delta t)] \,, \tag{4.39}$$

from which we deduce that the Δt-independent rescaling factor of the damping coefficient can be identified with $\varrho(L+1)$ in Eq. 4.39. The first few values of these rescaling factors are: $\varrho(3) = 2/3$, $\varrho(4) = 5/6$, $\varrho(5) = 7/8$, $\varrho(6) = 19/21$, in good agreement with numerical results. The exact value is only retrieved in the $L \to \infty$ limit, yet time lapse recordings in common motility observation experiments are typically composed by a much larger number of frames than those shown in Fig. 4.4. Although we showed that the wrong marginalization of the initial condition can play a role, in practice this effect can hopefully be neglected in many situations.

4.3.4 Interacting case

Following our original objective to develop an inference strategy for natural flocks of birds, we generalized the inference equations of Sec. 4.3.1 and performed numerical simulations of the topological inertial spin model (ISM) on a non-evolving random lattice at low temperature. The model, introduced to account for experimentally observed features that could not be explained within the framework of first order processes (17; 19), represents a second-order generalization of the well-known Vicsek model. The stochastic equations

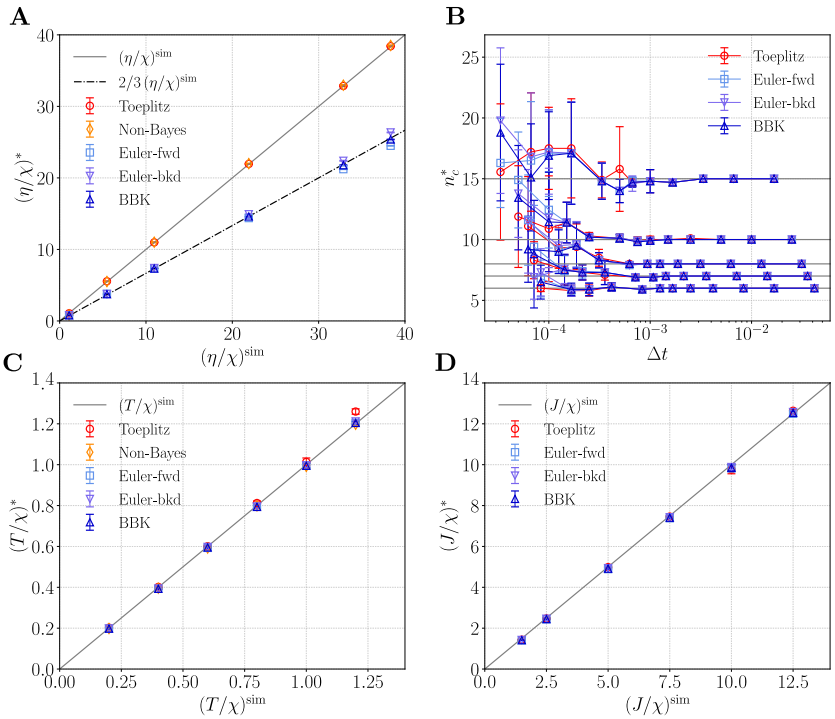

Figure 4.5: **Inference results for the Inertial Spin Model. A.** Inferred values for the effective damping coefficient η/χ. We notice the emergence of a 2/3 rescaling factor for naïve methods derived from first order Taylor-Itô expansions. **B.** Inferred topological interaction range from numerical minimization of the reduced minus-log-likelihood, which is properly defined only in the Toeplitz scheme and in the three lower order variants of the Euler scheme. **C.** Inferred values for the parameter T/χ, as derived from Eq. 4.41. One notices a slight divergence from the slope-1 line, which is especially evident at large temperatures. This is due to the spin-wave approximation (SWA), whose first correction only impacts the temperature parameter and can be explicitly evaluated, as explained in App. A.1.3. **D.** Inferred values of the interaction strength, $(J/\chi)^*$ vs the parameter value used in simulations, $(J/\chi)^{\rm sim}$. All methods retrieve the correct results. We remark that only the parameters in the left panels, η/χ and T/χ, can be estimated by the non-Bayesian method. In all the simulations we took flocks of $N = 1000$ birds. Additional information about the choice of the model parameters and numerical methods can be found in Methods. Points in **A-C** and **D** are obtained as in the case of the harmonic oscillator (see Fig. 4.1). For the $O(\Delta t^{1/2})$ methods we consider different integration schemes: standard Euler (Euler-fwd), inverse (Euler-bkd) and BKK defined in section A.1.2).

of motion in three dimensions read:

$$\begin{cases} \dot{\mathbf{r}}_i = \mathbf{v}_i \\ \dot{\mathbf{v}}_i = -\frac{1}{\chi}\mathbf{v}_i \times \mathbf{s}_i \\ \dot{\mathbf{s}}_i = -\frac{\eta}{\chi}\mathbf{s}_i + \frac{1}{v_0^2}\sum_j J_{ij}\left(\mathbf{v}_i \times \mathbf{v}_j\right) + \boldsymbol{\xi}_{i\perp}, \end{cases} \tag{4.40}$$

where the indexes $i, j = 1, \ldots, N$ label different individuals, v_0 is the constant modulus of each velocity vector $\mathbf{v}_i$, and $\boldsymbol{\xi}_{i\perp}$ is the orthogonal projection to $\mathbf{v}_i$ of a three-dimensional white noise of parameters T and η: $\langle \boldsymbol{\xi}_{i\perp}(t) \cdot \boldsymbol{\xi}_{j\perp}(s) \rangle = 2\delta_{ij} 2T\eta\delta(t-s)$. Motivated by the findings of (89), we choose to parametrize the coupling constant as $J_{ij} = J\, n_{ij}$, where $n_{ij} = 1$ if bird j is among the first n_c nearest neighbours of bird i, whereas it takes a null value otherwise.

In the ordered phase, the spin-wave expansion of the equations of motion of the inertial spin model linearizes the force terms, and Eq. 4.40 takes the form of a set of SDEs for N coupled harmonic oscillators (80):

$$\chi\ddot{\boldsymbol{\pi}}_i = -\eta\dot{\boldsymbol{\pi}}_i - J\sum_{j=1}^{N}\Lambda_{ij}\boldsymbol{\pi}_j + \tilde{\boldsymbol{\xi}}_{i\perp}\,, \quad i = 1, \ldots, N. \tag{4.41}$$

Here $\boldsymbol{\pi}_i$ are the birds' normalized velocity fluctuations, lying on the orthogonal plane to the direction of collective motion, $\Lambda_{ij} = n_c\delta_{ij} - n_{ij}$ is the discrete Laplacian of the birds' network, and $\tilde{\boldsymbol{\xi}}_{i\perp}$ is now a two-dimensional white noise that lives on the same plane as $\boldsymbol{\pi}_i$. To leading order, it is described by the parameters T and η appearing in Eq. 4.40. For a full derivation of the equations of motion in the spin-wave approximation see App. A.1.3. Thanks to the linearity of Eq. 4.41, the same inference strategy one can develop for a system of coupled harmonic oscillators applies also to the inertial spin model in the highly polarized phase.

For the sake of simplicity, in our simulations we discarded the first equation of Eq. 4.40 and kept the birds' reciprocal positions fixed. The dynamical maximum likelihood approach, however, should work even when reshuffling birds' reciprocal positions and static approaches fail, since at each time step it is possible to reconstruct the neighborhood of each individual and compute the associated time-dependent observables (88; 80; 20). This would introduce an effective nonlinearity which, like in the non-interacting case, is not supposed to modify the leading Gaussian nature of the propagator at small Δt.

We applied and compared different inference strategies to the synthetic trajectories. Results are in qualitative agreement to those of the harmonic oscillator. In particular, the expected rescaling factor of 2/3 for the damping coefficient is retrieved using any EM-like scheme, as shown in Fig. 4.5A. This fact corroborates that the emergence of this 2/3 factor is a universal feature of second order stochastic processes, coming from the interplay between the terms containing second and first order time derivatives, rather than the kind of conservative forces which are applied to the system. Again, Bayesian and non-Bayesian inference schemes derived from a higher order expansion do not require any rescaling – at least for sufficiently long trajectories.

As already mentioned, however, there are some relevant differences with respect to the simple non-interacting case. First of all, the additional difficulty we must face in the case of N-body dynamics is that of estimating the interaction range. Since an explicit

analytical minimization of the minus-log-likelihood is not operable, a numerical approach is needed. The problem is however algorithmically tractable, since it simply consists of a one-dimensional optimization problem. Moreover, if the parametrization of the n_{ij} matrix discussed above is adopted, n_c is a discrete parameter, so the exact minimum value can always be found (see Fig. 4.5B). Wrong estimations of the topological interaction range can be due to a blurred reconstruction of the likelihood from the data. As the number of birds N or the number of trajectory points L is increased, the improved statistics smoothens the rugged reconstructed likelihood and the real minimum becomes easier to detect. To this end, another parameter playing a relevant role is the time lapse Δt: when the separation between subsequent datapoints is very small compared to the time scales of the system, increments are also very small. Smaller increments correspond to smaller quantities to minimize, which are then subject to bigger relative errors. This effect is at the origin of what we observe in Fig. 4.5B.

Once the optimal value of n_c is recovered, it is then used to compute the spatially structured correlation functions which enter into the formulas of the remaining parameters. Non-Bayesian methods are not based on any likelihood definition, and, as a result, do not allow us to infer n_c. Despite that, an approximated estimation of the effective temperature T/χ and of the damping coefficient η/χ is still possible, as shown in Figs. 4.5A and Fig 4.5C. On the contrary, the parameters associated to the interaction potential, n_c and J, are not evaluated within this framework.

Applied to large interacting systems, our non-Markovian maximum likelihood method performs well even for relatively short trajectories. Taking, for instance, trajectories of length $L = 200$ for systems of $N = 1000$ particles already enables us to achieve good accuracy, with undistinguishable features in the inference of η/χ and T/χ compared to the non-Bayesian method (see Fig. 4.5). As already pointed out, the need for very long trajectories in the max-likelihood scheme, for both single particle and many particle models, stems from two different facts. Firstly, the shift-invariance approximation introduced by enforcing a Toeplitz structure for the noise covariance matrix results in better performance for longer trajectories. Secondly, the empirical reconstruction of two-time correlations, which are the quantities that enter into inference formulas, improves when achieved from longer trajectories as compared to shorter ones. In other words, the larger the number of datapoints, the higher the amount of available information. The advantage of moving from the single oscillator to the many-body interacting case is that a restricted number of "local" quantities turn out to dominate and self-average in sufficiently large systems. So the statistical issue can be at least partially mitigated by averaging over the sample size, rather than relying only on temporal averages as we are compelled to do in the case of the harmonic oscillator.

4.3.5 Effect of experimental errors

So far, we have not included observation errors in the developed inference scheme, but we assumed that stochastic trajectories are sampled with infinite accuracy. However, data are typically affected by accuracy limitations and other sources of experimental errors. In the current section we show the effects of an additional source of noise on the estimation of the model parameters.

The simplest (still realistic, in many practical cases) way to model experimental errors is through a superposition of the discretely sampled trajectory with a sequence of i.i.d.

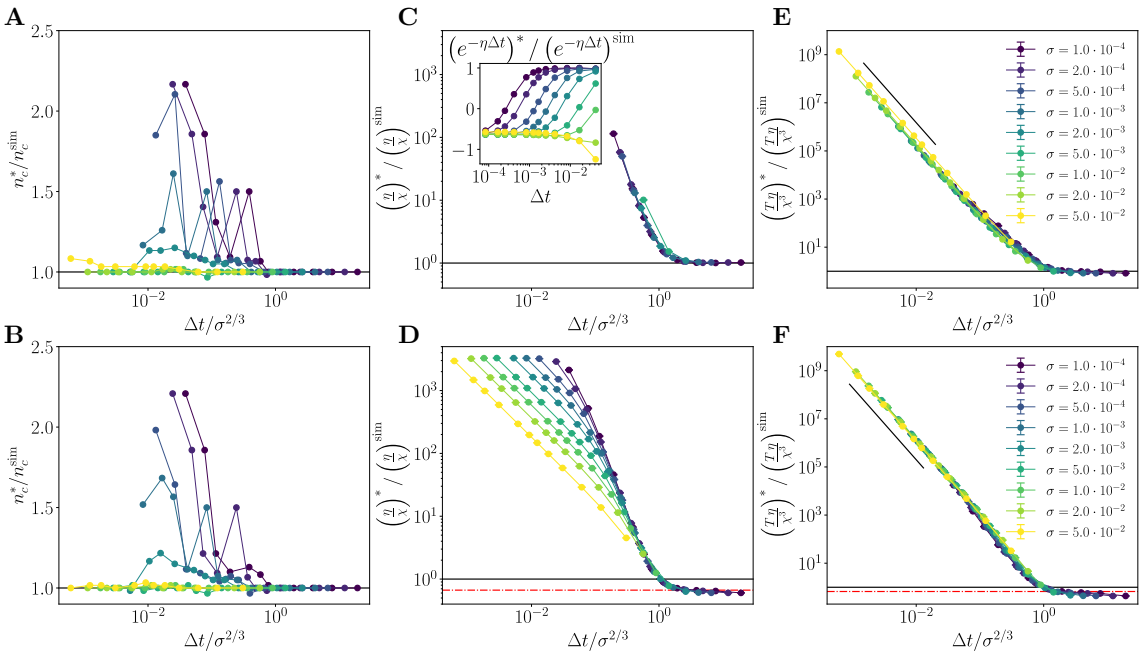

Figure 4.6: **Effect of measurement error for the ISM.** In the top row results from the Toeplitz inference scheme are reported; in the bottom row results from the BBK inference scheme are reported. The rescaling of the inverse sampling rate in the abscissa make the curves in **C-F** to depart at the same point ($\Delta t/\sigma^{2/3} \sim 1$) from the expected value in absence of experimental errors (1 for the Toeplitz method, 2/3, marked by the red dot-dashed line, for the BBK method). The collapse of the curves shown in **E-F** proves that the control parameter is the ratio between stochastic and experimental noise: $T\eta\Delta t^3/\sigma^2$. The black lines, having a slope -3, are a guide for the eye. We notice that for large noise-to-signal ratio the estimate of η with the Toeplitz method may be problematic since estimators of positive definite quantities built with noisy data can become negative, as visible in the inset of **C**. We refer to App. A.1.2 for details on the inference formulas. Errorbars on **A-B** are not shown, for sake of clarity, whereas in **C-F** the 0.95 CI is smaller than the markersize.

Gaussian random variables $\mathcal{N}(0, \sigma^2)$.

As pointed out by several authors (47; 46; 95), even when σ^2 is very small measurement noise can impact dynamical inference. A large modification of the high-frequency region of the power spectrum of reconstructed velocities is introduced (47), which in turns results in a diverging bias in parameter estimation as $\Delta t \to 0$ (46). This bias and its trend with Δt appear also in our inference method (see Fig. 4.6). Intuitively, the inference procedure relies on the increments of the measured degree of freedom, Δx, whose average absolute value has a monotonic dependence on Δt, and need to be compared with the amplitude of measurement errors σ, which we assume to be independent of the data acquisition sampling rate. At very high sampling rates experimental errors will dominate over the effective dynamics, resulting into an artificial trend $\sim \Delta t^{-1}$ for the parameter η, and $\sim \Delta t^{-2}$ for the effective temperature and pulsation of the harmonic oscillator (the same dimensional analysis argument can be extended to the parameters of the inertial spin model).

Since noise cannot be ignored, we include it in the model in the form of a hidden (non) Markov model. Suppose we measure noisy discrete datapoints $\{(\hat{x}_0, \hat{x}_1, \dots, \hat{x}_L)^\alpha\}$ corresponding to trajectory points $\{(x_0, x_1, \dots, x_L)^\alpha\}$. Following a maximum likelihood argument, we estimate the parameters $\boldsymbol{\lambda}$ of the dynamical hidden model as

$$\begin{aligned} \boldsymbol{\lambda}^*_H &= \arg\max_{\boldsymbol{\lambda}} P(\boldsymbol{\lambda}|\hat{x}_0, \dots, \hat{x}_L) \\ &= \arg\max_{\boldsymbol{\lambda}} P(\hat{x}_0, \dots, \hat{x}_L|\boldsymbol{\lambda}), \end{aligned} \tag{4.42}$$

where

$$P(\hat{x}_0, \dots, \hat{x}_L|\boldsymbol{\lambda}) = \int dx_0 \dots dx_L P(x_0, \dots, x_L|\boldsymbol{\lambda}) \cdot \prod_{n=0}^{L} P(\hat{x}_n|x_n). \tag{4.43}$$

We assume $P(\hat{x}_n|x_n) = \frac{1}{\sqrt{2\pi\sigma^2}} \exp - \frac{(\hat{x}_n - x_n)^2}{2\sigma^2}$ and $P(x_0, \dots, x_L|\boldsymbol{\lambda})$ is determined by the hypothesized dynamical model. As long as we deal with linear models, as in the interacting and non-interacting cases considered above, $P(\hat{x}_0, \dots, \hat{x}_L|\boldsymbol{\lambda})$ reduces to Gaussian integrals and the marginalization over the hidden variables can be performed explicitly. A full treatment at any noise-to-signal ratio is then possible, but not easily generalizable beyond the harmonic case. For this reason here we limit ourselves to showing the predicted effect of experimental uncorrelated noise on numerical simulations. Explicit rewriting of the likelihood in Eq. 4.43 allows us to identify the combination of parameters that control the transition from the small to large noise regime. If $T\eta\Delta t^3/\sigma^2 \ll 1$, noise dominates and, to lowest order, $P(\hat{x}_0, \dots, \hat{x}_L|\boldsymbol{\lambda}) \simeq \prod_{n=0}^{L} \frac{1}{\sqrt{2\pi\sigma^2}} e^{-\frac{1}{2\sigma^2}\hat{x}_n^2}$. If $T\eta\Delta t^3/\sigma^2 \gg 1$, the effect of noise will be small, and the likelihood will converge to the one we found in absence of experimental errors.

We conclude, in agreement with Ref. (95; 46), that whenever the experimental apparatus and the observed process are such that the chain of conditions $\sigma^2 \ll T\eta\Delta t^3 \ll 1$ holds, the developed inference strategy still provides a reliable methodology to infer the parameters of the dynamics. When that condition is not fulfilled, controlled denoising procedures or inference strategies based on hidden modelling must be employed.

4.4. Conclusions

We proposed a maximum likelihood inference strategy to tackle the problem of learning the best continuous inertial stochastic model from time lapse recordings of an observed process. The problems arising in this context are general, as they stem from the combination of the following three ingredients: the second (or higher) order nature of the process, when described in terms of the directly measurable degrees of freedom, stochasticity, and the use of discrete sequences of datapoints. Because of that, contrary to first order processes, reconstructing the continuous-time dynamical model from the data is not a straightforward task in the case of second order dynamics. Careful attention must be paid to the mathematical peculiarities of Brownian motion, and in particular to the minimum order of convergence of the Taylor-Itô expansion allowing for a correct description of infinitesimal fluctuations.

We want a robust inference methodology which could be applied to a wide class of inertial processes, without knowing their exact time-dependent solution. Such a method must then exploit only the local dynamical information carried by the differential equation.

Locally in time, the statistical properties of a Markovian or non-Markovian process are determined by the random variable appearing in the discretized Langevin or generalized Langevin equation respectively. It is then crucial to evaluate correctly the incremental fluctuations, at least to leading order in Δt.

In the considered non-Markovian scenario, the minimum order of convergence required for the Taylor-Itô expansion is $O(\Delta t^{3/2})$. We showed that lower order approximations lead to the emergence of a 2/3 rescaling factor for the inferred damping coefficient, as already pointed out in Ref. (45) and in Ref. (46; 47) in non-Bayesian settings. Employing known numerical integration schemes (48; 49), we developed, to the best of our knowledge, the first max-likelihood inference approach for non-Markovian dynamics (or, equivalently, partially observed Markovian dynamics, since the Markovian embedding is not exploited). We demonstrated the robustness and wide applicability of the method by applying it to different processes: an exactly solvable stochastic oscillator with additive noise with a Gaussian propagator; the Brownian motion of a particle in an anharmonic potential in thermal contact with a heat bath at constant temperature T; a stochastic harmonic oscillator driven by multiplicative noise. While the first two examples are described in equilibrium by Gibbs-Boltzmann distribution, the latter is intrinsically out of equilibrium. In all these cases our maximum likelihood estimators for the model parameters are in good agreement with the values used in simulations.

The method can also be successfully and efficiently applied to large interacting systems, with prior modelling of the interaction mechanism. It is in this aspect that the most promising applications of our max-likelihood method possibly lie. The class of processes for which the method has been developed correspond to the simplest way of incorporating memory effects in the equilibrium dynamics of complex Hamiltonian systems. Its fundamental ingredients are linear dissipation and additive noise. With these conditions fulfilled, the problem is computationally efficient and tractable. For non-interacting systems we showed it is possible to generalize the Bayesian inference approach to non equilibrium processes driven by multiplicative noise. This generalization should work also for interacting ones.

An important remark is that in this setting only single valued parameters can be inferred. Heterogeneities in time and space are not taken into account. The proposed method is able to cope with slow time dependence of the parameters compared to the available experimental frame rate, by assuming effectively constant parameters along long sub-trajectories. For fast varying parameters, a better approach is to describe the parameter as a random variable drawn from an unknown distribution and infer the parameters of this distribution. For the spatial heterogeneity in very large systems, unless it is modelled using a small number of parameters, a brute force maximum likelihood approach is not feasible and more sophisticated strategies must be developed, as for static inverse problems (98).

Another possible extension of the method is to include a position dependent dissipation coefficient. This modification would not alter the Gaussian nature of the propagator at short times, even if the noise covariance matrix will no longer be tridiagonal. Nonlinearities in the first derivative of the measured degree of freedom x and v-dependent multiplicative noise could also be considered. Finally, one could try to generalize the approach to higher order processes, provided that this is motivated by some experimental evidence.

Relating the exact maximum likelihood procedure to alternative effective inference

schemes, like Gloter's minimum contrast strategy (45), also remains an open question. Specifically, is it possible to associate to these non-Markovian processes an effective Markovian description with uncorrelated noise (corresponding to factorized dynamical likelihood) and rescaled parameters? Our analysis suggests that it should be possible to adopt, even if incorrectly, one of the naïve methods discussed in Sec. 4.3.1 and introduce an *a posteriori* correction of the wrongly estimated parameter, to take into account the effect of the lowest order discretization.

Another interesting development would be to provide a reliable inference method even in the presence of strong measurement errors. The maximum likelihood framework provides a natural formulation for the problem in terms of hidden Markov models.

The natural use of the developed framework is application to real data. Technical specifications of acquisition systems have remarkably improved in the last decades, and it is now possible to collect well resolved trajectories for long enough time windows. This is also true for animal groups on the move, where experiments are performed in the field and strong limitations are usually set on the acquisition length due to global motion. We know from previous work that the emergent dynamics of groups of birds is dominated by an effective rotational inertia (17). This inertia allows information to propagate linearly and in an almost undamped way allowing flocks to turn coherently. Retrieving the effective damping coefficient in this case will allow us to predict the scales where damping becomes relevant, setting a size limit for groups able to collectively change direction. In the context of swarm dynamics, recent theoretical findings (114; 115) suggest that the value of the damping coefficient sets — again — a size crossover for groups displaying different critical behavior on the large scale. Understanding the interplay between size, information propagation and response is a key issue in collective behavior and a reliable inference approach is crucial to provide well grounded answers to these questions.

4.5. Methods

4.5.1 ISM simulations

We implemented a numerical integrator for the ISM in $d = 3$ that combines the leapfrog method with Boris's trick to ensure speed conservation (116). We performed simulations on fixed Poisson random lattices (i.e. sites are randomly chosen points with uniform distribution), discarding the update of particle positions and consequent reshuffling effects. As a result, the adjacency matrix of the graph associated to the interacting particle system is time-independent and the constant speed v_0 of each bird does not play any role. Thus the numerical integrator we used consists of the following set of update equations:

$$\begin{cases} \mathbf{v}_i{}^{n+1} = \mathbf{v}_i{}^{n} + (\mathbf{v}_i{}^{n} + \mathbf{v}_i{}^{n} \times \mathbf{t}^n) \times \mathbf{u}^n \\ \mathbf{s}_i{}^{n+1/2} = \left(1 + \frac{\eta \Delta t}{2\chi}\right)^{-1} \left\{ \left(1 - \frac{\eta \Delta t}{2\chi}\right) \mathbf{s}_i{}^{n-1/2} + \mathbf{v}_i{}^{n} \times \left[\frac{J \Delta t}{\chi} \sum_j n_{ij} \mathbf{v}_j{}^{n} + \mathbf{\Xi}_i{}^{n} \right] \right\}, \end{cases} \tag{4.44}$$

with $\mathbf{t}^n = -\frac{1}{2\chi} \Delta t \mathbf{s}^{n+1/2}$ and $\mathbf{u}^n = 2\mathbf{t}^n/(1 + |\mathbf{t}^n|^2)$. $\mathbf{\Xi}_i{}^{n}$ is a three-dimensional isotropic Gaussian variable of zero mean and of variance:

$$\langle \mathbf{\Xi}_i{}^{n} \cdot \mathbf{\Xi}_j{}^{m} \rangle = \delta_{ij} \delta_{mn} \, 2 \cdot 3 \cdot T \eta \, \Delta t. \tag{4.45}$$

Additionnally, the adjacency matrix explicitly reads:

$$n_{ij} = \begin{cases} 1 & \text{if } r_{ij} \leq n_c \\ 0 & \text{if } r_{ij} > n_c \end{cases} \tag{4.46}$$

with r_{ij} the rank of bird j as a neighbour of bird i (excluding the bird itself, to which we conventionally associate rank $r_{ii} = 0$). In all of our simulations we worked with periodic boundary conditions. We tried to ensure that the system was sampled in a stationary regime by starting from microscopic configurations corresponding to polarization values close to the equilibrium ones. The polarization is the macroscopic order parameter of the system and it is defined, in perfect analogy to the magnetization in a 3-dimensional Heisenberg model, as $\Phi = \frac{1}{Nv_0}\left|\sum_{i=1}^{N} \mathbf{v}_i\right|$.

Flocks of $N = 1000$ birds are simulated to obtain the results shown in this paper, with topological range of interaction $n_c = 6$ (except for the data in Fig. 4.5B), alignment strength $J/\chi = 5$ and effective temperature T/χ in the range $[0.2, 1.2]$. When not explictly indicated, we took $T/\chi = 0.4$, approximately corresponding to a polarization of 0.97 (for $n_c = 6$). We chose an integration time step of $\tau_{\text{sim}} = 0.0005/(Jn_c)$ for all the simulations. Different damping regimes have been explored, and the performance of the inference method was tested in each of them, and for various choices of the time lag Δt. In order to disentangle the effects of the discrete nature of the simulation from proper malfunctioning of the inference schemes, the minimum inference time step Δt displayed in Figs. 4.5B and S2 is $5\tau_{\text{sim}}$.

5

Modeling the immune response

In the first part of this manuscript we have used models inspired by the physics of stochastic processes to study biological networks consisting of a well-identified small set of interacting agents. These agent-based models allow for a statistical description of the emergence of collective behaviors in biological networks, like collective motion in animal groups (72) or self-organization in cell biology (1). However, this complex systems approach fails to describe the organisation of biological networks at the level of organisms, where an uncountable number of agents interact at multiple scales. In the mammalian adaptive immune system, interactions range from a cellular scale, with local lymphocytes dynamics, to an organismal scale with the communication and exchange of cells across the entire body. To circumvent these difficulties, we develop in chapter 6 an optimization approach to study the B cell immune response. As a preamble, in this chapter we introduce relevant notions of immunology and we present the different modeling approaches necessary to understand the research directions taken.

5.1. Overview of the immune system

Biological organisms are constantly threatened by the invasion of a variety of microorganisms ranging from bacteria to viruses, parasites and fungi (117). While some microorganisms are endogenous to their host, like the gut microbiota in mammals, others are detrimental and have led to the development of a variety of host immune defense mechanisms (118). In vertebrates, this immune defense consists of two branches: innate and adaptive. Innate immunity is shared by plants and animals and is usually considered the most primitive sort of immunity that allowed early organisms to distinguish self and non-self (119; 120; 121). This immunity is the first line of defense triggered by an infection, and is mediated by germline encoded pattern recognition receptors (PRRs) that can recognize molecular motifs harboured by microorganisms. These motifs, called pathogen-associated molecular patterns (PAMPs), are conserved across many microorganisms and typical examples are membrane carbohydrates and lipids or nucleic acids (117). By targeting PAMPs with PRRs, innate immunity recognizes a set of warning features that are associated with an infection, and in return recruits specific cells, called neutrophils and macrophages, to eliminate the pathogens.

By constrast, adaptive immunity is involved in the late phase of pathogen elimination, as well as in the generation of an immunological memory about pathogen-specific molecular patterns. Contrarily to PAMPs, these molecular motifs, called antigens, are specific to each pathogen and are extremely diverse. While this diversity cannot reasonably be encoded in the germline like PRRs, it constitutes from the viewpoint of immune defense a potentially very useful pathogen fingerprint. Adaptive immunity solves this problem and exploits the diversity of antigens to recognize and remember pathogens individually. The

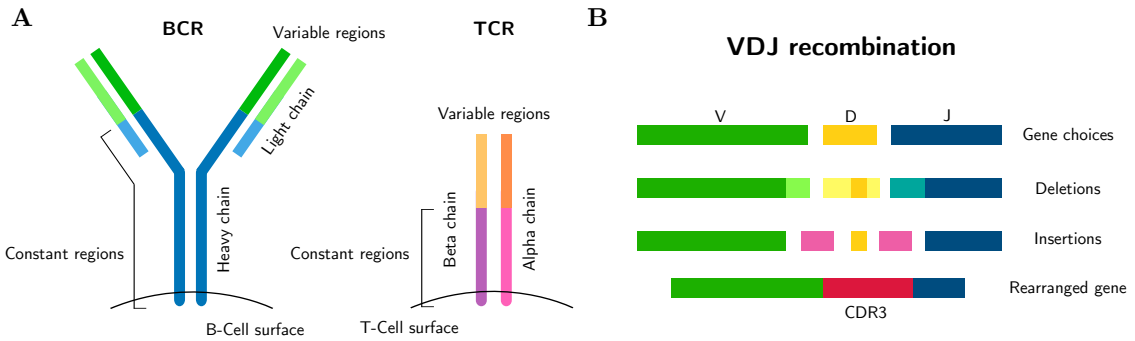

Figure 5.1: **Antigen receptors structures and VDJ recombination. A.** B-cell receptor (BCR) and T-cell receptor (TCR). The BCR, or immunoglobulin, is a Y-shaped receptor composed of two copies of two chains called heavy and light. The TCR is composed only of two chains called alpha and beta. All these chains have a constant region at the stem of the receptor, and a variable region at its extremities. In this variable region is located the most variable segment of the receptor, called CDR3, with which it binds foreign antigen. **B.** VDJ recombination for the heavy and beta chains proceeds sequentially: gene templates are chosen and followed by random deletions and insertions. The resulting gene contains a hypervariable region coding for the CDR3 loop of the receptor.

mechanisms by which it achieves this daunting task involve elaborated somatic rearrangements of germline encoded molecular patterns (118). As a consequence, as opposed to innate immunity, this branch of immune response is restricted to vertebrates (122; 123). Importantly, even though they are successive stages of an immune response, the innate and adaptive branches constantly communicate with each other (124). For instance, dendritic cells are activated by PAMPs and play the role of antigen presenting cells for the adaptive immunity. In the following we focus on the specific case of adaptive immunity in mammals.

5.2. The adaptive immune system

As outlined in the previous section, adaptive immunity is characterized by its ability to adapt to any threat, ensuring complete pathogen identification and clearance. It owes its flexibility to mechanisms of somatic gene modifications that generate a virtually infinitely diverse pool of lymphocytes, each displaying on their surfaces unique antigen receptors. This lymphocyte population, also called a repertoire, is comprised of two cell types: T and B cells. They both bind antigens with a particular receptor protein, respectively called TCR and BCR. Structurally, the two receptors differ in their protein structure: the BCR is made of two copies of heavy and light chains, while the TCR is made of two alpha and beta chains Fig. 5.1A. They both harbour a conserved region, shared by differents cells, and a variable region encoding the antigen diversity and used for pattern recognition.

5.2.1 Receptor diversity

Contrarily to PRRs, the diversity of all antigens cannot possibly be encoded in the germline (22). To solve this task, the adaptive immune system relies on a stochastic gene rearrangement called V(D)J recombination (125; 126). This recombination relies on a

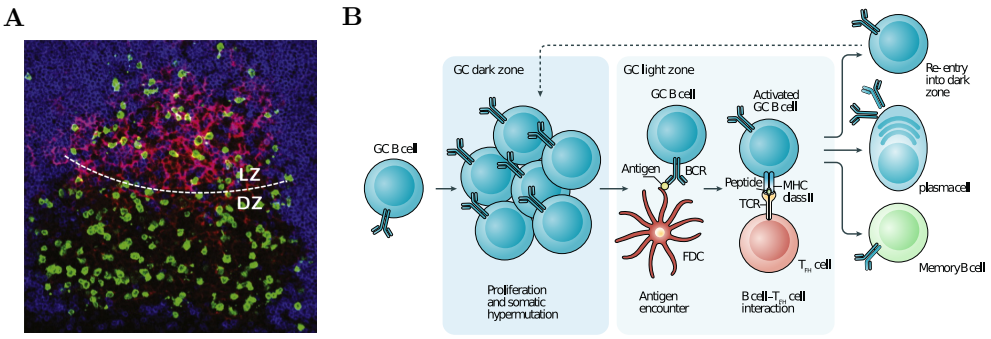

Figure 5.2: **Germinal centers and affinity maturation. A.** Multiphoton-microscopy imaging of a germinal center. Germinal center B cells (GC B cells) are marked in green, Follicular Dendritic Cells (FDCs) in red, and naive B cells in blue. The boundary between light zone (LZ) and dark zone (DZ) is marked with a dashed line and is illustrative. A germinal center has a typical size of $\sim$ 100 to 500μm. This image was adapted from (130). **B.** Schematic representation of affinity maturation in a germinal center. GC B cells proliferate and mutate in the dark zone before migrating in the light zone where they compete for antigen uptake and T-cell help. Surviving cells are either exported from the germinal center (as plasma or memory cells) or they undergo further rounds of affinity maturation. This schematic was adapted from (131).

germlined encoded library of gene templates, called V, D and J for the heavy and beta chains, and V and J for the light and alpha chains.

Upon cell differentiation, the lymphocyte DNA is edited (see Fig. 5.1B) and one of each templates are chosen among the germline encoded ones. They are subsequently joined with randomly inserted and deleted nucleotides at the junctions. Thanks to the randomness of these insertions and deletions, the newly obtained gene harbours a hypervariable region overlapping the two recombination junctions (22). This hypervariable region is the one with which the receptor binds its cognate antigen, and is referred as the complementary-determining-region 3 (CDR3). The diversity of CDR3s that can be generated through V(D)J recombination is enormous, allowing for a specific detection of potentially any antigen (22).

While the diversity of antigen receptors generated by recombination endows the immune system with a remarkably accurate pathogen fingerprinting technique, it also comes with undesirable properties. V(D)J recombination can generate a important amount of antigen receptors recognizing self-proteins (22), potentially leading to auto-immune reactions (127; 128; 129). The adaptive immune system solves this issue by implementing a negative selection mechanism for auto-reactive lymphocytes called central tolerance.

5.2.2 Clonal selection theory

Once generated and selected for self-tolerance, T and B cells form a pre-exposure repertoire called the naive repertoire. This naive repertoire of cells recirculates constantly in the peripheral lymphoid tissues, awaiting activation by foreign antigens. The subsequent clonal dynamics obeys a set of rules proposed by Burnet in his clonal selection theory (132) and long-verified by experiments (133; 134). First, each T and B lymphocytes has up to 10^5 copies of a unique type of antigen receptor on their surface. Second, activation by

receptor-antigen binding is required for cell proliferation. Finally, the offspring of any lymphocyte carries the same type of receptor as its parent. This set of rules define a theory for the population dynamics and selection of lymphocytes based on their affinity for the available antigens.

Beyond this unified theory of clonal selection is hidden a highly entangled biological reality. Both T and B cells can be subdivided in phenotypically distinct subsets serving different functions. This distinction is experimentally assessed by elucidating the molecular markers at the surface of the cells. For instance, T cells expressing the CD4 glycoprotein on their surface are known as helper T cells and modulate the immune response with the aid of signaling molecules called cytokines. On the other hand, T cells expressing the CD8 glycoprotein on their surface are known as cytotoxic T cells as they kill abnormal cells, like cancer cells or cells infected by viruses.

Similarly, upon antigen activation, naive lymphocytes can differentiate towards effector cells or memory cells. Broadly speaking, effector cells express surface proteins promoting cell-adhesion and migration to increasingly navigate peripheral lymphoid tissues and recognize antigens. On the contrary, memory cells express surface proteins enhancing long term survival and co-stimulation to keep a long-lasting immunological memory of the infection. This refinement of the different cell phenotypes goes well beyond this two simplified subsets and lymphocytes are subject to a large number of different interactions dictating their fate and their function in the repertoire. As a consequence, while clonal selection theory provides an incredibly successful framework to understand adaptive immune response, it remains particularly difficult to draw quantifiable predictions from it.

Finally, the clonal selection theory proposed that individual lymphocytes are specific for a single antigen. However, the number of potential antigens exceeds by order of magnitudes the number of cells in the body (135; 136), and full protection can only be achieved if every receptor can bind many antigens. This degeneracy in the receptor-antigen mapping is common to T- and B-cell repertoires (137; 135; 138) and is called cross-reactivity. This assumption of cross-reactivity is essential to ensure a proper immune coverage by the adaptive repertoire, and will be at the center of our analysis.

5.3. B-cell repertoire

B cells perform their function in the adaptive immunity thanks to their antigen receptor called immunoglobulin. Contrarily to T cells, not only do B cell express their receptor in a membrane-bound form, but they also express it in a soluble form, called an antibody. This soluble form of the receptor is free to circulate in the organism and to bind to its cognate antigen at the surface of the pathogen, potentially forbidding it to replicate. However, there is no guarantee that antibodies generated after a primary antigen exposure will bind strongly enough to efficiently neutralize the pathogens. In fact the opposite is more likely, and the antibodies generated by the naive response bind poorly to the antigens (139). To circumvent this limited efficacy, the activated naive cells can undergo a process of affinity maturation increasing the affinity of their receptor for the antigen.

5.3.1 Affinity maturation

Affinity maturation is crucial to increase the affinity of naive cells to the challenging antigens. Upon antigenic stimulus and with help from the CD4 T cells, secondary struc-

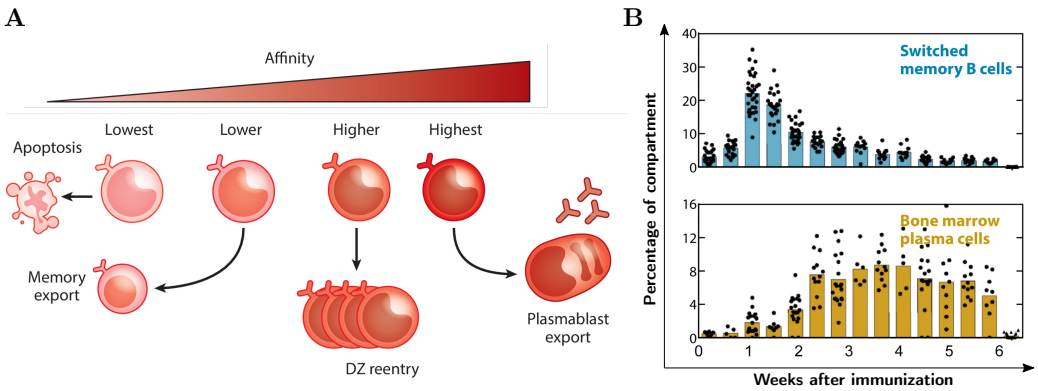

Figure 5.3: **Affinity maturation exports.** **A.** Affinity dependent model for post-germinal-center B cell fate choice. Surviving cells with lower affinity become memory B cells. Cells with the highest affinity differentiate into plasma cells, while cells of intermediate affinity reenter the dark zone to undergo further rounds of affinity maturation. This schematic was adapted from (140) **B.** Temporal switch in the germinal B-cell fate in mice experiments. B-cell fate shifts from memory to plasma as time goes (and as the affinity increases). This figure was adapted from (51)

tures called germinal centers form in lymph nodes. (139). These structure form a few days after infection, and typically last up to three weeks, with the exception of chronic infections (141). As revealed by microscopy in Fig. 5.2A, germinal centers are made of two zones, the *dark zone* dedicated to cell mutations and proliferation and the *light zone* dedicated to B-cell competition for antigen capture (130). The role of this structure is to generate BCR variants via an increase in the mutation rate and select the largest affinity ones. The separation between the two zones allows the process to operate iteratively, continuously increasing the affinity of B cells for the antigen.

Selection for antigen affinity

Antigen-activated B cells enter the dark zone (Fig. 5.2B) where they express an enzyme inducing mutations in the Ig-coding gene. Under the action of this enzyme, the natural rate of DNA mutations reaches up to 10^6 times the typical germline mutation rate (142), and proliferating B cells accumulate changes in their BCR. Additionaly, most recent evidence indicates that B-cell proliferation in this zone is positively selecting for antigen affinity, such that high-affinity cells proliferate more than low-affinity ones (140). These B cells then migrate into the light zone Fig. 5.2B where they compete for antigen capture and T-cell help.

In the light zone, B cells compete for the extraction of antigen presented at the surface of follicular dendritic cells Fig. 5.2B. This captured antigen is then displayed on the B-cell surface to be probed by helper T cells. The strength and duration of the binding with helper T cells is a measure of the cell affinity for the antigen. The poor binders die by apoptosis, while the good binders are allowed to reenter the dark zone and undergo another round of affinity maturation. Cycling between dark and light zone steadily increases B cells' affinity and reduces the clonality of the B-cell pool (143). While some germinal centers eventually harbour ~ 1 clonal family (ie. phylogenetically related B cells), the clonality in germinal centers is largely sensitive to stochastic effects, allowing them to

maintain clonal diversity even in the presence of a strong selection (140).

Germinal center exports

To actively take part in the immune response, B cells with increased affinity must be exported from germinal centers into the effector cell compartment. Effector B cells secrete large amounts of antibodies and are referred to as plasma cells. Plasma cells can be either short-lived and participate in the immediate immune response, in which case they are called plasmablasts, or they can be long-lived and sustain high antibody titers in the blood for years (139; 144). While plasmablasts aim at a fast pathogen clearance and host recovery, long-lived plasma cells constitute a form of long-term immune protection. Importantly, long-lived plasma cells primarily reside in the bone-marrow where their survival niche is located. The humoral immunity offered by plasma cells is usually referred to as antibody based immunity and is one of the goals of vaccination (145).

Germinal center B cells are also exported into the memory cell compartment, whose role is distinct from the plasma cell one. While memory cells are also long-lived, contrarily to plasma cells they do not secrete antibodies. They are known to respond to re-activation by fast differentiation into plasmablasts at low concentration of antigens (146; 51). Notably, the reactivation of 10 to 100 memory B cells is enough to generate biologically relevant antibody titers (51). To efficiently achieve this task, memory B cells are found in secondary lymphoid tissues (spleen, lymph nodes, peripheral tissues) and circulate in the blood.

The type of germinal center export, memory or plasma, is strongly related to the affinity of germinal center B cells. Contrarily to plasma cells (147), memory B cells have low affinity (25). In this line, in the most up to date mechanistic models (148; 140), antigen affinity is the main determinant of germinal B cell fate decision Fig. 5.3A. According to this model, in the light zone, B cells of no or low affinity die by apoptosis. Of the surviving cells, the ones with the lowest affinity are exported as memory B cells, while the other ones re-enter the dark zone and undergo more rounds of affinity maturation. Finally, cells with the highest affinity are exported from the light zone in the plasma cell compartment. As affinity increases with time, this model is compatible with observations Fig. 5.3B that germinal centers exports shift from memory B cells to plasma cells over time (147; 51).

5.3.2 Typical immune response

Depending on the presence or the absence of a pre-existing immunity, an immune response to an antigen is respectively referred to as a primary or a recall response. Because of cross-reactivity of immune cells, the notion of pre-existing immunity is ambiguous, and this observation will be at the center of chapter 6.

During a primary response, the pool of available cross-reactive cells is very limited, and is mostly comprised of naive cells. These cells are actived by antigen encounter at the interface between secondary lymphoid tissues (lymph nodes, spleen) and the blood. They migrate to extrafollicular sites where they undergo massive clonal expansion and differentiation into plasmablasts (144). Extrafollicular sites are defined by opposition to B-cell follicles which are essentially the niche within which germinal centers grow. This extrafollicular response peaks 4 to 6 days after infection (139) with large antibody titers. Ultimately, some of these plasmablasts can differentiate into plasma cells, forming a long term memory (149; 150).

Along with this early response, a small subset of activated B cells are directed toward

follicular sites where they seed germinal centers (139). As we mentionned, affinity maturation takes place over 2 to 4 weeks, leading to the production of high affinity plasma cells and a diverse pool of memory B cells. These plasma cells then produce high antibody titers that ensure a complete pathogen clearance and host recovery. The diverse pool of memory B cells is long-lived, and the general consensus is that not only does it serve as a memory of the antigenic stimuli, but it also helps anticipating future antigenic variants (25; 26). This perspective on the memory repertoire will be discussed and rationalized in the chapter 6.

A recall response corresponds to any subsequent stimulation of the B-cell repertoire by a similar antigen. It can correspond to a vaccination boost, or simply a reinfection after protecting antibody titers have waned (145; 151). Contrarily to the primary response where the pool of cross-reactive cells available was very limited and of low affinity, it is now made of a large amout of memory B cells with varying affinities. Among these cells, the largest affinity ones are recruited in an extrafollicular response to generate neutralizing antibodies. The similarity of this second antigenic stimuli with the primary one, as well as the diversity of the available memory pool completely determine the efficacy of the recall response. In particular, if the recall response is particularly strong because memory B cells of high affinity were available, it can limit the generation of *de novo* memory and plasma cells.

This preferential recall of memory B cells elicited by past exposure with respect to the generation of a de novo response specific to the infecting strain is called antigenic imprinting, or 'original antigenic sin'. It was first observed by Francis and colleagues (54) which showed that consecutive exposures to antigenically drifted influenza strains preferentially boost antibodies targeting strains encountered in early childhood. Recent refinements of this observation have shown a gradual shift with age (and number of reinfections) of the antibody response towards the conserved part of the hemagglutinin protein (152; 153; 154), showing that preferential recall of memory B cells targeting slowly evolving epitopes can inhibit the generation of a de novo response targeting the more fastly evolving ones (55).

Antigenic imprinting results from a negative feedback between a fast early response mediated by cross-reactive memory B cells and the generation of a de novo response via affinity maturation. In particular, because of an increased ability to proliferate upon antigen activation (155; 156), cross-reactive memory B cells can outcompete naive cells in recall responses and inhibit de novo affinity maturation (29; 55). Additionally, an early antibody response can also limit germinal center formation by decreasing antigen availability (157). Importantly, the amount of antigen presented and how it is delivered, through infection or vaccination (158), with an inactivated or activated virus (159), with or without adjuvant (160), is crucial to control the outcome of the B-cell response. As a rule of thumb, increasing the amount of antigen, repeateadly vaccinating or using adjuvants is useful to limit the extent of antigenic imprinting (55; 29). In chapter 6 we will rationalize this phenomenon by showing how the inhibition of affinity maturation by a cross-reactive B-cell response can emerge as a long-term optimal strategy for the immune system.

5.4. Modeling adaptive immunity

5.4.1 Repertoire dynamics

T and B cells are organized in groups of cells expressing the same antigen receptor, called clones. The first modeling attempts of adaptive repertoires treated lymphocytes population dynamics as an ecological process where clones compete for proliferation and survival signals in a given antigenic environment (161; 162; 163).

To describe repertoire dynamics we denote by C_i the size of clone i and a_j the concentration of antigen j. The cross-reactivity of receptor i with antigen j is denoted by K_{ij}. Antigens can be either bound to receptors in the form of antigen-receptor complexes, or free and available for binding. Beyond this binding-unbinding process, bound antigens can undergo division and receive increased survival signals. Under these dynamics, the concentration $F_j \leq a_j$ of free antigen j reaches a quasi steady state balanced by the binding, unbinding, division and death of lymphocytes (161). It follows that the determinant parameter for the dynamics of clone i is the overall concentration of free antigens available for interaction with a receptor, also called antigenic stimuli $S_i = \sum_{ij} K_{ij} F_j$. The resulting repertoire dynamics generically obey the following equation (164):

$$\frac{dC_i}{dt} = \Gamma(S_i) C_i, \tag{5.1}$$

with $\Gamma(S_i)$ denoting the effective growth rate under antigenic stimuli S_i. In the absence of antigenic stimuli, clones do not receive survival signals and $\Gamma(0) < 0$. Maintaining a steady state population of clonotypes requires a constant input of new clones. In practice, this input is provided by primary lymphoid organs: the thymus for T cells and the bone-marrow for B cells. The main conclusion of these models is that receptor cross-reactivity promotes the competitive exclusion of clonotypes responding to the same antigens (161). Importantly, it ensures a limited commonality between antigens cross-reacting with different receptors. As a consequence, the diversity of the repertoire is fixed by the diversity of the antigenic environment.

These early models disregarded stochastic effects, like birth-death noise and antigenic stimuli fluctuations. The former is crucial to investigate clone extinction by competitive exclusion (165; 166), while the latter is necessary to study the variability in clone sizes (167). Under random uncorrelated antigenic fluctuations, clonal dynamics Eq. 5.1 can be modeled by a geometric Brownian motion (167; 168):

$$\frac{dC_i}{dt} = \Gamma(0) C_i + \sqrt{2}\sigma C_i \xi_i, \tag{5.2}$$

with $\Gamma(0)$ the average antigenic stimulation, and $\sqrt{2}\sigma\xi_i$ its fluctuations. This fluctuating fitness model predicts power-law distributions $p(C) \sim C^{-1-\alpha}$ with $\alpha = |\Gamma(0)|/\sigma^2$ (167), in agreement with T-cell repertoire sequencing in healthy individuals (168). In particular, the stronger the antigenic fluctuations, the larger clones grow.

Importantly, in this fluctuating fitness model successive antigenic challenges are uncorrelated. This assumption is well suited for T cells which are known to have a large cross-reactivity and are likely to be reactivated by different pathogens (135). On the contrary, we know that B cells constantly need to update their BCR through affinity maturation to match new antigenic variants of evolving pathogens like influenza or SARS-CoV-2. In this setting, the fluctuating fitness felt by a clonotype is strongly correlated

from one infection to the other, and we can expect the shape of the clone-size distribution to change. In chapter 6 we will provide a new prediction for the clone-size distribution of memory B cells taking into account this observation.

5.4.2 Optimal immune response

Another class of model takes a top-down approach to describe the immune response from the viewpoint of cost-optimization. Interestingly, the first models proposed by Perelson and colleagues took this path to investigate strategies maximizing the efficiency of the B-cell response (23; 24). As we mentionned, during the extrafollicular response, naive B cells differentiate into plasmablasts, some of which ultimately become plasma cells. While the former are short-lived, the latter are long-lived and have a larger antibody secretion rate (169). Denoting $A(t)$ the amount of antibodies produced by both these cell types, they investigated the optimal differentiation rate $u^*(t)$ from plasmablasts to plasma cells minimizing the time T needed to reach an antibody titer A^*:

$$u^*(t) = \min_{u(t)} T, \tag{5.3}$$

$$A(T) = A^*. \tag{5.4}$$

They found the optimal plasmablasts to plasma cells differentiation rate to take the form of a 'bang-bang' control, with a normalized differentiation rate $u^*(t) = 0$ for $t < \tau^*$ and $u^*(t) = 1$ for $t > \tau^*$. These fascinating results are in agreement with the biological observation that plasmablasts appear at a late stage of the extrafollicular response (149; 150).

Recent work (9; 8) revived this success by studying optimal adaptive repertoires minimizing the duration of the infection. Contrarily to early works that focused on a single antigen-lymphocyte pair, these later studies investigated the optimal repertoire organization in the context of multiple cross-reacting antigen-lymphocyte pairs. In the absence of precise quantitative data, they modeled cross-reactivity in a conceptual space representing the receptor-antigen interaction. This shape space (170) is endowed with a metric (assumed to be Euclidean) quantifying the cross-reactivity between antigens and receptors. In this space, the cross-reactivity between receptor x and antigen a is usually denoted as a probability of interaction $0 < f(x, a) < 1$. In particular, the farther apart is a receptor from an antigen, the smaller is their cross-reactivity. Experimental evidence from hosts-influenza co-evolution identified a possible shape space candidate as a low dimensional feature space obtained by dimensional reduction of the combined genomic and neutralization assays data (58; 53; 59).

Using this construction, authors investigated the optimal distribution of lymphocytes minimizing the cost of an infection. The cost of an infection by an antigen at position a on the space, denoted F_a, depends on the ability of the host repertoire to recognize the infecting antigen. Similarly to the definition of the antigenic stimuli we introduced above, this ability to recognize an antigen a, also called coverage $C(a)$, is given by the average number of immune cells interacting with a through cross-reactivity $C(a) = \sum_x f(x, a) n_x$, with n_x the number of lymphocytes with receptor x. A convenient choice for the infection cost is then to depend on the coverage as a power law of exponent α, $F_a \sim C_a^{-\alpha}$ such that the smaller the coverage the larger the infection cost (9). In a static antigenic environ-

ment, the long-term cost over multiple infections is equal to the cost averaged over the distribution of pathogens Q_a, and the optimal distribution of lymphocytes $\{n_x^*\}$ minimizes this expected infection cost:

$$\{n_x^*\} = \arg\min_{\{n_x\}} \sum_a Q_a F_a(C_a) \text{ with } \sum_a Q_a = 1. \tag{5.5}$$

In line with the competitive exclusion of lymphocytes observed in repertoire dynamics models (161), they observed that cross-reactivity decreases repertoire diversity. Importantly, this connexion is made quantitative as they showed that optimal repertoires emerge as steady-state solutions of competitive repertoire dynamics.

In their more recent work (8), authors investigated the optimal distribution of lymphocytes in a changing and partially observed antigenic environment. The optimization problem Eq. 5.5 was replaced by a time dependent one:

$$\{n_x^*(t)\} = \arg\min_{\{n_x(t)\}} \sum_a \hat{Q}_a(t) F_a(C_a) \text{ with } \sum_a \hat{Q}_a(t) = 1, \tag{5.6}$$

where $\hat{Q}_a(t)$ denotes the antigenic environment estimation the host has built over the previous infections. This formulation provided theoretical insight into the problems of memory attrition and aging. However, the optimal repertoire instantaneously minimizes the expected cost upon infection, which can lead to massive rearrangements of the lymphocyte population. In other words, within this formulation the repertoire has an infinite plasticity. Solving this issue by introducing explicit constraints on the repertoire updates from one infection to the other is the main motivation of chapter 6.

5.5. Theory of decision making

A promising approach to describe the adaptive immune repertoire is based on Markov decision theory. It was recently applied to investigate memory formation in the T-cell repertoire (6) as well as in the B-cell one (7). Markov decision theory is interested in modeling decision making of an agent in a randomly evolving environment. The environment is modeled by a discrete-time stochastic process $\{x_k, k \in \mathbb{N}\}$, and upon observation of its state x_k the agent makes a decision u_k. The decision made can influence the evolution of the environment at later times, and the environment state x_{k+1} at time $k+1$ is drawn from a transition probability p:

$$x_{k+1} \sim p(x_{k+1}|x_k, u_k). \tag{5.7}$$

Decisions $u_{k-1}, ..., u_0$ could also influence the environment state at time $k+1$, but we can always redefine the decision variable $u_k \leftarrow \{u_k, u_{k-1}, ..., u_0\}$ to be left with a Markovian evolution Eq. 5.7. We further assume that decisions taken upon observation of the environment state x_k are generated by a policy π_θ parametrized by parameters θ:

$$u_k \sim \pi_\theta(u_k|x_k). \tag{5.8}$$

Similarly, past environment states $x_{k-1}, ..., x_0$ could influence the action taken at time k, but we can always redefine the environment variable $x_k \leftarrow \{x_k, x_{k-1}, ..., x_0\}$ to have a Markovian evolution Eq. 5.8. For each decision u_k its performance is measured through

a reward $r_k = r(x_k, u_k)$ (or conversely through a cost). All this being defined, the triplet (p, π_θ, r) defines a Markov decision process.

We can let the process evolve for a duration T and we are left with a sequence of states and decisions $h_T = \{(x_1, u_1), ..., (x_T, u_T)\}$ forming the history of the process. The goal of optimal decision theory is to find the policy π_θ maximizing the accumulated reward (or conversely minimizing the accumulated cost). This overall reward to optimize upon is taken as a weighted sum of the rewards received over the course of the entire trajectory (171):

$$\mathcal{L}(\theta) = \mathbb{E}_{h_T}\left[\sum_{k=0}^{T} a_k r(x_k, u_k)\right], \tag{5.9}$$

where a_k are weighting factors summing up to 1. In chapter 6 we will use *average reward* with $a_k = 1/T$. Under the assumption $T \to \infty$ and that the joint evolution $\{(x_k, u_k), k \in \mathbb{N}\}$ is stationary ergodic, the long-term average reward can be written:

$$\mathcal{L}(\theta) = \lim_{T\to\infty} \frac{1}{T} \sum_{k=0}^{T} r(x_k, u_k). \tag{5.10}$$

Finally, maximizing this average reward (or conversely minimizing this average cost) with respect to θ gives us access to the optimal policy π_θ.

We have seen that upon antigenic stimuli, the B-cell repertoire makes a variety of decisions ranging from how long affinity maturation should last to how diverse the memory and the plasma pools should be or how many memory cells should be stored. These decisions are encoded in the interactions the different cell subsets have between themselves and with the antigen, and they serve a clear function: ensuring a long-term protective immunity. Markov decision theory therefore is a natural framework to model the B-cell immune response and investigate the optimal immune strategies π_θ that recapitulate clonal selection theory and affinity maturation. In the following chapter we will leverage this theory to model the optimal B-cell response to evolving pathogens.

6

Affinity maturation for an optimal balance between long-term immune coverage and short-term resource constraints

This chapter was previously published in:

- Chardès V., Vergassola M., Walczak A.M., Mora T. (2022) Affinity maturation for an optimal balance between long-term immune coverage and short-term resource constraints. *Proceedings of the National Academy of Sciences*, 119(8):e2113512119.

The section "Analytical results in a solvable model" has been moved from Appendix to Text. Part of the section "Mathematical model" has been moved from Methods to the end of section "Model".

In order to target threatening pathogens, the adaptive immune system performs a continuous reorganization of its lymphocyte repertoire. Following an immune challenge, the B cell repertoire can evolve cells of increased specificity for the encountered strain. This process of affinity maturation generates a memory pool whose diversity and size remain difficult to predict. We assume that the immune system follows a strategy that maximizes the long-term immune coverage and minimizes the short-term metabolic costs associated with affinity maturation. This strategy is defined as an optimal decision process on a finite dimensional phenotypic space, where a pre-existing population of cells is sequentially challenged with a neutrally evolving strain. We show that the low specificity and high diversity of memory B cells - a key experimental result - can be explained as a strategy to protect against pathogens that evolve fast enough to escape highly potent but narrow memory. This plasticity of the repertoire drives the emergence of distinct regimes for the size and diversity of the memory pool, depending on the density of de novo responding cells and on the mutation rate of the strain. The model predicts power-law distributions of clonotype sizes observed in data, and rationalizes antigenic imprinting as a strategy to minimize metabolic costs while keeping good immune protection against future strains.

6.1. Introduction

Adaptive immunity relies on populations of lymphocytes expressing diverse antigen-binding receptors on their surface to defend the organism against a wide variety of pathogens. B lymphocytes rely on a two-step process to produce diversity: first a diverse naive pool of cells is generated; upon recognition of a pathogen the process of affinity maturation allows B cells to adapt their B-cell receptor (BCR) to epitopes of the pathogen through somatic hypermutation (50). This process, which takes place in germinal centers (172), can increase the affinity of naive BCR for the target antigen by up to a thousand fold factor (173). Through affinity maturation, the immune system generates high-affinity, long-lived plasma cells, providing the organism with humoral immunity to pathogens through the secretion

of antibodies—the soluble version of the matured BCR—as well as a pool of memory cells with varying affinity to the antigens (51). However, the diversity and coverage of the memory pool, as well as the biological constraints that control its generation, have not yet been fully explored.

Analysis of high-throughput BCR sequencing data has revealed long tails in the distribution of clonotype abundances, identifying some very abundant clonotypes as well as many very rare ones (174; 175). Additionally, many receptors have similar sequences and cluster into phylogenetically related lineages (176; 142; 177; 178; 179). These lineages have been used to locally trace the evolution of antibodies in HIV patients (180; 181) and in influenza vaccinees (182; 183). Memory B-cell clones are more diverse and less specific to the infecting antigen than antibody-producing plasma cells (184; 147). This suggests that the immune system is trying to anticipate infections by related pathogens or future escape mutants (25).

Theoretical approaches have attempted to qualitatively describe affinity maturation as a Darwinian co-evolutionary process, and studied optimal affinity maturation schemes (185; 186; 187; 187), as well as optimal immunization schedules to stimulate antibodies with large neutralizing capabilities (188; 189; 190). Most of these approaches have been limited to short timescales, often with the goal of understanding the evolution of broadly neutralizing antibodies. Here we propose a mathematical framework to explore the trade-offs that control how the large diversity of memory cells evolves over a lifetime.

Despite long-lasting efforts to describe the co-evolution of pathogens and hosts immune systems (191; 192; 193; 194; 36), and recent theoretical work on optimal schemes for using and storing memory in the presence of evolving pathogens (7), few theoretical works have described how the B-cell memory repertoire is modified by successive immunization challenges. Early observations in humans (54) have shown that sequential exposure to antigenically drifted influenza strains was more likely to induce an immune response strongly directed towards the first strain the patients were exposed to (55). This immune imprinting with viral strains encountered early in life was initially called "original antigenic sin," as it can limit the efficiency of vaccination (195). This phenomenon has been observed in a variety of animal models and viral strains (196). Secondary infections with an antigenically diverged influenza strain can reactivate or "backboost" memory cells specific to the primary infecting strain (159). This response is characterized by lower binding affinity but can still have in-vivo efficiency thanks of cross-reactive antibodies (197; 198). There is a long-standing debate about how detrimental "original antigenic sin" is (29; 28). Under what conditions should the immune system invest in keeping an antibody memory of past infections, as opposed to responding de novo to each new infection? When developing memory is preferred to responding de novo, how diverse should that memory be?

We build a theoretical framework of joint virus and repertoire evolution in antigenic space, and investigate how acute infections by evolving pathogens have shaped, over evolutionary timescales, the B-cell repertoire response and re-organization. Pathogens causing acute infections may be encountered multiple times over time scales of years, especially when they show a seasonal periodicity, while the maturation processes in the B-cell repertoire take place over a few weeks. This observation allows us to consider that affinity maturation happens in a negligible time with respect to the reinfection period. Within this approximation, we investigate the optimal immune maturation strategies using a

framework of discrete-time decision process. We show the emergence of three regimes—monoclonal memory response, polyclonal memory response, and a de novo response—as trade-offs between immune coverage and resource constraint. Additionally, we demonstrate that reactivation of already existing memory clonotypes can lead to self-trapping of the immune repertoire to low reactivity clones, opening the way for "original antigenic sin."

6.2. Results

6.2.1 Affinity maturation strategies for recurring infections

B cells recognize pathogens through the binding of their BCR to parts of the pathogen's proteins, called epitopes, which we refer to as "antigens" for simplicity. To model this complex protein-protein interaction problem, we assume that both receptors and antigens may be projected into an effective, d-dimensional antigenic space (Fig. 6.1), following the "generalized shape space" idea pioneered by Perelson and Oster (199). Receptor-antigen pairs at close distance in that space bind well, while those that are far away bind poorly. Specifically, we define a cross-reactivity function $0 \leq f \leq 1$ quantifying the binding affinity between antigen a and receptor x, which we model by a stretched exponential,

$$f(x, a) = e^{-(\|x-a\|/r_0)^q}. \tag{6.1}$$

This choice of function is the simplest that allows for introducing a cross-reactivity radius, r_0, while controlling how sharply recognition is abrogated as the distance between antigen and receptor oversteps that radius, through the stretching exponent q.

For simplicity, we focus on a single pathogen represented by its immunodominant antigen, so that each viral strain is represented by a single point a_t in antigenic space (black square), where $t = 1, 2, \ldots$ is a discrete time counting the number of re-infections. It is difficult to estimate the rate of re-infections or exposures to the same pathogen. It can be fairly high in humans, where individuals are exposed to the most common viruses from less than once to several times a year (200). The numbers of lifetime exposures would then range from a few to a few hundreds.

The B cell repertoire, on the other hand, is represented by a collection of antigenic coordinates corresponding to each receptor clonotype. We distinguish memory cells (dark blue circles in Fig. 6.1A), denoted by P_t, which have emerged in response to the presence of the virus, and a dense background of naive and innate cells N (light blue circles) which together provide a uniform but weakly protective coverage of any viral strain (subsumed into the parameter ϕ defined later).

The viral strain evolves randomly in antigenic space, sequentially challenging the existing immune repertoire. This assumption is justified by the fact that for acute infections with a drifting viral strain, such as influenza, the immune pressure exerted on the strain does not happen in hosts but rather at the population level (191). Viral evolution is not neutral, but it is unpredictable from the point of view of individual immune systems. Specifically, we assume that, upon reinfection, the virus is represented by a new strain, which has moved from the previous antigenic position a_t to the new one a_{t+1} according to

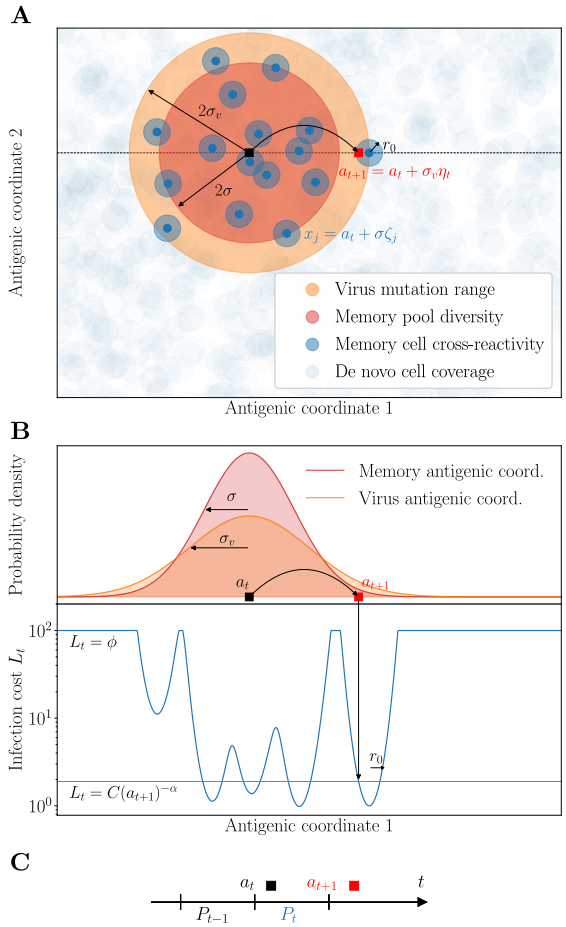

Figure 6.1: **Model of sequential affinity maturation.** **A.** An infecting strain is defined by its position a_n in antigenic space (dark square). In response, the immune system creates m new memory clonotypes x_j (blue points) from a Gaussian distribution of width σ centered in a_t (red area). These new clonotypes create a cost landscape (blue areas) for the next infection, complemented by a uniform background of naive, innate and T cells (basal coverage, light blue). The next infecting strain (red square) is drawn from a Gaussian distribution of width σ_v centered in a_t (orange area). The position of this strain on the infection landscape is shown with the arrow. Antigenic space is shown in 2 dimensions for illustration purposes, but can have more dimensions in the model. **B.** Cross-section of the distributions of memories and of the next strain, along with the infection cost landscape L_t (in blue). Memories create valleys in the landscape, on a background of baseline protection ϕ. **C.** Sequential immunization. Strain a_t modifies the memory repertoire into P_t, which is used to fight the next infection a_{t+1}. P_t is made of all newly created clonotypes (blue points in A) as well as some previously existing ones (not shown). Clonotype abundances are boosted following each infection as a function of the cross-reactivity, and each individual cell survives from one challenge to the other with a probability γ.

a Gaussian distribution with typical jump size σ_v, called “divergence":

$$a_{t+1} = a_t + \sigma_v \eta_{t+1}, \tag{6.2}$$

where η_t is a normally distributed d-dimensional variable with $\langle \eta_t \rangle = 0$ and $\langle \eta_t \cdot \eta_{t'} \rangle = \delta_{tt'}$.

Upon infection by a viral strain at a_t, available cross-reactive memory or naive cells will produce antibodies whose affinities determine the severity of the disease. We quantify the efficiency of this early response to the strain a_t with an infection cost I_t:

$$I_t = \min \Big[\phi, \Big(\sum_{x \in P_{t-1}} n_{x,t} f(x, a_t) \Big)^{-\alpha} \Big], \tag{6.3}$$

where $\phi > 0$ is a maximal cost corresponding to using a de novo response, and where $n_{x,t}$ denotes the size of clonotype x at time t. This infection cost is a decreasing function of the coverage of the virus by the pre-existing memory repertoire, P_{t-1}:

$$C(a_t) = \sum_{x \in P_{t-1}} n_{x,t} f(x, a_t), \tag{6.4}$$

with a power α governing how sharp that dependence is. Intuitively, the lower the coverage, the longer it will take for memory cells to mount an efficient immune response and clear the virus, incurring larger harm on the organism (9; 8).

When memory coverage is too low, the response of the naive B-cell repertoire and the rest of the immune system, including its innate branch as well as T-cell cytotoxic activity, offer protection through a de novo response, incurring a maximal cost fixed to ϕ. Memory cells respond more rapidly than naive cells, which is indirectly encoded in our model by the de novo cost ϕ being larger than the cost when specific memory cells are present (of order 1 or less). In the Supplementary Text we show how this de novo cut-off may be derived in a model where the immune system activates its memory and de novo compartments in response to a new infection, when, for example, naive clonotypes are very numerous but offer weak protection. In that interpretation, ϕ scales like the inverse density of naive cells. We will refer to ϕ^{-1} as “de novo density,” keeping in mind that this basal protection levels also includes other arms of the immune system. In Fig. 6.1B we plot an example of the infection cost along a cross-section of the antigenic space.

After this early response, activated memory cells proliferate and undergo affinity maturation to create new plasma and memory cells targeting the infecting strain. To model this immune repertoire re-organization in response to a new infection a_t, we postulate that its strategy has been adapted over evolutionary timescales to maximize the speed of immune response to subsequent challenges, given the resource constraints imposed by affinity maturation (9). This strategy dictates the stochastic rules according to which the BCR repertoire evolves from P_{t-1} to P_t as a result of affinity maturation (Fig. 6.1C).

We consider the following rules inspired by known mechanisms available to the immune system (172). After the infection by a_t has been tackled by existing receptors, and the infection cost has been paid, new receptors are matured to target future versions of the virus. Their number m_t is distributed according to a Poisson law, whose mean is controlled by the cost of infection, $\bar{m}(I_t)$. This dependence accounts for the feedback of the early immune response on the outcome of affinity maturation, consistent with extensive

experimental evidence of the history dependence of the immune response (201). Each new receptor is roughly located around a_t in antigenic space with some added noise $\sigma(I_t)$, and starts with clonotype size $n_{x,t} = 1$ by convention. The diversification parameter σ can be tuned by the immune system through the permissiveness of selection in germinal centers, through specific regulation factors induced at the early stage of affinity-based selection (202): $\sigma = 0$ means that affinity maturation only keeps the best binders to the antigens, while $\sigma > 0$ means that selection is weaker.

At the same time, each clonotype $x \in P_{t-1}$ from the previous repertoire may be re-activated and be subsequently duplicated through cell divisions (25), with probability $\mu f(x, a_t)$ (see Methods), proportional to the cross-reactivity, where $0 \leq \mu \leq 1$ is a proliferation parameter. These previously existing cells and their offspring may then die before the next infection. We denote by γ their survival probability, so that the average lifetime of each cell is $(1-\gamma)^{-1}$. The proliferation and death parameters μ and γ are assumed to be constrained and fixed. The net mean growth is thus given by:

$$\langle n_{x,t} \rangle = (1 + \mu f(x, a_t))\gamma n_{x,t-1}. \tag{6.5}$$

$\Gamma \equiv (1+\mu)\gamma$ is defined as the maximum growth factor. At the end of the process, the updated repertoire P_t combines the result of this proliferation and death process applied to P_{t-1} with the new receptors obtained from affinity maturation.

To assess the performance of a given strategy, we define an overall cost function at each time step:

$$L_t = I_t + \kappa m_t. \tag{6.6}$$

The second term κm_t corresponds to a plasticity cost encoding the resources necessary to generate and maintain new memory clonotypes with affinity maturation. This cost enforces a minimal homeostatic constraint on the memory repertoire. We neglect any dependence of the cost on the diversification σ, which is secondary and would require adding additional parameters without affecting the qualitative picture. We assume that, over evolutionary timescales, the immune system has minimized the average cumulative cost over a large number of infections:

$$\mathcal{L}(m, \sigma) = \lim_{T \to \infty} \frac{1}{T} \sum_{t=1}^{T} L_t. \tag{6.7}$$

This optimization yields the optimal parameters of the strategy, namely the best functions $m^*(I)$ and $\sigma^*(I)$ describing the extent and diversity of affinity maturation and how they should depend on the strength of the infection I:

$$(\bar{m}^*, \sigma^*) = \arg\min_{(m,\sigma)} \mathcal{L}(m, \sigma), \tag{6.8}$$

For the sake of simplicity, in the next three sections we will specialize to the case of constant functions $m(I) \equiv m$ and $\sigma(I) \equiv \sigma$. We will come back to the general case in the last section of the results.

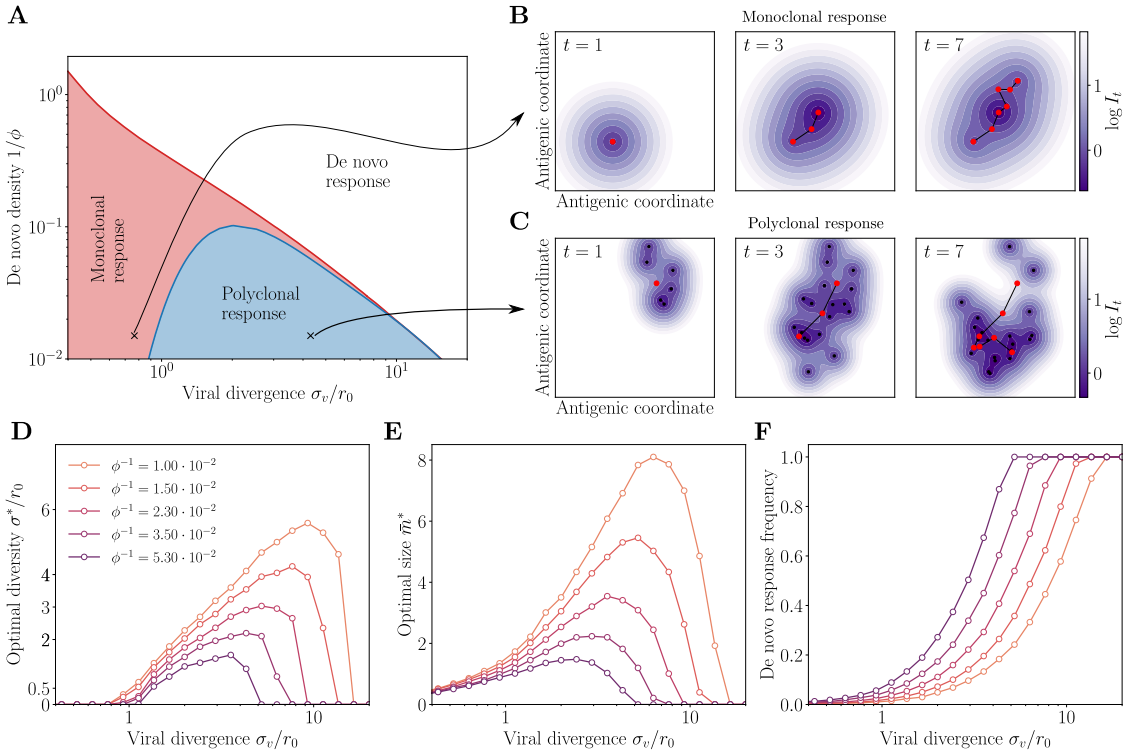

Figure 6.2: **Regimes of affinity maturation.** **A.** Phase diagram of the model as a function of the de novo density $1/\phi$, and viral divergence σ_v, in a two-dimensional antigenic map. Three phases emerge: monoclonal memory (red), polyclonal memory (purple) and de novo response (white). **B-C.** Snapshots in antigenic space of the sequential immunization by a viral strain in the (B) monoclonal and (C) polyclonal phases. We show the viral position (red dots), memory clonotypes (black dots), and viral trajectory (black line). The colormap shows the log infection cost. Parameters σ_v and ϕ correspond to the crosses on the phase diagram in A, with their respective optimal σ^*, $\bar{m}^*$ (see arrows). **D.** Diversity σ^*, **E.** optimal size $\bar{m}^*$, and **F.** frequency of de novo response usage to an immunization challenge for different de novo densities $1/\phi$. Parameters values: $\kappa = 3.3$, $\alpha = 1$, $q = 2$, $d = 2$, $\gamma = 0.85$, $\mu = 0.5$. Parameters values: $N_h = 10^{10}$, $M = 5$, $\beta_0 = 2$, $\gamma = 0.6$, $D_\alpha = 2 \cdot 10^{-6}$.

6.2.2 Phase diagram of optimal affinity maturation strategies

We obtain optimal constant strategies $\bar{m}(I) = m^*, \sigma(I) = \sigma^*$, by minimizing the simulated long-term cost $\mathcal{L}(\mathcal{S})$ (Eq. 6.7) in a 2-dimensional antigenic space (see Methods for details of the simulation, optimization procedures, and phase determination). By varying two key parameters, the cost ϕ associated to the use of the de novo response, and the virus divergence σ_v, we see a phase diagram emerge with three distinct phases: the de novo monoclonal response, and polyclonal response phases (Fig. 6.2A). In Figs. 6.2B-C we show examples of the stochastic evolution of memory repertoires with optimal rules in the two phases (monoclonal and polyclonal responses). Figs. 6.2D-F show the behaviour of the optimal parameters, as well as the fraction of infections for which the de novo response is used (when the maximal infection cost ϕ is paid). The general shape and behaviour of this phase diagram depends only weakly on the parameter choices (see Appendix, Fig. S4).

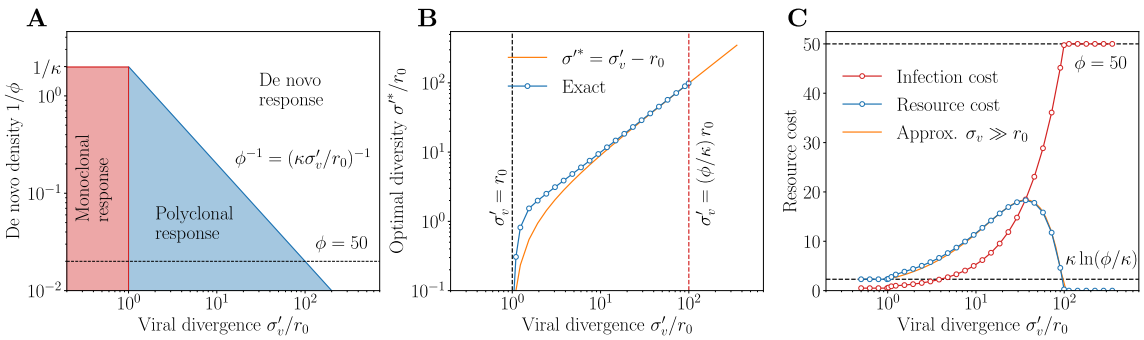

Figure 6.3: **Analytical solution of a tractable model. A.** Exact phase diagram in $d = 1$ for the simplified model ($q = \infty$, $\gamma = 0$, and all-or-nothing infection cost). The boundary between monoclonal is given by $\sigma'_v = r_0$ and the boundary between polyclonal by $\phi^{-1} = (\kappa\sigma'_v/r_0)^{-d}$. **B.** Optimal memory diversity $\sigma'^* \approx \sigma'_v$ and **C.** optimal infection and plasticity costs for as a function of σ'_v for $\phi = 50$. σ' and σ'_v are rescaled versions of the diversity and divergence to match the variances of the original model.

When the de novo response is sufficiently protective (small ϕ), or when the virus mutates too much between infections (large σ_v), the optimal strategy is to produce no memory cells at all ($\bar{m}^* = 0$), and rely entirely on the de novo response, always paying a fixed cost $L_t = \mathcal{L} = \phi$ (de novo phase).

When the virus divergence σ_v is small relative to the cross-reactivity range r_0, it is beneficial to create memory clonotypes ($\bar{m}^* > 0$), but with no diversity, $\sigma^* = 0$ (monoclonal response). In this case, all newly created clonotypes are invested into a single antigenic position a_t that perfectly recognizes the virus. This strategy is optimal because subsequent infections, typically caused by similar viral strains of the virus, are well recognized by these memory clonotypes.

For larger but still moderate virus divergences σ_v, this perfectly adapted memory is not sufficient to protect from mutated strains: the optimal strategy is rather to generate a polyclonal memory response, with $\bar{m}^* > 0$, $\sigma^* > 0$. In this strategy, the immune system hedges its bet against future infections by creating a large diversity of clonotypes that cover the vicinity of the encountered strain. The created memories are thus less efficient against the *current* infection, which they never will have to deal with. The advantage of this strategy is to anticipate future antigenic mutations of the virus. This diversified pool of cells with moderate affinity is in agreement with recent experimental observations (172; 203; 204; 25). The diversity of the memory pool is supported by a large number of clonotypes $\bar{m}^*$ (Fig. 6.2E). As the virus divergence σ_v is increased, the optimal strategy is to scatter memory cells further away from the encountered strain (increasing σ^*, Fig. 6.2D). However, when σ_v is too large, both drop to zero as the de novo response takes over (Fig. 6.2F). Increasing the de novo density ϕ^{-1} also favors the de novo phase. When there is no proliferation on average, i.e. $\Gamma = (1 + \mu)\gamma < 1$, there even exists a threshold ϕ_c^{-1} above which the de novo response strategy is always best (Appendix Fig. S4, and Text for estimates of that threshold).

6.2.3 Analytical results in a solvable model

To gain insight into the transitions observed in the phase diagram of Fig. 6.2, we can make a series of simplifications and approximations about the model that allow for analytical progress. We assume a step function for the cross-reactivity function $f(x, a) = 1$ for $\|x - a\| \leq r_0$, and 0 otherwise, corresponding the limit $q = \infty$. Likewise, we assume a uniform distribution of viral antigenic mutations $a_{t+1} = a_t + \sigma'_v \eta'_{t+1}$, where η'_t is a random point of the d-dimensional unit ball, with $\sigma'_v = \sigma_v \sqrt{1 + 2/d}$ (so that the variance is the same as in the Gaussian case), and similarly for memory diversification, with new clonotypes drawn from a uniform distribution is a ball of radius $\sigma' = \sigma\sqrt{1 + 2/d}$. The infection cost is approximated by an all-or-nothing function, with $I_t = 0$ if there is any coverage $C(a_t) > 0$, and $I_t = \phi$ if $C(a_t) = 0$. We further assume $\gamma = 0$: all clonotypes are discarded at each time step, so that memory may only be used once.

In this simplified version of the model, the phase diagram and optimal parameters can be computed analytically. We first summarize the main results below. In the subsequent paragraphs, we provide detailed derivations in the case of arbitrary dimensions, and also provide additional exact formulas in the one-dimensional case.

One can show (see Appendix) that the transition from monoclonal to polyclonal response occurs exactly when the radius of the ball within which viral mutations occur reaches the cross-reactivity radius r_0:

$$\sigma'_v = r_0. \tag{6.9}$$

Below this transition ($\sigma'_v < r_0$), the optimal strategy is to have no diversity at all and perfectly target the recognized antigen a_t, $\sigma'^* = 0$, as any memory cell at a_t will recognize the next infection. In this case the optimal mean number of memories $\bar{m}^* = \ln(\phi/\kappa)$ results in a trade off between the cost of new memories with the risk of not developing any memory at all by minimizing $\phi e^{-\bar{m}} + \kappa\bar{m}$. The transition from the monoclonal response to de novo phases is then given by $\phi = \kappa$, where $\bar{m}^* = 0$.

The polyclonal-to- de novo response transition may also be understood analytically. In the polyclonal response phase, the optimal strategy is, in either of the limits $\sigma'_v \gg r_0$ or $\bar{m}^* \ll 1$ (see Appendix):

$$\sigma'^* \approx \sigma'_v - r_0 \tag{6.10}$$

$$\bar{m}^* \approx \frac{{\sigma'_v}^d}{r_0^d} \ln\left(\frac{\phi}{\kappa}\frac{r_0^d}{{\sigma'_v}^d}\right). \tag{6.11}$$

In particular this result becomes exact at the transition from polyclonal to de novo response, where $\bar{m}^* = 0$. The transition is thus given by:

$$\phi^{-1} = \frac{r_0^d}{\kappa {\sigma'_v}^d}. \tag{6.12}$$

The polyclonal response is outcompeted by the de novo one when the density of de novo responding cells (ϕ^{-1}) becomes larger than the probability density of new strains falling within the cross-reactivity radius ($r_0^d/{\sigma'_v}^d$), rescaled by the memory cost coefficient κ^{-1}.

Fig. 6.3 shows the resulting phase diagram, as well as the optimal diversity σ'^* and predicted costs for a fixed ϕ and $d = 1$. These predictions reproduce the main features of

the full model, in particular the scaling of the immune diversity σ with σ_v (Fig. 6.2D vs. Fig. 6.3B) and the general shape of the optimal memory size $\bar{m}^*$ (Fig. 6.2E vs. Fig. 6.3C), which first increases as the virus becomes more divergent, to later drop to zero as memory becomes too costly to maintain and the system falls into the de novo phase.

In summary, the model predicts the two expected regimes of de novo response and memory use depending on the parameters that set the costs of infections and memory formation. But in addition, it shows a third phase of polyclonal response, where affinity maturation acts as an anticipation mechanism whose role is to generate a large diversity of cells able to respond to future challenges. The prediction of a less focused and thus weaker memory pool observed experimentally is thus rationalized as a result of a bet-hedging strategy.

6.2.4 Population dynamics of optimized immune systems

We now turn to the population dynamics of the memory repertoire. When the virus drifts slowly in antigenic space (small σ_v), the same clonotypes get reactivated multiple times, causing their proliferation, provided that $\Gamma = \gamma(1+\mu) > 0$. This reactivation continues until the virus leaves the cross-reactivity range of the original clonotype, at which point the memory clone decays and eventually goes extinct (Fig. 6.4A). Typical clonotype size trajectories from the model are shown in Fig. 6.4B. They show large variations in both their maximal size and lifetime. The distribution of clonotype abundances, obtained from a large number of simulations, is indeed very broad, with a power-law tail (Fig. 6.4C). The lifetime of clonotypes, defined as the time from emergence to extinction, is distributed according to an exponential distribution (Fig. 6.4D). The exponents governing the tails of these distributions, β and γ, depend on the model parameters, in particular the divergence σ_v.

We can understand the emergence of these distributions using a simple scaling argument, detailed in Supplementary Text. The peak size of a clonotype depends on the number of successive infections by viral strains remaining within a distance r^* from the clonotype:

$$r^* = r_0 \ln[\gamma\mu/(1-\gamma)]^{1/q}, \tag{6.13}$$

under which it continues expanding. This number has a long exponential tail with characteristic time $t_s \sim (r^*/\sigma_v)^2$. One can show that this translates into a power law tail for the distribution of clonotype sizes:

$$p(n^*) \sim \frac{1}{n^{*1+\beta}}, \quad \text{with } \beta \sim \frac{\sigma_v^2}{r^{*2}\ln\Gamma}, \tag{6.14}$$

and an exponential tail for the lifetime of clonotypes:

$$p(t_l) \sim e^{-\lambda t_l}, \quad \lambda \sim \frac{\sigma_v^2}{r^{*2}}\left(1+\frac{\ln\Gamma}{\ln(1/\gamma)}\right)^{-1}. \tag{6.15}$$

This simple scaling argument predicts the exponents β and λ fairly well: Figs. 6.4E-F confirm the validity of the scaling relations (6.14)-(6.15) against direct evaluation from simulations, for $d = 2$ and $q = 2$. These scalings still hold for different parameter choices (see Appendix, Fig. S5).

These scaling relations are valid up to a geometry-dependent prefactor, which is gov-

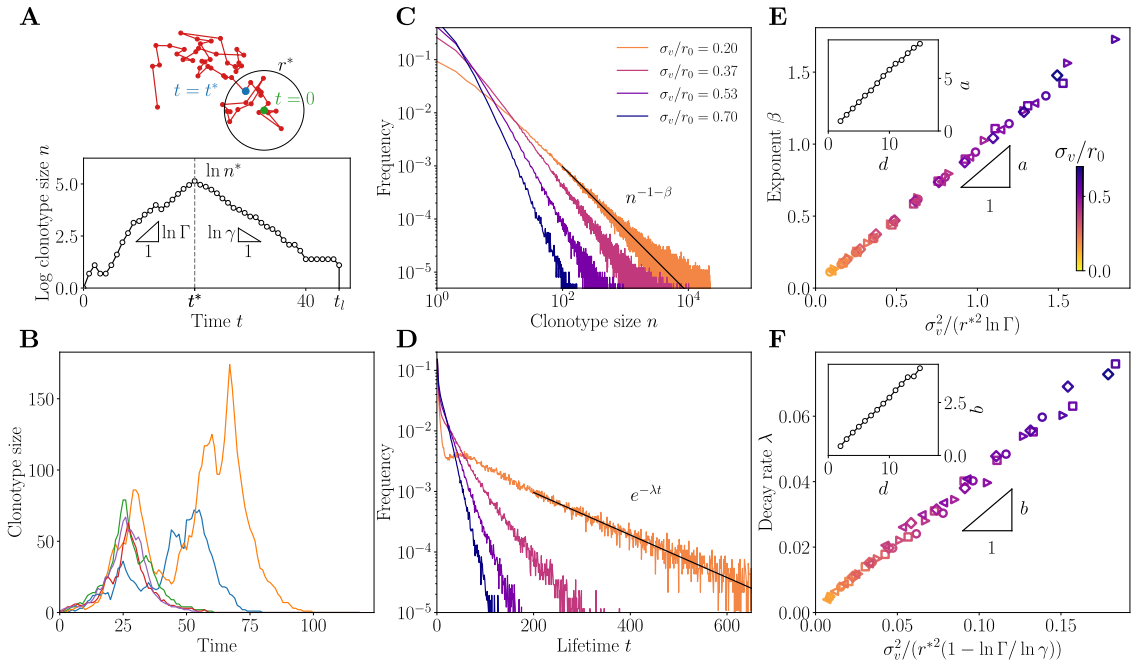

Figure 6.4: **Clonotype dynamics and distribution.** **A.** Sketch of a recall response generated by sequential immunization with a drifting strain. Clonotypes first grow with multiplicative rate $\Gamma = \gamma(1+\mu)$, until they reach the effective cross-reactivity radius r^*, culminating at n^*, after which they decay with rate γ until extinction at time t_l. **B.** Sample trajectories of clonotypes generated by sequential immunization with a strain of mutability $\sigma_v/r_0 = 0.53$. **C.** Distribution of clonotype size for varying virus mutability σ_v/r_0. **D.** Distribution of the lifetime of a clonotype for varying virus mutability σ_v/r_0. From **B** to **D** the proliferation parameters are set to $\gamma = 0.85$, $\gamma = 0.5$ ie. $\Gamma = 1.275$. **E.** Scaling relation of the power law exponent for varying values of the parameters. Inset: dependence of the proportionality factor a on dimension. **F.** Scaling relation of the decay rate λ for varying σ_v/r_0, with scaling of the proportionality factor b. In both **E-F.**, the different parameters used are $(\gamma = 0.82, \mu = 0.65)$ ie. $\Gamma = 1.353$ (diamonds), $(\gamma = 0.8, \mu = 0.62)$ ie. $\Gamma = 1.296$ (squares), $(\gamma = 0.85, \mu = 0.5)$ ie. $\Gamma = 1.275$ (circles), $(\gamma = 0.87, \mu = 0.4)$ ie. $\Gamma = 1.21$ (triangles >), $(\gamma = 0.9, \mu = 0.35)$ ie. $\Gamma = 1.21$ (triangles <). From **B** to **F**, the strategy was optimized for $\phi = 100$ and $\kappa = 0.5/(1-\gamma)$. The color code for σ_v/r_0 is consistent across the panels **C** to **F**. In this panel, the other parameters used are $\alpha = 1$, $q = 2$, $d = 2$.

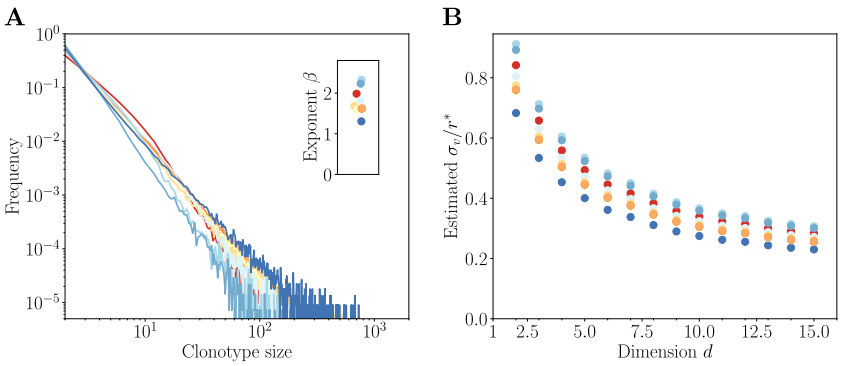

Figure 6.5: **Comparison to repertoire data. A.** Clonotype abundance distribution of IgG repertoires of healthy donors from (205). **B.** Estimated mutatibility σ_v in units of the rescaled cross-reactivity r^*, defined as the antigenic distance at which clonotypes stop growing. σ_v is obtained as a function of d by inverting the linear relationship estimated in the inset of Fig. 6.4E, assuming $q = 2$ and $\Gamma = 1.4$ (estimated from (25)).

erned by dimensionality and the shape of the cross-reactivity kernel. In the Supplementary Text, we calculate this prefactor in the special case of an all-or-nothing cross-reactivity function, $q = \infty$. Generally, β increases with d, as shown in the insets of Figs. 6.4E-F for $q = 2$. In higher dimensions, there are more routes to escape the cross-reactivity range, and thus a faster decaying tail of large clonotypes. This effect cannot be explained by having more dimensions in which to mutate, since the antigenic variance is distributed across each dimension, according to σ_v^2/d. Rather, it results from the absence of antigenic back-mutations: in high dimensions, each mutation drifts away from the original strain with a low probability of return, making it easier for the virus to escape, and rarer for memory clonotypes to be recalled upon infections by mutant strains.

6.2.5 Comparison to experimental clone-size distributions

The power-law behaviour of the clone-size distribution predicted from the model in Fig. 6.4E can be directly compared to existing data on bulk repertoires. While the model makes a prediction for subsets of the repertoire specific to a particular family of pathogens, the same power-law prediction is still valid for the entire repertoire, which is a mixture of such sub-repertoires. Power laws have been widely observed in immune repertoires: from early studies of repertoire sequencing data of BCR in zebrafish (174; 206), to the distribution of sizes of clonal families of human IgG BCR (number of unique sequences in a lineage stemming from a common naive ancestor) (182; 207), as well as in T-cell receptor repertoires (175). However, these power laws have not yet been reported in the clonotype abundance distribution of human BCR (number of copies of unique BCR sequences).

To fill this gap, we used publicly available IgG repertoire data of 9 human donors from a recent ultra-deep repertoire profiling study of immunoglobulin heavy-chains (IGH) (205). The data was downloaded from Sequence Read Archive and processed as in (207). Repertoires were obtained from the sequencing of IGH mRNA molecules to which unique molecular identifiers (UMI) were appended. For each IGH nucleotide clonotype found in the dataset, we counted the number of distinct UMI attached to it, as a proxy for the overall abundance of that clonotype in the expressed repertoire. The distributions of these

abundances are shown for all 9 donors in Fig. 6.5A. In agreement with the theory, they display a clear power-law decay $p(n) \sim n^{-1-\beta}$, with $\beta = 1.2$-2.4.

Since the experimental distribution is derived from small subsamples of the blood repertoire, the absolute abundances cannot be directly compared to those of the model. In particular, subsampling means that the experimental distribution focuses on the very largest clonotypes. Thus, comparisons between model and data should be restricted to the tail behavior of the distribution, namely on its power-law exponent β. The bulk repertoire is a mixture of antigen-specific sub-repertoires, each predicted to be a power law with a potentially different exponent. The resulting distribution is still a power-law dominated by the largest exponent.

We used this comparison to predict from the exponent β the virus divergence between infections. To do so, we fit a linear relationship to the inset of Fig. 6.4E, and invert it for various values of the dimension d to obtain σ_v/r^*. We fixed $\Gamma = 1.4$, which corresponds to a 40% boost of memory B cells upon secondary infection, inferred from a 4-fold boost following 4 sequential immunizations reported in mice (25). The result is robust to the choice of donor, but decreases substantially with dimension, because higher dimensions mean faster escape, and thus a lower divergence for a given measured exponent (Fig. 6.5B). The inferred divergence σ_v is always lower than, but of the same order as, the effective cross-reactivity range r^*, suggesting that the operating point of the immune system falls in the transition region between the monoclonal and polyclonal response phases (Fig. 6.2A).

6.2.6 Inhibition of affinity maturation and antigenic imprinting

In this section we come back to general strategies where the process of affinity maturation depends on the immune history through the infection cost I experienced by the system during the early immune response, which controls the number and diversity of newly created memories following that response: $\bar{m}(I)$, $\sigma(I)$. The optimization of the loss function (6.6) is now carried out with respect to two *functions* of I. To achieve this task, we optimize with respect to discretized functions $(\bar{m}_1, ..., \bar{m}_n)$ and $(\sigma_1, ..., \sigma_n)$ taken at n values of the infection cost I between 0 and ϕ. From this optimization, a clear transition emerges between a regime of complete inhibition of affinity maturation ($\bar{m}^*(I) = 0$) at small infection costs, and a regime of affinity maturation ($\bar{m}^*(I) > 0$) at larger infection costs (Fig. 6.6A). In the phase where affinity maturation occurs, the optimal diversity $\sigma^*(I)$ is roughly constant (Fig. 6.6B).

This transition means that when pre-existing protection is good enough, the optimal strategy is not to initiate affinity maturation at all, to save the metabolic cost κm_t. This inhibition of affinity maturation is called "antigenic imprinting," and is linked to the notion of "original antigenic sin," whereby the history of past infections determines the process of memory formation, usually by suppressing it. This phenomenon leads to the paradoxical prediction that a better experienced immune system is less likely to form efficient memory upon new infections. Importantly, in our model this behaviour does not stem from a mechanistic explanation, such as competition for antigen or T-cell help between the early memory response and germinal centers, but rather as a long-term optimal strategy maximizing immune coverage while minimizing the costs of repertoire re-arrangement.

To simplify the investigation of antigenic imprinting, we approximate the optimal strategies in Fig. 6.6A and B by step functions, with a suppressed phase, $\bar{m}(I) = 0$, for $I <$

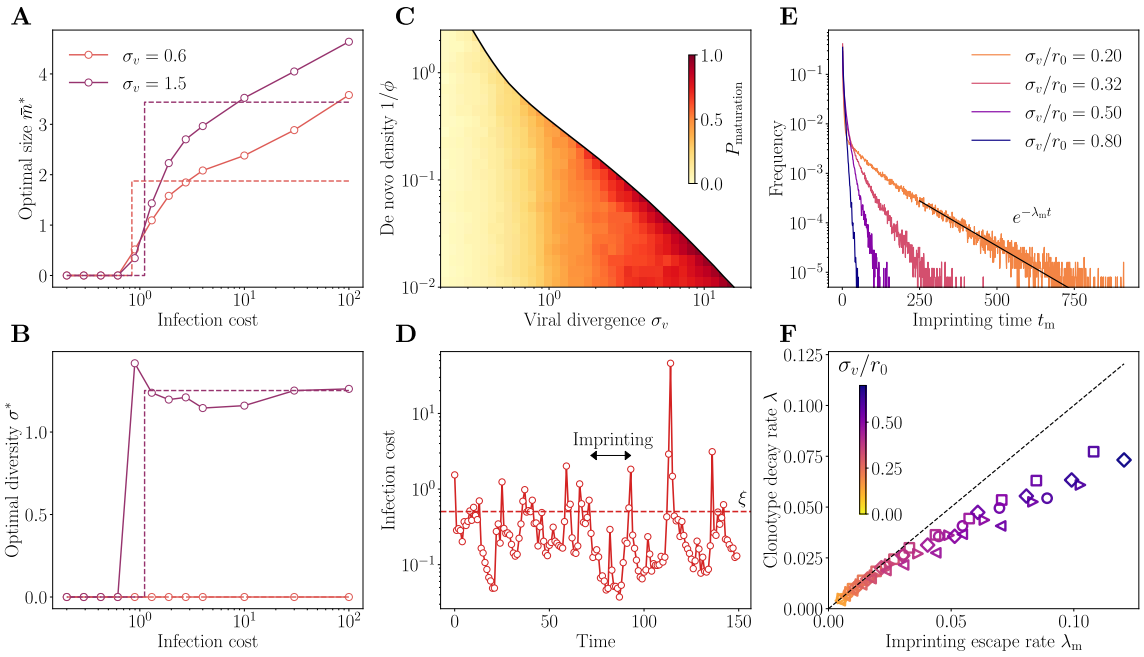

Figure 6.6: **Imprinting and backboosting.** **A,B.** Optimal regulatory functions for (**A**) the number $m^*(I)$ and (**B**) the diversity $\sigma^*(I)$ of new memories as a function of the infection cost I, for two values for the viral divergence. These functions show a sharp transition from no to some memory formation, suggesting to replace them by simpler step functions (dashed lines). This step function approximation is used in the next panels. **C.** Frequency of infections leading to affinity maturation in the optimal strategy. The frequency increases with the virus divergence σ_v, up to the point where the transitions to the de novo phase where memory is not used at all. **D.** Typical trajectory of infection cost in sequential infections at $\sigma_v/r_0 = 0.5$. When the cost goes beyond the threshold ξ, affinity maturation is activated, leading to a drop in infection cost. These periods of sub-optimal memory describe an "original antigenic sin," whereby the immune system is frozen in the state imprinted by the last maturation event. **E.** Distribution of imprinting times, i.e. the number of infections between affinity maturation events, decays exponentially with rate λ_m. The proliferation parameters in **A** to **E** are set to $\gamma = 0.85$ and $\mu = 0.5$. **F.** Predicted scaling of λ_m with the clonotype decay rate λ from Figs. 6.4D and F. In **F**, the different parameters used are $(\gamma = 0.82, \mu = 0.65)$ ie. $\Gamma = 1.353$ (diamonds), $(\gamma = 0.8, \mu = 0.62)$ ie. $\Gamma = 1.296$ (squares), $(\gamma = 0.85, \mu = 0.5)$ ie. $\Gamma = 1.275$ (circles), $(\gamma = 0.87, \mu = 0.4)$ ie. $\Gamma = 1.21$ (triangles >), $(\gamma = 0.9, \mu = 0.35)$ ie. $\Gamma = 1.21$ (triangles <). The color code for σ_v/r_0 is consistent across the panels **E** and **F**. From **D** to **F**, the strategy was optimized for $\phi = 100$ and $\kappa = 0.5/(1-\gamma)$. In this panel, the other parameters used are $\alpha = 1$, $q = 2$, $d = 2$.

ξ, and an active phase, $\bar{m}(I) \equiv \bar{m} > 0$ and $\sigma(I) \equiv \sigma$, for $I > \xi$. The threshold ξ is left as an optimization parameter, in addition to σ and $\bar{m}$. Optimizing with respect to these three parameters, we observe that the frequency of affinity maturation events mostly depends on σ_v (Fig. 6.6C). While this threshold remains approximately constant, the frequency of affinity maturation events increases as σ_v increases. At small σ_v, the optimal strategy is to extensively backboost existing memory cells; for large σ_v, the growing unpredictability of the next viral move makes it more likely to have recourse to affinity maturation. In other words, when the virus is stable (low σ_v), the immune system is more likely to capitalize on existing clonotypes, and not implement affinity maturation, because savings made on the plasticity cost outweigh the higher infection cost. As the virus drifts away with time, this infection cost also increases, until it reaches the point where affinity maturation becomes worthwile again.

Trajectories of the infection cost show the typical dynamics induced by backboosting, with long episodes where existing memory remains sufficient to keep the cost below ξ (Fig. 6.6D), interrupted by infections that fall too far away from existing memory, triggering a new episode of affinity maturation and concomitant drop in the infection cost.

We call the time between affinity maturation events t_{m}. Its mean $\langle t_{\mathrm{m}} \rangle$ is equal to the inverse of the frequency of maturation events, and thus decreases with σ_v. Its distribution, shown Fig. 6.6E, has an exponential tail with exponent λ_{m}. The exponential tail of the distribution of t_{m} is dominated by episodes where the viral strain drifted less than expected. In that case, the originally matured clonotype grows to a large size, offering protection for a long time, even after it has stopped growing and only decays. We therefore expect that in the case of a slowly evolving virus $\sigma_v \ll r_0$, the escape rate from the suppressed phase is given by the clonotype decay rate: $\lambda_{\mathrm{m}} \sim \lambda$. We verify this prediction in Fig. 6.6F. Interestingly, for slowly evolving viruses, the typical clonotype lifetime diverges, leading to a lifelong imprinting by the primary immune challenge. Conversely, as the viral divergence σ_v grows, the imprinting time decays faster than the typical clonotype lifetime and the extent of the imprinting phenomenon is limited.

6.3. Discussion

Adaptive immunity coordinates multiple components and cell types across entire organisms over many space and time scales. Because it is difficult to empirically characterize the immune system at the system scale, normative theories have been useful to generate hypotheses and fill the gap between observations at the molecular, cellular, and organismal scales (208; 22). Such approaches include clonal selection theory (132), or early arguments about the optimal size and organization of immune repertoires (199; 23; 24), and of affinity maturation (187; 186). While these theories do not rely on describing particular mechanisms of immune function, they may still offer quantitative insights and help predict new mechanisms or global rules of operation.

Previous work developed models of repertoire organization as a constrained optimization problem where the expected future harm of infection, or an *ad hoc* utility function, is minimized (9; 8; 5; 7). In Ref. (8), it was assumed clonotypes specific to all antigens are present at all times in the repertoire; the mechanism of immune memory then merely consists of expanding specific clonotypes at the expense of others. This assumption describes T-cell repertoires well, where there are naive cells with good affinity to essentially any

antigen (209). For B cells the situation is more complex because of affinity maturation. In addition, re-organizing the repertoire through mutation and selection has a cost, and is subject to metabolic and physical constraints.

Our work addresses these challenges by proposing a framework of discrete-time decision process to describe the optimal remodeling of the B-cell repertoire following immunization, through a combination of affinity maturation and backboosting. While similar to (7), our approach retains the minimal amount of mechanistic details and focuses on questions of repertoire remodeling, dynamics, and structure. The specific choices of the cost functions were driven by simplicity, while still retaining the ability to display emergent behaviour. Generalizing the metabolic cost function to include e.g. costs of diversification (through a dependence on σ) or of cell proliferation is not expected to affect our results qualitatively, although it may shift the exact positions of the transition boundaries.

We investigated strategies that maximize long-term protection against subsequent challenges and minimize short-term resource costs due to the affinity maturation processes. Using this model, we observed that optimal strategies may be organized into three main phases as the pathogen divergence and de novo coverage are varied. We expect these distinct phases to co-exist in the same immune system, as there exists a wide range of pathogen divergences, depending on their evolutionary speed and typical frequency of recurrence.

For fast recurring or slowly evolving pathogens, the monoclonal response ensures a very specific and targeted memory. This role could be played by long-lived plasma cells. These cells are selected through the last rounds of affinity maturation, meaning that they are very specific to the infecting strain (131). Yet, despite not being called memory cells, they survive for long times in the bone marrow, providing long-term immunity.

For slow recurring or fast evolving pathogens, the polyclonal response provides a diverse memory to preempt possible antigenic drift of the pathogen. The function could be fulfilled by memory B cells, which are released earlier in the affinity maturation process, implying that they are less specific to the infecting strain, but collectively can cover more immune escape mutations. While affinity maturation may start from both memory or naive B cells during sequential challenges, the relative importance of each is still debated (210; 211; 212). Our model does not commit on this question since we assume that the main benefit of memory is on the infection cost, rather than its re-use in subsequent rounds of affinity maturation.

For simplicity our model assumed random evolution of the virus. However, there is evidence, backed by theoretical arguments, that successive viral strains move in a predominant direction in antigenic space, as a result of immune pressure by the host population (52; 53; 36). While it is unlikely that the immune system has evolved to learn how to exploit this persistence of antigenic motion in a specific manner, such a bias in the random walk is expected to affect the optimal strategy, as we checked in simulations (Fig. S6). The bias of the motion effectively increases the effective divergence of the virus, favoring the need for more numerous and more diverse memory cells. However, it does not seem to affect the location of the polyclonal-to-de novo response transition.

The model is focused on acute infections, motivated by the assumption that recurring infections and antigenic drift are the main drivers of affinity maturation evolution. However, much of the model and its results can be re-interpreted for chronic infections. In that context, the sequential challenges of our model would correspond to selective sweeps in the

viral population giving rise to new dominant variants. While the separation of time scales between the immune response and the rate of reinfections would no longer hold, we expect some predictions, such as the distribution of clonotype sizes and the emergence of imprinting, to hold true. Chronic infections also imply that the virus evolves as a function of how the immune system responds. Including this feedback would require a game-theoretic treatment. We speculate that it would drive antigenic motion in a persistent direction, as argued earlier and evaluated in Fig. S6.

We investigated strategies where the outcome of affinity maturation is impacted by the efficiency of the early immune response. It is known that the extrafollicular response can drastically limit antigen availability and T-cell help, decreasing the extent of affinity maturation and the production of new plasma and memory cells (157). Our general framework allows for but does not presume the existence of such negative feedbacks. Instead, they naturally emerge from our optimization principle. We further predict a sharp transition from no to some affinity maturation as a function of the infection cost. This prediction can be interpreted as the phenomenon of antigenic imprinting widely described in sequential immunization assays (159), or "original antigenic sin" (196). It implies that having been exposed to previous strains of the virus is detrimental to mounting the best possible immune response. Importantly, while antigenic imprinting has been widely described in the literature, no evolutionary justification was ever provided for its existence. Our model explains it as a long term optimal strategy for the immune system, maximizing immune coverage while minimizing repertoire re-arrangements (encoded in the cost κm).

We believe this framework can be generalized to investigate interactions between slow and fast varying epitopes, which are known to be at the core of the low effectiveness of influenza vaccines (55). When during sequential challenges only one of multiple epitopes changes at a time, it may be optimal for the immune system to rely on its protections against the invariant epitopes. Only after all epitopes have escaped immunity does affinity maturation get re-activated concomitantly to a spike of infection harm, similar to our result for a single antigen.

Our model can explain previously reported power laws in the distributions of abundances of B-cell receptor clonotypes. However, there exist alternative explanations to such power laws (167; 213) that do not require antigenically drifting antigens. Our model predictions could be further tested in a mouse model, by measuring the B-cell recall response to successive challenges (159), but with epitopes carefully designed to drift in a controlled manner, to check the transition predicted in Fig. 6.6A. While not directly included in our model, our result also suggest that the size of the inoculum, which would affect the infection cost, should also affect backboosting. This effect could also be tested in mouse experiments. The predicted relationships between viral divergence and the exponents of the power law and clonotype lifetimes (Figs. 6.4E and F) could be tested in longitudinal human samples, by sequencing sub-repertoires specific to pathogens with different rates of antigenic evolution. This would require to computationally predict what B-cell receptors are specific to what pathogen, which in general is difficult.

We only considered a single pathogenic species at a time, with the assumption that pathogens are antigenically independent, so that the costs relative to different pathogens are additive. Possible generalizations could include secondary infections, as well as antigenically related pathogens showing patterns of cross-immunity (such as cowpox and smallpox, or different groups of influenza), which could help us shed light on complex immune

interactions between diseases and serotypes, such as negative interference between different serotypes of the Dengue fever leading to hemorrhagic fever, or of the human Bocavirus affecting different body sites or (196).

6.4. Methods

6.4.1 Mathematical model

The positions of newly created memory receptors upon infection are drawn at random according to:

$$x_j = a_t + \sigma\xi_j \,, j = 1, \ldots, m_t, \tag{6.16}$$

where ξ_j is normally distributed with $\langle\xi_j\rangle = 0$ and $\langle\xi_j^2\rangle = 1$. Their initial sizes are set to $n_{x_j,t} = 1$. Upon further stimulation, the new size $n'_{x,t}$ of a pre-existing clonotype right after proliferation is given by:

$$n'_{x,t} - n_{x,t-1} \sim \text{Binom}(n_{x,t-1}, \mu f(x, a_t)), \tag{6.17}$$

where $f(x, a) = e^{-(\|x-a\|/r_0)^q}$ is the cross-reactivity Kernel. After proliferation, each memory may die with probability γ, so that the final clonotype size after an infection cycle is given by $n_{x,t} \sim \text{Binom}(n'_{x,t}, \gamma)$.

In all results except in the last section of the Results, we use the Ansatz of constant functions, $m(I) \equiv m$, $\sigma(I) \equiv \sigma$. In the last section of the Results, we first perform optimization over discretized functions $m = (m_1, \ldots, m_n)$, $\sigma = (\sigma_1, \ldots, \sigma_n)$ defined over n chosen values of $I = (I_1, \ldots, I_n)$. Then, we parametrize the functions as step functions: $\sigma(I) = 0$ and $m(I) = 0$ for $I < \xi$, and $\sigma(I) = \sigma$ and $m(I) = m$ for $I > \xi$, and optimize over the 3 parameters σ, m, ξ.

6.4.2 Monte-Carlo estimation of the optimal strategies

The average cumulative cost $\mathcal{L}$ in Eq. 6.7 is approximated by a Monte-Carlo method. To ensure the simulated repertoire reaches stationarity, we start from a naive repertoire and discard an arbitrary number of initial viral encounters. Because the process is ergodic, simulating a viral-immune trajectory over a long time horizon is equivalent to simulating M independent trajectories of smaller length T. To ensure the independence of our random realizations across our M parallel streams we use the random number generators method *split* provided in Tina's RNG library (214). The cumulative cost function $\mathcal{L}$ is convex for the range of parameters tested. To optimize $\mathcal{L}$ under positivity constraints for the objective variables σ, $\bar{m}$ and ξ, we use Py-BOBYQA (215), a coordinate descent algorithm supporting noisy objective functions.

The polyclonal to monoclonal (red curve) and memory to de novo response (blue curve) boundaries of the phase diagrams in Fig. 6.2 and Fig. S4 are obtained by respectively solving $\partial\mathcal{L}/\partial\sigma = 0$ in the monoclonal phase and $\partial\mathcal{L}/\partial\bar{m} = 0$ in the de novo phase. Both these derivatives can be approximated by finite differences with arbitrary tolerances on σ and $\bar{m}$. We fix the tolerance on σ to 0.2 and the tolerance on $\bar{m}$ to 0.01. To obtain the root of these difference functions, we use a bisection algorithm. In order to further decrease the noise level, we compute the difference functions across pairs of simulations, each pair using an independent sequence of pathogens a_t of length $L = 400$. The number of independent pairs of simulations used for each value of σ_v and ϕ is $M \sim 10^5$.

7

Eco-evolutionary stability of viral strategies

This chapter is yet to be published:

- Chardès V., A. Mazzolini, Walczak A.M., Mora T. *In preparation.*

Antigenic variation is the main immune escape mechanism for RNA viruses like influenza or SARS-CoV-2. It promotes diversity in the viral population and leads to repeated epidemics and reinfections. This antigenic evolution is fueled by remarkably high viral mutation rates, and is sustained by continuous pathogen transmission between hosts. In chapter 6, we investigated the optimal immune response maximizing the long-term protection against these antigenically evolving pathogens. We found that the optimal diversity σ^* and number $\bar{m}^*$ of memory B cells generated upon affinity maturation increase with σ_v the typical viral divergence between two reinfections. In this sense, the immune system generates a diverse memory pool anticipating for future antigenic variants. Following these results, it is natural to ask how the immune pressure in return shapes the viral evolution, and in particular its escape rate σ_v. This is the question we address in the this chapter by investigating the evolutionary stable viral strategies under the immune pressure exerted by a population of hosts.

7.1. Introduction

The survival of viral strains is dictated by their ability to spread from host to host in the population. In classical SIR models (31; 32) this ability is measured through the basic reproduction ratio, which denotes the average number of secondary infections an infected individual generates in a population with no pre-existing immunity. In the absence of antigenic evolution, any variant increasing this average number of secondary infections successfully spreads in the population (56; 32), and as a consequence the viral population reaches its evolutionary stable strategy when its basic reproduction ratio is maximized (57). Similarly to the long-term cost of chapter 6 whose minimization provided the optimal immune strategy, the maximization of the basic reproduction ratio here provides the evolutionary stable viral strategy.

However, viruses adapt and can evade immunity thanks to mutations modifying the epitopes targeted by antibodies. In particular, in viruses like influenza this evolution is characterized by a traveling wave of adaptation with new antigenic variants continuously appearing in the population (58; 53; 59; 60). As a consequence, the survival of these viral strains not only depends on their basic reproduction ratio, but also on their ability to generate antigenic variation to escape immunity (61). In this case, recent results suggest that the evolutionary stable viral strategy maximizes the speed of antigenic evolution

rather than the basic reproduction ratio (37). However, these results were obtained in a fully deterministic model of viral escape, ignoring finite population size effects, which are known to be ubiquitous in antigenic adaptation (38; 39). In this light, it remains unclear how antigenic escape coupled with finite size demographic effects constrain the evolution of the viral population.

To tackle these challenges, following chapter 6, we describe both the host immune memories and the viral strains as living in the same antigenic space (216; 36; 37; 33), corresponding to a space of "molecular similarity", also called "shape space" (170). This construction has been linked to a low dimensional projection of experimental data on which influenza and host antibodies co-evolve (58; 53; 59). In this antigenic space, we describe with a Susceptible-Infected-Recovered formalism (31; 32) the co-evolution of finite size populations of susceptible and infected hosts. Within this framework, the pathogen is transmitted from host to host at a rate β while hosts die of infection at a rate α and recover at rate γ. Together with the pathogen mutation rate, these parameters define a viral strategy. While the influence of in-host eco-evolutionary feedbacks on the evolution and control of pathogens causing chronic infections has already been studied (217; 218), in this chapter we investigate how inter-host immune pressure shapes the evolutionary stable strategy of viruses causing acute infections.

We show using simulations and analytical approximations that the capacity of antibodies to neutralize different viral variants, called cross-reactivity, determines the speed of antigenic evolution. We demonstrate that as the cross-reactivity increases, the viral evolution slows down and crosses-over from a Fisher-KPP wave (219) to a linear fitness wave (220; 221). Following these results, we find that the evolutionary stable viral strategy is dictated by a trade off between maximizing the speed of antigenic evolution when the cross-reactivity is small, and maximizing the reproduction ratio as it becomes larger. As a consequence, we show that a reduced cross-reactivity favors the evolution of highly transmissible and deadly pathogens with mutation rates close to the extinction threshold.

7.2. Results

7.2.1 Coarse-grained SI(R) model for antigenically evolving pathogens

Following the shape space idea introduced by Perelson and Oster (199), we describe the co-evolution of a viral population - infected hosts - and of immune receptors in a one dimensional continuous antigenic space. The closer a receptor-virus pair is in this space, the stronger is their binding. To quantify this affinity, we introduce a cross-reactivity function $0 < f < 1$ between a strain at position y and a receptor at position x, which we choose to be an exponential function:

$$f(x, y) = \exp\left(\frac{|x - y|}{r_0}\right), \tag{7.1}$$

where r_0 denotes the cross-reactivity range and modulates the distance over which a receptor x is effective in protecting from the strain y. In this space, viruses continuously mutate, each time changing their antigenic position by an infinitesimal distance $\delta x \ll r_0$, and proliferate through infection of new susceptible hosts. A randomly chosen host is susceptible to a given strain x if and only if its most recent infection is not due to a variant y *too similar* to x. We quantify the degree of susceptibility of hosts via a probability

$P_{\text{infect}}(x,t)$ that a strain at position x can infect a randomly chosen host in the population.

To treat the probability of infection, we define $h(x,t)$ the probability density for a randomly chosen host to have an immune memory of the virus located at position x. To model the evolution of this probability density, we take a recently introduced mean-field approach (36), assuming that hosts are exchangeable and have each M stored receptors that were elicited by past encounters with the virus. In particular, every time a host is infected by a strain x, a new memory is added at the position x and an old memory is discarded uniformly at random in the pool of all the memories elicited by the virus in the host population. As a consequence, the cross-reactivity function directly controls the degree of cross-immunity between strains: a past challenge with a strain y protects a host from the strain x proportionally to the cross-reactivity $f(x,y)$. The population density of host infected by strain x at time t is denoted $n(x,t)$, and the population dynamics of the immune repertoire are modeled by:

$$\partial_t h(x,t) = \frac{1}{MN_h}\left[n(x,t) - N(t)h(x,t)\right], \tag{7.2}$$

where N_h is the total number of hosts. We have the normalization $\int dx h(x,t) = 1$, such that $n_h(x,t) = MN_h h(x,t)$ is the density of immune receptors in the host population. Following this prescription for $h(x,t)$, a randomly chosen host in the host population is susceptible to a strain x if and only if none of its M stored immune receptors recognize the threat:

$$P_{\text{infect}}(x,t) = \left[\int dy h(y,t)(1 - f(x-y))\right]^M = (1 - c(x,t))^M, \tag{7.3}$$

where we introduced $c(x,t)$ the coverage, ie. the probability that an individual immune receptor of the host recognizes the variant. Following standard SI(R) modeling, we denote β the pathogen transmission rate, α the death rate of infected individuals, called virulence, and γ the recovery rate. We assume that deaths caused by the viral infection are balanced by a constant birth rate, ensuring that the host population size remains constant and equal to N_h.

The effective growth rate or "fitness" of a strain x is linearly related to the probability of infection: $f(x,t) = \beta P_{\text{infect}}(x,t) - (\alpha+\gamma)$. Additionally, we assume that viral mutations are unbiased $\langle \delta x \rangle = 0$, such that in the limit of infinitely small mutations happening at a rate U_x the density of infected hosts effectively diffuses with constant $D = U_x \langle \delta x^2 \rangle / 2$. The dynamics of the viral population are then described by the following stochastic differential equation:

$$\partial_t n(x,t) = f(x,t)n(x,t) + D\partial_x^2 n(x,t) + \sqrt{n(x,t)}\eta(x,t), \tag{7.4}$$

where η is a gaussian white noise $\langle \eta(x,t)\eta(x',t')\rangle = \delta(t-t')\delta(x-x')$. The total viral population size is $N(t) = \int dx n(x,t)$ and can fluctuate while the total size of the immune repertoire remains fixed to M receptors per host for a total of MN_h immune memories. Under the assumption the the viral population reaches a steady state $N(t) = N$, we can integrate Eq. 7.2:

$$h(x,t) = \frac{1}{N}\int_{-\infty}^{t} \frac{dt'}{\tau} e^{-\frac{t-t'}{\tau}} n(x,t'), \tag{7.5}$$

where $\tau = MN_h/N$ defines the turnover time scale of immune receptors. Together,

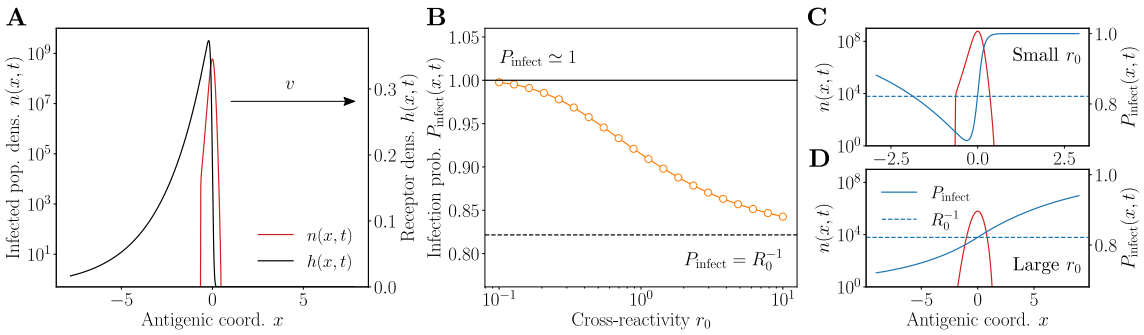

Figure 7.1: **Antigenic wave cross-over. A.** Snapshot of the viral evolution. The viral population $n(x,t)$ (red) travels to the right with a speed v, pushed by a density of immune receptors $h(x,t)$ (black). **B.** Cross-over in the infection probability P_{infect} at the tip of the wave as a function of the cross-reactivity r_0. At small r_0 the host population is fully susceptible to the most mutated strains, while it reaches the equilibrium susceptibility R_0^{-1} (56; 32) at large r_0. **C-D.** Snapshot of the viral evolution at small **C** and large **D** cross-reactivity. At large cross-reactivity the susceptibility profile is linear over the viral population. The legend in **A** is consistent across panels **A**, **C** and **D**. Parameters values: $N_h = 10^{10}$, $M = 5$, $\beta_0 = 2$, $\gamma = 0.6$. For details about the simulations see Methods.

Eqs. 7.2–7.4 describe the co-evolution of the infected host population and of the immune protections. This approach is largely inspired by a model recently introduced to study antigenic waves in virus-immune co-evolution (36).

7.2.2 Finite size induced cross-over in antigenic evolution

Finite size effects arising from demographic stochasticity have long been included in intra-hosts (222) and inter-host models of viral evolution (223; 216; 36; 35). Similarly, the effects of cross-reactivity on viral antigenic evolution have been studied in intra-host models (224). However, no model yet has described the combined effect of demographic stochasticity and of varying the cross-reactivity on antigenic escape. In this section we investigate the modes of antigenic evolution as we vary the cross-reactivity. To do so, we propose a deterministic approximation to the full stochastic dynamics where we introduce a cut-off in the viral population growth rate when $n(x,t) < n_c$:

$$\partial_t n(x,t) = \left[\beta P_{\text{infect}}(x,t) - (\alpha+\gamma)\right] \Theta(n-n_c) n(x,t) + D\partial_x^2 n(x,t), \tag{7.6}$$

where Θ is a heaviside function and $R_0 = \beta/(\alpha+\gamma)$ is the basic reproduction ratio. In the context of antigenic evolution, the speed of antigenic evolution, the viral population size and the viral population diversity obtained from stochastic simulation are in agreement with the approximated cut-off theory (36).

We simulated by finite differences (see Methods) Eq. 7.6 and Eq. 7.2 on a one dimensional lattice and we find Fig. 7.1A a stable traveling wave solution moving ballistically with a constant population size N. In Fig. 7.1B we see that at small cross-reactivity, strains at the front of the wave are antigenically far enough from the bulk of the wave to experience a fully susceptible host population $P_{\text{infect}} \simeq 1$. When the cross-reactivity increases, the susceptibility of the host population to the most antigenically mutated strains decreases. In the limit of infinite cross-reactivity any immune receptor can recognize any

strain with equal probability. In this case, the model is equivalent to classical SI(R) models without antigenic evolution (57), and the susceptibility of the host population to any strain is the equilibrium one $P_{\text{infect}}(x,t) = R_0^{-1}$.

At small cross-reactivity, the host population is fully susceptible to the most antigenically mutated strains and the probability of infection is flat and equal to unity at the tip of the wave. This is the scenario of a FKPP wave where the fitness is maximum at the front of the wave (Fig. 7.1C), and the speed of the wave reads as (219; 225; 226):

$$v = 2\sqrt{(\beta - (\alpha+\gamma))D}\left(1 - \frac{\pi^2}{\ln^2 N}\right) \tag{7.7}$$

On the contrary, at large cross-reactivity the leading strains at the front of the wave experience a partially immunized host population, and a new antigenic variant has a fitness advantage over less mutated ones. In particular, in Fig. 7.1D the fitness landscape over the extent of the traveling wave becomes linear.

We can gain insight into this linear regime by assuming that the width of the traveling wave solution is negligeable with respect to the typical distance $v\tau$ over which the immune protection decays. The wave density can then be replaced in Eq. 7.5 by a Dirac delta function moving on the antigenic space at speed v. The immune density h and the receptor coverage c then simplify as:

$$h(x,t) \simeq \frac{1}{v\tau} \exp\left(-\frac{vt-x}{v\tau}\right) \Theta(vt-x), \tag{7.8}$$

$$c(x,t) \simeq \frac{e^{-(x-vt)/r_0}}{1+v\tau/r_0},\ x > vt, \tag{7.9}$$

where Θ denotes a heaviside function. Within this approximation, the fittest strains at a distance $u \ll v\tau$ feel a linearized fitness gradient s:

$$f(vt+u,t) = \beta\left(1 - c(vt+u,t)\right)^M - (\alpha+\gamma) \simeq f_0 + su, \tag{7.10}$$

where f_0 is the average viral population fitness and s the selection strength reads:

$$s = (\alpha+\gamma)\frac{M}{v\tau} \tag{7.11}$$

We expect the average fitness f_0 to be zero since the viral population is at steady state, which in turn constrains the value of $v\tau$ and the fitness gradient s:

$$v\tau = r_0\left(R_0^{1/M} - 1\right)^{-1}. \tag{7.12}$$

Importantly $s \sim r_0^{-1}$ such that as the cross-reactivity increases, receptors with increasingly remote antigenic positions can recognize the threat and the fitness gradient vanishes until the susceptibility of the host population to any antigenic variant reaches the equilibrium limit of the dotted line in Fig. 7.1. In this sense, increasing the cross-reactivity decreases the fitness advantage of strains at the tip of the wave: the immune pressure for new antigenic variant decreases and the wave slows down. Finally, in this linear fitness regime the dynamical equation governing the evolution of the traveling wave Eq. 7.6 can be

simplified:

$$\partial_t n(x,t) = s(x-vt)\Theta(n(x,t)-n_c)n(x,t) + D\partial_x^2 n(x,t). \tag{7.13}$$

This equation has been extensively studied in fitness wave theory (220; 221; 227) and the resulting speed of adaptation depends weekly on the viral population size. For our model Eq. 7.13, the speed of the wave reads as (see App. A.3.1):

$$v = 2(D^2 s)^{1/3}\left[\left(3\ln(\frac{N}{n_c}(s/D)^{1/3})\right)^{1/3} + \xi_0\left(3\ln(\frac{N}{n_c}(s/D)^{1/3})\right)^{-1/3}\right] \tag{7.14}$$

This equation along with Eq. 7.12 and the expression for s close the system of equations and entirely determine v and N. This construction tells us that the most antigenically mutated strains at the tip of the wave are at a distance $u_c \simeq v^2/(4Ds)$ from the bulk of the wave (see App. A.3.1).

Following the first observation from Fig. 7.1, as the cross-reactivity increases we expect the traveling wave to cross-over from a FKPP wave with speed Eq. 7.7 to a linear fitness wave with speed Eq. 7.14. In particular, in the large population size limit, we expect this cross-over between regimes to be scale invariant after rescaling $v \to v/r_0$ and $D \to D/r_0^2$. We verify this prediction by plotting the rescaled speed v/r_0 as a function of the antigenic escape rate D/r_0^2 for different values of D and r_0. The numerical results in Fig. 7.2B-C collapse on a single curve showing a cross-over between two distinct regimes as the cross-reactivity decreases. At small antigenic escape rate the viral population experiences a linear fitness profile and the speed (Fig. 7.2B) is predicted by Eq. 7.14, while at larger antigenic escape rate hosts are fully susceptible to the most antigenically mutated strains and the speed of evolution is given by Eq. 7.7. Similarly, at low escape rates the incidence rate (Fig. 7.2C) is predicted by Eq. 7.12 and Eq. 7.14, while it becomes larger and deviates from this prediction as the escape rate grows.

7.2.3 Invasion criteria and the evolution of viral strategies

In the previous section we identified the modes of viral evolution given the parameters of the eco-evolutionary process. We now address the more general question of predicting the evolutionary stable viral strategy. To do so, we will derive the conditions for a successful invasion of the viral population by a mutant with a different strategy (228; 229). This mutant has a viral strategy $(D_m, \alpha_m, \beta_m, \gamma_m)$, while the wild-type strain has a strategy $(D, \alpha, \beta, \gamma)$. Additionally, we consider that this mutant appears at negligible frequency with respect to the wild type. In the frame $u = x - vt$ moving with the wild type population at speed v, the mutant population obeys the equation:

$$\partial_t n_m = \left(v\partial_u + D_m\partial_u^2\right) n_m(u,t) + \left[\beta_m P_{\text{infect}}(u,t) - (\alpha_m + \gamma_m)\right]\Theta(n-n_c)n_m. \tag{7.15}$$

We are interested in establishing a criterion for this mutant population to invade the wild type population. In particular, we know that the wave is driven by its tip (39; 38), and that in order to invade the wild type population, a mutant must be able to proliferate at the tip of the wave. We will therefore treat the mutant growth at the tip of the wild type wave, and linearize Eq. 7.15 for each of the regimes described in the previous section.

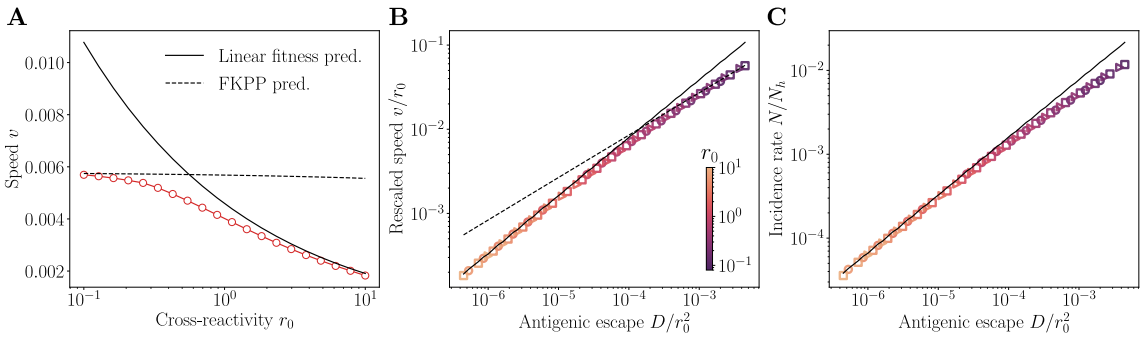

Figure 7.2: **Regimes of antigenic escape. A.** Speed of antigenic evolution v as a function of cross-reactivity r_0. At small r_0 the speed matches the FKPP prediction, Eq. 7.7, while at larger r_0 it matches the linear fitness prediction, Eq. 7.14. **B.** Rescaled speed v/r_0 as a function of the antigenic escape rate D/r_0^2. The points collapse on a single curve and match FKPP prediction at small r_0 while at larger r_0 they follow the linear fitness prediction. **C.** Incidence rate as a function of the dimensionless escape rate D/r_0^2. At large r_0 the incidence rate N/N_h is fully determined by Eq. 7.7, Eq. 7.11 and Eq. 7.12. In **B-C.** the antigenic escape rates are $D = 2 \cdot 10^{-5}$ (circle) $D = 4.5 \cdot 10^{-5}$ (square) and $D = 1 \cdot 10^{-4}$ (triangles >). The legend of **A** is consistent across all panels. Parameters values: $N_h = 10^{10}$, $M = 5$, $\beta_0 = 2$, $\gamma = 0.6$. For details about the simulations see Methods.

Evolutionary stable viral strategy in the FKPP regime

In the FKPP regime at small cross-reactivity, the fittest strains at the front of the wave experience a fully susceptible host population $P_{\text{infect}} \simeq 1$. In the co-moving frame, the mutant population at the tip of the wave obeys the following approximate equation:

$$\partial_t n_m = \left(v\partial_u + D_m\partial_u^2\right) n_m(u,t) + f_m\Theta(n - n_c)n_m, \tag{7.16}$$

$$\text{with } f_m = \beta_m - (\alpha_m + \gamma_m). \tag{7.17}$$

Importantly, f_m here is the growth rate of the mutant in a fully susceptible host population. Up to the tip of the wave u_c, this equation has a simple solution (see App. A.3.2), and the mutant population invades if and only if:

$$f_m > \frac{v^2}{4D_m}. \tag{7.18}$$

In particular, we see here that for a large enough viral population, the mutant can invade if and only if the steady-state speed of its own wave $v_m \simeq 2\sqrt{f_m D_m}$ is larger than that of the wild type. In other words, the evolutionary stable state of the viral population is reached when the speed of evolution is maximized.

Evolutionary stable strategy in the linear fitness regime

At large cross-reactivity, the fittest strains experience a linear gradient. The approximate equation for the mutant population of virulence α_m at the tip of the wave reads in

the co-moving frame:

$$\partial_t n_m = \left(v\partial_x + D_m\partial_x^2\right) n_m(x,t) + \left[\Delta f_m + s_m x\right]\Theta(n-n_c)n_m(x,t), \tag{7.19}$$

$$\text{with } \Delta f_m = \beta_m\left(\frac{1}{R_0} - \frac{1}{R_{0,m}}\right) \text{ and } s_m = \frac{\beta_m}{\beta}s. \tag{7.20}$$

where $R_0 = \beta/(\alpha+\gamma)$ and $R_{0,m} = \beta_m/(\alpha_m+\gamma_m)$ are respectively the reproduction ratio of the wild-type and of the mutant strain. Here Δf_m is the fitness advantage of the mutant population under the immune pressure exerted by a host population immunized by the wild-type. Similarly, s_m is the fitness gradient felt by the mutant strain under the immune pressure of a host population immunized by the wild type strain. Up to the tip of the wave u_c, this equation has a closed-form solution (see App. A.3.2), and the mutant invades if and only if:

$$s_m u_c + \Delta f_m > \frac{v^2}{4D_m}. \tag{7.21}$$

As the cross-reactivity increases, the fitness gradient decreases and the wave slows down. Asymptotically the antigenic evolution stops, and the remaining condition for the mutant to invade is to have a positive growth advantage with respect to the wild-type in a host population fully immunized by the wild-type, ie:

$$\Delta f_m = \beta_m\left(\frac{1}{R_0} - \frac{1}{R_{0,m}}\right) > 0. \tag{7.22}$$

As a consequence, the evolutionary stable state of the viral population is reached when the basic reproduction ratio is maximized.

We have here the central message of this work: the evolutionary stable viral strategy is dictated by a trade off between maximizing the speed of antigenic evolution when the cross-reactivity is small and maximizing the reproduction ratio as it becomes larger. The specific shape of this trade-off then depends on the ecological feedback between the trait evolving and the immune pressure exerted by the recovered hosts. To illustrate the applicability of our approach, we first investigate the evolution of virulence, and we later study the evolution of the mutation rate.

7.2.4 Evolutionary stable virulence

We now apply the general approach introduced before to predict the evolutionary stable virulence at fixed values of D and γ. In the absence of antigenic escape, the evolutionary stable viral strategy maximizes the reproduction ratio R_0 (56; 32), which at fixed values of β and γ is satisfied when the death rate of infected individuals $\alpha = 0$. To account for the observed non-zero virulence in real-life pathogens, it is assumed that strains with an increased transmissibility cause shorter infections (230; 65; 231). Biologically, this hypothesis comes from the idea that an increased viral load increases transmission but also host mortality. This constraint is mathematically described with a function $\beta(\alpha)$, with $\beta''(\alpha) < 0$. This concavity ensures the evolutionary stability of non-zero virulence in non-antigenically evolving pathogens (232). Following the previous section, we assume that the mutant has evolved a virulence very close to the wild type strain such that $\alpha_m = \alpha + \delta\alpha$ with $\delta\alpha \ll \alpha$.

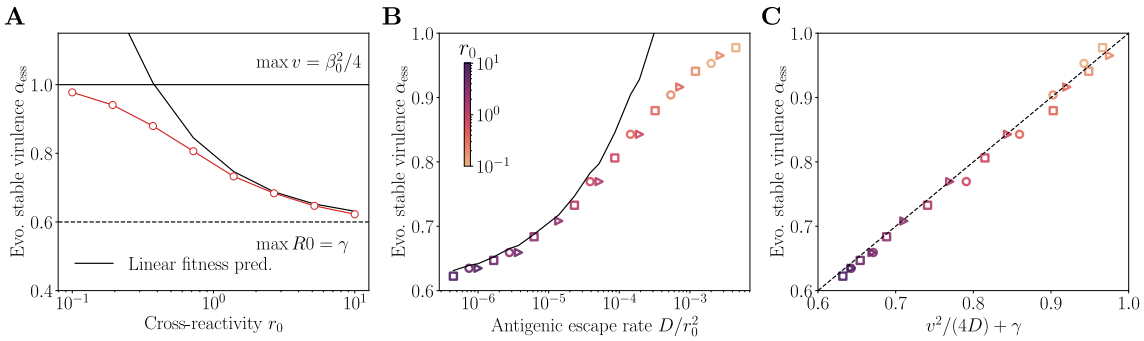

Figure 7.3: **Evolutionary stable virulence. A.** Evolutionary stable virulence α_{ess} as a function of cross-reactivity r_0 for $D = 4.5 \cdot 10^{-5}$. The simulated α_{ess} (circles, see Methods) is dictated by a trade-off between maximizing the speed of antigenic evolution v at small cross-reactivity and maximizing the reproduction ratio R_0 at large cross-reactivity. The dark line is the prediction from Eq. 7.28 using the speed in the linear fitness regime Eq. 7.14. **B.** Evolutionary stable virulence α_{ess} as a function of rescaled antigenic escape rate D/r_0^2 for different values r_0 and D. The points collapse on a single curve and we recover the trade-off described in **A** as r_0 is varied (colormap in inset). **C.** Prediction from Eq. 7.30 for different values of r_0 and D. The data points align with the identity line, confirming the validity of the relation. In **B-C.** the antigenic escape rates are $D = 2 \cdot 10^{-5}$ (circle) $D = 4.5 \cdot 10^{-5}$ (square) and $D = 1 \cdot 10^{-4}$ (triangles >). Parameters values: $N_h = 10^{10}$, $M = 5$, $\beta_0 = 2$, $\gamma = 0.6$. For details about the simulations see Methods.

At small cross-reactivity, the viral population is in the FKPP regime and the invasion criterion Eq. 7.18 reads as:

$$\beta(\alpha_m) - (\alpha_m + \gamma) > \frac{v^2}{4D} \tag{7.23}$$

Expanding it with respect to $\delta\alpha$ and making use of Eq. 7.7 in the large viral population size limit $(\beta - (\alpha + \gamma)) \simeq v^2/(4D)$ the criterion becomes:

$$\delta\alpha \left(\beta'(\alpha) - 1\right) > 0. \tag{7.24}$$

The fixed point of the dynamics reads:

$$\beta'(\alpha) = 1. \tag{7.25}$$

As $\beta'(\alpha)$ is a monotonically decreasing function this fixed point is stable and corresponds to the evolutionary stable strategy. We recover here the result derived in (37). This result is strictly equivalent to maximizing the FKPP speed of evolution Eq. 7.7.

When the cross-reactivity is large, the viral population is in the linear fitness regime and the invasion criterion Eq. 7.21 reads as:

$$\frac{\beta(\alpha_m)}{\beta(\alpha)} s u_c + \beta(\alpha_m) \frac{\alpha + \gamma}{\beta(\alpha)} - (\alpha_m + \gamma) > \frac{v^2}{4D}. \tag{7.26}$$

Again expanding it with respect to $\delta\alpha$ and using $su_c \simeq v^2/4D$ the criterion becomes:

$$\delta\alpha \frac{\beta'(\alpha)}{\beta(\alpha)} \left(\alpha + \gamma + v^2/4D - 1\right) > 0. \tag{7.27}$$

The fixed point of the dynamics then reads as:

$$\frac{\beta'(\alpha)}{\beta(\alpha)} \left(\alpha + \gamma + \frac{v^2}{4D}\right) = 1. \tag{7.28}$$

This result is original to this work and relates the speed of antigenic adaptation to the evolutionary stable virulence through the shape of the virulence-transmission trade-off. When $r_0 \to 0$, in the large viral population limit using Eq. 7.7 we recover the equation Eq. 7.28. On the contrary, when $r_0 \to \infty$, the fitness gradient $s \to 0$ and the evolutionary stable state satisfies:

$$\beta'(\alpha) = \frac{\beta(\alpha)}{\alpha + \gamma}. \tag{7.29}$$

This is equivalent to maximizing R_0 since $R_0'(\alpha) = (\beta'(\alpha)(\alpha + \gamma) - \beta(\alpha))/(\alpha + \gamma)^2$.

To verify this prediction, we extend our co-evolutionary framework to account for virulence evolution. We subject virulence to diffusion (see Methods) under a transmission-virulence trade-off $\beta(\alpha) = \beta_0\sqrt{\alpha}$. We simulate the evolution of virulence, and we verify in Fig. 7.3A that the evolutionary stable virulence maximizes v at small cross-reactivity and maximizes R_0 at large cross-reactivity. We verify with these observations that the fixed point of the dynamics Eq. 7.25 and Eq. 7.28 are stable and correspond to the evolutionary stable strategy of the viral population. The "linear fitness" prediction Eq. 7.28 (black line Fig. 7.3A-B) agrees remarkably well in a large range of cross-reactivities with the evolutionary stable virulence. With our choice of $\beta(\alpha)$ both Eq. 7.25 and Eq. 7.28 predict the following relation for the evolutionary stable virulence:

$$\alpha = \gamma + \frac{v^2}{4D}. \tag{7.30}$$

While we expect this relation to hold only in the linear fitness and FKPP regimes, we see in Fig. 7.2C. that the simulated evolutionary stable virulence collapses to the prediction of Eq. 7.30 along the entire cross-over and for various values of D and r_0.

7.2.5 Evolutionary stable mutation rate

The mutation rate is known to extensively vary across pathogens, with remarkably high values attained in RNA viruses (233; 62; 234; 235). A majority of mutations occuring in viruses do not affect either the virulence or the antigenic traits and generically decrease the intrinsic fitness of the strain (236; 237; 63; 238). The larger the total mutation rate the more these deleterious mutations accumulate and decrease the pathogen's infectivity. As a consequence, increasing this already very high mutational load can lead to extinction of the viral population and is a widely used antiviral strategy (64). Under this constraint, the optimal mutation rate maximizing the intra-host antigenic escape has already been investigated for pathogens causing chronic infections (239; 240). However, for pathogens causing acute infections like influenza, the role of inter-host dynamics is crucial and can't be ignored. In this section, using the arguments developed in Sec.7.2.3 we investigate

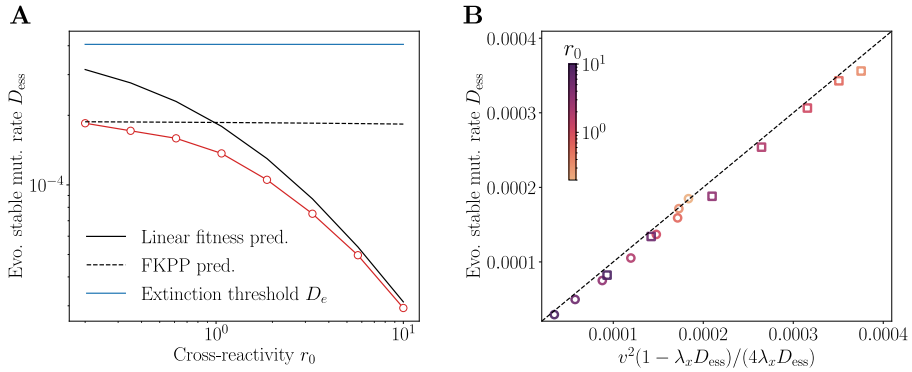

Figure 7.4: **Evolutionary stable mutation rate. A.** Evolutionary stable mutation rate D_{ess} as a function of cross-reactivity r_0. The simulated D_{ess} (circles, see Methods) matches the FKPP prediction (dashed line) at small cross-reactivity, and follows the linear fitness prediction at large cross-reactivity (dark line). The extinction threshold D_e is shown in blue. **B.** Prediction from Eq. 7.38 for different values of r_0 and λ_x. The simulated D_{ess} align with the idendity line, confirming the validity of the relation. The values of λ_x are $\lambda_x = 500$ (squares) and $\lambda_x = 1000$ (circles). Parameters values: $N_h = 10^{10}$, $M = 5$, $R_0 = 1.5$. For details about the simulations see Methods.

how inter-host immune pressure determines the evolutionary stable mutation rate of RNA viruses.

To account for deleterious mutations the effective reproduction ratio of the pathogen is recasted as $R = R_0 e^{-U_d}$ (63), where U_d denotes the rate of occurence of deleterious mutation. Introducing λ the ratio of deleterious to antigenic mutations we can rewrite it as:

$$R = R_0 e^{-\lambda U} \equiv R_0 e^{-\lambda_x D}, \tag{7.31}$$

where $\lambda_x = 2\lambda/\langle \delta x^2 \rangle$. We further assume that a change in the total mutation rate of the pathogen does not significatively change the ratio of deleterious to antigenic mutations. Finally, the evolution equation Eq. 7.6 for the density of infected individuals can be rewritten as:

$$\partial_t n(x,t) = (\alpha+\gamma)\left(R_0 e^{-\lambda_x D} P_{\text{infect}}(x,t) - n_c\right)\Theta(n-1)n(x,t) + D\partial_x^2 n(x,t). \tag{7.32}$$

In order to investigate the evolution of the mutation rate we decouple it from the virulence by assuming the latter is fixed and we set $\alpha + \gamma = 1$. Following the previous sections, we consider that a mutator mutant arise with a diffusion constant $D_m = D + \delta D$ and $\delta D \ll D$, and we analytically estimate the evolutionary stable mutation rate in both the FKPP and the linear fitness regimes.

At small cross-reactivity, the viral population is in the FKPP regime and the invasion criterion Eq. 7.18 reads as:

$$\left(R_0 e^{-\lambda_x D_m} - 1\right) > \frac{v^2}{4D_m}. \tag{7.33}$$

Expanding with respect to δD, and making use of Eq. 7.7 in the large viral population

size limit $R_0 e^{-\lambda_x D} - 1 \simeq v^2/(4D)$ the criterion becomes:

$$\delta D \left(v^2/(4D^2) - \lambda_x R_0 e^{-\lambda_x D} \right) > 0. \tag{7.34}$$

The fixed point of the dynamics is then:

$$v^2/(4D^2) - \lambda_x R_0 e^{-\lambda_x D} = 0. \tag{7.35}$$

In the large viral population size limit this result is equivalent to maximizing with respect to D the FKPP speed Eq. 7.7.

When the cross-reactivity is large, the viral population is in the linear fitness regime and the invasion criterion Eq. 7.21 reads as:

$$e^{-\lambda_x (D_m - D)} s u_c + \left(e^{-\lambda_x (D_m - D)} - 1 \right) > \frac{v^2}{4D}. \tag{7.36}$$

Expanding with respect to δD and using $s u_c \simeq v^2/(4D)$ we are left with:

$$\delta D \left(\frac{v^2}{4D^2} - \lambda_x \left(\frac{v^2}{4D} + 1 \right) \right) > 0. \tag{7.37}$$

The fixed point of the dynamics then reads as:

$$D = \frac{v^2}{4\lambda_x D} \left(1 - \lambda_x D \right). \tag{7.38}$$

Interestingly, Eq. 7.35 can be rewritten as Eq. 7.38, and in both regimes the evolutionary stable mutation rate obey the relation Eq. 7.38. To verify this prediction, we extend our co-evolutionary framework to account for the evolution of the mutation rate. We simulate the evolution of the mutation rate (see Methods) for different cross-reactivity values in Fig. 7.4. At small cross-reactivity in Fig. 7.4A, the evolutionary stable mutation rate maximizes the speed of evolution and is particularly close to the viral extinction threshold $D_e = \ln R_0/\lambda_x$ (237; 63), above which the reproduction ratio is smaller than unity. This result is reminiscent of previously derived evolutionary stable mutation rate for in-hosts dynamics of continuously evading pathogens (239). As the cross-reactivity increases in Fig. 7.4A the viral population crosses over to the linear fitness regime and the evolutionary stable mutation rate decreases. Asymptotically, as the cross-reactivity range increases, the viral population tends to maximize the reproduction ratio and the evolutionary stable mutation rate vanishes. We verify with these observations that the fixed point of the dynamics Eq. 7.35 and Eq. 7.38 are stable and correspond to the evolutionary stable strategy of the viral population. Finally, we see in Fig. 7.4C. that the simulated evolutionary stable mutation rate collapses on the prediction Eq. 7.38 along the entire cross-over and for various values of λ_x and r_0.

7.3. Conclusions

In this work we have developped an analytical co-evolution framework for studying the evolution of viral strategies in finite size viral population in response to immune pressure. Within this SI(R) inspired framework, we observed that the viral population

forms an antigenic wave escaping the ecological pressure resulting from immune memories elicited by past infections in the host population. We showed that, as the cross-reactivity of immune receptors increases, the selection for antigenic adaptation decreases and the antigenic wave crosses over from a FKPP regime to a linear fitness regime. In both regimes we derived general invasion conditions for the evolution viral strategies, and we showed that the evolutionary stable point of any viral strategy is shaped by a trade off between maximizing the speed of antigenic evolution when the cross-reactivity is small and maximizing the reproduction ratio as it becomes larger. Applied to the evolution of the virulence, this observation reconciles in one model results about virulence evolution of recent studies in presence of antigenic escape (37) and of classical studies about pathogens at endemic equilibrium (65; 57).

Our analysis further revealed the critical role played by strains showing the largest degree of antigenic variation in the population. Not only do they rule the antigenic evolution (39; 38), but we show that they also dictate the evolution of viral strategies. This observation has particularly interesting epidemiological consequences regarding the evolution of pathogenic virulence. According to our results, if the host population is almost fully susceptible to the most antigenically mutated variants, the pathogen is expected to evolve towards large transmission rates and virulence. On the contrary, when a large degree of cross-immunity exists between different variants, the virulence should rather reach intermediate levels maximizing the reproduction ratio. In this light, the level of cross-immunity between strains could potentially be used as a predictor for virulence evolution. As a consequence, a natural extension to our framework is to use it to investigate optimal control strategies limiting the evolution of more transmissible and virulent variants (241).

While it is clear that high levels of deleterious mutations are detrimental to the viral population, it remains debated whether high mutation rates in RNA viruses have been selected because they offer a mechanism of antigenic escape, or simply because they correlate with faster in-host replication speed (233; 234; 235). Our work provides a quantitative description of the first hypothesis by predicting the evolutionary stable mutation rate as a function of the speed of antigenic adaptation and the rate of deleterious to antigenic mutations. In particular, we observe that while mutation rates close to the extinction threshold are obtained at small cross-reactivity, the evolutionary stable mutation rate decreases as cross-reactivity increases.

Overall, our work offers a robust analytical framework to study the evolution of viral strategies in the context of antigenically escaping pathogens. It provides new theoretical insight into the eco-evolutionary feedbacks dictating the evolution of viral strategies, and can be used to study the evolution of any non-antigenic trait in antigenically evolving populations.

7.4. Methods

7.4.1 Simulations of viral immune co-evolution

In Sec. 7.2.2 we simulated Eq. 7.6 using a finite differences approximation. We choose a time step Δt, a mesh size Δx, and use Euler discretization for the first derivative and

Verlet discretization for the second derivative:

$$\frac{n(x,t+\Delta t)-n(x,t)}{\Delta t} = \left[\beta P_{\text{infect}}(x,t) - (\alpha+\gamma)\right]\Theta(n(x,t)-n_c)n(x,t) + D\frac{n(x+\Delta x,t)+n(x-\Delta x,t)-2n(x,t)}{\Delta x^2}. \tag{7.39}$$

We make sure that the Courant-Friedrich-Levy condition is verified $D\Delta t/\Delta x^2 < 1$. This condition simply requires that the time step is small enough to capture diffusion over a distance Δx. To compute $P_{\text{infect}}(x,t)$ we first solve Eq. 7.2 by finite differences using Euler discretization:

$$\frac{n_h(x,t+\Delta t)-n_h(x,t)}{\Delta t} = n(x,t) - \frac{N(t)}{MN_h}n_h(x,t), \tag{7.40}$$

and we compute the convolution Eq. 7.3 with a Fast Fourier Transform with periodic boundary conditions (242). We make sure that the antigenic space is large enough for the viral wave not to interact with the tail of immune memories when reaching the boundaries.

We chose $\Delta t = 0.04$ and $\Delta x = \min(fr_0, 0.18)$ for Fig. 7.1 and Fig. 7.2, with $f = 0.03$ for $D = 2\cdot 10^{-5}$, $f = 0.0625$ for $D = 4.5\cdot 10^{-5}$ and $f = 0.1$ for $D = 10^{-4}$. For Fig. 7.3 we chose $\Delta t = 0.04$ and $\Delta x = \min(fr_0, 0.2)$ for Fig. 7.1 and Fig.7.3, with $f = 0.04$ for $D = 2\cdot 10^{-5}$, $f = 0.07$ for $D = 4.5\cdot 10^{-5}$ and $f = 0.1$ for $D = 10^{-4}$. For Fig. 7.4 we chose $\Delta t = 0.06$ and $\Delta x = \min(0.05r_0, 0.02)$ for all values of λ_x.

7.4.2 Simulations of the evolutionary dynamics of viral strategies

We denote D_χ the diffusion constant of the viral parameter χ we investigate. In Sec. 7.2.4 this viral parameter is the virulence and in Sec. 7.2.5 it is the mutation rate D. Generically, the evolutionary dynamics of the viral strategy obey the following diffusion equation:

$$\partial_t n(x,\chi,t) = f(x,\chi,t)\Theta(n-n_c)n(x,\chi,t) + \left[D\partial_x^2 + D_\chi\partial_\chi^2\right]n(x,\chi,t) \tag{7.41}$$

We simulate this equation using a finite differences approximation. We choose a time step Δt, a mesh shize Δx and a parameter step size $\Delta\chi$. The finite difference equation reads:

$$\begin{aligned}\frac{n(x,\chi,t+\Delta t)-n(x,\chi,t)}{\Delta t} &= f(x,\chi,t)\Theta(n(x,\chi,t)-n_c)n(x,\chi,t)\\ &+ D\frac{n(x+\Delta x,\chi,t)+n(x-\Delta x,\chi,t)-2n(x,\chi,t)}{\Delta x^2}\\ &+ D_\chi\frac{n(x,\chi+\Delta\chi,t)+n(x,\chi-\Delta\chi,t)-2n(x,\chi,t)}{\Delta\chi^2}\end{aligned} \tag{7.42}$$

We make sure the Courant-Friedrich-Levy conditions are satisfied, and we implement the evolution of the immune memories as described in Method. 7.4.1. For Fig. 7.3 we took $D_\alpha = 2\cdot 10^{-6}$ and $\Delta\alpha = 0.012$. For Fig. 7.3, we assumed that the mutation rate evolves logarithmically and we took $D_{\ln D} = 2\cdot 10^{-6}$ and $\Delta\ln D = 0.037$.

8

Conclusions

8.1. Main contributions of this thesis

In the context of active matter, statistical-physics inspired models have been successfully applied to study the emergence of collective behaviour, but their connections to experimental data remains sparse. Recent evidence showed that the observed collective dynamics in flocks of European starlings are better described by inertial stochastic models for the birds' velocities (17; 18; 78) than by first order ones. Following this observation, the objective of the first part of this thesis was to advance towards a quantitative confrontation of these models by developing a Bayesian inference method for second order models of collective behaviour

To tackle this inference problem of reconstructing a continuous-time stochastic dynamical model from experimental discrete time series, an essential ingredient is to choose a discretization of the continuous-time dynamics. While doing so, it is often assumed that all the degrees of freedom of the continuous dynamics are measured independently by the experimental apparatus. However, in the case of partially observed dynamics, it has been observed that the choice of discretization is crucial, and that low order discretization schemes provide inconsistent estimators (46; 47). In chapter 4 we explained this observation by showing how the choice of discretization reflects the observability of the degrees of freedom of the dynamics. In particular, we demonstrated that Euler discretizations used to reconstruct fully observed first order dynamics provide inconsistent estimators when the dynamics are partially observed. We circumvented this difficulty by developing a novel inference scheme for second order stochastic dynamics based on a higher order discretization of the continuous-time equations. We were able to derive an analytical expression for the likelihood of partially observed trajectories, and obtained maximum-likelihood estimators consistent in the limit of infinitely long time series. Finally, we showed that not only does this method apply to equilibrium processes like Brownian particles in an anharmonic potential, but it also applies to non-equilibrium processes like stochastic harmonic oscillators with multiplicative noise.

Motivated by this success, we applied our method to the inertial spin model introduced to describe bird flocks. This model of collective behaviour constitutes a strongly interacting system of underdamped of Langevin equations, for which no inference scheme had yet been developed. By studying velocity fluctuations around the collective direction of motion we derived estimators consistent in the limit of long time series for all the parameters of the model. Notably, this showed that our inference scheme can be applied to non-equilibrium models of active matter with a large number of interacting agents. This work paves the way for this inference scheme to be applied to real recordings of flocks of starlings.

In the second part of this thesis we shifted our interest towards the immune system, a biological network of increased complexity. Contrarily to the assemblies of cells or animals studied in chapter 3–4, the immune system is composed of an uncountable number of

agents interacting across time and space at various scales. As a consequence, agent-based approaches are difficult to use to gain insight into the organization of the immune system. To tackle this challenge, the objective of the second part of this thesis was to develop a new approach using decision making theory to describe how the B cell subset of the immune system is organized to respond optimally to evolving pathogens.

To this end, in chapter 6 we modeled as a discrete-decision process the B-cell response elicited by sequential reinfections by an evolving pathogen. Within this framework, we investigated affinity maturation and backboosting strategies maximizing the long-term protection against future infections, and minimizing short-term resource costs due to the creation of new B-cell clones. We showed that optimal immune strategies are highly dependent on the antigenic divergence between infections. While for slow evolving pathogens the B-cell response generated by affinity maturation is monoclonal and specific to the infecting strain, for fast evolving pathogens the response is polyclonal with a diversity matching the pathogen typical antigenic divergence between subsequent infections. This last result suggests that the diversity of the memory pool constitutes a mechanism of anticipation of escape mutations, which is in agreement with the current consensus about the role of memory B cells (26; 25). Our model also predicted power-law distributed clone sizes in agreement with experimental sequencing data from healthy donors. Contrarily to other models of immune repertoire dynamics where clone-size diversity was generated by random non-correlated reinfections (167), in our model the main force driving it is the antigenic divergence between successive infections. Discriminating the different models is a promising idea for future research.

In a second time, we investigated how the efficiency of the extrafollicular response can limit the extent of affinity maturation and the production of new plasma and memory cells. To this end, we allowed affinity maturation to be modulated by the infection cost as a proxy of the speed of response. We showed that under this new strategy, the extrafollicular response inhibits affinity maturation as long as the existing memory cells respond fast enough, a phenomenon reminiscent of antigenic imprinting, or "original antigenic sin' (196; 29; 28; 30). Importantly, these results showed that antigenic imprinting emerges as a long term optimal strategy without requiring built-in negative feedbacks between the early response and affinity maturation.

In the last part of this thesis we studied how in return a population of hosts influences the fate of viral populations. To this end we used a SI(R) inspired approach to model the feedbacks from the host population on the viral evolution. This immune pressure not only drives the virus antigenic evolution of viral populations but also selects for the strain's mutation rate, transmission rate and virulence. The objective of this part of the thesis was to understand the properties of the evolutionary optimum reached by these viral strategies under the effect of immune pressure.

We first showed that the speed of antigenic escape is highly dependent on the degree of cross-reactivity of antibodies elicited by past infections. While for small cross-reactivity the host population is fully susceptible to the most antigenically advanced strains and the speed of antigenic evolution is maximum, as the cross-reactivity increases the susceptibility to the newest strains decreases and the antigenic evolution slows down. As a consequence of this cross-over, we then demonstrated how evolutionary stable viral strategies obey a trade off between maximizing the speed of antigenic evolution at small cross-reactivity and maximizing the basic reproduction ratio at large cross-reactivity. This result is general

and holds for the evolution of any non-antigenic trait.

To prove the applicability of this approach, we first applied it to study the evolution of virulence in antigenically evolving viral populations. Recent results showed that antigenic escape promotes larger transmissilibity and virulence than expected for non-evolving pathogens (37). Our approach refined this observation by reconciling both results: at small cross-reactivity antigenic escape promotes high virulence and transmissibility, but as cross-reactivity is increased the evolutionary stable virulence reaches the one predicted by models at endemic equilibrium. We believe that this result paves the way for predictors of the evolution of virulence to be built using the degree cross-immunity between strains. In a second time we applied our approach to study the evolution of the mutation rate in viruses causing acute infections. While we found that at low cross-reactivity the evolutionary stable mutation rate is close to the extinction threshold, we showed that an increased cross-reactivity (and thus a decreased selection for new antigenic variants) leads to more moderate mutation rates. Additionally we derived an analytical prediction for the evolutionary stable mutation rate linking the ecological pressure from the host population and the rate of deleterious to antigenic mutations. We believe that these results could be used to discriminate the different hypotheses justifying the emergence of particularly high mutation rates in RNA viruses (233; 234; 235).

8.2. Directions for future research

Applying inference on real recordings of flocks of starlings

In chapter 4 we developed a versatile inference approach for second order stochastic models. The natural prospect for this approach is to be applied to discrete time trajectories reconstructed from recordings of flocks of starlings. However, preliminary analysis revealed that, when applied to real data, the inference scheme is in the high noise regime described in Fig. 4.6, thereby compromising the retrieval of the stochastic information from the trajectories.

The analysis presented in Sec. 4.3.5 shows that estimators remain consistent in the limit of a measurement noise negligeable with respect to the stochastic contribution to infer. While the former is considered uncorrelated and independent of the acquisition rate, the latter depends on it through the choice of the discretization. Increasing the time step is an option to counteract the effect of measurement noise, as it increases the stochastic contribution to infer, but it also decreases the precision of the inference as it is accurate in the limit of small time steps. As a consequence, it is necessary to increase the inference scheme robustness to measurement noise before being able to apply it on data. To this end, a first approach is to exploit discretizations of the stochastic equations ensuring an efficient canceling of the measurement noise. This method is the one adopted by Frishman et al. (82), which were able to build noise robust estimators. However, the applicability of this idea to our specific scheme remains unclear, and it may come at the cost of the generality of our approach by being parameter dependent. A more pragmatic idea is to rewrite Eq. 4.35 for the noisy measurements, and learn the noise amplitude along with other parameters of the model. Preliminary work revealed that following this path an analytical formula for the likelihood can be obtained in the small noise limit. We can hope that taking into account measurement noise directly in the likelihood, along with model parameters to infer, will extend the applicability of our inference scheme to noisy

data.

Increasing the robustness of the inference approach presented in chapter 4 is an achievable, although cumbersome, task. We believe however that drastic improvements can be done without loosing the generality and applicability of the approach. This is a necessary step to take before being able to apply it on recordings of flocks of starlings.

Analyzing B-cell repertoire dynamics at level of functional families

The fundamental idea we developed in chapter 6 is that the main driver of the B-cells population dynamics is the frequency of reinfections and the mutation rate of pathogens. As hinted in chapter 5, this idea goes beyond usual B-cell population dynamics models that mostly ignore correlations between successive antigen exposures. To be able to go beyond our theoretical work and discriminate our predictions on the repertoire dynamics of memory B cell from previous models, a data-driven analysis of the population dynamics of B cells responding to specific antigens, or functional families, is necessary.

The clustering of T-cells in functional families has already profoundly changed the way we analyze the immune response, allowing for the identification of antigen-specific T-cells from single bulk repertoire snapshots (243). The construction of functional families in the T-cell repertoire relied on experimental evidence that antigen-specific T-cell pools differed by up to 4 amino acids in the CDR3 (244; 245; 246). Extending this approach to B cells is particularly challenging since the B-cell-to-peptide interaction is more complex than the T-cell-to-peptide one. Notably, B-cells CDR3s are significantly longer than T-cells CDR3s and their 3-dimensional structure is essential to the recognition of peptides. However, contrarily to T cells, B cells undergo affinity maturation, and thus can be clonally related through a common evolutionary history. As B cells of common ancestry are expected to share functionality, we can first leverage this information to cluster B-cell clonotypes into functional families. Their identification is enabled by genomic data itself, thus not requiring structural measurements a priori. The sequences statistics of these functional families can, in a second step, be reduced to a number of structural factors such as the Kidera factors to inform on the molecular specificity of the different families (247; 248). We believe that this ability is essential to dissect the immune response at the level of where it happens, rather than from bulk repertoire snapshots. To draw a parallel, a description of the B-cell repertoire at this level amounts to investigating it at a mesoscopic scale, where both structural and statistical effects matter.

Studying the B-cell repertoire at the level of functional families is an ambitious task, but we believe that it is a necessary step to elucidate the drivers of B-cell population dynamics, and in particular disentangle the role of viral evolution from factors intrinsic to the immune response.

Appendix

1.1. Building general Langevin models from discrete datasets

A.1.1 Discretization procedure

Let us briefly summarize two possible systematic strategies to obtain a discretized equation in the space of the x variables up to the desired $O(\Delta t^{3/2})$ order. Following (92), we can derive from (4.3) the associated GLE by formally solving the second equation of the system:

$$v(t) = \int_0^t ds\, e^{-\eta(t-s)} \left[f(x(s)) + \xi(s)\right] + v_0 e^{-\eta t}. \tag{A.1}$$

Plugging this expression back into the equation for x, we get a closed equation in x space:

$$\dot{x} = \int_0^t dsK(t-s)f(x(s)) + \zeta(t) + v_0 e^{-\eta t}, \tag{A.2}$$

where $K(t) = e^{-\eta t}$ and $\zeta(t) = \int_0^t dse^{-\eta(t-s)}\xi(s)$. Discrete update equations on the scale Δt can now be obtained by integrating (A.2) between t_n and t_{n+1} and between t_{n-1} and t_n. An exponentially decaying memory kernel propagates both the noise and the initial condition v_0 in (A.2); it is then possible to identify an appropriate reweighing of its integrated counterparts in order to get rid of both effects. Indeed the combination $x_{n+1} - x_n - e^{-\eta\Delta t}(x_n - x_{n-1})$ does not contain v_0 and has a short correlated effective noise:

$$x_{n+1} - x_n - e^{-\eta\Delta t}(x_n - x_{n-1}) = \frac{1 - e^{-\eta\Delta t}}{\eta} \int_{t_{n-1}}^{t_{n+1}} \Psi(t - t_n) f(x(t)) dt + \zeta_n \tag{A.3}$$

with

$$\zeta_n = \int_{t_{n-1}}^{t_{n+1}} \Psi(t - t_n)\xi(t)dt,$$

$$\Psi(t) = \frac{e^{\eta t} - e^{-\eta\Delta t}}{1 - e^{-\eta\Delta t}} \left[\theta(t + \Delta t) - \theta(t)\right] + \frac{1 - e^{\eta(t-\Delta t)}}{1 - e^{-\eta\Delta t}} \left[\theta(t) - \theta(\Delta t - t)\right] , \tag{A.4}$$

$\theta(t)$ being the Heaviside function. We can check that $\langle\zeta_n\zeta_m\rangle$ has the nearest neighbor structure of (4.26):

$$\langle\zeta_n\zeta_m\rangle = C_{nm} = a\delta_{n,m} + b\delta_{n,m\pm1}.$$

From (A.4) one deduces that, to order $O(\Delta t^3)$, the coefficients a and b of the covariance matrix assume the expression reported in (4.27).

So far, these equations are exact. Some approximation is needed at this stage to evaluate the integral of the force. Various methods have been investigated in the literature;

among the simplest is the Langevin Impulse method (49), which approximates the integral with the function at the midpoint, leading to

$$x_{n+1} = x_n + e^{-\eta\Delta t}(x_n - x_{n-1}) + \frac{1 - e^{-\eta\Delta t}}{\eta}\Delta t f(x_n) + \zeta_n. \tag{A.5}$$

Alternatively, taking the first order expansion of the force around the midpoint, $f(x(t)) \simeq f(x_n) + \frac{t-t_n}{\Delta t}\left[f(x_n) - f(x_{n-1})\right]$ in (A.3), one recovers the stochastic Verlet algorithm (111), which is one order more accurate than (A.5).

Another approach, followed in (48) (see also (249)), is to consider the full system of equations in the (x, v) phase space in integral form:

$$\begin{cases} x_{n+1} = x_n + \int_{t_n}^{t_{n+1}} v(t)dt \\ \\ v_{n+1} = v_n + \int_{t_n}^{t_{n+1}} f(x(t))dt + \int_{t_n}^{t_{n+1}} \xi(t)dt \end{cases} \tag{A.6}$$

and perform a second order Taylor-Itô expansion around the point t_n:

$$\begin{cases} x_{n+1} = x_n + v_n\Delta t + D_n \\ v_{n+1} = (1 - \eta\Delta t)v_n + \frac{1}{2}\Delta t\left[f(x_{n+1}) + f(x_n)\right] + \sigma\Delta t^{1/2}\xi_n - \eta D_n, \end{cases} \tag{A.7}$$

where D_n is defined as follows:

$$D_n = \frac{1}{2}\Delta t^2\left[f(x_n) - \eta v_n\right] + \sigma\Delta t^{3/2}\left[\frac{1}{2}\xi_n + \frac{1}{2\sqrt{3}}\theta_n\right] \tag{A.8}$$

and ξ_n and θ_n are i.i.d. Gaussian variables sampled from $\mathcal{N}(0, 1)$. Eliminating the velocity variables v_n and v_{n-1}, we find a difference equation of the form of (4.21):

$$\begin{aligned} x_{n+1} = 2x_n - x_{n-1} - \eta\Delta t\left(1 - \frac{\eta\Delta t}{2}\right)(x_n - x_{n-1}) \\ - \Delta t^2 f(x_n) + \frac{\eta\Delta t^3}{4}\left[f(x_n) - 3f(x_{n-1})\right] + \Delta t^{3/2}\zeta_n, \end{aligned} \tag{A.9}$$

with α and β coinciding, up to $O(\Delta t^2)$, to the Taylor expansion of the coefficients in (A.5). The noise variable ζ_n is defined from (A.7) as a linear combination of $\xi_n,\ \xi_{n-1},\ \theta_n,\ \theta_{n-1}$. As a result, due to overlapping Wiener processes, correlations between subsequent noise extractions emerge, which are still described by (4.26).

This second derivation is helpful in justifying the quasi-Toeplitz structure of the covariance matrix discussed in the main text. Indeed, fixing x_1 implies fixing the first random increment which is responsible for position update in the integration scheme (A.7), when the known initial conditions are (x_0, v_0). Since this stochastic increment enters into the definition of ζ_1 but not in that of ζ_2, the true covariance matrix must have a different entry C_{11} than the other elements on the main diagonal, as in (4.28).

A.1.2 Inference formulas

Naïve max-likelihood approaches for the harmonic oscillator

Several Euler-like schemes for the numerical integration of second order stochastic differential equations can be defined. From each of them, inconsistently retaining only the

diagonal $O(\Delta t^{3/2})$ stochastic terms when we write the update equations in x space, we can extract a factorized expression for the dynamical likelihood, such as (4.10).

Let us focus on three particular examples: the standard explicit Euler-Maruyama scheme (EM-fwd), its implicit variant (EM-bkd), and the symmetric BBK scheme (250). The three of them may be obtained from the second order SDE (4.1) by approximating first and second time derivatives adopting a forward, backward or symmetric prescription respectively. The resulting update equations in the three cases read:

$$\text{[EM-fwd]} \quad x_{n+1} - (2 - \eta\Delta t)x_n + (1 - \eta\Delta t + \omega_0^2\Delta t^2)x_{n-1} = \sigma\Delta t^{3/2} r_{n-1} \tag{A.10}$$

$$\text{[EM-bkd]} \quad (1 + \eta\Delta t)x_{n+1} - (2 + \eta\Delta t - \omega_0^2\Delta t^2)x_n + x_{n-1} = \sigma\Delta t^{3/2} r_{n+1} \tag{A.11}$$

$$\text{[BBK]} \quad \left(1 + \tfrac{\eta\Delta t}{2}\right) x_{n+1} - (2 - \omega_0^2\Delta t^2)x_n + \left(1 - \tfrac{\eta\Delta t}{2}\right) x_{n-1} = \sigma\Delta t^{3/2} r_n \tag{A.12}$$

with $\sigma = \sqrt{2T\eta}$ and $\{r_n\}$ a sequence of $L-1$ i.i.d. Gaussian random variables of null mean and unit variance.

Thanks to the independence of the random variables appearing in (A.10)–(A.12), the discrete propagator takes an approximate factorized form, which we can generally write as:

$$P_{(1)}(x_2, \ldots, x_L | x_0, x_1) = \prod_{n=1}^{L-1} \frac{1}{Z_n} e^{-S_n(x_{n+1}, x_n, x_{n-1})}. \tag{A.13}$$

The reduced minus-log likelihood, defined as

$$\frac{\mathcal{L}}{L-1} := \frac{-\ln P(x_2, \ldots, x_L | x_0, x_1)}{L-1}, \tag{A.14}$$

corresponds in the factorized case to the temporal average of the quantity $(S_n + \ln Z_n)$. This quantity is defined in a slightly different way in the three cases above; consequently, in each of these cases the reduced minus-log-likelihood will be slightly different, as reads in the following. We recall the notation used in the main text to indicate the equal-time, one-step and two-step experimental correlation functions:

$$C_s = \frac{1}{L-1}\sum_{n=1}^{L-1} x_n x_n; \; C'_s = \frac{1}{L-1}\sum_{n=1}^{L-1} x_{n+1} x_{n+1};$$
$$C''_s = \frac{1}{L-1}\sum_{n=1}^{L-1} x_{n-1} x_{n-1}; \; G_s = \frac{1}{L-1}\sum_{n=1}^{L-1} x_n x_{n+1};$$
$$G'_s = \frac{1}{L-1}\sum_{n=1}^{L-1} x_n x_{n-1}; \; F_s = \frac{1}{L-1}\sum_{n=1}^{L-1} x_{n-1} x_{n+1}.$$

$$\text{[EM-fwd]} \qquad \frac{\mathcal{L}}{L-1} = \frac{1}{2}\ln\left(4\pi T\eta\Delta t^3\right) + \frac{1}{4T\eta\Delta t^3}[C'_s + (2-\eta\Delta t^2)^2 C_s + (1-\eta\Delta t+\omega_0^2\Delta t^2)^2 C''_s - 2(2-\eta\Delta t)G_s + 2(1-\eta\Delta t+\omega_0^2\Delta t^2)F_s - 2(2-\eta\Delta t)(1-\eta\Delta t+\omega_0^2\Delta t^2)G'_s], \tag{A.15}$$

$$\text{[EM-bkd]} \qquad \frac{\mathcal{L}}{L-1} = \frac{1}{2}\ln\left(4\pi T\eta\Delta t^3\right) - \ln(1+\eta\Delta t) + \frac{1}{4T\eta\Delta t^3}[(1+\eta\Delta t)^2 C'_s + (2+\eta\Delta t-\omega_0^2\Delta t^2)^2 C_s + C''_s - 2(1+\eta\Delta t)(2+\eta\Delta t-\omega_0^2\Delta t^2)G_s + 2(1+\eta\Delta t)F_s - 2(2+\eta\Delta t-\omega_0^2\Delta t^2)G'_s], \tag{A.16}$$

$$\text{[BBK]} \qquad \frac{\mathcal{L}}{L-1} = \frac{1}{2}\ln\left(4\pi T\eta\Delta t^3\right) - \ln\left(1+\frac{\eta\Delta t}{2}\right) + \frac{1}{4T\eta\Delta t^3}[\,(1+\eta\Delta t/2)^2 C'_s + (2-\omega_0^2\Delta t^2)^2 C_s + (1-\eta\Delta t/2)^2 C''_s - 2(2-\omega_0^2\Delta t^2)(1+\eta\Delta t/2)G_s + 2(1+\eta\Delta t/2)(1-\eta\Delta t/2)F_s - 2(2-\omega_0^2\Delta t^2)(1-\eta\Delta t/2)G'_s]\,. \tag{A.17}$$

Minimization of (A.15)–(A.17) with respect to the parameters of the model yields the following optimal values, according to the adopted scheme:

◦ Euler-forward:

$$\eta^*_{fwd} = \frac{1}{\Delta t}\frac{G_s + G'_s - 2C_s + \frac{G'_s}{C''_s}(2G'_s - C''_s - F_s)}{-C_s + \frac{G'^2_s}{C''_s}}\,; \tag{A.18}$$

$$\omega_{0\,fwd}^{2*} = \frac{1}{\Delta t^2}\frac{(2-\eta\Delta t)G'_s - (1-\eta\Delta t)C''_s - F_s}{C''_s}\,; \tag{A.19}$$

$$T^*_{fwd} = \frac{1}{2\eta\Delta t^3}[C'_s + (2-\eta\Delta t^2)^2 C_s + (1-\eta\Delta t+\omega_0^2\Delta t^2)^2 C''_s - 2(2-\eta\Delta t)G_s + 2(1-\eta\Delta t+\omega_0^2\Delta t^2)F_s - 2(2-\eta\Delta t)(1-\eta\Delta t+\omega_0^2\Delta t^2)G'_s]\,; \tag{A.20}$$

◦ Euler-backward:

$$\eta^*_{bkd} = \frac{1}{\Delta t}\frac{C''_s + F_s - \frac{G'_s}{C_s}(G_s + G'_s)}{\frac{G_s G'_s}{C_s} - F_s}\,; \tag{A.21}$$

$$\omega_{0\,bkd}^{2*} = \frac{1}{\Delta t^2}\frac{(2+\eta\Delta t)C_s - G'_s - (1+\eta\Delta t)G_s}{C_s}\,; \tag{A.22}$$

$$T^*_{bkd} = \frac{1}{2\eta\Delta t^3}[(1+\eta\Delta t)^2 C'_s + (2+\eta\Delta t-\omega_0^2\Delta t^2)^2 C_s + C''_s - 2(1+\eta\Delta t)(2+\eta\Delta t-\omega_0^2\Delta t^2)G_s + 2(1+\eta\Delta t)F_s - 2(2+\eta\Delta t-\omega_0^2\Delta t^2)G'_s]\,; \tag{A.23}$$

◦ BBK:

$$\eta^*_{BBK} = \frac{2}{\Delta t}\frac{C_s'' + F_s - \frac{G_s'}{C_s}(G_s + G_s')}{C_s'' - F_s - \frac{G_s'}{C_s}(G_s' - G_s)} \; ; \tag{A.24}$$

$$\omega_0^{2*}{}_{BBK} = \frac{1}{\Delta t^2}\frac{2C_s - \left(1 + \frac{\eta\Delta t}{2}\right)G_s - \left(1 - \frac{\eta\Delta t}{2}\right)G_s'}{C_s} \; ; \tag{A.25}$$

$$\begin{aligned} T^*_{BBK} = & \frac{1}{2\eta\Delta t^3}[\,(1+\eta\Delta t/2)^2\, C_s' + (2-\omega_0^2\Delta t^2)^2 C_s + \\ & (1-\eta\Delta t/2)^2\, C_s'' - \\ & 2(2-\omega_0^2\Delta t^2)\,(1+\eta\Delta t/2)\, G_s + \\ & 2\,(1+\eta\Delta t/2)\,(1-\eta\Delta t/2)\, F_s - \\ & 2(2-\omega_0^2\Delta t^2)\,(1-\eta\Delta t/2)\, G_s'] \; . \end{aligned} \tag{A.26}$$

All of the schemes above are derived from numerical integrators with weak and strong convergence order $O(\Delta t)$, and consequently give a 2/3 rescaling factor for the inferred damping coefficient η^*. This can be checked using the procedure outlined to derive (4.15), which consists of replacing the experimental two-time quantities with the known correlation functions for the harmonic oscillator:

$$C(t) = \frac{T}{\omega_0^2} e^{-\gamma t}\left[\cos\left(\sqrt{\omega_0^2 - \gamma^2}t\right) + \gamma\frac{\sin(\sqrt{\omega_0^2-\gamma^2}t)}{\sqrt{\omega_0^2-\gamma^2}}\right], \tag{A.27}$$

where $\gamma = \eta/2$, and performing a Taylor expansion around the zero temporal distance. In the same way, the exactness of the inference formulas for T^* and ω_0^{2*} can be checked for the three methods.

Shift-invariant $O(\Delta t^{3/2})$ Bayesian approach

We argued that the joint probability of sequences of points in real space is not factorized into a chain of conditional probabilities. This happens because the dynamics of the harmonic oscillator, when projected into the x space, is governed by evolution equations containing a colored noise. The right scheme to adopt is then of the kind of (4.21): as discussed in the main text, this requires correlations between subsequently extracted random variables to be taken into account, resulting, in the case of additive noise, in a covariance matrix with a (quasi-)Toeplitz symmetric tridiagonal structure (cfr. (4.28) and (4.26)). We pursue a maximum likelihood approach taking as the function of the parameters of the model to maximize:

$$\begin{aligned} & P_{(2)}(x_L, \ldots, x_2 | x_1, x_0) = \frac{1}{Z}\exp \\ & -\frac{1}{2}\sum_{n,m=1}^{L-1}(x_{n+1} + F(x_n, x_{n-1}; \boldsymbol{\mu}))C^{-1}{}_{nm}(x_{m+1} + F(x_m, x_{m-1}; \boldsymbol{\mu})). \end{aligned} \tag{A.28}$$

The partition function is specified by (4.24) and (4.30), whereas the relation between $\boldsymbol{\mu}$ and the physical parameters of the dynamical model depends on the details of the discretization scheme which is adopted.

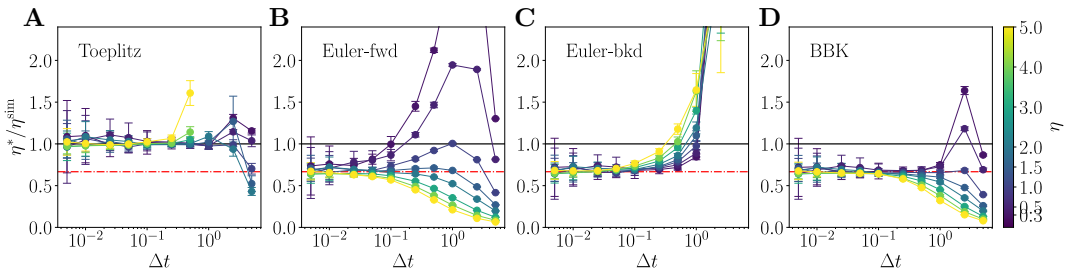

Figure S1: **Accuracy of the different likelihood-based methods for the harmonic oscillator.** Max-likelihood accuracy in inferring the damping coefficient of the harmonic oscillator, in varying damping regimes: **A.** shows the $O(\Delta t^{3/2})$ Toeplitz method; **B**–**D.** show the three $O(\Delta t^{1/2})$ variants corresponding, respectively, to the Euler forward, Euler backward and BBK schemes. The main features to highlight are the appearance of the 2/3 rescaling factor for the $O(\Delta t^{1/2})$ scheme (red dot-dashed line), compared to the absence of any rescaling for the $O(\Delta t^{3/2})$ scheme, and the higher stability of the latter with respect to Δt filtering. Different damping regimes are explored: the sampled values of $\eta^{\rm sim}$ are indicated in the colorbar. The remaining parameters are: $T = 1$, $\omega_0 = 1$. Each point is the average of the inference results of 10 different trajectories of 5000 points (for any Δt). Errorbars are taken as 0.95 CI.

Thanks to the peculiar structure of this likelihood, one can go pretty far with simple algebra in the optimization problem. First of all, it is convenient to reformulate the issue as a minimization problem for the minus log-likelihood:

$$\begin{aligned}\mathcal{L} = &\frac{L-1}{2}\ln\left(2\pi\frac{2}{3}T\eta\Delta t^3\right) + \frac{1}{2}\sum_{k=1}^{L-1}\ln\left(2+\cos\left(\frac{k\pi}{L}\right)\right)\\ &+\frac{3/2}{LT\eta\Delta t^3}\sum_{n,m=1}^{L-1}\Big[(x_{n+1}+F(x_n,x_{n-1};\boldsymbol{\mu}))\tilde{A}_{nm}(x_{m+1}+F(x_m,x_{m-1};\boldsymbol{\mu}))\Big],\end{aligned} \tag{A.29}$$

being

$$\tilde{A}_{nm} = \sum_{k=1}^{L-1}\frac{\sin\left(\frac{nk\pi}{L}\right)\sin\left(\frac{mk\pi}{L}\right)}{2+\cos\left(\frac{k\pi}{L}\right)}. \tag{A.30}$$

As usual, the temperature just appears as a prefactor for the effective action, without affecting its actual dynamical structure. The optimal value is given by:

$$T^* = \frac{3}{L(L-1)\eta\Delta t^3}\sum_{n,m=1}^{L-1}\Big[(x_{n+1}+F(x_n,x_{n-1};\boldsymbol{\mu}))\tilde{A}_{nm}(x_{m+1}+F(x_m,x_{m-1};\boldsymbol{\mu}))\Big]. \tag{A.31}$$

Replacing it into (A.29) and getting rid of additional constants, we obtain a reduced minus-log-likelihood:

$$\mathcal{L} \propto \frac{1}{L-1}\sum_{n,m=1}^{L-1}\sum_{k=1}^{L-1}\frac{\sin\left(\frac{nk\pi}{L}\right)\sin\left(\frac{mk\pi}{L}\right)}{2+\cos\left(\frac{k\pi}{L}\right)}(x_{n+1}+F(x_n,x_{n-1};\boldsymbol{\mu}))(x_{m+1}+F(x_m,x_{m-1};\boldsymbol{\mu})). \tag{A.32}$$

One can now split all the terms appearing in the sum and derive with respect to the effective parameters $\boldsymbol{\mu}$. Focusing on the case of the simple stochastic harmonic oscillator, $F(x_n, x_{n-1}; \boldsymbol{\mu}) = \alpha x_n + \beta x_{n-1}$, the set of effective parameter corresponds to $\boldsymbol{\mu} = (\alpha, \beta)$. By adopting the Langevin Impulse integrator (see App. A.1.1), they correspond to:

$$\begin{cases} \alpha = -1 - e^{-\eta\Delta t} + \omega_0^2 \Delta t \left(1 - e^{-\eta\Delta t}\right)/\eta \\ \beta = e^{-\eta\Delta t}. \end{cases} \tag{A.33}$$

By adopting a second order Taylor expansion around the prepoint, they correspond to:

$$\begin{cases} \alpha = -2 + \eta\Delta t \left(1 - \frac{\eta\Delta t}{2}\right) + \omega_0^2 \Delta t^2 \\ \beta = 1 - \eta\Delta t \left(1 - \frac{\eta\Delta t}{2}\right). \end{cases} \tag{A.34}$$

As required for them to be consistent, the two variants are equivalent up to $O(\Delta t^3)$. The numerical results shown in this paper are obtained using (A.33).

Imposing that the derivatives of $\mathcal{L}$ w.r.t. α and β are zero leads to:

$$\alpha^* = -\frac{T_1 + \beta^* T_3}{2T_4}\ ; \quad \beta^* = \frac{T_1 T_3 - 2T_2 T_4}{-T_3^2 + 4T_4 T_5}, \tag{A.35}$$

where, with implicit sum over the indexes n, m form 1 to $L-1$,

$$\begin{aligned} T_1 &= \frac{2}{L}\tilde{A}_{nm}\, x_n x_{m+1}\ ;\ T_2 = \frac{2}{L}\tilde{A}_{nm}\, x_{n-1} x_{m+1}\ ; \\ T_3 &= \frac{2}{L}\tilde{A}_{nm}\, x_{n-1} x_m\ ;\ T_4 = \frac{1}{L}\tilde{A}_{nm}\, x_n x_m\ ; \\ T_5 &= \frac{1}{L}\tilde{A}_{nm}\, x_{n-1} x_{m-1}\ . \end{aligned} \tag{A.36}$$

This procedure can be applied to find explicit formulas for any non-interacting system described by a Kramers process with velocity-independent forces $f(x)$, as in (4.1). We report here those we derived and used for the anharmonic model with force $f(x) = -kx - \lambda x^3$. Referring again to the Langevin Impulse integrator, one possible set of independent parameters is given by $\boldsymbol{\mu} = (\beta, K, \Lambda)$, where $\beta = e^{-\eta\Delta t}$, $K = k\Delta t/\eta$, $\Lambda = \lambda\Delta t/\eta$. The Toeplitz inference formulas for those parameters read:

$$\begin{aligned} \beta^* =& \left[P_5 - \frac{P_6 P_8}{P_2} - \frac{(P_2P_9 - P_3P_8)(P_2P_7 - P_3P_6)}{P_2(P_2P_4 - P_3^2)}\right] \\ & \cdot \left[P_1 - \frac{P_6^2}{P_2} - \frac{(P_2P_7 - P_3P_6)^2}{P_2(P_2P_4 - P_3^2)}\right]^{-1}\ ; \end{aligned} \tag{A.37}$$

$$\Lambda^* = \frac{\beta^*(P_2P_7 - P_3P_6) - (P_2P_9 - P_3P_8)}{(1-\beta^*)(P_2P_4 - P_3^2)}\ ; \tag{A.38}$$

$$K^* = \frac{\beta^* P_6 - P_8}{(1-\beta^*)P_2} - \Lambda^* \frac{P_3}{P_2}\ ; \tag{A.39}$$

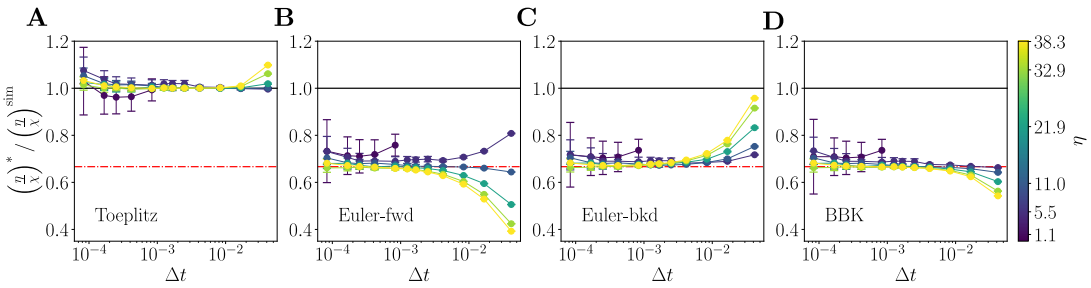

Figure S2: **Accuracy of the different likelihood-based methods for the ISM.** Max-likelihood accuracy in inferring the effective parameter η/χ of the inertial spin model: **A.** shows the $O(\Delta t^{3/2})$ Toeplitz method; **B**–**D.** show the three $O(\Delta t^{1/2})$ variants corresponding, respectively, to the Euler forward, Euler backward and BBK schemes. We see the 2/3 factor for the $O(\Delta t^{1/2})$ schemes (red dot-dashed line), and no rescaling for the $O(\Delta t^{3/2})$ scheme. ISM simulations are performed in different damping regimes: the sampled values for the parameter $\eta^{\rm sim}$ are indicated along the colorbar. The remaining parameters are: $\chi = 1$, $T = 0.4$, $J = 5.0$, $n_c = 6$, $N = 1000$. Each point is the average of the inference results of 10 different trajectories of 200 points (for any Δt). Errorbars correspond to 0.95 CI.

where

$$
\begin{aligned}
&P_1 = (x_n - x_{n-1})\tilde{A}_{nm}(x_m - x_{m-1})\ ;\\
&P_2 = x_n\tilde{A}_{nm}x_m\ ;\ P_3 = x_n\tilde{A}_{nm}x_m^3\ ;\ P_4 = x_n^3\tilde{A}_{nm}x_m^3\ ;\\
&P_5 = (x_n - x_{n-1})\tilde{A}_{nm}(x_{m+1} - x_m)\ ;\\
&P_6 = (x_n - x_{n-1})\tilde{A}_{nm}x_m\ ;\ P_7 = (x_n - x_{n-1})\tilde{A}_{nm}x_m^3\ ;\\
&P_8 = (x_{n+1} - x_n)\tilde{A}_{nm}x_m\ ;\ P_9 = (x_{n+1} - x_n)\tilde{A}_{nm}x_m^3\ .
\end{aligned}
\tag{A.40}
$$

From these equations, the max-likelihood estimators for the physical parameters λ^*, k^* and η^* can be found.

Generalization to the interacting case (ISM)

As one moves from single to many particle systems, extra parameters are needed: position and velocity variables are conveniently represented as N-component vectors, N being the number of constituents of the group, and model parameters become matrices. For the equations of motion of the three-dimensional ISM on a fixed lattice in the spin-wave approximation (4.41), the update rule becomes:

$$\boldsymbol{\zeta}_n^i = \boldsymbol{\pi}_{n+1}^i + \alpha^{ij}\boldsymbol{\pi}_{nj} + \beta^{ij}\boldsymbol{\pi}_{n-1j}, \tag{A.41}$$

with

$$\alpha^{ij} = \alpha^0\delta^{ij} + \alpha^1\Lambda^{ij} \text{ and } \beta^{ij} = \beta\delta^{ij},$$

where Λ^{ij} is the discrete Laplacian, and sums over the j index are implicit.

The definitions of α^0, α^1 and β depend on the details of the discretization. Using, for

instance, the Langevin impulse integrator (LI),

$$\left(\frac{\eta}{\chi}\right)^*_{LI} = -\frac{\ln\beta^*}{\Delta t}\ ; \quad \left(\frac{J}{\chi}\right)^*_{LI} = -\frac{\ln\beta^*}{1-\beta^*}\frac{\alpha^*}{\Delta t^2}\ . \tag{A.42}$$

Using instead a second order Taylor expansion, we get:

$$\left(\frac{\eta}{\chi}\right)^*_{IIT} = \frac{1-\sqrt{2\beta^*-1}}{\Delta t}\ ; \quad \left(\frac{J}{\chi}\right)^*_{IIT} = \frac{\alpha^*}{\Delta t^2}\ . \tag{A.43}$$

The three parameters α^0, α^1 and β are not independent, since the extra independent parameters of the interacting problem are hidden in the adjacency matrix. In both of the cases considered above ((A.43) and (A.42)), α^0 and β are linked by the same relation: $\alpha^0 = -\beta - 1$. Renaming $\alpha^1 = \alpha$, the minus-log-likelihood reads:

$$\begin{aligned}\mathcal{L} = {} & \frac{(L-1)(d-1)}{2}\ln\left(\frac{T\eta}{\chi^2}\Delta t^3\right) + \text{const} \\ & + \frac{3/2}{L\frac{T\eta}{\chi^2}\Delta t^3}\sum_{n,m=1}^{L-1}\frac{1}{N}\sum_{i=1}^{N}\tilde{A}_{nm}\left[\boldsymbol{\pi}^i_{n+1} - \boldsymbol{\pi}^i_n - \beta(\boldsymbol{\pi}^i_n - \boldsymbol{\pi}^i_{n-1}) + \alpha\Lambda^{ij}\boldsymbol{\pi}_{nj}\right] \\ & \cdot\left[\boldsymbol{\pi}^i_{m+1} - \boldsymbol{\pi}^m_i - \beta(\boldsymbol{\pi}^i_m - \boldsymbol{\pi}^i_{m-1}) + \alpha\Lambda^{il}\boldsymbol{\pi}_{ml}\right].\end{aligned} \tag{A.44}$$

Again, one can proceed with an analytic minimization with respect to T, α and β, giving:

$$\alpha^* = \frac{\beta K_4 - K_3}{2K_5}\ ; \tag{A.45}$$

$$\beta^* = \frac{-K_3K_4 + 2K_1K_5}{-K_4^2 + 4K_2K_5}\ ; \tag{A.46}$$

$$T^* = \frac{3}{(d-1)\,(\eta/\chi)^*\,\Delta t^3}\left[K_0 - \beta^*K_1 + \beta^{*2}K_2 + \alpha^*K_3 - \alpha^*\beta^*K_4 + \alpha^{*2}K_5\right]\ , \tag{A.47}$$

with $K_0 \ldots K_5$ the generalization to the many-particle case of the combinations of experimental observables $T_1, \ldots, T_5$ defined above (again with implicit sums over n, m):

$$
\begin{aligned}
K_0 &= \frac{1}{N}\sum_{i=1}^{N}\frac{\tilde{A}_{nm}}{L(L-1)}(\boldsymbol{\pi}^i_{n+1}-\boldsymbol{\pi}^i_n)\cdot(\boldsymbol{\pi}^i_{m+1}-\boldsymbol{\pi}^i_m)\ ;\\
K_1 &= \frac{2}{N}\sum_{i=1}^{N}\frac{\tilde{A}_{nm}}{L(L-1)}(\boldsymbol{\pi}^i_{n+1}-\boldsymbol{\pi}^i_n)\cdot(\boldsymbol{\pi}^i_{m}-\boldsymbol{\pi}^i_{m-1})\ ;\\
K_2 &= \frac{1}{N}\sum_{i=1}^{N}\frac{\tilde{A}_{nm}}{L(L-1)}(\boldsymbol{\pi}^i_{n}-\boldsymbol{\pi}^i_{n-1})\cdot(\boldsymbol{\pi}^i_{m}-\boldsymbol{\pi}^i_{m-1})\ ;\\
K_3 &= \frac{2}{N}\sum_{i,j=1}^{N}\frac{\tilde{A}_{nm}}{L(L-1)}\Lambda^{ij}(\boldsymbol{\pi}^i_{n+1}-\boldsymbol{\pi}^i_n)\cdot\boldsymbol{\pi}^j_m\ ;\\
K_4 &= \frac{2}{N}\sum_{i,j=1}^{N}\frac{\tilde{A}_{nm}}{L(L-1)}\Lambda^{ij}(\boldsymbol{\pi}^i_{n}-\boldsymbol{\pi}^i_{n-1})\cdot\boldsymbol{\pi}^j_m\ ;\\
K_5 &= \frac{1}{N}\sum_{i=1}^{N}\frac{\tilde{A}_{nm}}{L(L-1)}\Lambda^{ij}\Lambda^{il}\boldsymbol{\pi}^j_n\cdot\boldsymbol{\pi}^l_m\ .
\end{aligned}
$$

Generalization to the multiplicative case

From (4.33) – (4.34), which define the discrete update rule for the multiplicative process described by (4.32), one can derive max-likelihood estimators for the parameters of the model by minimizing the effective cost function in (4.36). Let us carry on this explicitly for the following reference example:

$$\ddot{x} = -\eta v - kx + \sqrt{a+bx^2}\xi, \tag{A.48}$$

such that the quantities appearing in (4.36) read:

$$F(x_n, x_{n-1};\boldsymbol{\mu}) = x_n - e^{-\eta\Delta t}(x_n - x_{n-1}) + (1-e^{-\eta\Delta t})\frac{k\Delta t}{\eta}x_n, \tag{A.49}$$

with $\boldsymbol{\mu} = \left(e^{-\eta\Delta t}, k\Delta t/\eta\right)$ and

$$C_{nm} = \left(a+bx_n^2\right)\delta_{n,m} + \sqrt{\left(a+bx_n^2\right)\left(a+bx_m^2\right)}\delta_{n,m\pm1}. \tag{A.50}$$

Simple manipulations allow us to reduce to the minimization problem to a one-dimensional numerical optimization, since analytical formulas for the optimal values of the effective parameters $\beta = e^{-\eta\Delta t}$, $K = k\Delta t/\eta$ and b can easily be found:

$$
\begin{aligned}
b^* &= \frac{3}{L-1}\left[P_0 - \frac{P_4^2}{P_2} - \frac{\left(P_3P_2 - P_4P_5\right)\left(P_3P_2-P_4P_5\right)}{P_1P_2-P_5^2}\right];\\
\beta^* &= \frac{P_3^*P_2^* - P_4^*P_5^*}{P_1^*P_2^* - (P_5^*)^2}; \qquad K^* = \frac{\beta^*P_5^* - P_4^*}{(1-\beta^*)P_2^*}\ .
\end{aligned}
\tag{A.51}
$$

where we renamed $\alpha = a/b$ and $P_i^* = P_i(\alpha^*)$. The optimal value of the new effective parameter α^* is the minimizer of the following function of α:

$$\mathcal{L} = \frac{1}{L-1}\sum_{k=1}^{L-1}\ln\tilde{\lambda}_k + \ln\left[P_0 - \frac{P_4^2}{P_2} - \frac{\left(P_3P_2 - P_4P_5\right)\left(P_3P_2-P_4P_5\right)}{P_1P_2-P_5^2}\right], \tag{A.52}$$

where $\{\tilde{\lambda}_k\}$ is the set of eigevnvalues of the reduced covariance matrix

$$\begin{aligned} {A^{-1}}_{nm} &= 3C_{nm}/(b\Delta t^3) \\ &= 2\left(\alpha + x_n^2\right)\delta_{n,m} + \frac{1}{2}\sqrt{(\alpha + x_n^2)\,(\alpha + x_m^2)}\delta_{n,m\pm 1}\,, \end{aligned} \tag{A.53}$$

and

$$\begin{aligned} P_0 &= \frac{1}{L-1}\sum_{n,m=1}^{L-1}(x_{n+1}-x_n)A_{nm}(x_{m+1}-x_m)\;; \\ P_1 &= \frac{1}{L-1}\sum_{n,m=1}^{L-1}(x_n-x_{n-1})A_{nm}(x_m-x_{m-1})\;; \\ P_2 &= \frac{1}{L-1}\sum_{n,m=1}^{L-1}x_nA_{nm}x_m\;; \\ P_3 &= \frac{1}{L-1}\sum_{n,m=1}^{L-1}(x_{n+1}-x_n)A_{nm}(x_m-x_{m-1})\;; \\ P_4 &= \frac{1}{L-1}\sum_{n,m=1}^{L-1}(x_{n+1}-x_n)A_{nm}x_m\;; \\ P_5 &= \frac{1}{L-1}\sum_{n,m=1}^{L-1}(x_n-x_{n-1})A_{nm}x_m\;. \end{aligned}$$

Non-Bayesian approach: inference formulas without a likelihood

We build in this section an alternative approach to the Bayesian one, as outlined in Section 4.3.2 of the main text. To be explicit, we need to choose a discrete update equation in x space: let us choose again the one corresponding to the usual continuation rule of the LI:

$$x_{n+1} = x_n + e^{-\eta\Delta t}(x_n - x_{n-1}) + \frac{1-e^{-\eta\Delta t}}{\eta}\omega_0^2\Delta t\, x_n + \zeta_n, \tag{A.54}$$

and multiply its r.h.s. and l.h.s. by x_n, x_{n+1} and x_{n-1} and take the average over the noise distribution. The resulting equations are:

$$\begin{aligned} \langle x_{n+1}x_n\rangle &= \langle {x_n}^2\rangle + e^{-\eta\Delta t}(\langle {x_n}^2\rangle - \langle x_nx_{n-1}\rangle) \\ &\quad + \frac{1-e^{-\eta\Delta t}}{\eta}\omega_0^2\Delta t\langle {x_n}^2\rangle + \langle x_n\zeta_n\rangle\;; \end{aligned} \tag{A.55}$$

$$\begin{aligned} \langle x_{n+1}x_{n+1}\rangle &= \langle x_nx_{n+1}\rangle + e^{-\eta\Delta t}(\langle x_nx_{n+1}\rangle - \langle x_{n-1}x_{n+1}\rangle) \\ &\quad + \frac{1-e^{-\eta\Delta t}}{\eta}\omega_0^2\Delta t\langle x_nx_{n+1}\rangle + \langle \zeta_nx_{n+1}\rangle\;; \end{aligned} \tag{A.56}$$

$$\begin{aligned} \langle x_{n+1}x_{n-1}\rangle &= \langle x_nx_{n-1}\rangle + e^{-\eta\Delta t}(\langle x_nx_{n-1}\rangle - \langle x_{n-1}^2\rangle) \\ &\quad + \frac{1-e^{-\eta\Delta t}}{\eta}\omega_0^2\Delta t\langle x_nx_{n-1}\rangle\;. \end{aligned} \tag{A.57}$$

Using again (A.54) – combined with the covariance matrix of the Gaussian variables – to compute $\langle\zeta_nx_n\rangle$ and $\langle\zeta_nx_{n+1}\rangle$, the relations we find are:

$$G_s = C_s + e^{-\eta\Delta t}(C_s - G'_s) + \frac{1 - e^{-\eta\Delta t}}{\eta}\omega_0^2 \Delta t\, C_s + b\ ; \tag{A.58}$$

$$C'_s = G_s + b + a + e^{-\eta\Delta t}(G_s - F_s + b) + \frac{1 - e^{-\eta\Delta t}}{\eta}\omega_0^2 \Delta t (G_s + b)\ ; \tag{A.59}$$

$$F_s = G'_s + e^{-\eta\Delta t}(G'_s - C''_s) + \frac{1 - e^{-\eta\Delta t}}{\eta}\omega_0^2 \Delta t\, G'_s\ . \tag{A.60}$$

In order to find (A.58)–(A.60), we identified the actual correlation functions with the empirical ones, denoted with C, G and F symbols, and we hypothesized a stationarity assumption to hold to explicitly compute them. After proper manipulation, one can extract "inference relations" for b, $e^{-\eta\Delta t}$ and $\omega_0^2\Delta t$, and derive from them the physical parameters of the model. In order, $e^{-\eta\Delta t}$ is given as the solution of the second-degree polynomial equation:

$$\begin{aligned}&(2G'_s - C_s - C''_s)e^{-2\eta\Delta t} + \left[2G_s + C''_s - C_s - 2F_s + 5(2G'_s - C_s - C''_s)\right] e^{-\eta\Delta t} \\ &+ \left[G_s - G'_s + F_s - C'_s + 5(G'_s - C_s - F_s + G_s)\right] = 0;\end{aligned} \tag{A.61}$$

then b and $\omega_0^2\Delta t$ are computed as follows:

$$b = G'_s - F_s + G_s - C_s + e^{-\eta\Delta t}\left(2G'_s - C''_s - C_s\right)\ ; \tag{A.62}$$

$$\omega_0^2\Delta t = \frac{-\eta}{1 - e^{-\eta\Delta t}}\left[\frac{G_s - C_s - b}{C_s} - e^{-\eta\Delta t}\frac{C_s - G'_s}{C_s}\right]\ . \tag{A.63}$$

Notice that these inference equations are not unique. Combining the starting equations in a different way would result into slightly different inference formulas, which, however, should provide the same result if the experimental correlation functions faithfully reproduce ensemble averages at the steady state.

This strategy cannot be adapted to interacting problems, outside of the mean field approximation. The obstacle comes from the parametrization of the interaction matrix, which is the discrete counterpart of the introducing an interaction range in the corresponding field theory. Without a priori parametrization, the issue of sufficient statistics arises: one can think about repeating the same procedure in the multi-particle case for each particle pair and look for independent inference formulas for any matrix element $J\Lambda^{ij}$. Bypassing the technical difficulties related to solving the resulting system of N^2+2 second degree equations for the unknowns b, $e^{-\eta\Delta t}$ and $\{J\Lambda^{ij}\}_{i,j=1\dots N}$, we have a much greater number of parameters to infer than of points in each frame. This problem becomes totally untractable if one also allows Λ^{ij} to evolve in time, as in active animal groups (251; 88).

Assumptions about the structure of the matrix Λ_{ij} dramatically diminish the number of parameters and help us deal with the worry of insufficient statistics, but require an alternative strategy to estimate the interaction range, since this physically motivated parametrization does not allow us to find closed-form equations.

It is possible yet to approximately estimate the damping coefficient and the effective temperature of the system of interacting particles, assuming that they are all immersed in the same uniform thermal bath. Under this assumption, (A.55)–(A.57) can be adapted to the interacting case and properly manipulated to find the following relations:

$$F_s - G'_s - G_s + C_s = e^{-\frac{\eta}{\chi}\Delta t}\left(2G'_s - C''_s - C_s\right) + \frac{G'_{int} - C_{int}}{C_{int}}\left[G_s - C_s - b - e^{-\frac{\eta}{\chi}\Delta t}(C_s - G'_s)\right] - b\,; \tag{A.64}$$

$$C'_s - 2G_s + C_s = e^{-\frac{\eta}{\chi}\Delta t}\left(G_s - F_s - C_s + G'_s\right) + b\left\{4 + e^{-\frac{\eta}{\chi}\Delta t} + \frac{n_c}{C_{int}}\left[G_s - C_s - b - e^{-\frac{\eta}{\chi}\Delta t}(C_s - G'_s)\right]\right\} + \frac{G_{int} - C_{int}}{C_{int}}\left[G_s - C_s - b - e^{-\frac{\eta}{\chi}\Delta t}(C_s - G'_s)\right]\,; \tag{A.65}$$

where we have used the third independent equation to eliminate J/χ and exploited the fact that $a = 4b$, with $b = \frac{1}{6}2\frac{T\eta}{\chi^2}\Delta t^3$. Let us define the empirical spatio-temporal correlation functions involved in these inference formulas:

- Equal-time correlations:

$$C_{ij} = \frac{1}{L-1}\sum_{n=1}^{L-1} \boldsymbol{\pi}_n^i \cdot \boldsymbol{\pi}_n^j\,; \tag{A.66}$$

$$C'_{ij} = \frac{1}{L-1}\sum_{n=1}^{L-1} \boldsymbol{\pi}_{n+1}^i \cdot \boldsymbol{\pi}_{n+1}^j\,; \tag{A.67}$$

$$C''_{ij} = \frac{1}{L-1}\sum_{n=1}^{L-1} \boldsymbol{\pi}_{n-1}^i \cdot \boldsymbol{\pi}_{n-1}^j\,; \tag{A.68}$$

- One-step correlations:

$$G_{ij} = \frac{1}{L-1}\sum_{n=1}^{L-1} \boldsymbol{\pi}_{n+1}^i \cdot \boldsymbol{\pi}_n^j\,; \tag{A.69}$$

$$G'_{ij} = \frac{1}{L-1}\sum_{n=1}^{L-1} \boldsymbol{\pi}_n^i \cdot \boldsymbol{\pi}_{n-1}^j\,; \tag{A.70}$$

- Two-step correlations:

$$F_{ij} = \frac{1}{L-1}\sum_{n=1}^{L-1} \boldsymbol{\pi}_{n+1}^i \cdot \boldsymbol{\pi}_{n-1}^j\,. \tag{A.71}$$

The observables appearing in (A.64)–(A.65) are defined from (A.66)–(A.71) as in the following. We can distinguish the contribution of self-correlations, encoded by:

$$C_s = \frac{1}{N}\operatorname{Tr}\mathbf{C} \quad ;\; C'_s = \tfrac{1}{N}\operatorname{Tr}\mathbf{C}' \quad ;\; C''_s = \frac{1}{N}\operatorname{Tr}\mathbf{C}''\,;$$
$$G_s = \frac{1}{N}\operatorname{Tr}\mathbf{G} \quad ;\; G'_s = \tfrac{1}{N}\operatorname{Tr}\mathbf{G}' \quad ;\; F_s = \frac{1}{N}\operatorname{Tr}\mathbf{F}\,;$$

and that of correlations between directly interacting birds, encoded by the quantities:

$$C_{int} = \frac{\operatorname{Tr}(\boldsymbol{\Lambda}\mathbf{C})}{N}\,;\; G_{int} = \frac{\operatorname{Tr}(\boldsymbol{\Lambda}^\top\mathbf{G})}{N}\,;\; G'_{int} = \frac{\operatorname{Tr}(\boldsymbol{\Lambda}\mathbf{G}')}{N}\,;$$

where $\Lambda_{ij} = n_c\delta_{ij} - n_{ij}$. Notice that all of them are by definition self-averaging quantities,

which obviously tend to be more and more stable as the size of the system increases.

As already stressed, in absence of a proper likelihood, an unattainable task is that of dealing with functions denoted with an *int* subscript; however, the manipulation we carried out to derive (A.64)–(A.65) confines them into sub-leading terms. This can be checked by looking at the combinations:

$$\frac{G_{int} - C_{int}}{C_{int}} \left[\left(1 - e^{-\frac{\eta}{\chi}\Delta t} \right) (G_s - C_s) - b \right] \simeq O(\Delta t^5) \,, \tag{A.72}$$

the one obtained replacing G_{int} with G'_{int}, and

$$b \cdot \frac{n_c}{C_{int}} \left[(1 - e^{-\frac{\eta}{\chi}\Delta t})(G_s - C_s) - b \right] \simeq O(\Delta t^6). \tag{A.73}$$

Under the working hypothesis that Δt is sufficiently small, we can neglect these terms and find usable relations to extract the effective parameters of the thermal bath (η/χ, T/χ) from the experimental self-correlations only. Precisely, η/χ is found as a solution of the equation:

$$\begin{aligned} &(C''_s + C_s - 2G_s)e^{-2\frac{\eta}{\chi}\Delta t} + 2(F_s - 5G'_s - G_s + 3C_s + 2C''_s)e^{-\frac{\eta}{\chi}\Delta t} \\ &\quad + 4F_s - 4G'_s - 6G_s + 5C_s + C'_s = 0 \,, \end{aligned} \tag{A.74}$$

whereas the effective temperature is extracted from b, being:

$$b = G'_s + G_s - F_s - C_s + e^{-\frac{\eta}{\chi}\Delta t} \left(2G'_s - C_s - C''_s \right) \,. \tag{A.75}$$

Notice that this formula is exactly equivalent to (A.62), since we defined the effective damping coefficient of the harmonic oscillator as $\eta = \mu/m$, whereas the corresponding quantity, having the dimension of an inverse time scale, is η/χ for the ISM. These formulas have been applied to find the results shown in Fig. 4.5.

A.1.3 Equations of motion of the ISM in the spin wave approximation

We derive in this appendix the equations of motion of the inertial spin model (ISM) in the so-called *spin wave* approximation (SWA). The name comes from the analogy with ideal Heisenberg ferromagnets which, at very low temperatures, can be studied using an approximate theory, whose basic idea is that the lowest energy excitations in a ferromagnet are those produced by a single reversed spin over a large number of otherwise aligned spins in a crystal lattice. Dyson1956 showed that an interaction between spin-wave states arises from this approximation and it should be taken into account to consistently work out the spin wave expansion (252). In a similar way, since natural flocks of starling are in a deeply ordered phase, we can perform an expansion around the perfectly ordered state of the flock, where all of the birds' velocities are aligned along the same direction.

Let us denote by $\mathbf{n}$ the collective direction of motion of the flock. Each vector $\mathbf{v}_i$ can be decomposed into its longitudinal and transverse components with respect to $\mathbf{n}$:

$$\mathbf{v}_i = v_i^L \mathbf{n} + \boldsymbol{\pi}_i. \tag{A.76}$$

In the case of bird flocks, the spin-wave approximation reduces to approximating the

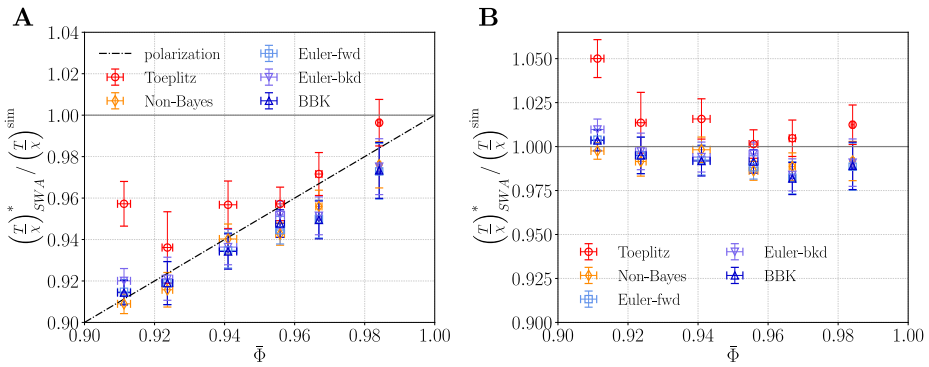

Figure S3: **First correction to the SWA.** The comparison between the plots shows the effect of the SWA: in **A.** the raw inferred values of T/χ, obtained using the inference formulas derived from (4.41), are reported. In **B.** we included the first correction by rescaling the output with the time-averaged polarization, for each sample trajectory. $\bar{\Phi}$ is the average of the averaged polarizations among different simulated flocks, at any given temperature. Errorbars for $\bar{\Phi}$ correspond to standard errors, whereas vertical bars represent, as in the other figures, 0.95 CI.

longitudinal components as follows:

$$v_i^L = \sqrt{1 - |\boldsymbol{\pi}_i|^2} \simeq 1 - \frac{1}{2}|\boldsymbol{\pi}_i|^2, \tag{A.77}$$

having $\mathbf{v}_i$ a unit length. The equations of motion of the ISM (with fixed interaction network) can be written in the form of a set of second order SDEs for the velocity variables:

$$\frac{d^2\mathbf{v}_i}{dt^2} = \left(-\eta\frac{d\mathbf{v}_i}{dt} - J\sum_{j=1}^{N} n_{ij}\mathbf{v}_j + \boldsymbol{\xi}_i\right)_{\perp} - \left|\frac{d\mathbf{v}_i}{dt}\right|^2 \mathbf{v}_i, \tag{A.78}$$

where the $\perp$ symbol indicates the projection onto the orthogonal plane to the direction of motion of the i-th bird, $\mathbf{v}_i$. This projection operator and the last term of (A.78) are the required ingredients to ensure individual speed conservation: $|\mathbf{v}_i(t)| = v_0 = 1\ \forall i, t$. Thanks to this property, (A.78) further simplifies:

$$\frac{d^2\mathbf{v}_i}{dt^2} = -\eta\frac{d\mathbf{v}_i}{dt} - J\sum_{j=1}^{N} n_{ij}\mathbf{v}_{j\perp} + \boldsymbol{\xi}_{i\perp} - \left|\frac{d\mathbf{v}_i}{dt}\right|^2 \mathbf{v}_i. \tag{A.79}$$

Using (A.76) – (A.77), and exploiting the fact that, for any vector $\mathbf{a}$,

$$\mathbf{a}_\perp = -\mathbf{v}_i \times (\mathbf{v}_i \times \mathbf{a})\,, \tag{A.80}$$

one can evaluate all the terms appearing in (A.79), at the desired order of approximation.

Let us focus firstly on time derivatives: we notice that, in principle, they also produce terms containing $\frac{d\mathbf{n}}{dt}$ and $\frac{d^2\mathbf{n}}{dt^2}$. In the following we will assume that the direction of collective motion $\mathbf{n}$ is constant. This is legitimate in the limit $N \to \infty$, when the wandering of the order parameter is suppressed, or at least when it is very slow compared to the relaxational dynamics of the degrees of freedom. If, on the contrary, one wants to take this effect into

account, apparent forces emerge because the chosen reference frame is non-inertial.

Neglecting apparent forces enables to segregate *on-plane* (i.e. perpendicular to $\mathbf{n}$) and *off-plane* (i.e. parallel to $\mathbf{n}$) contributions, and completely disentangle the corresponding equations. One can then consider the equations in the $\boldsymbol{\pi}$-plane only:

$$\frac{d^2\boldsymbol{\pi}_i}{dt^2} + \eta\frac{d\boldsymbol{\pi}_i}{dt} + J\Lambda_{ij}\boldsymbol{\pi}_j = \hat{P}\boldsymbol{\xi}_{i\perp} + O(|\boldsymbol{\pi}|^3), \tag{A.81}$$

where $\Lambda_{ij} = n_{ij} - n_c\delta_{ij}$ and $\hat{P}$ is the projection operator onto the plane perpendicular to the collective velocity $\mathbf{V} = \frac{1}{N}\sum_{i=1}^{N}\mathbf{v}_i \equiv \Phi\mathbf{n}$. The velocity fluctuations $\boldsymbol{\pi}_i$ play in this case the same role as spin excitations in Dyson1956's SWA, both becoming the new degrees of freedom and displaying a linear interaction.

At this stage, what remains to explicitly evaluate is only $\hat{P}\boldsymbol{\xi}_{i\perp}$. We know that $\boldsymbol{\xi}_{i\perp}$ lives in the plane perpendicular to $\mathbf{v}_i$, so that the perpendicular component to the plane spanned by $\mathbf{V}$ and $\mathbf{v}_i$ is left unchanged by this projection operator, while the other one is contracted with a factor $\cos\theta_i$, with θ_i the angle between $\mathbf{v}_i$ and $\mathbf{n}$. As a result:

$$\langle\hat{P}\boldsymbol{\xi}_i(t)\cdot\hat{P}\boldsymbol{\xi}_i(s)\rangle = 2(1+\cos^2\theta_i)\frac{T\eta}{\chi^2}\delta(t-s). \tag{A.82}$$

The second moment of each noise term is then rescaled, with respect to the original one, by a factor:

$$\frac{1}{2}(1+\cos^2\theta_i) = \frac{1}{2}\left(1+\left(v_i^L\right)^2\right) = 1 - \frac{1}{2}|\boldsymbol{\pi}_i|^2 \simeq v_i^L. \tag{A.83}$$

In order to let the fluctuation-dissipation theorem hold, this rescaling can be re-adsorbed by the temperature parameter T/χ, which is in principle different for each bird. At an averaged level, we can define a new spin wave temperature that differs form the original temperature of the inertial spin model by a factor $\frac{1}{N}\sum_{i=1}^{N}v_i^L$, which is by definition equivalent to the polarization of the flock $\Phi = |\frac{1}{N}\sum_{i=1}^{N}\mathbf{v}_i|$. In the low temperature case, where $|\boldsymbol{\pi}| \ll 1$, $\Phi = 1 + O(|\boldsymbol{\pi}|^2)$; the first correction to the temperature parameter is then of a lower order with respect to the terms which have been neglected in the deterministic part of (A.81) and shall correctly be included through this simple effective rescaling.

As long as the experimental or statistical errors are wide enough and the system pretty ordered, this SWA-related correction is negligible. Thanks to the large statistics and high accuracy we managed to have with our simulations and inference machinery, we are able to detect it in Fig. 4.5C, where points are systematically placed below the line of slope 1, especially for higher values of the temperature, which in turn correspond to lower polarization values. A comparison between the two panels of Fig. S3 confirms that this is truly the origin of the observed trend and not an intrinsic defect of the inference procedure.

1.2. Affinity maturation for an optimal balance between long-term immune coverage and short-term resource constraints

A.2.1 Mean-field de novo coverage

Here we show how the infection cost function defined in the main text,

$$I_t = \min\left[\phi, \left(\sum_{x\in P_{t-1}} c_{x,t} f(x,a_t)\right)^{-\alpha}\right], \tag{A.84}$$

may be derived as the mean-field limit of a repertoire with memory and de novo compartments.

In addition to the evolving memory repertoire P_t already described in the main text, we define a de novo response made of random receptors $\mathcal{N}$, distributed uniformly with density ρ. Viruses may be recognized by either the memory or de novo clonotypes. The de novo coverage is defined as:

$$C_{\text{denovo}}(a_t) = \sum_{x\in\mathcal{N}} f(x,a_t), \tag{A.85}$$

and the memory coverage as before:

$$C(a_t) = \sum_{x\in P_{t-1}} c_{x,t} f(x,a_t). \tag{A.86}$$

(In this convention, each de novo clonotype has size one in arbitrary units.)

Depending on the values of these coverages, the system will choose to use either the de novo response, or an existing memory. In this decision, we factor in the fact that using the de novo response is more costly, which we account for using a prefactor $\beta < 1$. The cost is then defined as:

$$L_t = \max\left[\beta C_{\text{denovo}}(a_t), C(a_t)\right]^{-\alpha}. \tag{A.87}$$

We can simplify this expression in the limit where de novo responding clonotypes are very numerous, but each offer weak coverage. In the limit of high density of de novo responding cells, $\rho \to \infty$, the coverage self-averages to its mean value:

$$C_{\text{denovo}} \approx \langle C_{\text{denovo}}\rangle = \rho \int d^d x\, f(x,a_t) = \rho U_d(q) r_0^d, \tag{A.88}$$

with

$$U_d(q) = \int d^d y\, e^{-\|y\|^q} = S_d \int r^{d-1} dr\, e^{-r^q}, \tag{A.89}$$

where we have done the change of variable $x = a_t + y r_0$, and where $S_d = 2\pi^{d/2}/\Gamma(d/2)$ is the surface area of the unit sphere.

Taking the $\rho \to \infty$ and $\beta \to 0$ limits, while keeping $\beta\rho$ finite, corresponds to a dense de novo response but where each de novo responding cell weakly covers the antigenic space. In this limit we recover the model of the main text

$$I_t = \min\left[\phi, C(a_t)^{-\alpha}\right], \tag{A.90}$$

with $\phi = (\rho\beta U_d(q) r_0^d)^{-\alpha}$.

A.2.2 Transition from monoclonal to de novo phase at $\sigma_v = 0$

Here we derive an expression for the phase boundary between the monoclonal and polyclonal phases in the limit $\sigma_v = 0$, where the virus does not move.

In the special case where $\mu = 0$, clonotypes cannot multiply. At each time step, a number m_n of new clonotypes at created at $a_n = \text{const}$, distributed according to a Poisson law of mean $\bar{m}$. This number is added to existing clonotypes, of which a random fraction γ survives. If the previous number of clonotypes, M_n, is Poisson distributed with mean $\bar{M}_n$, the number of surviving ones M'_n is also Poisson distributed with mean $\gamma\bar{M}_n$ (since subsampling a Poisson-distributed number still gives a Poisson law). Then, the new number of clonotypes, $M_{n+1} = M'_n + m_n$, is also Poisson distributed, with the recurrence relation:

$$\bar{M}_{n+1} = \gamma\bar{M}_n + \bar{m}. \tag{A.91}$$

At steady state, we have

$$\bar{M}_n \to \frac{\bar{m}}{1-\gamma}. \tag{A.92}$$

Since all clonotypes are at $x = a_n$, the coverage is $C(a_n) = M$, so that the expected cost reads:

$$\mathcal{L} = \phi \exp\left(-\frac{\bar{m}}{1-\gamma}\right) + \sum_{M=1}^{+\infty} \frac{1}{M^\alpha} \exp\left(-\frac{\bar{m}}{1-\gamma}\right) \frac{1}{m!}\left(\frac{\bar{m}}{1-\gamma}\right)^M + \kappa\bar{m}. \tag{A.93}$$

To find the transition from monoclonal to de novo response, $\bar{m} = 0$, we need to find the value of ϕ for which $\partial\mathcal{L}/\partial\bar{m}$ changes sign at $\bar{m} = 0$: if this derivative is positive, it is better to have $\bar{m} = 0$ (since the function is convex); if it is negative, there is benefit to be gained by increasing $\bar{m} > 0$. The condition:

$$\left.\frac{\partial\mathcal{L}}{\partial\bar{m}}\right|_{\bar{m}=0} = \kappa - \frac{\phi}{1-\gamma} + \frac{1}{1-\gamma} \tag{A.94}$$

gives the transition point

$$\phi_c = 1 + \kappa(1-\gamma) \tag{A.95}$$

For $\mu > 0$, we redefine M_n as the sum of all clonotype sizes, which is equal to the coverage, $C = M_n = \sum_{x\in P_n} c_{x,n}$. The recurrence relation is replaced by:

$$\bar{M}_{n+1} = \gamma(1+\mu)\bar{M}_n + \bar{m}. \tag{A.96}$$

For $\gamma(1+\mu) > 1$, this number explodes, so that M is infinite, reducing the infection cost to 0 regardless of $\bar{m}$. The transition point is then

$$\phi_c = 0. \tag{A.97}$$

For $\gamma(1+\mu) < 1$, $\bar{M}_n$ reaches a steady state value,

$$\bar{M}_n \to \frac{\bar{m}}{1-\gamma(1+\mu)}. \tag{A.98}$$

Although M_n is not strictly distributed according to a Poisson law, it is still a good

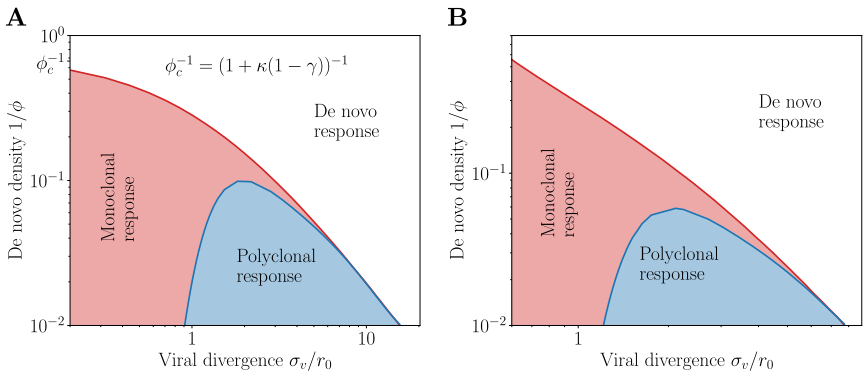

Figure S4: **Phase diagram for various parameters. A.** Phase diagram for parameters $\mu = 0$, $\gamma = 0.85$ and $d = 2$. We observe the upper transition point $\phi_c = (1+\kappa(1-\gamma))^{-1}$ at $\sigma_v = 0$. **B.** Phase diagram for parameters $\mu = 0.5$, $\gamma = 0.85$ and $d = 3$. Since $\gamma(1+\mu) > 1$ the transition point $\phi_c = \infty$. In both **A** and **C** we observe that the phase diagram retains the same shape. In this panel $\alpha = 1$, $q = 2$ and $\kappa = 0.5/(1-\gamma)$.

approximation, so that we can repeat the same argument as with $\mu = 0$,

$$\phi_c \approx 1 + \kappa(1 - \gamma(1+\mu)). \tag{A.99}$$

A.2.3 Analytical results in a solvable model

General formulation

Define $P_{\text{hit}}(\sigma', r_0, r)$ as the probability that a random memory will recognize the next infection at distance r, i.e. the probability that a random point in the ball of radius σ' and a point at distance r from its center are at distance $\leq r_0$. The probability that none of m clonotypes recognize the virus, where m is drawn from a Poisson distribution of mean $\bar{m}$, reads:

$$P_{\text{miss}}(\sigma', r_0, r) = \sum_m e^{-\bar{m}} \frac{\bar{m}^m}{m!} (1 - P_{\text{hit}}(\sigma', r_0, r))^m = e^{-\bar{m} P_{\text{hit}}(\sigma', r_0, r)}. \tag{A.100}$$

The best strategy maximizes this probability, averaged over the location of the next infection, over σ':

$$\bar{P}_{\text{miss}}(\sigma', \bar{m}, r_0, \sigma'_v) = \left\langle e^{-\bar{m} P_{\text{hit}}(\sigma', r_0, r)} \right\rangle_{\mathcal{B}(\sigma'_v)} = \frac{1}{{\sigma'_v}^d V_d} \int_0^{\sigma'_v} S_d r^{d-1} dr \, e^{-\bar{m} P_{\text{hit}}(\sigma', r_0, r)} \tag{A.101}$$

where $\mathcal{B}_{\sigma'_v}$ is the ball of radius σ'_v, $V_d = \pi^{d/2}/\Gamma(d/2+1)$ is the volume of a unit ball, and $S_d = 2\pi^{d/2}/\Gamma(d/2)$ the area of the unit sphere.

Then the expected overall cost reads:

$$\mathcal{L} = \phi \bar{P}_{\text{miss}}(\sigma', \bar{m}, r_0, \sigma_v) + \kappa \bar{m} = \phi \left\langle e^{-\bar{m} P_{\text{hit}}(\sigma', r_0, r)} \right\rangle_{\mathcal{B}(\sigma'_v)} + \kappa \bar{m}. \tag{A.102}$$

Exact location of the phase transitions, and approximate solution in the polyclonal phase

The location of the optimal σ' may be rigorously bounded from above and below. If $\sigma' < \sigma'_v - r_0$, then only part of the future positions of the virus are covered, so increasing σ' can bring no harm. Likewise, for $\sigma' > \sigma'_v + r_0$, memory covers parts of the antigenic space that have no chance of harboring the next virus, so that decreasing σ' is also always advantageous. Thus, the optimum σ'^* must satisfy:

$$\sigma'_v - r_0 \leq \sigma'^* \leq \sigma'_v + r_0. \tag{A.103}$$

As already argued in the main text, when $\sigma'_v < r_0$, there is clearly no benefit to having $\sigma' > 0$, so the optimum is reached at $\sigma' = 0$. (A.103) further shows that if $\sigma'_v > r_0$, then $\sigma'^* > 0$, so that a polyclonal phase is optimal. As a consequence, the transition from the monoclonal to polyclonal phases happens exactly at:

$$\sigma'_v = r_0. \tag{A.104}$$

In the monoclonal phase, memory always recognizes the next virus. The only risk of paying ϕ is when no memory is created, which happens with probability $e^{-\bar{m}}$, so that the cost reads:

$$\mathcal{L} = \phi e^{-\bar{m}} + \kappa \bar{m}. \tag{A.105}$$

The optimal $\bar{m}^* = \ln(\phi/\kappa)$ cancels at the monoclonal-to- de novo response transition:

$$\phi = \kappa. \tag{A.106}$$

In the polyclonal phase, we could not find a general analytical solution, but there are two limits in which the solution may be calculated. The first limit is when $\sigma_v \gg r_0$. In that case, (A.103) implies $\sigma'^* \approx \sigma'_v$, and

$$P_{\text{hit}}(\sigma'^*, r_0, r) \approx \frac{r_0^d}{\sigma_v'^d}, \tag{A.107}$$

which doesn't depend on r. Then, minimizing

$$\mathcal{L} \approx \phi e^{-\bar{m} P_{\text{hit}}} + \kappa \bar{m} \tag{A.108}$$

with respect to $\bar{m}$ yields:

$$\bar{m}^* = \frac{1}{P_{\text{hit}}} \ln\left(\frac{\phi}{\kappa} P_{\text{hit}}\right) = \frac{\sigma_v'^d}{r_0^d} \ln\left(\frac{\phi}{\kappa} \frac{r_0^d}{\sigma_v'^d}\right). \tag{A.109}$$

The second limit in which things simplify is for small $\bar{m}$. Then the exponential in (A.101) may be expanded at first order, yielding:

$$\mathcal{L} = \phi \left(1 - \bar{m} \langle P_{\text{hit}}(\sigma', r_0, r) \rangle_{\mathcal{B}(\sigma'_v)}\right) + \kappa \bar{m}, \tag{A.110}$$

where $\langle \cdot \rangle_r$ is the mean of over the ball of radius σ'_v. Minimizing with respect to σ' is equivalent to maximizing $\langle P_{\text{hit}}(\sigma', r_0, r) \rangle_r$, which is the probability that a random point

in the ball of radius σ' and a random point in the ball of radius σ'_v are separated by less than r_0. This probability is maximized for any $\sigma' \leq \sigma_v - r_0$, where it is equal to $(r_0/\sigma'_v)^d$. Increasing σ' beyond $\sigma_v - r_0$ can only lower the probability of recognition. Thus:

$$\min_{\sigma'} \mathcal{L} = \phi + \bar{m}\left(\kappa - \phi \frac{r_0^d}{{\sigma'_v}^d}\right). \tag{A.111}$$

This gives us the condition for the transition from polyclonal to de novo response, where $\bar{m}^* = 0$. This happens when:

$$\phi = \kappa \frac{{\sigma'_v}^d}{r_0^d}. \tag{A.112}$$

This condition gives us an exact expression for the location of the transition.

Exact solution in dimension 1

For $d = 1$, the cost $\mathcal{L}$ in (A.102) may be calculated analytically, by using exact expressions of $P_{\text{hit}}(\sigma', r_0, r)$. When $\sigma'_v \leq r_0$, the optimal σ' is zero as explained in the main text. When $\sigma'_v > r_0$, we distinguish two cases: $r_0 < \sigma'_v \leq 2r_0$, and $\sigma'_v > 2r_0$.

Case $r_0 < \sigma'_v \leq 2r_0$. Since we know that the optimal σ' is between $\sigma'_v - r_0$ and $\sigma'_v + r_0$, we focus on that range. Then there are two subcases for σ'.

If $\sigma'_v - r_0 < \sigma' \leq r_0$, there are two contributions to the integral of $\bar{P}_{\text{miss}}$ over the position of the virus r. Either $r \leq r_0 - \sigma'$, then all memories recognize the virus, $P_{\text{hit}} = 1$; or $r_0 - \sigma' < r < \sigma'_v < r_0 + \sigma'$, in which case the recognition probability is given by the normalized intersection of two balls at distance r of radii σ' and r_0,

$$P_{\text{hit}} = \frac{\sigma' + r_0 - r}{2\sigma'}. \tag{A.113}$$

Thus we obtain doing the integral over r in (A.101), if $\sigma'_v - r_0 < \sigma' \leq r_0$:

$$\bar{P}_{\text{miss}}(\sigma', \bar{m}, r_0, \sigma'_v) = \frac{1}{\sigma'_v}\left[(r_0 - \sigma')e^{-\bar{m}} + \int_{r_0-\sigma'}^{\sigma'_v} \exp\left(-\bar{m}\frac{\sigma' + r_0 - r}{2\sigma'}\right) dr\right]. \tag{A.114}$$

If $r_0 < \sigma' \leq \sigma'_v + r_0$, there are also two contributions. Either $r \leq \sigma' - r_0$, in which case there is no boundary effect, and the recognition probability is just $P_{\text{hit}} = r_0/\sigma'_v$; or $\sigma' - r_0 < r \leq \sigma'_v \leq \sigma' + r_0$, in which case we have again (A.113). Performing the integration in (A.101) we obtain, if $r_0 < \sigma' \leq \sigma'_v + r_0$:

$$\bar{P}_{\text{miss}}(\sigma', \bar{m}, r_0, \sigma'_v) = \frac{1}{\sigma'_v}\left[\exp\left(-\bar{m}\frac{r_0}{\sigma'}\right)(\sigma' - r_0) + \int_{\sigma'-r_0}^{\sigma'_v} \exp\left(-\bar{m}\frac{\sigma' + r_0 - r}{2\sigma'}\right) dr\right]. \tag{A.115}$$

Numerical analysis shows that (A.114) admits a minimum as a function of σ' in its interval of validity, $\sigma'_v - r_0 < \sigma'^* \leq r_0$, while (A.115) is always increasing.

Case $\sigma'_v > 2r_0$. In this case, there is only a single subcase in the range of interest $\sigma'_v - r_0$ and $\sigma'_v + r_0$. This case is the same as the previous one considered, and the result is given by the same formula (A.115). However, for $\sigma'_v > 2r_0$, this expression now admits a minimum $\sigma'_v - r_0 < \sigma'^* \leq \sigma'_v + r_0$.

We recover that in both cases (a and b), in the limit $\bar{m} \to 0$, this minimum is reached at $\sigma_v' - r_0$.

A.2.4 Population dynamics in sequential immunization

Clonotype growth and decay as a first-passage problem

We now want to study clonotype proliferation induced by a recall response. We focus on the limit of small mutation rates $\sigma_v \ll r_0$. Within this regime, the system is in the monoclonal phase with $\sigma^* = 0$. We can therefore focus on the case of a single clonotype at position $x = 0$ on the phenotypic space, and ask how successive challenges will modify its size. (Different initial conditions will only change the prefactor in front of the exponential modes in the distribution of first passage times, so the large time behavior of this probability distribution will be the same as discussed below.)

The clonotype has an initial size $c = 1$, and the virus drifts away from $x = 0$ with viral divergence σ_v. In the general model, cells have probability γ to survive from one challenge to the other. Proliferation is taken to be proportional to the cross reactivity radius, $\mu e^{-(r/r_0)^q}$. The population dynamics is thus given by the approximate recursion:

$$n_{t+1} \approx n_t \gamma \left[1 + \mu e^{-(r/r_0)^q}\right], \tag{A.116}$$

where we have neglected birth-death noise. We can further simplify this equation to $n_{t+1} = \gamma(1 + \mu\Theta(r - r^*))n_t$, where $r^* = r_0 \ln(\gamma\mu/(1-\gamma))^{1/q}$ is defined as the radius at which the net fold-change factor crosses 1, i.e. when birth is exactly compensated by death. This means that, as long as the virus is within distance r^*, the clonotype grows with fold-change factor $\sim \Gamma$. As soon as it reaches r^*, and neglecting possible returns below r^* (which happen with probability 1 for $d \leq 2$, but with a frequency that does not affect the overall decay), it will decay with fold-change factor $\sim \gamma$. The problem is thus reduced to determining the first-passage time of the viral antigenic location at radius r^*.

We use a continuous approximation corresponding to a slowly evolving strain, $\sigma_v \ll r_0$:

$$a(0) = 0, \qquad da = \frac{\sigma_v}{\sqrt{d}} dW, \tag{A.117}$$

where W is a Wiener process. The radius, given by $r(t) = |a(t)|$, behaves on average as:

$$\langle r(t)^2 \rangle = t\sigma_v^2. \tag{A.118}$$

The time it takes for $r(t)$ to reach r^*, denoted by t^*, is approximately given by $\langle t^* \rangle \sim (r^*/\sigma_v)^2$. The tail of the distribution for this first-passage time is dominated by rare events when the virus mutates less than expected between infections, leading to larger episodes of growth. We will show in the next two sections that the distribution of these exceptionally long t^* has an exponential tail:

$$P(t^* > t) \sim e^{-t/t_s}, \quad t_s \sim \langle t^* \rangle \sim \frac{r^{*2}}{\sigma_v^2}. \tag{A.119}$$

This translates into a power-law tail for the peak clonotype abundance,

$$p(n^*) \sim \frac{1}{n^{*1+\beta}}, \quad \text{with } \beta \sim \frac{\sigma_v^2}{r^{*2} \ln \Gamma}. \tag{A.120}$$

The same scaling holds for the distribution of all abundances, since the peak determines the rest of the trajectory.

Within the same simplified picture, the lifetime t_l of a clonotype is the sum of the time it takes to reach the peak, t^*, and the decay time until extinction, which is approximately $\ln(n^*)/\ln(1/\gamma)$:

$$t_l = t^* + \frac{\ln(n^*)}{\ln(1/\gamma)} = \left(1 + \frac{\ln \Gamma}{\ln(1/\gamma)}\right) t^*. \tag{A.121}$$

Thus, t_l is proportional to t^*, and therefore also exponentially distributed:

$$p(t_l) \sim e^{-\lambda t_l}, \quad \lambda \sim \frac{\sigma_v^2}{r^{*2}} \left(1 + \frac{\ln \Gamma}{\ln(1/\gamma)}\right)^{-1}. \tag{A.122}$$

Next we derive in detail the distributions of the first passage time of $r(t)$ to r^* to obtain Eq. A.119.

First passage time in $d = 1$

The distribution of first passage time, $p(t)$, can be computed solving diffusion with a box of size $2r^*$ in $d = 1$ (253):

$$p(t) = \sum_{n=0}^{+\infty} \frac{(2n+1)\sigma_v^2 \pi}{2r^{*2}} (-1)^n \exp\left(-\frac{(2n+1)^2 \pi^2 \sigma_v^2 t}{8r^{*2}}\right) \tag{A.123}$$

The dominant term ($n = 0$) at long times gives an exponential decay:

$$p(t) \approx \frac{\sigma_v^2 \pi}{2r^{*2}} \exp\left(-\frac{\pi^2 \sigma_v^2 t}{8r^{*2}}\right). \tag{A.124}$$

First passage in higher dimensions

We define $f(r, t)$ as the probability density that the virus has not yet reached r^* at time t, and is at radius r. This probability density is solution to the diffusion equation with spherical symmetry and absorbing boundary conditions in arbitrary dimension $d > 1$:

$$\frac{\partial f}{\partial t} = \frac{\sigma_v^2}{2d}\left[\frac{\partial^2 f}{\partial r^2} + \frac{d-1}{r}\frac{\partial f}{\partial r}\right], \qquad f(r^*, t) = 0. \tag{A.125}$$

Assuming separation of variables, $f(r, t) = T(t)R(r)$, we have:

$$\frac{T'(t)}{T(t)} = \frac{\sigma_v^2}{2d}\frac{R''(r) + \frac{d-1}{r}R'(r)}{R(r)} \equiv -\frac{\sigma_v^2}{2dr^{*2}}\lambda, \tag{A.126}$$

where λ is to be determined later. This implies $T(t) = Ce^{-\lambda \frac{\sigma_v^2}{2dr^{*2}} t}$ where C is a constant. The radial part $R(r)$ is solution to:

$$R''(r) + \frac{d-1}{r}R'(r) = -\frac{\lambda}{r^{*2}}R(r). \tag{A.127}$$

For $d = 1$ this equation reduces to a harmonic equation and we recover the above solution in 1D. Using the change of variable $R(r) = r^{1-d/2}g(r)$ we derive the following equation:

$$r^2 g''(r) + rg'(r) + \left(\lambda \frac{r^2}{r^{*2}} - \left(\frac{d}{2} - 1\right)^2\right) g(r) = 0. \tag{A.128}$$

Changing the variable $x = \sqrt{\lambda} r/r^*$, the function $\tilde{g}(x) = g(xr^*/\sqrt{\lambda})$ is solution to the Bessel differential equation of order $d/2-1$. It can therefore be written as a superposition of a Bessel function of the first kind and a Bessel function of the second kind, both of order $d/2 - 1$. The Bessel function of the second kind having a singularity at $x = 0$, our solution is only given by the Bessel function of the first kind $g(xr^*/\sqrt{\lambda}) = BJ_{d/2-1}(x)$. The radial function R now reads:

$$R(r) = Br^{1-d/2} J_{d/2-1}(\sqrt{\lambda} r/r^*). \tag{A.129}$$

The absorbing boundary condition at $r = r^*$ gives us the condition $J_{d/2-1}(\sqrt{\lambda}) = 0$, which has an infinite number of solutions $j_{0,d/2-1}, ..., j_{n,d/2-1}, ...$, so that λ can take values

$$\lambda_n = j^2_{n,d/2-1}. \tag{A.130}$$

The general solution to (A.125) is given as a linear combination of all possible modes, with coefficients C_n determined from boundary conditions and the Dirac delta initial condition, $f(r, 0) = \delta(r)$:

$$f(r,t) = \sum_{n=0}^{+\infty} C_n r^{1-d/2} J_{d/2-1}\left(\frac{j_{n,d/2-1}}{r^*} r\right) \exp\left(-\frac{j^2_{n,d/2-1}}{2dr^{*2}} \sigma_v^2 t\right). \tag{A.131}$$

The distribution of first passage times asymptotically follows the largest mode of this series, $n = 0$, so that:

$$p(t) \sim \exp\left(-\frac{j^2_{0,d/2-1}}{2dr^{*2}} \sigma_v^2 t\right). \tag{A.132}$$

For instance for $d = 2, 3, 4$ we have $j_{0,0} \approx 2.40483$, $j_{0,1/2} = \pi$, $j_{0,1} \approx 3.83171$.

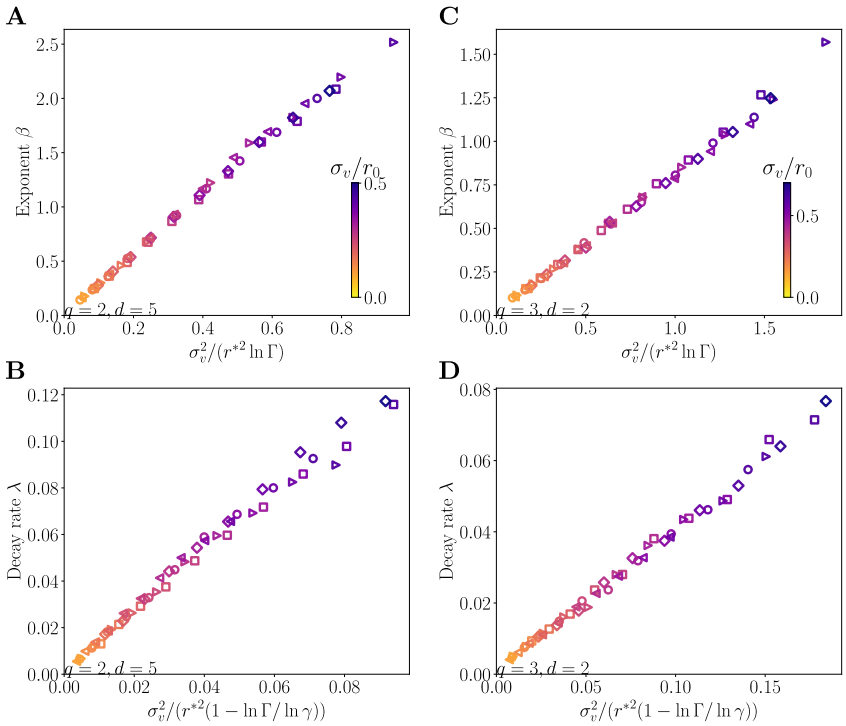

Figure S5: **Scaling relations for various parameters. A-B.** Power law exponent β and lifetime decay rate λ in dimension $d = 5$ with a Gaussian cross-reactivity kernel with $q = 2$. **C-D.** Power law exponent β and lifetime decay rate λ in dimension $d = 2$ with a cross-reactivity kernel with $q = 3$. The different parameters used are $(\gamma = 0.82, \mu = 0.65)$ i.e. $\Gamma = 1.353$ (diamonds), $(\gamma = 0.8, \mu = 0.62)$ i.e. $\Gamma = 1.296$ (squares), $(\gamma = 0.85, \mu = 0.5)$ i.e. $\Gamma = 1.275$ (circles), $(\gamma = 0.87, \mu = 0.4)$ i.e. $\Gamma = 1.21$ (triangles $>$), $(\gamma = 0.9, \mu = 0.35)$ ie. $\Gamma = 1.21$ (triangles $<$). The strategy is optimized with $\phi = 100$, $\kappa = 0.5/(1 - \gamma)$. We used $\alpha = 1$ throughout.

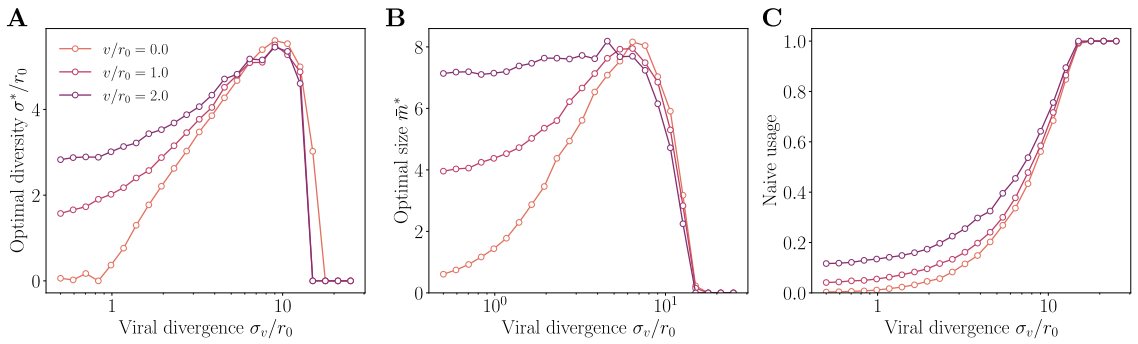

Figure S6: **Optimal strategy in presence of drift.** **A.** Optimal diversity **B.** size and **C.** frequency of naive usage in response to an immunization challenge for different strain drift v/r_0. The strain follows a random walk with drift v in a fixed direction e_0: $a_{t+1} = a_t + ve_0 + \sigma_v \eta_t$. Parameters values: $\mu = 0.5$, $\gamma = 0.85$, $\kappa = 3.3$, $\alpha = 1$, $q = 2$, $d = 2$.

1.3. Eco-evolutionary stability of viral strategies

A.3.1 Calculation of the speed of the wave

We solve here the steady-state diffusion reaction equation in the vicinity of the tip of the wave. We follow steps very similar to (220), and we define n_c the cut-off value on the density:

$$v\phi' + D\phi'' + sx\Theta(\phi - n_c)\phi = 0. \tag{A.133}$$

Although our velocities can be around $v \sim 10^{-3}$, our diffusion constants are usually orders of magnitude less, and around the bulk of the wave were the population size is large we can neglect diffusion. The equation there reads as:

$$v\phi' + sx\phi = 0. \tag{A.134}$$

And the bulk solution for $x \ll x_c$ is $\phi = e^{-sx^2/(2v)}$. When approaching the tip, the population size drops and the diffusion can't be neglected. In this case, we rewrite the solution as $\phi = e^{-vx/(2D)}\psi$ such that we now have:

$$D\psi'' + \left(sx - \frac{v^2}{4D}\right)\psi = 0. \tag{A.135}$$

By a change of variable we find an Airy equation, such that the full solution can be written:

$$\phi = e^{-vx/(2D)}\left[A\mathrm{Ai}\left(\frac{\gamma - x}{\delta}\right) + B\mathrm{Bi}\left(\frac{\gamma - x}{\delta}\right)\right], \text{with } \gamma = \frac{v^2}{4Ds} \text{ and } \delta = \left(\frac{D}{s}\right)^{1/3}. \tag{A.136}$$

The diffusionless solution in the bulk and this one must have the same behavior, such that as x increases Bi term will decay and the overall decay of ϕ will be faster than the one of the bulk solution. Therefore, the only term that can remain is the Airy function Ai. The solution now reads as:

$$\phi = e^{-vx/(2D)}A\mathrm{Ai}\left(\frac{\gamma - x}{\delta}\right). \tag{A.137}$$

We now have the full solution up to the tip of the wave, defined up to a constant A which is defined by the normalization. We still need to solve it beyond the tip of the wave and match the two solutions at x_c. Beyond x_c the equation reads as:

$$v\phi' + D\phi'' = 0. \tag{A.138}$$

The solution is $\phi = n_c e^{-v(x-x_c)/D}$ as it needs to take the value n_c at the tip (by definition the tip of the wave being the point where the density drops below n_c. We match the two solutions at x_c as well as their derivatives, which gives:

$$A = n_c e^{vx_c/(2D)} \Big/ \mathrm{Ai}\left(\frac{\gamma - x_c}{\delta}\right), \tag{A.139}$$

$$\frac{v}{2D} = \delta^{-1}\frac{\mathrm{Ai}'\left[\frac{\gamma - x_c}{\delta}\right]}{\mathrm{Ai}\left[\frac{\gamma - x_c}{\delta}\right]}. \tag{A.140}$$

As we said that $v \gg D$ even if we have small speeds, such that the fraction on the r.h.s. of the second equation should be large. This requires that the Airy function is close to its

first zero, in other words $(\gamma - x_c)/\delta = \xi_0 + \eta$ where $\eta \ll 1$. We therefore have:

$$\frac{\mathrm{Ai}'[\frac{\gamma - x_c}{\delta}]}{\mathrm{Ai}[\frac{\gamma - x_c}{\delta}]} = \frac{\mathrm{Ai}'(\xi_0)}{\mathrm{Ai}(\xi_0) + \eta \mathrm{Ai}'(\xi_0)} = \eta^{-1}, \tag{A.141}$$

and we are left with:

$$\delta\eta = \gamma - x_c - \xi_0\delta = \frac{2D}{v}, \tag{A.142}$$

$$\text{ie. } x_c = \gamma - \xi_0\delta = \frac{v^2}{4Ds} - \xi_0\left(\frac{D}{s}\right)^{1/3}, \tag{A.143}$$

where we have neglected the term $2D/v$. This first root of the Airy function is $\xi_0 = -2.3381$. Finally we need to eliminate A using the normalization:

$$N = \int_{-\infty}^{x_c} \phi(x)dx. \tag{A.144}$$

We introduce ξ:

$$\xi = \xi_0 + \frac{x_c - x}{\delta}, \tag{A.145}$$

and the normalization becomes:

$$\frac{N}{n_c} = \delta \frac{e^{-\eta^{-1}\xi_0}}{\mathrm{Ai}(\xi_0 + \eta)} \int_{\xi_0}^{+\infty} e^{\eta^{-1}\xi} \mathrm{Ai}(\xi + \eta)d\xi. \tag{A.146}$$

We can extend the integral to $-\infty$ as the Airy function oscillates below ξ_0 and the overall contribution to the total integral will be negligible. Then, using the Laplace transform of the Airy function we are left with the following equation:

$$\frac{N}{n_c} = \delta \frac{e^{-\eta^{-1}\xi_0 + \eta^{-3}/3 + 1}}{\mathrm{Ai}(\xi_0 + \eta)}, \tag{A.147}$$

and after expanding the Airy function at small η we have:

$$\ln\left(\frac{N}{n_c}\delta^{-1}\right) = \ln\eta^{-1} - \xi_0\eta^{-1} + \frac{1}{3}\eta^{-3} + 1 - \ln\mathrm{Ai}'(\xi_0). \tag{A.148}$$

At leading order in η^{-1} we have:

$$v = D\delta^{-1}\left(24\ln\left(\frac{N}{n_c}\delta^{-1}\right)\right)^{1/3} = (D^2 s)^{1/3}\left(24\ln\left(\frac{N}{n_c}(s/D)^{1/3}\right)\right)^{1/3}. \tag{A.149}$$

We can also estimate the second order correction to the speed that also matters in the regime we investigate. To compute this second order correction we simply plug-in the first order guess in the second order term in Eq; A.148. After Taylor expanding we are left with the result:

$$v = 2(D^2 s)^{1/3}\left[\left(3\ln\left(\frac{N}{n_c}(s/D)^{1/3}\right)\right)^{1/3} + \xi_0\left(3\ln\left(\frac{N}{n_c}(s/D)^{1/3}\right)\right)^{-1/3}\right]. \tag{A.150}$$

In particular, in the large population size limit we have:

$$f_{\text{tip}} = sx_c \simeq \frac{v^2}{4D}. \tag{A.151}$$

A.3.2 Solution of the diffusion equation with linear growth rate

We provide here a solution of the diffusion equation with an linear growth rate and no cut-off:

$$\partial_t \phi_m = v\partial_x \phi_m + D_m \partial_x^2 \phi_m + (f_m + s_m x)\phi_m. \tag{A.152}$$

Taking the fourier transform of the equation we have:

$$\partial_t \hat{\phi}_m = (ivk - D_m k^2 + f_m)\hat{\phi}_m + s_m i \partial_k \hat{\phi}_m. \tag{A.153}$$

To solve this equation we try the following ansatz $\hat{\phi}_m = A(k,t)e^{i\psi(k,t)}$ where A and ψ are real functions. Separating between imaginary and real parts we are left with the following set of equations:

$$\partial_t A = (-D_m k^2 + f_m)A - s_m A \partial_k \psi, \tag{A.154}$$

$$A\partial_t \psi = vkA + s_m \partial_k A, \tag{A.155}$$

The solution to the second equation reads as:

$$A = A_0(t) \exp\left[\frac{1}{s_m}\left(-\frac{vk^2}{2} + \int \partial_t \psi dk\right)\right]. \tag{A.156}$$

Injecting it in (A.154), under the condition that A is always non zero, and differentiating with respect to k we obtain:

$$\frac{1}{s_m}\partial_t^2 \psi + s_m \partial_k^2 \psi = -2D_m k. \tag{A.157}$$

We now suppose that $\partial_k^2 \psi = 0$. Integrating (A.157) twice with respect to t and computing it's integral with respect to k, we have:

$$\begin{aligned}\hat{\phi}_m = A_0(t) \exp\left[\frac{1}{s_m}\left(-\frac{vk^2}{2} - D_m s_m k^2 t + \int A_1(k)dk\right)\right] \\ \times \exp\left[i\Big(-D_m s_m k t^2 + A_1(k)t + A_2(k)\Big)\right],\end{aligned} \tag{A.158}$$

where A_1 and A_2 are functions of k. Since the initial condition is a Dirac delta centered at y_0 $\phi_m(y,0) = \epsilon\delta(y - y_0)$ and $\hat{\phi}_m(k,0) = \epsilon e^{-iky_0}$. It gives:

$$\frac{-vk^2}{2} + \int A_1(k)dk = 0, \tag{A.159}$$

$$A_0(0)e^{iA_2(k)} = \epsilon e^{-iky_0}. \tag{A.160}$$

So we have $A_1(k) = vk$ and the final solution reads as:

$$\hat{\phi}_m = \epsilon \frac{A_0(t)}{A_0(0)} \exp\left(-D_m k^2 t\right) \exp\left[ik\Big(- D_m s_m t^2 + vt - y_0\Big)\right]. \tag{A.161}$$

We still have to work out the dependency of A_0 with time. To find it we can reinject the value of A and ψ in (A.154). Using the non-negativity of A we can solve the equation for A_0. Fourier transforming back to real space, the solution reads as:

$$\begin{aligned}\phi_m(y,t) = \exp\left[- s_m\left(\frac{vt^2}{2} - D_m s_m \frac{t^3}{3} - y_0 t\right) + f_m t\right] \frac{\epsilon}{\sqrt{4\pi D_m t}} \\ \times \exp\left(-\frac{((y-y_0) + vt - D_m s_m t^2)^2}{4 D_m t}\right).\end{aligned} \tag{A.162}$$

Bibliography

[1] Karsenti E (2008) Self-organization in cell biology: A brief history. *Nature Reviews Molecular Cell Biology* 9:255–262.

[2] Burla F, Mulla Y, Vos BE, Aufderhorst-Roberts A, Koenderink GH (2019) From mechanical resilience to active material properties in biopolymer networks. *Nature Reviews Physics* 1:249–263.

[3] Procaccini A, et al. (2011) Propagating waves in starling, Sturnus vulgaris, flocks under predation. *Animal Behaviour* 82:759–765.

[4] Storms RF, Carere C, Zoratto F, Hemelrijk CK (2019) Complex patterns of collective escape in starling flocks under predation. *Behavioral Ecology and Sociobiology* 73:10.

[5] Marsland R, Howell O, Mayer A, Mehta P (2021) Tregs self-organize into a computing ecosystem and implement a sophisticated optimization algorithm for mediating immune response. *Proceedings of the National Academy of Sciences* 118:e2011709118.

[6] Kato T, Kobayashi TJ (2021) Understanding adaptive immune system as reinforcement learning. *Physical Review Research* 3:013222.

[7] Schnaack OH, Nourmohammad A (2021) Optimal evolutionary decision-making to store immune memory. *eLife* 10:e61346.

[8] Mayer A, Balasubramanian V, Walczak AM, Mora T (2019) How a well-adapting immune system remembers. *Proceedings of the National Academy of Sciences* 116:8815–8823.

[9] Mayer A, Balasubramanian V, Mora T, Walczak AM (2015) How a well-adapted immune system is organized. *Proceedings of the National Academy of Sciences* 112:5950–5955.

[10] Vicsek T, Czirók A, Ben-Jacob E, Cohen I, Shochet O (1995) Novel Type of Phase Transition in a System of Self-Driven Particles. *Physical Review Letters* 75:1226–1229.

[11] Toner J, Tu Y (1998) Flocks, herds, and schools: A quantitative theory of flocking. *Physical Review E* 58:4828–4858.

[12] Surrey T, Nédélec F, Leibler S, Karsenti E (2001) Physical Properties Determining Self-Organization of Motors and Microtubules. *Science* 292:1167–1171.

[13] Sanchez T, Chen DTN, DeCamp SJ, Heymann M, Dogic Z (2012) Spontaneous motion in hierarchically assembled active matter. *Nature* 491:431–434.

[14] Sumino Y, et al. (2012) Large-scale vortex lattice emerging from collectively moving microtubules. *Nature* 483:448.

[15] Copenhagen K, Alert R, Wingreen NS, Shaevitz JW (2021) Topological defects promote layer formation in Myxococcus xanthus colonies. *Nature Physics* 17:211–215.

[16] Deisboeck TS, Couzin ID (2009) Collective behavior in cancer cell populations. *BioEssays* 31:190–197.

[17] Attanasi A, et al. (2014) Information transfer and behavioural inertia in starling flocks. *Nature Physics* 10:691–696.

[18] Attanasi A, et al. (2015) Emergence of collective changes in travel direction of starling flocks from individual birds' fluctuations. *Journal of The Royal Society Interface* 12:20150319.

[19] Cavagna A, et al. (2015) Flocking and turning: a new model for self-organized collective motion. *Journal of Statistical Physics* 158:601–627.

[20] Bialek W, et al. (2012) Statistical mechanics for natural flocks of birds. *Proceedings of the National Academy of Sciences* 109:4786–4791.

[21] Marchetti MC, et al. (2013) Hydrodynamics of soft active matter. *Reviews of Modern Physics* 85:1143–1189.

[22] Altan-Bonnet G, Mora T, Walczak AM (2020) Quantitative Immunology for Physicists. *Physics Reports* 849:1–83.

[23] Perelson AS, Mirmirani M, Oster GF (1976) Optimal strategies in immunology. I. B-cell differentiation and proliferation. *Journal of Mathematical Biology* 3:325–367.

[24] Perelson AS, Mirmirani M, Oster GF (1978) Optimal strategies in immunology. II. B memory cell production. *Journal of Mathematical Biology* 5:213–256.

[25] Viant C, et al. (2020) Antibody Affinity Shapes the Choice between Memory and Germinal Center B Cell Fates. *Cell* 183:1298–1311.e11.

[26] Shlomchik MJ, Luo W, Weisel F (2019) Linking signaling and selection in the germinal center. *Immunological Reviews* 288:49–63.

[27] Monto AS, Malosh RE, Petrie JG, Martin ET (2017) The Doctrine of Original Antigenic Sin: Separating Good From Evil. *The Journal of Infectious Diseases* 215:1782–1788.

[28] Worobey M, Plotkin S, Hensley SE (2020) Influenza Vaccines Delivered in Early Childhood Could Turn Antigenic Sin into Antigenic Blessings. *Cold Spring Harbor Perspectives in Medicine* p a038471.

[29] Yewdell JW, Santos JJS (2020) Original Antigenic Sin: How Original? how Sinful? *Cold Spring Harbor Perspectives in Medicine* p a038786.

[30] Zhang A, Stacey HD, Mullarkey CE, Miller MS (2019) Original Antigenic Sin: How First Exposure Shapes Lifelong Anti–Influenza Virus Immune Responses. *The Journal of Immunology* 202:335–340.

[31] Kermack WO, McKendrick AG, Walker GT (1927) A contribution to the mathematical theory of epidemics. *Proceedings of the Royal Society of London. Series A, Containing Papers of a Mathematical and Physical Character* 115:700–721.

[32] Anderson RM, May RM (1992) *Infectious Diseases of Humans: Dynamics and Control* (Oxford University Press, Oxford, New York).

[33] Gog JR, Grenfell BT (2002) Dynamics and selection of many-strain pathogens. *Proceedings of the National Academy of Sciences* 99:17209–17214.

[34] Boni MF, Gog JR, Andreasen V, Feldman MW (2006) Epidemic dynamics and antigenic evolution in a single season of influenza A. *Proceedings of the Royal Society B: Biological Sciences* 273:1307–1316.

[35] Yan L, Neher RA, Shraiman BI (2019) Phylodynamic theory of persistence, extinction and speciation of rapidly adapting pathogens. *eLife* 8:e44205.

[36] Marchi J, Lässig M, Walczak AM, Mora T (2021) Antigenic waves of virus–immune coevolution. *Proceedings of the National Academy of Sciences* 118:e2103398118.

[37] Sasaki A, Lion S, Boots M (2021) Antigenic escape selects for the evolution of higher pathogen transmission and virulence. *Nature Ecology & Evolution* pp 1–12.

[38] Hallatschek O (2011) The noisy edge of traveling waves. *Proceedings of the National Academy of Sciences* 108:1783–1787.

[39] Desai MM, Fisher DS (2007) Beneficial Mutation–Selection Balance and the Effect of Linkage on Positive Selection. *Genetics* 176:1759–1798.

[40] Ferretti F, Chardès V, Mora T, Walczak AM, Giardina I (2020) Building General Langevin Models from Discrete Datasets. *Physical Review X* 10:031018.

[41] Chardès V, Vergassola M, Walczak AM, Mora T (2022) Affinity maturation for an optimal balance between long-term immune coverage and short-term resource constraints. *Proceedings of the National Academy of Sciences* 119:e2113512119.

[42] Gautrais J, et al. (2009) Analyzing fish movement as a persistent turning walker. *Journal of Mathematical Biology* 58:429–445.

[43] Gautrais J, et al. (2012) Deciphering interactions in moving animal groups. *PLOS Computational Biology* 8:1–11.

[44] Cavagna A, et al. (2017) Dynamic scaling in natural swarms. *Nature Physics* 13:914 EP –.

[45] Gloter A (2006) Parameter estimation for a discretely observed integrated diffusion process. *Scandinavian Journal of Statistics* 33:83–104.

[46] Lehle B, Peinke J (2015) Analyzing a stochastic time series obeying a second-order differential equation. *Phys. Rev. E* 91:062113.

[47] Pedersen JN, et al. (2016) How to connect time-lapse recorded trajectories of motile microorganisms with dynamical models in continuous time. *Phys. Rev. E* 94:062401.

[48] Vanden-Eijnden E, Ciccotti G (2006) Second-order integrators for langevin equations with holonomic constraints. *Chemical Physics Letters* 429:310 – 316.

[49] Skeel RD, Izaguirre JA (2002) An impulse integrator for langevin dynamics. *Molecular Physics* 100:3885–3891.

[50] Nieuwenhuis P, Opstelten D (1984) Functional anatomy of germinal centers. *American Journal of Anatomy* 170:421–435.

[51] Weisel F, Shlomchik M (2017) Memory B Cells of Mice and Humans. *Annual Review of Immunology* 35:255–284.

[52] Bedford T, Rambaut A, Pascual M (2012) Canalization of the evolutionary trajectory of the human influenza virus. *BMC Biology* 10:38.

[53] Bedford T, et al. (2014) Integrating influenza antigenic dynamics with molecular evolution. *eLife* 3:e01914.

[54] Francis T (1960) On the Doctrine of Original Antigenic Sin. *Proceedings of the American Philosophical Society* 104:572–578.

[55] Cobey S, Hensley SE (2017) Immune history and influenza virus susceptibility. *Current Opinion in Virology* 22:105–111.

[56] May RM, Anderson RM (1990) Parasite—host coevolution. *Parasitology* 100:S89–S101.

[57] Lion S, Metz JAJ (2018) Beyond R0 Maximisation: On Pathogen Evolution and Environmental Dimensions. *Trends in Ecology & Evolution* 33:458–473.

[58] Smith DJ, et al. (2004) Mapping the Antigenic and Genetic Evolution of Influenza Virus. *Science* 305:371–376.

[59] Fonville JM, et al. (2014) Antibody landscapes after influenza virus infection or vaccination. *Science* 346:996–1000.

[60] Neher RA, Bedford T, Daniels RS, Russell CA, Shraiman BI (2016) Prediction, dynamics, and visualization of antigenic phenotypes of seasonal influenza viruses. *Proceedings of the National Academy of Sciences* 113:E1701–E1709.

[61] Lange A, Ferguson NM (2009) Antigenic Diversity, Transmission Mechanisms, and the Evolution of Pathogens. *PLOS Computational Biology* 5:e1000536.

[62] Sanjuán R, Nebot MR, Chirico N, Mansky LM, Belshaw R (2010) Viral Mutation Rates. *Journal of Virology* 84:9733–9748.

[63] Bull JJ, Sanjuán R, Wilke CO (2007) Theory of Lethal Mutagenesis for Viruses. *Journal of Virology* 81:2930–2939.

[64] Swanstrom R, Schinazi RF (2022) Lethal mutagenesis as an antiviral strategy. *Science* 375:497–498.

[65] Alizon S, Hurford A, Mideo N, Van Baalen M (2009) Virulence evolution and the trade-off hypothesis: history, current state of affairs and the future. *Journal of Evolutionary Biology* 22:245–259.

[66] Kasza KE, et al. (2007) The cell as a material. *Current Opinion in Cell Biology* 19:101–107.

[67] Fletcher DA, Mullins RD (2010) Cell mechanics and the cytoskeleton. *Nature* 463:485–492.

[68] Mora T, Bialek W (2011) Are Biological Systems Poised at Criticality? *Journal of Statistical Physics* 144:268–302.

[69] Doostmohammadi A, Ignés-Mullol J, Yeomans JM, Sagués F (2018) Active nematics. *Nature Communications* 9:3246.

[70] Ladoux B, Mège RM (2017) Mechanobiology of collective cell behaviours. *Nature Reviews Molecular Cell Biology* 18:743–757.

[71] Peruani F, et al. (2012) Collective Motion and Nonequilibrium Cluster Formation in Colonies of Gliding Bacteria. *Physical Review Letters* 108:098102.

[72] Giardina I (2008) Collective behavior in animal groups: Theoretical models and empirical studies. *HFSP Journal* 2:205–219.

[73] Gardiner C (2009) *Stochastic Methods*, 0172-7389 (Springer-Verlag Berlin Heidelberg) Vol. 13.

[74] Mermin ND, Wagner H (1966) Absence of Ferromagnetism or Antiferromagnetism in One- or Two-Dimensional Isotropic Heisenberg Models. *Physical Review Letters* 17:1133–1136.

[75] Chaté H (2020) Dry Aligning Dilute Active Matter. *Annual Review of Condensed Matter Physics* 11:189–212.

[76] Chaté H, Ginelli F, Grégoire G, Peruani F, Raynaud F (2008) Modeling collective motion: Variations on the Vicsek model. *The European Physical Journal B* 64:451–456.

[77] Martin D, et al. (2021) Fluctuation-Induced Phase Separation in Metric and Topological Models of Collective Motion. *Physical Review Letters* 126:148001.

[78] Cavagna A, Giardina I, Grigera TS (2018) The physics of flocking: Correlation as a compass from experiments to theory. *Physics Reports* 728:1 – 62.

[79] Romanczuk P, Bär M, Ebeling W, Lindner B, Schimansky-Geier L (2012) Active Brownian particles. *The European Physical Journal Special Topics* 202:1–162.

[80] Cavagna A, et al. (2014) Dynamical maximum entropy approach to flocking. *Phys. Rev. E* 89:042707.

[81] Kantz H, Schreiber T (2003) *Nonlinear Time Series Analysis* (Cambridge University Press, Cambridge), Second edition.

[82] Frishman A, Ronceray P (2020) Learning Force Fields from Stochastic Trajectories. *Physical Review X* 10:021009.

[83] Brückner DB, et al. (2019) Stochastic nonlinear dynamics of confined cell migration in two-state systems. *Nature Physics* 15:595–601.

[84] Friedrich R, Peinke J, Sahimi M, Reza Rahimi Tabar M (2011) Approaching complexity by stochastic methods: From biological systems to turbulence. *Physics Reports* 506:87–162.

[85] Brückner DB, Ronceray P, Broedersz CP (2020) Inferring the Dynamics of Underdamped Stochastic Systems. *Physical Review Letters* 125:058103.

[86] MacKay DJ (2003) *Information Theory, Inference and Learning Algorithms* (Cambridge University Press).

[87] Newey W, McFadden D (1986) Large sample estimation and hypothesis testing., (Elsevier), Handbook of Econometrics.

[88] Mora T, et al. (2016) Local equilibrium in bird flocks. *Nature Physics* 12:1153–1157.

[89] Ballerini M, et al. (2008) Interaction ruling animal collective behaviour depends on topological rather than metric distance: Evidence from a field study. *PNAS* 105:1232.

[90] Gerbal F, Chaikin P, Rabin Y, Prost J (2000) An elastic analysis of listeria monocytogenes propulsion. *Biophysical Journal* 79:2259 – 2275.

[91] Stephens GJ, Johnson-Kerner B, Bialek W, Ryu WS (2008) Dimensionality and dynamics in the behavior of c. elegans. *PLOS Computational Biology* 4:1–10.

[92] Zwanzig R (2001) *Nonequilibrium statistical mechanics* (Oxford University Press, USA).

[93] Miguel MS, Sancho JM (1980) A colored-noise approach to brownian motion in position space. corrections to the smoluchowski equation. *Journal of Statistical Physics* 22:605–624.

[94] Hanggi P, Thomas H, Grabert H, Talkner P (1978) Note on time evolution of non-markov processes. *Journal of Statistical Physics* 18:155–159.

[95] Brückner DB, Ronceray P, Broedersz CP (2020) Inferring the non-linear dynamics of stochastic inertial systems.

[96] Lehle B, Peinke J (2018) Analyzing a stochastic process driven by ornstein-uhlenbeck noise. *Phys. Rev. E* 97:012113.

[97] Pressé S, Ghosh K, Lee J, Dill KA (2013) Principles of maximum entropy and maximum caliber in statistical physics. *Rev. Mod. Phys.* 85:1115–1141.

[98] Nguyen HC, Zecchina R, Berg J (2017) Inverse statistical problems: from the inverse ising problem to data science. *Advances in Physics* 66:197–261.

[99] Sørensen M (1997) *Estimating functions for discretely observed diffusions: A review*, IMS Lecture Notes - Monograph Series eds I. V. Basawa VPG, Taylor RL (Hayward: Institute of Matehmatical Statistics), Vol. 32, pp 305–325.

[100] Monthus C (2011) Non-equilibrium steady states: maximization of the shannon entropy associated with the distribution of dynamical trajectories in the presence of constraints. *Journal of Statistical Mechanics: Theory and Experiment* 2011:P03008.

[101] Otten M, Stock G (2010) Maximum caliber inference of nonequilibrium processes. *The Journal of Chemical Physics* 133:034119.

[102] El Beheiry M, et al. (2016) A primer on the bayesian approach to high-density single-molecule trajectories analysis. *Biophysical journal* 110:1209–1215.

[103] Türkcan S, Alexandrou A, Masson JB (2012) A bayesian inference scheme to extract diffusivity and potential fields from confined single-molecule trajectories. *Biophysical journal* 102:2288–2298.

[104] Gloter A (2001) Parameter estimation for a discrete sampling of an intergrated ornstein-uhlenbeck process. *Statistics* 35:225–243.

[105] Drozdov AN, Morillo M (1996) Path integral solution of the kramers problem. *Phys. Rev. Lett.* 77:5324–5327.

[106] Platen PEKE, Kloeden PE (1992) *Numerical Solution of Stochastic Differential Equations*, Stochastic Modelling and Applied Probability (Springer-Verlag Berlin Heidelberg) Vol. 23, 1 edition.

[107] Gillespie DT (1996) Exact numerical simulation of the ornstein-uhlenbeck process and its integral. *Phys. Rev. E* 54:2084–2091.

[108] Cavagna A, et al. (2016) Spatio-temporal correlations in models of collective motion ruled by different dynamical laws. *Physical Biology* 13:065001.

[109] Jia J, Sogabe T, El-Mikkawy M (2013) Inversion of k-tridiagonal matrices with toeplitz structure. *Computers & Mathematics with Applications* 65:116 – 125.

[110] Meurant G (1992) A review on the inverse of symmetric tridiagonal and block tridiagonal matrices. *SIAM Journal on Matrix Analysis and Applications* 13:707–728.

[111] van Gunsteren W, Berendsen H (1982) Algorithms for brownian dynamics. *Molecular Physics* 45:637–647.

[112] Dequidt A, Solano Canchaya JG (2015) Bayesian parametrization of coarse-grain dissipative dynamics models. *The Journal of Chemical Physics* 143:084122.

[113] Harmandaris V, Kalligiannaki E, Katsoulakis M, Plecháč P (2016) Path-space variational inference for non-equilibrium coarse-grained systems. *Journal of Computational Physics* 314:355 – 383.

[114] Cavagna A, et al. (2019) Renormalization group crossover in the critical dynamics of field theories with mode coupling terms. *Phys. Rev. E* 100:062130.

[115] Cavagna A, et al. (2019) Dynamical renormalization group approach to the collective behavior of swarms. *Phys. Rev. Lett.* 123:268001.

[116] Boris JP (1970) *Relativistic plasma simulation-optimization of a hybrid code* eds Boris J, Shanny R (Naval Research Laboratory), pp 3–67.

[117] Akira S, Uematsu S, Takeuchi O (2006) Pathogen Recognition and Innate Immunity. *Cell* 124:783–801.

[118] Medzhitov R (2007) Recognition of microorganisms and activation of the immune response. *Nature* 449:819–826.

[119] Buchmann K (2014) Evolution of Innate Immunity: Clues from Invertebrates via Fish to Mammals. *Frontiers in Immunology* 5.

[120] Medzhitov R, Janeway CA (2002) Decoding the Patterns of Self and Nonself by the Innate Immune System. *Science* 296:298–300.

[121] Gonzalez S, et al. (2011) Conceptual aspects of self and nonself discrimination. *Self Nonself* 2:19–25.

[122] Litman GW, Rast JP, Fugmann SD (2010) The origins of vertebrate adaptive immunity. *Nature Reviews Immunology* 10:543–553.

[123] Boehm T, et al. (2012) VLR-Based Adaptive Immunity. *Annual Review of Immunology* 30:203–220.

[124] Chaplin DD (2010) Overview of the immune response. *Journal of Allergy and Clinical Immunology* 125:S3–S23.

[125] Hozumi N, Tonegawa S (1976) Evidence for somatic rearrangement of immunoglobulin genes coding for variable and constant regions. *Proceedings of the National Academy of Sciences* 73:3628–3632.

[126] Dupic T, Marcou Q, Walczak AM, Mora T (2019) Genesis of the $A\beta$ T-cell receptor. *PLOS Computational Biology* 15:e1006874.

[127] Anderton SM, Wraith DC (2002) Selection and fine-tuning of the autoimmune T-cell repertoire. *Nature Reviews Immunology* 2:487–498.

[128] Zuckerman NS, et al. (2010) Somatic hypermutation and antigen-driven selection of B cells are altered in autoimmune diseases. *Journal of Autoimmunity* 35:325–335.

[129] Goodnow CC, Vinuesa CG, Randall KL, Mackay F, Brink R (2010) Control systems and decision making for antibody production. *Nature Immunology* 11:681–688.

[130] Victora GD, et al. (2010) Germinal Center Dynamics Revealed by Multiphoton Microscopy with a Photoactivatable Fluorescent Reporter. *Cell* 143:592–605.

[131] Akkaya M, Kwak K, Pierce SK (2020) B cell memory: Building two walls of protection against pathogens. *Nature Reviews Immunology* 20:229–238.

[132] Burnet FM (1957) A modification of Jerne's theory of antibody production using the concept of clonal selection. *The Australian Journal of Science* 20:67–69.

[133] Billingham RE, Brent L, Medawar PB (1953) 'Actively Acquired Tolerance' of Foreign Cells. *Nature* 172:603–606.

[134] Nossal GJV, Lederberg J (1958) Antibody Production by Single Cells. *Nature* 181:1419–1420.

[135] Sewell AK (2012) Why must T cells be cross-reactive? *Nature Reviews Immunology* 12:669–677.

[136] Bianconi E, et al. (2013) An estimation of the number of cells in the human body. *Annals of Human Biology* 40:463–471.

[137] Mason D (1998) A very high level of crossreactivity is an essential feature of the T-cell receptor. *Immunology Today* 19:395–404.

[138] Zarnitsyna V, Evavold B, Schoettle L, Blattman J, Antia R (2013) Estimating the Diversity, Completeness, and Cross-Reactivity of the T Cell Repertoire. *Frontiers in Immunology* 4.

[139] Elsner RA, Shlomchik MJ (2020) Germinal Center and Extrafollicular B Cell Responses in Vaccination, Immunity, and Autoimmunity. *Immunity* 53:1136–1150.

[140] Victora GD, Nussenzweig MC (2022) Germinal Centers. *Annual Review of Immunology* 40:413–442.

[141] Mesin L, Ersching J, Victora GD (2016) Germinal Center B Cell Dynamics. *Immunity* 45:471–482.

[142] Kleinstein SH, Louzoun Y, Shlomchik MJ (2003) Estimating Hypermutation Rates from Clonal Tree Data. *The Journal of Immunology* 171:4639–4649.

[143] Victora GD, Mesin L (2014) Clonal and cellular dynamics in germinal centers. *Current Opinion in Immunology* 28:90–96.

[144] Khodadadi L, Cheng Q, Radbruch A, Hiepe F (2019) The Maintenance of Memory Plasma Cells. *Frontiers in Immunology* 10.

[145] Amanna IJ, Carlson NE, Slifka MK (2007) Duration of Humoral Immunity to Common Viral and Vaccine Antigens. *New England Journal of Medicine* 357:1903–1915.

[146] Palm AKE, Henry C (2019) Remembrance of Things Past: Long-Term B Cell Memory After Infection and Vaccination. *Frontiers in Immunology* 10.

[147] Weisel FJ, Zuccarino-Catania GV, Chikina M, Shlomchik MJ (2016) A Temporal Switch in the Germinal Center Determines Differential Output of Memory B and Plasma Cells. *Immunity* 44:116–130.

[148] Inoue T, Moran I, Shinnakasu R, Phan TG, Kurosaki T (2018) Generation of memory B cells and their reactivation. *Immunological Reviews* 283:138–149.

[149] MacLennan ICM, et al. (2003) Extrafollicular antibody responses. *Immunological Reviews* 194:8–18.

[150] Nutt SL, Hodgkin PD, Tarlinton DM, Corcoran LM (2015) The generation of antibody-secreting plasma cells. *Nature Reviews Immunology* 15:160–171.

[151] Iyer AS, et al. (2020) Persistence and decay of human antibody responses to the receptor binding domain of SARS-CoV-2 spike protein in COVID-19 patients. *Science Immunology* 5:eabe0367.

[152] Miller MS, et al. (2013) Neutralizing Antibodies Against Previously Encountered Influenza Virus Strains Increase over Time: A Longitudinal Analysis. *Science Translational Medicine* 5:198ra107–198ra107.

[153] Henry C, et al. (2019) Influenza Virus Vaccination Elicits Poorly Adapted B Cell Responses in Elderly Individuals. *Cell Host & Microbe* 25:357–366.e6.

[154] Ranjeva S, et al. (2019) Age-specific differences in the dynamics of protective immunity to influenza. *Nature Communications* 10:1660.

[155] Tangye SG, Avery DT, Deenick EK, Hodgkin PD (2003) Intrinsic Differences in the Proliferation of Naive and Memory Human B Cells as a Mechanism for Enhanced Secondary Immune Responses. *The Journal of Immunology* 170:686–694.

[156] Tomayko MM, et al. (2008) Systematic Comparison of Gene Expression between Murine Memory and Naive B Cells Demonstrates That Memory B Cells Have Unique Signaling Capabilities. *The Journal of Immunology* 181:27–38.

[157] Arulraj T, Binder SC, Robert PA, Meyer-Hermann M (2021) Germinal Centre Shutdown. *Frontiers in Immunology* 12:2730.

[158] Dugan HL, et al. (2020) Preexisting immunity shapes distinct antibody landscapes after influenza virus infection and vaccination in humans. *Science Translational Medicine* 12.

[159] Kim JH, Skountzou I, Compans R, Jacob J (2009) Original Antigenic Sin Responses to Influenza Viruses. *The Journal of Immunology* 183:3294–3301.

[160] Kim JH, Davis WG, Sambhara S, Jacob J (2012) Strategies to alleviate original antigenic sin responses to influenza viruses. *Proceedings of the National Academy of Sciences* 109:13751–13756.

[161] De Boer RJ, Perelson AS (1994) T Cell Repertoires and Competitive Exclusion. *Journal of Theoretical Biology* 169:375–390.

[162] De Boer RJ, Perelson AS (1997) Competitive control of the self-renewing T cell repertoire. *International Immunology* 9:779–790.

[163] De boer RJ, Freitas AA, Perelson AS (2001) Resource Competition Determines Selection of B Cell Repertoires. *Journal of Theoretical Biology* 212:333–343.

[164] Desponds J, Mayer A, Mora T, Walczak AM (2021) in *Mathematical, Computational and Experimental T Cell Immunology*, eds Molina-París C, Lythe G (Springer International Publishing, Cham), pp 203–221.

[165] Stirk ER, Molina-París C, van den Berg HA (2008) Stochastic niche structure and diversity maintenance in the T cell repertoire. *Journal of Theoretical Biology* 255:237–249.

[166] Stirk ER, Lythe G, van den Berg HA, Molina-París C (2010) Stochastic competitive exclusion in the maintenance of the naïve T cell repertoire. *Journal of Theoretical Biology* 265:396–410.

[167] Desponds J, Mora T, Walczak AM (2016) Fluctuating fitness shapes the clone-size distribution of immune repertoires. *Proceedings of the National Academy of Sciences* 113:274–279.

[168] Koraichi MB, Ferri S, Walczak AM, Mora T (2022) Inferring the T-cells repertoire dynamics of healthy individuals.

[169] Tellier J, Nutt SL (2019) Plasma cells: The programming of an antibody-secreting machine. *European Journal of Immunology* 49:30–37.

[170] Segel LA, Perelson AS (1989) Shape space: an approach to the evaluation of cross-reactivity effects, stability and controllability in the immune system. *Immunology Letters* 22:91–99.

[171] Peters J, Schaal S (2008) Reinforcement learning of motor skills with policy gradients. *Neural Networks* 21:682–697.

[172] Victora GD, Nussenzweig MC (2012) Germinal Centers. *Annual Review of Immunology* 30:429–457.

[173] Eisen HN, Siskind GW (1964) Variations in Affinities of Antibodies during the Immune Response *. *Biochemistry* 3:996–1008.

[174] Weinstein JA, Jiang N, White RA, Fisher DS, Quake SR (2009) High-Throughput Sequencing of the Zebrafish Antibody Repertoire. *Science* 324:807–810.

[175] Mora T, Walczak AM (2019) in *Systems Immunology* (CRC Press).

[176] Kocks C, Rajewsky K (1988) Stepwise intraclonal maturation of antibody affinity through somatic hypermutation. *Proceedings of the National Academy of Sciences* 85:8206–8210.

[177] Kepler TB (2013) Reconstructing a B-cell clonal lineage. I. Statistical inference of unobserved ancestors. *F1000Research* 2:103.

[178] Yaari G, Kleinstein SH (2015) Practical guidelines for B-cell receptor repertoire sequencing analysis. *Genome Medicine* 7:121.

[179] Ralph DK, Iv FAM (2016) Likelihood-Based Inference of B Cell Clonal Families. *PLOS Computational Biology* 12:e1005086.

[180] Liao HX, et al. (2013) Co-evolution of a broadly neutralizing HIV-1 antibody and founder virus. *Nature* 496:469–476.

[181] Nourmohammad A, Otwinowski J, Łuksza M, Mora T, Walczak AM (2019) Fierce Selection and Interference in B-Cell Repertoire Response to Chronic HIV-1. *Molecular Biology and Evolution* 36:2184–2194.

[182] Jiang N, et al. (2013) Lineage Structure of the Human Antibody Repertoire in Response to Influenza Vaccination. *Science Translational Medicine* 5:171ra19–171ra19.

[183] Horns F, Vollmers C, Dekker CL, Quake SR (2019) Signatures of selection in the human antibody repertoire: Selective sweeps, competing subclones, and neutral drift. *Proceedings of the National Academy of Sciences* 116:1261–1266.

[184] Smith KGC, Light A, Nossal GJV, Tarlinton DM (1997) The extent of affinity maturation differs between the memory and antibody-forming cell compartments in the primary immune response. *The EMBO Journal* 16:2996–3006.

[185] Oprea M, Perelson AS (1997) Somatic mutation leads to efficient affinity maturation when centrocytes recycle back to centroblasts. *The Journal of Immunology* 158:5155–5162.

[186] Oprea M, Van Nimwegen E, Perelson AS (2000) Dynamics of one-pass germinal center models: Implications for affinity maturation. *Bulletin of Mathematical Biology* 62:121–153.

[187] Kepler TB, Perelson AS (1993) Somatic Hypermutation in B Cells: An Optimal Control Treatment. *Journal of Theoretical Biology* 164:37–64.

[188] Wang S, et al. (2015) Manipulating the Selection Forces during Affinity Maturation to Generate Cross-Reactive HIV Antibodies. *Cell* 160:785–797.

[189] Sachdeva V, Husain K, Sheng J, Wang S, Murugan A (2020) Tuning environmental timescales to evolve and maintain generalists. *Proceedings of the National Academy of Sciences* 117:12693–12699.

[190] Molari M, Eyer K, Baudry J, Cocco S, Monasson R (2020) Quantitative modeling of the effect of antigen dosage on B-cell affinity distributions in maturating germinal centers. *eLife* 9:e55678.

[191] Grenfell BT (2004) Unifying the Epidemiological and Evolutionary Dynamics of Pathogens. *Science* 303:327–332.

[192] Blanquart F, Gandon S (2013) Time-shift experiments and patterns of adaptation across time and space. *Ecology Letters* 16:31–38.

[193] Cobey S, Wilson P, Matsen FA (2015) The evolution within us. *Philosophical Transactions of the Royal Society B: Biological Sciences* 370:20140235.

[194] Koelle K, Cobey S, Grenfell B, Pascual M (2006) Epochal Evolution Shapes the Phylodynamics of Interpandemic Influenza A (H3N2) in Humans. *Science* 314:1898–1903.

[195] Hoskins TW, Davies J, Smith AJ, Miller C, Allchin A (1979) Assessment of inactivated influenza-A vaccine after three outbreaks of influenza A at Christ's Hospital. *The Lancet* 313:33–35.

[196] Vatti A, et al. (2017) Original antigenic sin: A comprehensive review. *Journal of Autoimmunity* 83:12–21.

[197] Smith DJ, Forrest S, Ackley DH, Perelson AS (1999) Variable efficacy of repeated annual influenza vaccination. *Proceedings of the National Academy of Sciences* 96:14001–14006.

[198] Linderman SL, Hensley SE (2016) Antibodies with 'Original Antigenic Sin' Properties Are Valuable Components of Secondary Immune Responses to Influenza Viruses. *PLOS Pathogens* 12:e1005806.

[199] Perelson AS, Oster GF (1979) Theoretical studies of clonal selection: Minimal antibody repertoire size and reliability of self-non-self discrimination. *Journal of Theoretical Biology* 81:645–670.

[200] Cohen C, et al. (2021) Asymptomatic transmission and high community burden of seasonal influenza in an urban and a rural community in South Africa, 2017–18 (PHIRST): A population cohort study. *The Lancet Global Health* 9:e863–e874.

[201] Oidtman RJ, et al. (2021) Influenza immune escape under heterogeneous host immune histories. *Trends in Microbiology* 29:1072–1082.

[202] Nakagawa R, et al. (2021) Permissive selection followed by affinity-based proliferation of GC light zone B cells dictates cell fate and ensures clonal breadth. *Proceedings of the National Academy of Sciences* 118.

[203] Tas JMJ, et al. (2016) Visualizing antibody affinity maturation in germinal centers. *Science* 351:1048–1054.

[204] Kuraoka M, et al. (2016) Complex Antigens Drive Permissive Clonal Selection in Germinal Centers. *Immunity* 44:542–552.

[205] Briney B, Inderbitzin A, Joyce C, Burton DR (2019) Commonality despite exceptional diversity in the baseline human antibody repertoire. *Nature* 566:393–397.

[206] Mora T, Walczak AM, Bialek W, Callan CG (2010) Maximum entropy models for antibody diversity. *Proceedings of the National Academy of Sciences* 107:5405–5410.

[207] Spisak N, Walczak AM, Mora T (2020) Learning the heterogeneous hypermutation landscape of immunoglobulins from high-throughput repertoire data. *Nucleic Acids Research* 48:10702–10712.

[208] Chakraborty AK (2017) A Perspective on the Role of Computational Models in Immunology. *Annual Review of Immunology* 35:403–439.

[209] Moon JJ, et al. (2007) Naive CD4+ T Cell Frequency Varies for Different Epitopes and Predicts Repertoire Diversity and Response Magnitude. *Immunity* 27:203–213.

[210] Turner JS, et al. (2020) Human germinal centres engage memory and naive B cells after influenza vaccination. *Nature* 586:127–132.

[211] Mesin L, et al. (2020) Restricted Clonality and Limited Germinal Center Reentry Characterize Memory B Cell Reactivation by Boosting. *Cell* 180:92–106.e11.

[212] Wong R, et al. (2020) Affinity-Restricted Memory B Cells Dominate Recall Responses to Heterologous Flaviviruses. *Immunity* 53:1078–1094.e7.

[213] Gaimann MU, Nguyen M, Desponds J, Mayer A (2020) Early life imprints the hierarchy of T cell clone sizes. *eLife* 9:e61639.

[214] Bauke H, Mertens S (2007) Random numbers for large-scale distributed Monte Carlo simulations. *Physical Review E* 75:066701.

[215] Cartis C, Fiala J, Marteau B, Roberts L (2019) Improving the Flexibility and Robustness of Model-based Derivative-free Optimization Solvers. *ACM Transactions on Mathematical Software* 45:32:1–32:41.

[216] Rouzine IM, Rozhnova G (2018) Antigenic evolution of viruses in host populations. *PLOS Pathogens* 14:e1007291.

[217] Fischer A, Vázquez-García I, Mustonen V (2015) The value of monitoring to control evolving populations. *Proceedings of the National Academy of Sciences* 112:1007–1012.

[218] Lässig M, Mustonen V (2020) Eco-evolutionary control of pathogens. *Proceedings of the National Academy of Sciences* 117:19694–19704.

[219] Fisher RA (1937) The Wave of Advance of Advantageous Genes. *Annals of Eugenics* 7:355–369.

[220] Tsimring LS, Levine H, Kessler DA (1996) RNA Virus Evolution via a Fitness-Space Model. *Physical Review Letters* 76:4440–4443.

[221] Cohen E, Kessler DA, Levine H (2005) Front propagation up a reaction rate gradient. *Physical Review E* 72:066126.

[222] Sasaki A, Haraguchi Y (2000) Antigenic Drift of Viruses Within a Host: A Finite Site Model with Demographic Stochasticity. *Journal of Molecular Evolution* 51:245–255.

[223] Minayev P, Ferguson N (2009) Incorporating demographic stochasticity into multi-strain epidemic models: application to influenza A. *Journal of The Royal Society Interface* 6:989–996.

[224] Haraguchi Y, Sasaki A (1997) Evolutionary pattern of intra–host pathogen antigenic drift: effect of cross–reactivity in immune response. *Philosophical Transactions of the Royal Society of London. Series B: Biological Sciences* 352:11–20.

[225] Brunet E, Derrida B (1997) Shift in the velocity of a front due to a cutoff. *Physical Review E* 56:2597–2604 Publisher: American Physical Society.

[226] van Saarloos W (2003) Front propagation into unstable states. *Physics Reports* 386:29–222.

[227] Neher RA, Hallatschek O (2013) Genealogies of rapidly adapting populations. *Proceedings of the National Academy of Sciences* 110:437–442.

[228] Frank SA (1996) Models of Parasite Virulence. *The Quarterly Review of Biology* 71:37–78.

[229] Lipsitch M, Siller S, Nowak MA (1996) The Evolution of Virulence in Pathogens with Vertical and Horizontal Transmission. *Evolution* 50:1729–1741.

[230] Lenski RE, May RM (1994) The Evolution of Virulence in Parasites and Pathogens: Reconciliation Between Two Competing Hypotheses. *Journal of Theoretical Biology* 169:253–265.

[231] Messenger SL, Molineux IJ, Bull JJ (1999) Virulence evolution in a virus obeys a trade off. *Proceedings of the Royal Society of London. Series B: Biological Sciences* 266:397–404.

[232] Alizon S, van Baalen M (2005) Emergence of a convex trade-off between transmission and virulence. *The American Naturalist* 165:E155–E167.

[233] Belshaw R, Gardner A, Rambaut A, Pybus OG (2008) Pacing a small cage: mutation and RNA viruses. *Trends in Ecology & Evolution* 23:188–193.

[234] Duffy S (2018) Why are RNA virus mutation rates so damn high? *PLOS Biology* 16:e3000003.

[235] Peck KM, Lauring AS (2018) Complexities of Viral Mutation Rates. *Journal of Virology.*

[236] Gabriel W, Lynch M, Burger R (1993) Muller's Ratchet and Mutational Meltdowns. *Evolution* 47:1744–1757.

[237] Bull JJ, Meyers LA, Lachmann M (2005) Quasispecies Made Simple. *PLOS Computational Biology* 1:e61.

[238] Silander OK, Tenaillon O, Chao L (2007) Understanding the Evolutionary Fate of Finite Populations: The Dynamics of Mutational Effects. *PLOS Biology* 5:e94.

[239] Sasaki A (1994) Evolution of Antigen Drift/Switching: Continuously Evading Pathogens. *Journal of Theoretical Biology* 168:291–308.

[240] Kamp C, Wilke CO, Adami C, Bornholdt S (2002) Viral evolution under the pressure of an adaptive immune system: Optimal mutation rates for viral escape. *Complexity* 8:28–33.

[241] Grubaugh ND, Cobey S (2021) Of variants and vaccines. *Cell* 184:6222–6223.

[242] Nussbaumer HJ (1981) in *Fast Fourier Transform and Convolution Algorithms*, Springer Series in Information Sciences, ed Nussbaumer HJ (Springer, Berlin, Heidelberg), pp 80–111.

[243] Pogorelyy MV, et al. (2019) Detecting T cell receptors involved in immune responses from single repertoire snapshots. *PLOS Biology* 17:e3000314.

[244] Glanville J, et al. (2017) Identifying specificity groups in the T cell receptor repertoire. *Nature* 547:94–98.

[245] Dash P, et al. (2017) Quantifiable predictive features define epitope-specific T cell receptor repertoires. *Nature* 547:89–93.

[246] Madi A, et al. (2017) T cell receptor repertoires of mice and humans are clustered in similarity networks around conserved public CDR3 sequences. *eLife* 6:e22057.

[247] Kidera A, Konishi Y, Oka M, Ooi T, Scheraga HA (1985) Statistical analysis of the physical properties of the 20 naturally occurring amino acids. *Journal of Protein Chemistry* 4:23–55.

[248] Kidera A, Konishi Y, Ooi T, Scheraga HA (1985) Relation between sequence similarity and structural similarity in proteins. Role of important properties of amino acids. *Journal of Protein Chemistry* 4:265–297.

[249] Mannella R, Palleschi V (1989) Fast and precise algorithm for computer simulation of stochastic differential equations. *Phys. Rev. A* 40:3381–3386.

[250] Brünger A, Brooks CL, Karplus M (1984) Stochastic boundary conditions for molecular dynamics simulations of st2 water. *Chemical Physics Letters* 105:495 – 500.

[251] Cavagna A, Queirós SMD, Giardina I, Stefanini F, Viale M (2013) Diffusion of individual birds in starling flocks. *Proceedings of the Royal Society B* 280.

[252] Dyson FJ (1956) General theory of spin-wave interactions. *Physical Review* 102:1217.

[253] Redner S (2001) *A Guide to First-Passage Processes* (Cambridge University Press, Cambridge).

RÉSUMÉ

Les réseaux biologiques sont des collections d'entités biologiquement actives qui s'auto-organisent pour assurer une fonction émergente. Par exemple, les oiseaux s'alignent collectivement en nuées pour augmenter leur capacité à échapper aux prédateurs, et les cellules immunitaires s'organisent en divers sous-ensembles de cellules pour assurer une protection efficace contre les infections.
Dans les nuées d'oiseaux, le nombre d'oiseaux est faible et leurs interactions sont locales dans l'espace et le temps. Pour décrire ce système biologique, nous adoptons dans la première partie de cette thèse une approche de physique statistique utilisant des modèles de Langevin sur- et sous-amortis. Nous développons un nouveau schéma d'inférence Bayésien pour les modèles stochastiques du second ordre en équilibre et hors équilibre, et nous relions l'échec des schémas d'inférence naïfs au problème de l'inférence des équations du mouvement à partir de dynamiques partiellement observées. Nous démontrons ensuite l'applicabilité de notre approche à un modèle récent de mouvement collectif des nuées d'oiseaux.
En revanche, dans le système immunitaire le nombre de cellules est presque incalculable et leurs interactions vont de l'échelle moléculaire à l'échelle de l'organisme. Pour contourner ce problème, nous développons dans la deuxième partie de cette thèse un nouveau modèle décrivant l'organisation du système immunitaire comme résultant d'un principe d'optimalité. En maximisant la protection à long terme et en minimisant l'utilisation de ressources à court terme, nous démontrons l'existence de stratégies immunitaires optimales correspondant à des sous-ensembles du répertoire de lymphocytes B quantifiés expérimentalement. En outre, nous rationalisons le phénomène de l'empreinte antigénique, ou "péché antigénique originel", comme une stratégie immunitaire optimale à long terme.
Dans la dernière partie de cette thèse, nous étudions comment, à son tour, la pression immunitaire d'une population hôte influence l'évolution virale. Nous constatons que la stratégie virale optimale sur le plan évolutif maximise le taux d'évolution antigénique lorsque l'immunité croisée est faible et maximise le taux de reproduction de base lorsqu'elle devient plus importante. En conséquence, nous montrons qu'une faible immunité croisée favorise l'émergence de variants hautement transmissibles et virulents avec des taux de mutation proches du seuil d'extinction.

MOTS CLÉS

Réseaux Biologiques, Immunologie, Modélisation Biophysique, Processus Stochastiques, Inférence Bayesienne, Biologie des Systèmes, Epidémiologie, Evolution

ABSTRACT

Biological networks are collections of biologically active entities self-organizing to provide an emergent function. For example, birds collectively align in flocks to increase their ability to escape predators, and immune cells form diverse subsets of cells to ensure efficient protection against infections.
In bird flocks, the number of birds is small and their interactions are local in space and time. To describe this biological system, we adopt in the first part of this thesis a statistical physics approach using over- and under-damped Langevin models. We develop a new Bayesian inference scheme for second-order stochastic models in equilibrium and out of equilibrium, and we relate the failure of naive inference schemes to the problem of inferring equations of motion from partially observed dynamics. We then demonstrate the applicability of our approach to a recent model of collective motion of flocks of birds.
In the immune system, on the other hand, the number of cells is uncountable and their interactions range from the molecular to the organismal scale. To circumvent this problem, we develop in the second part of this thesis a new model describing the organization of the immune system as the result of an optimality principle. By maximizing long-term protection and minimizing short-term resource costs, we find optimal immune strategies consistent with experimentally quantified subsets of the B cell repertoire. Furthermore, we rationalize the phenomenon of antigenic imprinting, or “original antigenic sin”, as an long-term optimal immune strategy.
In the final part of this thesis, we study how in return the immune pressure of a host population drives viral evolution. We find that the evolutionarily stable viral strategy maximizes the rate of antigenic evolution when cross-immunity is low and maximizes the basic reproduction ratio as it becomes larger. As a result, we show that low cross-immunity favors highly transmissible and virulent variants with mutation rates near the extinction threshold.

KEYWORDS

Biological Networks, Immunology, Biophysical Modeling, Stochastic Processes, Bayesian Inference, Systems Biology, Epidemiology, Evolution